Texas Tech University

Multidisciplinary Research in Transportation

Optimizing Reinforcing Steel in 12-in and 13-in Continuously Reinforced Concrete Pavement (CRCP)

Heejun Lee, Niwesh Koirala, Fouzieh Rouzmehr, Christopher Jabonero, and Moon C. Won

Performed in cooperation with the Texas Department of Transportation and the Federal Highway Administration

Research Project 0-7026
Research Report 0-7026-R1
https://library.ctr.utexas.edu/hostedpdfs/texastech/0-7026-1.pdf

1. Report No. FHWA/TX-23/0-7026-1	2. Government Accession No.:	3. Recipient's Catalog No.:
4. Title and Subtitle: Optimizing Reinforcing Steel in 12-in and 13-in Continuously Reinforced Concrete Pavement (CRCP)		5. Report Date: August 2023
7. Author(s): Heejun Lee, Niwesh Koirala, Fouzieh Rouzmehr, Christopher Jabonero, and Moon Won		8. Performing Organization Report No. 0-7026-R1
9. Performing Organization Name and Address: Texas Tech University College of Engineering Box 41023 Lubbock, Texas 79409-1023		10. Work Unit No.(TRAIS): 11. Contract or Grant No.: Project 0-7026
12. Sponsoring Agency Name and Address: Texas Department of Transportation Research and Technology Implementation Division 125 E. 11th Street Austin, TX 78701		13. Type of Report and Period Technical Report September 2019 – August 2022 14. Sponsoring Agency Code:
15. Supplementary Notes: Project performed in cooperation with Texas Department of Transportation and the Federal Highway Administration		

16. Abstract: The performance of continuously reinforced concrete pavement (CRCP) in Texas has been excellent. However, truck traffic in Texas has been increasing, which required thicker slabs. Since TxDOT placed steel at the mid-depth of the slab, the use of thicker slabs increased the distance between top of the slab and longitudinal steel. This increase resulted in larger crack spacing and occasional horizontal cracking. Continued wheel loading applications degrade the top half of the concrete and partial depth distress. Traditionally, punchout has been reported as a major and only structural distress in CRCP. However, it has been observed that different types of cracking and resulting distresses have taken place in CRCP that has had improved design features such as thicker slabs, stabilized bases, and tied concrete shoulders. These cracks, which cannot be explained by traditional theories related to punchout and spalling, are normally associated with horizontal cracking at approximately mid-depth of the slab. This horizontal cracking has been observed in CRCP with thicker slabs, thickness of 12 inches or larger. It was also observed that horizontal cracks occurred at early ages before the pavement was open to traffic. These findings strongly indicate that horizontal cracks are not due to structural deficiencies of CRCP. Rather, concrete material properties, environmental conditions during and right after concrete placement, and most importantly longitudinal steel placement layouts must play a significant role in the development of horizontal cracking. The primary objective of this study is to identify the mechanisms and associated variables of horizontal cracking in CRCP and to develop mitigation methodologies. To this end, theoretical analyses of early-age CRCP behavior were conducted using 3-dimensional CRCP modeling, and field testing was conducted at 4 different CRCP construction projects. The behavior of CRCP at early ages under environmental loading (temperature and moisture variations) obtained from the field testing was compared with numerical analysis results and the model was calibrated. The effect of each variable related to design, material, and construction on the horizontal cracking potential was evaluated through comprehensive numerical analysis with a calibrated model. One of the major findings is that steel depth has significant effects on CRCP behavior and a modest decrease in the distance between slab surface and steel depth reduces horizontal cracking potential substantially. It is expected that the implementation of the findings from this study is expected to improve CRCP performance substantially for thicker CRCP.

17. Key Words: CRCP, Horizontal Cracking, Punchout	18. Distribution Statement No Restrictions. This document is available to the public through the National Technical Information Service, Springfield, VA 22161, www.ntis.gov		
19. Security Classif. (of this report) Unclassified	20. Security Classif. (of this page) Unclassified	21. No. Of Pages 271	22. Price

TEXAS TECH UNIVERSITY
Multidisciplinary Research *in* Transportation

Optimizing Reinforcing Steel in 12-in and 13-in Continuously Reinforced Concrete Pavement (CRCP)

Heejun Lee
Graduate Student, MSCE
Center for Multidisciplinary Research in Transportation
Texas Tech University

Niwesh Koirala
Graduate Student, MSCE
Center for Multidisciplinary Research in Transportation
Texas Tech University

Fouzieh Rouzmehr
Graduate Research Assistant, MSCE
Center for Multidisciplinary Research in Transportation
Texas Tech University

Christopher Jabonero
Post-Doctoral Researcher, Ph.D.
Center for Multidisciplinary Research in Transportation
Texas Tech University

Moon C. Won
Professor, P.E., Ph.D.
Civil, Environmental, and Construction Engineering
Texas Tech University

Project Number: 0-7026
Project Title: *Optimizing Reinforcing Steel in 12-in and 13-in Continuously Reinforced Concrete Pavement (CRCP)*
Research Report Number: 0-7026-R1

Conducted for the Texas Department of Transportation

AUTHOR'S DISCLAIMER

The contents of this report reflect the views of the authors who are responsible for the facts and the accuracy of the data presented herein. The contents do not necessarily reflect the official view of policies of the Texas Department of Transportation or the Federal Highway Administration. This report does not constitute a standard, specification, or regulation.

PATENT DISCLAIMER

There was no invention or discovery conceived or first actually reduced to practice in the course of or under this contract, including any art, method, process, machine, manufacture, design or composition of matter, or any new useful improvement thereof, or any variety of plant which is or may be patentable under the patent laws of the United States of America or any foreign country.

ENGINEERING DISCLAIMER

Not intended for construction, bidding, or permit purposes.

TRADE NAMES AND MANUFACTURERS' NAMES

The United States Government and the State of Texas do not endorse products or manufacturers.

Trade or manufacturers' names appear herein solely because they are considered essential to the object of this report.

ACKNOWLEDGMENTS

This research study was sponsored by the Texas Department of Transportation in cooperation with the Federal Highway Administration. The support provided by the Project Team of this project – Mr. Andy Naranjo, Ms. Rachel Cano, Mr. Ruben Carrasco, and Mr. Pangil Choi – is greatly appreciated. The support provided by Mr. Hal Stanford and Mr. Joe With of HNTB, Raba Kistner Inc, and Jordan Foster Construction LLC for the field testing is greatly appreciated.

Table of Contents

List of Figures

List of Tables

Chapter 1 Introduction

Punchout has been reported as a major and only structural distress in continuously reinforced concrete pavement (CRCP). However, it has been observed that different types of cracking, other than normal transverse cracks, and resulting distresses have taken place in CRCP with improved design and construction practices such as thicker slabs, stabilized bases, and tied concrete shoulders. These “other” cracks, which have not been identified by traditional theories related to concrete volume changes due to temperature and moisture variations and resulting warping/curling, take place at the depth of longitudinal steel and in the horizontal direction. This horizontal cracking has been normally observed in CRCP with thicker slabs, thickness of 12 inches or larger. It was also observed that horizontal cracks must have occurred at early ages before the pavement was open to traffic. These findings strongly indicate that horizontal cracks are not due to structural deficiencies of CRCP. Rather, concrete material properties, environmental conditions during and right after concrete placement, and longitudinal steel placement layouts might play a significant role in the development of horizontal cracking. More specifically, steel placement depth, or the distance between concrete slab surface and longitudinal steel, appears to play an important role, since these horizontal cracking is rarely observed in CRCP with small slab thicknesses. In Texas, as the truck traffic volume increased and pavement design life was increased from 20 years to 30 years, slab thicknesses increased from 6 inches in the 1960s to 15 inches in the late 1980s. The Texas Department of Transportation (TxDOT) traditionally placed longitudinal steel at the mid-depth of the slab. The primary reason for this practice was the premise that placing steel at where concrete stresses due to environmental loading – temperature and moisture variations – were the smallest would minimize potential debonding between concrete and steel, thus limiting crack widths to a minimum. This practice stayed the same while the slab thicknesses increased, resulting in larger distances between slab surface and longitudinal steel for thicker slabs. This practice reduced the effectiveness of longitudinal steel on concrete volume changes due to environmental loading, which resulted in larger transverse crack spacing and a higher potential for horizontal cracking. Even though the depth of longitudinal steel could have significant effects on transverse crack spacing and horizontal cracking, most of the research on steel design in CRCP was focused on the amount of longitudinal steel needed, not on the optimum location or the depth of the longitudinal steel. The primary objective of this study was to identify the optimum depth of longitudinal steel in CRCP by investigating the mechanisms of horizontal cracking in CRCP. To this end, mechanistic behavior of CRCP at early ages under various design and environmental conditions was investigated and compared with actual CRCP behavior obtained from field testing. A factorial experiment that included a number of design, materials and construction variables, such as slab thickness and steel depth, coefficient of thermal expansion (CTE) and modulus of concrete, and setting and seasonal minimum temperatures of concrete, was developed and CRCP mechanistic behavior was evaluated for each combination of the variables (cell) using 3-dimensional finite element method (FEM). Field experiments were limited to 4 test sections, and extensive information on CRCP behavior as affected by the selected variables was obtained, which included concrete strains in longitudinal and vertical directions, slab curling behavior and steel strains. The behavior of CRCP thus obtained was compared with numerical analysis results. It is expected that this study could help develop or improve design standards and/or material or construction specifications to prevent horizontal cracking and associated distresses in CRCP.

Scope of the Report

This report comprises seven (7) chapters.

Chapter 2 presents a discussion on the distresses in CRCP, specifically on spalling, punchouts and failures at the transverse construction joints (TCJ).

Chapter 3 discusses horizontal cracking in CRCP, its mechanisms and the resulting distresses.

Chapter 4 covers the discussion on the analysis of the structural responses of CRCP, particularly the concrete principal stresses at the location of the longitudinal steel that could initiate horizontal cracking. FEM simulations were conducted for one-mat and two-mat steel designs. The factors considered in the simulations are slab thickness, steel depth, concrete CTE and modulus, temperature drop from concrete setting to minimum temperature, ultimate drying shrinkage, temperature variation through the slab, modulus of subgrade reaction and crack spacing.

Chapter 5 provides an overview of the field-testing programs conducted throughout the research project and a detailed analysis of the results of all the instrumentation activities using the acquired data. This chapter presents the site information, material properties, and field-testing plan, including sensor information and gauge installation setup. Subsequently, a comprehensive discussion is provided on the results covering the temperature and strain patterns, crack distribution over time and concrete and steel strain analysis related to varying environmental conditions.

Chapter 6 presents the results of the calibration of the FEM model using the actual data acquired from the field-tests. The calibrated model was then used to estimate the structural responses of CRCP with various design, materials and construction conditions to develop optimum steel depths for various slab thicknesses.

Chapter 7 summarizes the findings and conclusions of this study and presents recommendations on the optimum steel configuration in CRCP to prevent horizontal cracking.

Chapter 2 Distresses in CRCP

Traditionally, only 2 distress types have been identified in CRCP, even though other distress types exist. One is spalling and the other is punchout. Spalling is not a structural distress; it is related to concrete material, more specifically, coarse aggregate type used, whereas punchout is a structural distress, caused by deficiencies in CRCP structural capacity. Other distress types in CRCP include distresses at transverse construction joints (TCJs) or at repair joints. These “other distress types” have more to do with construction/repair quality than design issues, and brief discussions will be made.

2.1 Spalling

Spalling in CRCP is defined as the cracking, breaking, chipping, or fraying of slab edges within 2.4 inches of a crack (Miller, et al, 2003). In CRCP, spalls are primarily caused by high deflections, infiltration of incompressible materials, weak concrete, or the corrosion of reinforcing steel. Secondary causes include reinforcement misalignment, inadequate concrete cover, and materials-related distresses. However, most of the spalling in Texas are observed when siliceous river gravel (SRG) is used as coarse aggregates, but not by the mechanisms described in the study by Miller, et al. Figure 2.1 illustrates typical spalling observed in Texas. This project – 10-in CRCP + 1-in ASB + 6-in CTB on BW-8 frontage road in Houston eastbound just east of Antoine Dr – was placed in November 1989. The pavement is about 33 years old when this picture was taken. There have been numerous spalling distresses in this project and repairs made continuously over the years. The spalling shown in Figure 2.1 occurred after decades of service. In this project, crushed limestone was also used in other areas, and no single spalling occurred in those areas, indicating that spalling in CRCP has more to do with coarse aggregate type than any other factors.

There are more than 100 coarse aggregate quarries in TxDOT Aggregate Quality Monitoring Program (AQMP) and the majority of the coarse aggregate types produced in those quarries is either crushed limestone (CLS) or SRG. TxDOT has understood the propensity of spalling when SRG is used in CRCP, but also recognized the importance of utilizing local coarse aggregates in PCC pavements. To maximize the use of local coarse aggregates in CRCP construction, TxDOT has sponsored numerous research projects since the middle of 1980s, with the primary objective of identifying ways to eliminate spalling when SRG is used. Unfortunately, despite decades of research on spalling, no good methods were identified that could eliminate spalling when SRG is used. It is because spalling mechanism is quite complicated, with a number of factors involved, as well as the time it takes for spalling to take place being as long as 30 years or more. The last research study on spalling found a good correlation between CTE of concrete and spalling in CRCP, and recommended limiting the CTE of concrete to 5.5 microstrain/ºF. This recommendation was implemented at TxDOT, and it is expected that spalling will not be a problem in Texas.

Figure 2.1 Typical spalling in CRCP observed in Texas

2.2 Punchouts

Per FHWA document, punchout is defined as an area enclosed by two closely spaced (usually < 2-ft) transverse cracks, a short longitudinal crack, and the edge of the pavement or a longitudinal joint. Punchout also includes "Y" cracks that exhibit spalling, breakup, or faulting. Figure 2.2 is an example of punchout presented in several documents (NCHRP 1-37, Jeff, Wouter). The most commonly cited theory describes how traffic loads induce high-tensile stresses at the top of the slab in the transverse direction (perpendicular to the direction of traffic) between two closely spaced transverse cracks. If the subbase shifts or pumps between the two transverse cracks, the small concrete segment can deflect and bend like a cantilever beam. As the deflections increase, the cracks wear out, and the load transfer decreases. Crack widths subsequently begin to increase, and the transverse cracks eventually spall and fault. Finally, a longitudinal crack develops in this cantilevered section, and a punchout results. Time and traffic increase the severity of a punchout as the distressed area continues to push down into the subbase and subgrade materials. In this theory, punchout is caused by fatigue failure of concrete at the top of the concrete slab (i.e., longitudinal crack at the top of the slab between two closely spaced transverse cracks). Another theory, which is quite similar to the theory just described, is as follows:

1. Presence of narrow transverse crack spacing (2-ft or less) in the crack spacing distribution
2. Loss of load transfer efficiency (LTE) across the transverse cracks due to aggregate interlock deterioration from excessive crack opening and heavy repeated loads

3. Loss of support along the pavement edge due to base erosion
4. Negative temperature gradients through the slab thickness and top of the slab drying shrinkage further magnify bending stresses.
5. Passage of heavy axles causing repetitive cycles of excessive tensile bending stresses leading to longitudinal fatigue cracking that defines the punchout.

Figure 2.3 illustrates the above punchout development process.

Figure 2.2 CRCP distress presented as a punchout in several documents

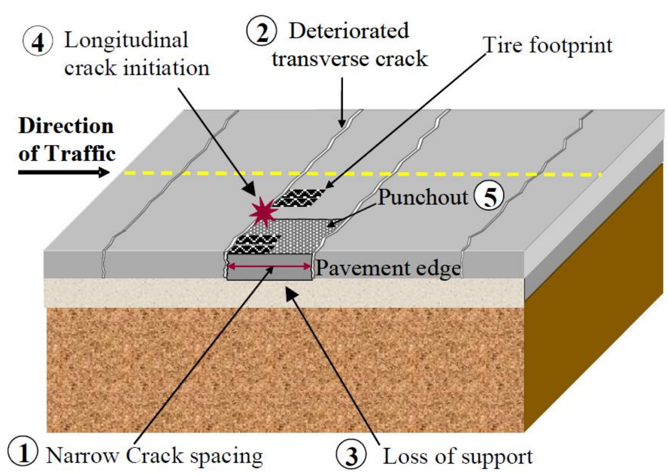

Figure 2.3 Punchout distress process adopted in MEPDG

A major difference between these two theories is that the latter one includes degradation in the slab support, while the former one does not. In other words, the former theory assumes the longitudinal crack between two closely-spaced transverse cracks is due to pure fatigue damage with uniform slab support, while the latter theory incorporates degradation in the base and its effects in the process. On the other hand, they share common attributes in punchout development – narrow transverse crack spacing, degradation in transverse crack LTEs and top-down nature of longitudinal crack. However, extensive field evaluations of punchouts in Texas reveal that those three attributes in punchout process in the two theories – narrow crack spacing, crack degradations and resulting low LTEs, and top-down longitudinal cracking – are not correct.

First, narrow crack spacing does not necessarily cause punchout. CRCP shown in Figure 2.4 – 8-in CRCP + 6-in ACP base on US 287 in the Fort Worth District (CSJ: 013-08-044), was built in March, 1969. Slab segments with quite narrow crack spacing did not develop into punchout. The latest traffic data indicates 33,241 AADT in 2021 for both directions with 30 % BC on this highway. Even though it is not known when those cracks occurred, considering the age of the pavement (51 years when the pictures were taken), this slab segments with narrow crack spacing endured a large number of truck traffic without causing punchout distresses.

Figure 2.4-(a) Y-crack with no distress (left); (b) Short crack spacing (right)

Figure 2.5 shows a punchout distress on IH 45 in Dallas. This 8-in CRCP on 6-in soil cement base was completed in October 1975 (CSJ: 092-14-016). The latest traffic data indicates 88,744 AADT in 2021 for both directions with 19 % BC on this highway. The pavement was 46 years old when the picture was taken. The distress shown here meets the definition of a punchout; however, the crack spacing is 5.5-ft, which is considered within an ideal range per the AASHTO, which is between 3.5-ft and 8.0-ft. Another observation is that the two transverse cracks have not deteriorated, which implies that this punchout distress was caused by neither narrow crack spacing nor deteriorated transverse cracks. Rather, it appears that degradation in the slab support increased slab deflections, which further exacerbated the condition of the slab support.

The pavement conditions shown in Figures 2.4 and 2.5 do not necessarily indicate that CRCP slab segments with a larger crack spacing have higher probability of punchouts than those with a smaller crack spacing. Rather, it implies that transverse crack spacing may not be a primary factor for punchout development.

Figure 2.5 Punchout distress with a medium crack spacing

Figure 2.6 shows another example of a punchout on IH-35W in Denton in the Dallas District. This 8-in CRCP + 2-in ASB + 6-in lime treated subgrade (LTS) was completed in October 1969 (CSJ: 0081-13-005). When this picture was taken, the pavement was 32 years old. There are several observations that could be made:

1) Evidence of pumping is shown at the slab edge.
2) Transverse crack spacing at deteriorated area is relatively small.
3) There are 2 longitudinal cracks within the punchout area.
4) Transverse cracks are quite deteriorated in the outer half of the lane, while those in the inner half of the lane are in a good condition.
5) A half-moon shaped crack developed at pavement edge.

The above observations indicate that the distress developed in accordance with the following sequence:

1) Water penetrated the base/subgrade through the longitudinal joint between concrete slab and asphalt shoulder.

2) Edge slab deflections from truck traffic applications caused degradations in base/subgrade materials and pumping.
3) Repeated truck traffic applications caused further deteriorations in base/subgrade materials and pumping, which resulted in small voids and larger slab deflections.
4) Larger slab deflections caused a top-down half-moon shape crack as well as deteriorations in transverse cracks.
5) Deteriorated transverse cracks allowed water into base/subgrade layers, which further degraded base/subgrade materials.
6) With deteriorated slab support, further applications of truck traffic pushed down concrete slab segment between two deteriorated transverse cracks, causing two longitudinal cracks under the outer wheel path.

Figure 2.6 Punchout distress on IH-35W in Denton, Dallas District

Among the two longitudinal cracks in punchout area, it appears that the one in the middle of the lane was a top-down crack, at least initially as a part of a half-moon shape crack, and the other in the outer wheel path is a bottom-up crack. This punchout did not follow the punchout process described along with Figure 2.3. It is also noted that asphaltic materials were placed over time to make the surface of the punchout area even, indicating that the deteriorated concrete segments continued being pushed down.

Figure 2.7-(a) shows another example of a typical punchout. This 8-in CRCP + 4-in CTB + 4-in Foundation Course (density controlled) on US 287 in Harrold, Wichita Falls District, was

completed in August 1973 (CSJ: 0043-07-023). This picture was taken in 2007, and the pavement was 34 years old. It shows that the punchout distress indeed developed between two narrow transverse cracks. However, close observations reveal the following:

1) Evidence of pumping and depression of pavement edge, as indicated by a longitudinal crack in the asphalt shoulder, is noted. (Severe pumping was observed in this project, as shown in Figure 2.7-(b).)
2) A half-moon shaped longitudinal crack developed.
3) In the punchout distress, the two transverse cracks are quite deteriorated in the outer half of the lane, while those in the inner half of the lane are in a good condition.
4) There are 2 longitudinal cracks under the outside wheel path in the punchout distress area.
5) However, the slab segment between the two narrow transverse cracks next to the punchout distress is in a good condition, as is the slab segment with quite narrow transverse cracks in Figure 2.7-(b).

Figure 2.7-(a) Punchout distress on US 287 in Harrold (left); (b) Severe pumping on US 287 in Harrold (right)

The above observations indicate that the distress developed in accordance with the following sequence:

1) Water penetrated the base/subgrade through the longitudinal joint between concrete slab and asphalt shoulder.
2) Edge slab deflections from truck traffic applications caused degradations in base/subgrade materials and pumping.
3) Repeated truck traffic applications caused further deteriorations in base/subgrade materials and pumping, which resulted in small voids and larger slab deflections.
4) Larger slab deflections caused a top-down half-moon shape crack as well as deteriorations in transverse cracks.
5) Deteriorated transverse cracks allowed water into base/subgrade layers, which further degraded base/subgrade materials.

6) With deteriorated slab support, further applications of truck traffic pushed down concrete slab segment between two deteriorated transverse cracks, causing two longitudinal cracks under the outer wheel path.

This punchout process is quite similar to that on IH-35W in the Dallas District, as shown in Figure 2.6. The narrow transverse cracks were not the cause of this punchout distress; rather, larger deflections due to pumping and potential voids under the slab degraded the two narrow transverse cracks, as they are located towards the end of the half-moon shaped crack.

The distress mechanisms hypothesized in the two punchouts presented indicate:

1) Degradation in the slab support and resulting large slab deflection is the primary cause of punchout distress. (This coincides with the major finding at the AASHO Road Test, where all the distresses developed by pumping.)
2) Those punchouts did not follow one of the hypotheses in punchout mechanisms adopted in MEPDG – increase in crack widths increase over time and resulting decrease in LTE at transverse cracks, along with negative temperature gradient, causes top-down longitudinal cracking and punchout.
3) Where the slab support is degraded, a half-moon shape longitudinal crack occurs first, which is top-down cracking due to wheel loading applications, followed by degradations of two transverse cracks with a narrow spacing in the outer-half of the lane. Finally, a bottom-up longitudinal cracking under the outside wheel path develops between the two narrow transverse cracks, which completes the punchout process.

There are punchout distresses with an appearance somewhat different from the two punchouts presented above. Figure 2.8 shows a distress in 8-in CRCP + 1-in ASB + 6-in cement treated base (CTB) on Loop 610 E connector to IH 10 in Houston, built in the early 1970s. It shows a large longitudinal crack in the middle of the outside lane, which is rather straight, but not of a half-moon shape. Also, concrete slab segmented into a number of smaller pieces, even though the few inches of slab edge was preserved. It appears that the distress mechanisms are similar to those discussed above – deteriorated slab support, top-down longitudinal cracking in the middle of the lane, followed by a longitudinal bottom-up crack under the outside wheel path. It appears that the slab support in the distressed area was much inferior to other areas. It is also observed that transverse cracks in the inside half of the outside lane are quite tight, implying that the distress was not caused by larger crack width/low LTEs. Instead, larger deflections caused deteriorations of transverse cracks. Accordingly, even though the characteristics of this distress may appear to be different from those in the two punchouts presented previously, the distress mechanisms are quite similar.

Figure 2.8-(a) Punchout distress on Loop 610 (left); (b) Punchout on Loop 610 (right)

In the punchout mechanism adopted in the MEPDG, loss of load transfer efficiency (LTE) at transverse cracks is one of the critical elements responsible for the top-down longitudinal cracking between two narrow transverse cracks. It is stated that crack widths increase over time due to continued drying shrinkage of concrete, which reduces LTEs. Figures 2.9 show variations in crack width over time and resulting LTEs from MEPDG. Crack width varies throughout the slab depth, and crack widths shown here are at the depth of longitudinal steel. Figure 2.9-(a) illustrates crack widths vary with temperature condition – small in the summer and large in the winter, which is reasonable – and increase over time, rapidly at first few years and slowly at later years, again due to continued drying shrinkage of concrete. However, field measurements of crack widths for the first 3 years after construction indicate crack widths actually decreased, as shown in Figure 2.10. Researchers placed 6-in long vibrating wire strain gages (VWSGs) at the mid-depth of 11-in thick concrete slab on US 183 in Austin on September 25 in 2003 and induced a transverse crack over the gages. Crack widths were calculated by multiplying concrete strains from VWSGs by the gage length (6-in). This estimation of the crack width is based on the assumption that longitudinal concrete stresses within 3-in longitudinally from the induced crack are negligible. Since concrete stresses near a transverse crack are quite small, it is believed that any errors associated with this assumption could be quite small.

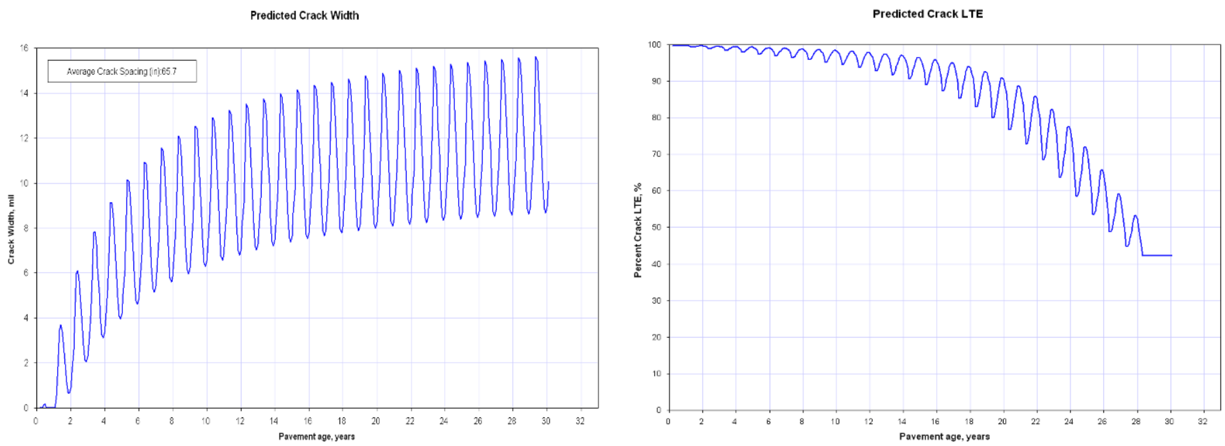

Figure 2.9-(a) Crack width variations over time (left); (b) LTE variations over time (right)

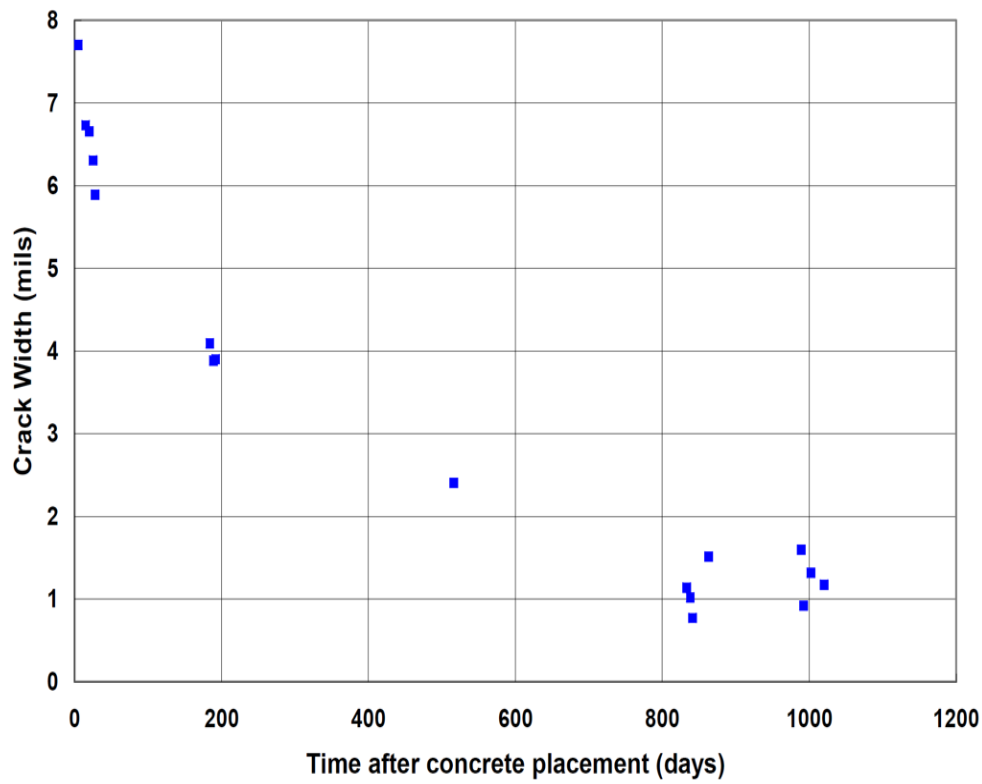

Figure 2.10 Variations of crack width over 3-yr time period

The data in Figure 2.10 is contradictory to the information shown in Figure 2.9-(a). From a theoretical standpoint, the information in Figure 2.9-(a) appears to make sense, since Portland cement concrete undergoes drying shrinkage, and its values increase over time. However, in addition to the information shown in Figure 2.10, there is anecdotal evidence that the concrete in some CRCP projects is in compression, not in tension. Figure 2.11-(a) shows a section of CRCP on IH-45 in Houston. About 100-ft or so of 2 lanes were removed for reconstruction. Next day, slab expanded about 3 inches, as shown in Figure 2.11-(a). A sliding failure occurred at stapling repairs installed at a longitudinal construction joint to prevent lane separations. It implies that the concrete in CRCP was in substantial compression. Another example of concrete in CRCP being in tension is illustrated in Figure 2.11-(b). From the transverse saw cut made for full-depth repairs, it is observed that the existing concrete – bottom left portion – expanded, causing bending of tie bars and failure of repaired concrete.

Figure 2.11-(a) Stapling failure due to slab expansion (left); (b) Failure of full-depth repair due to slab expansion (right)

It has been an accepted theory that concrete in CRCP is in tension and steel stresses at transverse cracks are thus in tension as well, unless concrete temperature is much higher than the setting temperature. The dates of the pictures taken for Figures 2.11-(a) and 2.11-(b) were Oct 3, 2008, and November 12, 2010, respectively, and ambient temperature conditions during a week prior to the pictures were taken were 56°F/87°F (min/max) and 48°F /79°F, respectively. Even though it is not known what the temperature condition was when the pavements shown in Figure 2.11 were placed, it may be unlikely that high temperatures during the repairs are the only cause for the slab expansions. Efforts were made to identify the causes of slab expansions in CRCP, and it appears that construction sequence may contribute to the slab expansions. Figure 2.12-(a) shows the instrumentation for the slab movements at a transverse construction joint. Four LVDTs were installed at a transverse construction joint (TCJ) right after the headers were removed. This 13-in CRCP on US 287 in Iowa Park in the Wichita Falls District was under construction in 2005. The concrete shown was placed on August 25, 2005 (Thursday), and gages were installed on August 26, 2005. The monitoring continued until 4:00 pm on August 28, 2005 (Sunday), when the gages were removed so that the construction crew prepared for concrete placement the next day. Figure 2.12-(b) illustrates the data obtained. It shows that (1) the variations in the LVDT readings at a reference point (LVDT #4) against an invar are small, (2) the differences in the LVDT readings among the rest 3 LVDTs are small as well, (3) slab contractions were a little bit smaller in the middle of the slab compared with the other two locations, and (4) slab contracted as much as 0.2 inches during approximately 1.6 days (from 8 pm of 8/26 to 10 am of 8/28). Since the air temperatures at those two times are quite similar, this contraction appears to be due to primarily drying shrinkage of concrete. During that process, the longitudinal reinforcements in the concrete must be in compression, especially the reinforcing steel close to the TCJ. The slab displacements measured were at close to mid-depth. It is construed that the slab contractions were larger near the slab surface, and smaller near the bottom of the slab than the values shown in Figure 2.12-(b). The data obtained here illustrates the significant effects of drying shrinkage of concrete at early ages on the slab behavior.

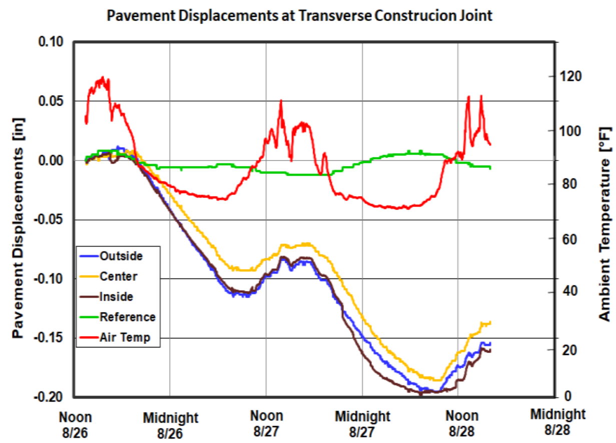

Figure 2.12-(a) Field instrumentation for slab movements at transverse construction joint (left); (b) Slab movements at transverse construction joint (right)

The significant effects of drying shrinkage of concrete on CRCP behavior were observed at a TCJ in a 13-in CRCP project on US 62 in Lubbock, Texas. In Figure 2.13-(a), the slab left of a TCJ was placed on 11/15/2010 and the slab on the right on 12/15/2011. In other words, there was one-year and one-month difference in concrete age. As can be seen, three concrete displacement gages – one in the old slab, another in the new slab, and another across the TCJ – were installed to measure longitudinal concrete slab movements. Data was collected for about 20 days, which is shown in Figure 2.13-(b). In the y-axis, positive values indicate the slabs are moving to the left, or the previously placed concrete is pulling the new concrete. It is noted that concrete temperature measured at the mid-depth continuously went down for a week, until 12/23/2011. The data during the week shows that both slabs moved to the right, i.e., newly placed concrete was pulling one-year old concrete. During this period, the stiffness of newly placed concrete must have been lower than that of one-year old concrete. Still, less stiff concrete was pulling more stiff concrete – about 0.035 inches within 3 days. The large slab movements indicate the effects of large thermal contraction and drying shrinkage of newly placed concrete. It is also shown that starting on December 19, slabs were moving to the left even concrete temperatures were going down until December 22. In this project site, there was a 0.5-in rain on December 19. It appears that newer concrete swelled, while older concrete did not as much. It is construed that the porosity of the newer concrete was larger than more mature concrete, and absorbed more rainwater, resulting in swelling and pushing the concrete to the left. The green line shows the relative displacements across the TCJ. Plus, numbers represent widening of the joint. If the slab behavior is purely axial, the differences in displacements between the 2 gages placed in old and new concrete should be identical to the values obtained in the gage placed across the joint. Examination of the graph shows relatively good agreements. Minute discrepancies may be due to (1) curling and warping of the concrete and (2) different vertical locations of the gages. Curling and warping will result in larger numbers for the gags placed closer to the surface (the gage across the joint). The data shown here indicates horizontal components of the slab displacements. After 2 weeks of new concrete placement, there is a good correlation between concrete temperature and slab displacement behavior: as temperature decreases, older concrete moves more to the left than newer concrete, resulting in larger relative displacements. On the other hand, when the temperature went up,

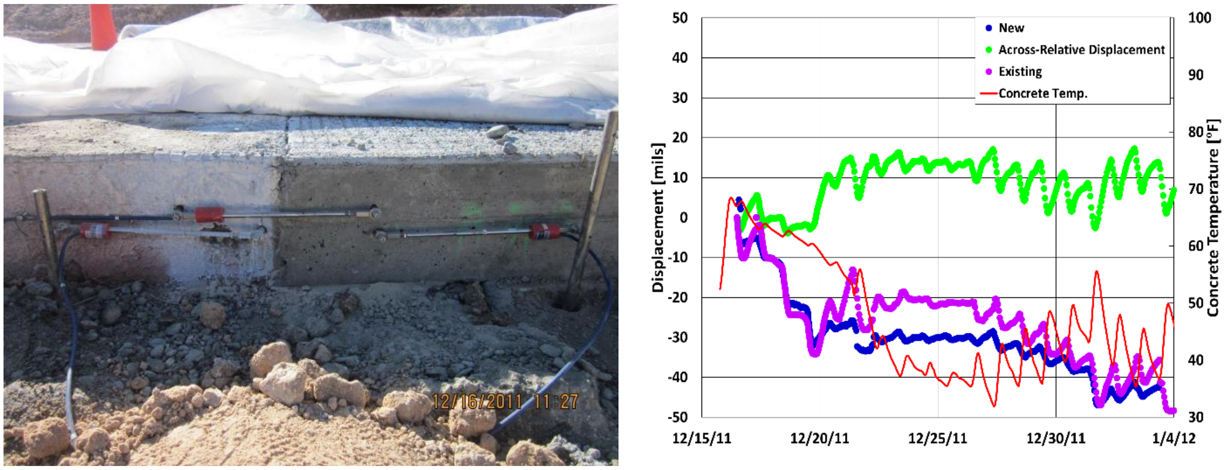

Figure 2.13-(a) Field instrumentation at a TCJ (left); (b) Slab displacements (right)

The concrete was placed on Friday. In CRCP, it has been hypothesized that (1) drying shrinkage and temperature drop from a setting temperature cause tensile stresses in concrete and transverse cracking, (2) continued drying shrinkage will keep the concrete in CRCP in tension and increase crack widths, and (3) larger crack widths will decrease load transfer efficiency at transverse cracks. It is true that drying shrinkage of concrete and temperature variations cause transverse cracks at early ages. However, these transverse cracks generally do not go through the slab depth; rather, they are limited to the top few inches where the drying shrinkage and temperature variations are maximum. Once a crack occurs to a depth of few inches, tensile stresses in concrete are relieved and the crack does not propagate further. Figure 2.14 shows transverse crack profiles through the slab depth on US 290 in Houston. This 10-in CRCP + ¾-in ASB + 6-in CTB was completed in 1982, and longitudinal cuts were made for widening in 2010, which provided a good opportunity to observe transverse crack profiles through the slab depth. As can be seen in Figure 2.14-(a), the transverse crack is quite wide on the slab surface. However, the crack was confined only near the surface.

Figure 2.14-(a) Wide crack width on the slab surface (left); (b) Transverse crack profile through slab depth (right)

Figure 2.15 shows transverse crack profiles through the slab depth on IH-35W in Fort Worth. This 8-in CRCP + 4-in ASB + 8-in lime treated subgrade (LTS) was completed in 1977, and longitudinal cuts were made along a longitudinal construction joint for widening in 2007, which provided a good opportunity to observe transverse crack profiles through the slab depth. As can be seen in Figure 2.15-(a), the transverse crack is quite wide on the slab surface. However, the crack propagated only about 2 inches from the surface, as can be seen in Figure 2.15-(b).

Figure 2.15-(a) Wide crack width on the slab surface (left); (b) Transverse crack profile through slab depth (right)

The above 2 crack profiles indicate transverse cracks do not necessarily propagate through the slab depth, since they develop to relieve stresses from temperature and moisture variations in concrete, which is the largest near the slab surface. Once those stresses are relieved, cracks do not need to propagate further down. Some transverse cracks may propagate through the slab depth, even though crack widths will vary along the slab depth, with a minimum value at the depth of longitudinal steel. If transverse cracks are observed on the side of the slab right after construction, almost all the cracks appear to be full-depth cracks. However, the concrete behaviors near the slab edge subject to temperature and moisture variations are different from those away from the slab edge.

LTE has been cited as a major attribute in CRCP affecting structural performance of CRCP, and extensive evaluations of LTEs at transverse cracks over 8-year time period in Texas revealed that LTEs were maintained quite high, regardless of pavement age, crack spacing, or time of the year (summer vs winter). In the evaluations, FWD testing was conducted in a total of 27 CRCP projects throughout Texas, with 12 cracks selected in a project (4 cracks with small, medium and large crack spacings). LTE was evaluated in those pre-selected cracks in the summer and in the winter. Figure 2.16 shows the summary results. As can be seen, LTEs at transverse cracks are maintained quite high. The reason for LTEs over 100 % is potentially due to the two geophone sensors not having been placed at equal distances from a crack.

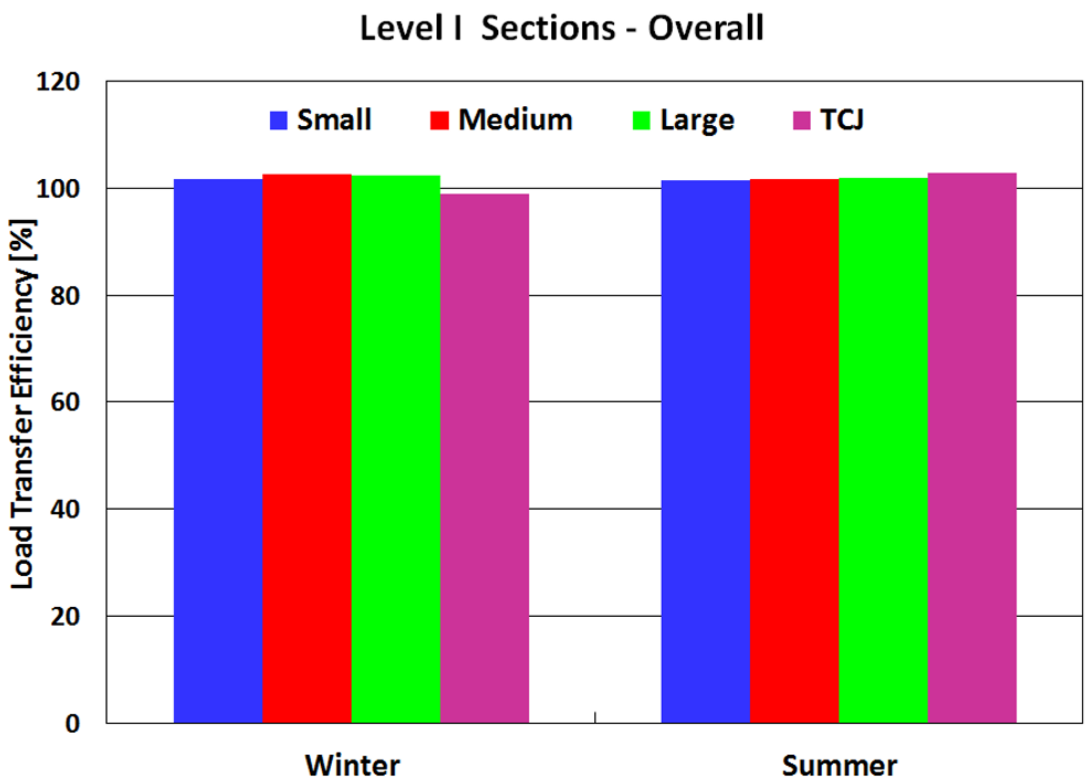

Figure 2.16 LTE at cracks and TCJ in Texas

2.3 Transverse Construction Joints (TCJ)

Another form of distress in CRCP is at transverse construction joint (TCJ). Figure 2.17 illustrates a typical distress at TCJ. This form of distress has been considered due to deficiency of structural capacity of pavement. Currently, it is a design standard that additional tie bars are inserted at TCJ. However, the measurements of stresses in additional tie bars and longitudinal steel at TCJs indicated those bars behave quite differently, and as a matter of fact, placing additional tie bars could contribute to the development of distress. It appears that the concrete placed in the morning (left side of TCJ) cracked at the end of the additional tie bars. Research efforts conducted for TxDOT reveal that the primary cause of the distress is not the deficiency of structural capacity; rather, it is lack of proper consolidation of concrete at TCJ areas.

Figure 2.17 Typical distress at TCJ

Chapter 3 Horizontal Crack in CRCP

3.1 Horizontal cracking

As discussed in the previous chapter, punchout is the only structural distress in CRCP. It occurs at the edge of the pavement, where a slab segment containing two transverse cracks connected by a longitudinal crack is pushed down by wheel loads, even though some researchers report that negative temperature gradients contribute to the longitudinal cracking under wheel loading. It has long been accepted by researchers and practitioners that punchout takes place either from subbase erosion and/or from fatigue damage in concrete due to environmental and wheel load applications. This well-accepted punchout theory assumes that the distress is caused by structural deficiencies of the pavement system, resulting in full depth punchout. To address punchout problems, TxDOT made several changes, in the mid-1980s, in pavement design and construction, which included the use of thicker slabs, stabilized bases, and tied concrete shoulders.

However, during the repair of punchout in Texas and elsewhere, it was observed that usually what appeared to be full-depth punchout was not actually the typical punchout; rather, it was partial depth failure with horizontal cracking at approximately mid-depth of the slab. This type of failure was observed also in CRCP that had the structural improvements mentioned above (i.e., thicker slabs, stabilized bases, and tied concrete shoulders). Based on the field observation, it was known that horizontal cracking usually took place at early ages. Horizontal cracking is believed to be affected by concrete material properties, environmental conditions, and longitudinal steel placement layouts. Wheel loading appears to contribute to horizontal cracking; however, wheel loading effect was not included in this paper. There are numerous cases of this type of failure in Texas.

In addition, it should be noted that distresses from horizontal cracking take different forms, which has not been known to the industry for a long time. However, it appears that a large portion of distresses reported as punchouts in the past were actually distresses caused by horizontal cracking.

Figure 3.1 shows a typical horizontal cracking in CRCP, and Figure 3.2 illustrates distresses caused by horizontal cracking.

Figure 3.1 Horizontal cracking in new CRCP

3.2 Horizontal cracking mechanism

When concrete is cast in place, substantial changes in temperature and moisture can occur. The development of temperature and moisture variations in concrete depends not only on material properties but also on environmental conditions. A nonlinear temperature gradient would develop along the depth of concrete slab and result in slab movement. In a cracked or free surface, the slab movement consists of axial and bending components. In CRCP, however, the longitudinal steel restrains the slab movement because the steel is continuous across the transverse crack.

Longitudinal movement of the slab in a cracked surface, which is proportional to uniform temperature drop, will be restrained by the steel because the steel is continuous across the transverse crack, as the two adjacent slabs across the crack create a line of symmetry. Figure 3.3-(a) illustrates one slab with steel under uniform temperature drop. The longitudinal restraint of steel due to symmetry creates forces in steel, bond stress, and reaction at the center of the slab. Because the restraining force of steel is applied eccentrically to the upper and lower halves of the slab, local bending moment will be generated. This local moment may cause vertical stress of the concrete element near the steel.

Figure 3.3-(b) explains how the concrete element near steel is restrained by the longitudinal steel when the concrete is subject to a linear temperature gradient. The curling-up of the two adjacent slabs across the transverse crack is rotationally restrained by the flexural rigidity of steel due to the symmetry at the transverse crack. This rotational restraint will give rise to additional force that is vertically exerted to the concrete at steel depth. As a result, a substantial stress in the vertical direction, which is closely related to the horizontal cracking, could develop in concrete at the steel's depth. Because slab curling is dependent on the temperature difference between the top and bottom surfaces of a slab, it is expected that greater vertical stress would develop in concrete as the temperature difference increases.

(a) Longitudinal restraint of steel on concrete subject to uniform temperature drop

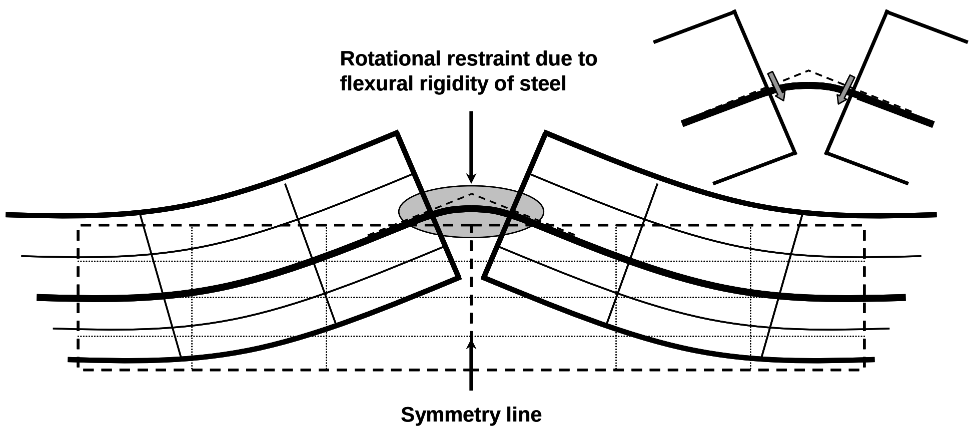

(b) Rotational restraint of steel on concrete subject to linear temperature gradient

Figure 3.2 Horizontal cracking mechanisms

3.3 Distresses caused by horizontal cracking

As discussed earlier, horizontal cracking could be caused by either environmental loading at early ages, or wheel load stresses. Figure 3.3 illustrates a distress in 12-in CRCP on IH 20 in the Fort Worth District. This distress was caused by environmental loading at early ages, and subsequent truck wheel loading applications caused this distress. This is not a typical punchout, since this CRCP has tied concrete shoulder. Two transverse cracks are observed; one on the right appears to have occurred at early ages, since the crack is a little wide, whereas the one on the left was caused later due to horizontal cracking. In other words, the left crack coincides with the end of horizontal cracking.

Figure 3.4 shows a distress on IH 35 northbound at a milepost between 51 and 52. This 10-in CRCP was placed on existing asphalt pavement in 2002. The objective was to evaluate the feasibility of rather thin CRCP under heavy truck traffic. The truck traffic in that corridor is quite large, and unfortunately, there were large number of illegal overweight trucks, as shown in Figure 3.5.

Figure 3.3 Distress caused by horizontal cracking on IH 20

Figure 3.4 Distress caused by horizontal cracking on IH 35

The excessive wheel loading applications caused concrete stresses at the mid-depth of the slab excessive and caused this type of distress. In other words, even though the distresses shown in Figures 3.4 and 3.5 could be classified as punchouts, they are not “traditional” punchouts that occur in accordance with the mechanism described in Chapter 2.

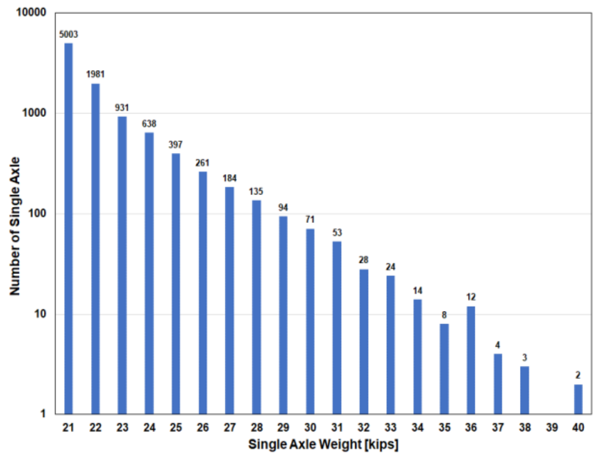

Figure 3.5 Illegal overweight single axle loading

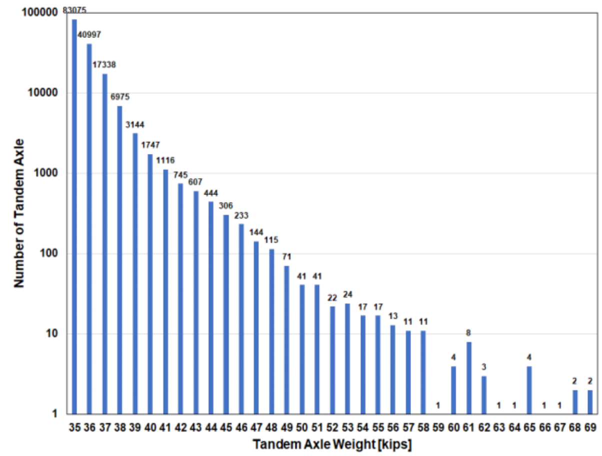

Figure 3.6 Illegal overweight tandem axle loading

Chapter 4 Horizontal Crack Modelling

4.1 Introduction

In this section, structural responses of CRCP with various steel designs are analyzed. The objective is to investigate the structural responses of CRCP, particularly the concrete principal stresses at the depth of longitudinal steel at transverse crack areas which, if excessive, could generate horizontal cracks in various steel designs. The results assisted in the selection and confirmation of steel designs implemented at the experimental sections. The mechanistic analysis tool utilized in this task is the 3D finite element analysis. A 13-in slab thickness is used in the models since the same thickness was planned to be implemented in the experimental sections.

For one-mat steel designs, 3.5-in and 4.0-in depths from the surface are not practical unless changes are made on saw-cut depths for longitudinal warping joint from T/3 to T/4, where T is a slab thickness. However, the inclusion of the said steel designs in the analysis will provide valuable information in establishing general trends in CRCP structural behavior. The mechanistic responses of CRCP which are of primary interest in these analyses are: (1) maximum principal stresses in concrete at the depth of longitudinal steel near transverse cracks, which is a good indicator of the potential for horizontal cracking, (2) maximum concrete stresses at the top (negative temperature gradient) or bottom (positive temperature gradient) of the slab that is somewhere close to the middle of two adjacent transverse cracks, which could indicate whether additional transverse crack might develop, and (3) stresses in longitudinal steel at transverse cracks, which would suggest whether the steel stresses are within an elastic range and crack width will be kept tight. These structural responses (primarily maximum principal stresses in concrete, as long as steel stress does not exceed yield stress) of CRCP will be used to select steel designs to be utilized in field experiments.

4.2 3-D FEM Model

4.2.a Preliminary Analysis

To evaluate the reasonableness of the FE analysis results, slab responses of a 24 ft-wide and 40 ft long slab with a thickness of 13 in. and no reinforcement was analyzed as shown in Figure 4.1. The program used for FE modeling in this project is ANSYS. The preliminary and further mechanistic analyses were conducted in High Performance Computing Center (HPCC) at Texas Tech University. The preliminary analysis results showed that a length extending 20 ft on each side of the loaded area with no boundary restraints is adequate to consider the structural characteristics of CRCP (Ha et al., 2012).

A 9,000-lb single-wheel loading was uniformly distributed over a circular area having a radius of six inches and is located at the center of the slab. The model is assumed to be homogeneous, isotropic, and linear elastic, and the material properties are as follows:

- Elastic modulus and Poisson's ratio of concrete are 5×106 psi and 0.15 respectively,
- The modulus of subgrade reaction is 300 psi/in in vertical direction and 150 psi/in in horizontal direction.

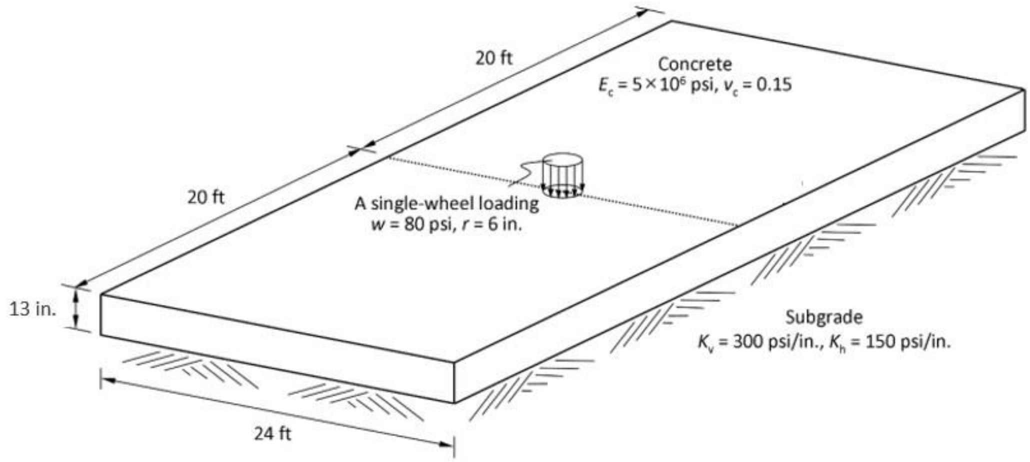

Figure 4.1 Geometric configuration of a concrete slab

Twenty-node solid brick elements were used in the mesh representation of concrete. Elastic support was used to model the modulus of subgrade reaction which allows the modeling of the stiffness effects of a distributed support on a surface without actual modeling details of the support.

Figure 4.2 shows the deformed shape of the slab and the numerical results under the given loading condition. The maximum deflection was 2.1 mils at the loading location. The maximum principal stress developed at the bottom of the slab was 75 psi. Stress and deflection values obtained from a closed-form solutions with Westergaard equations (Westergaard, 1927) were compared along with FEM analysis results in Table 4.1. Good agreements are observed between results from numerical modeling and Westergaard's equations signifying that the model assumptions could yield comparable results on both numerical analysis and closed-form equations, thereby enhancing the confidence on the numerical results. It is to be noted that this exercise was to confirm the accuracy of the FEM analysis, since the accuracy of Westergaard's equations for slab deflections was validated with field measurements.

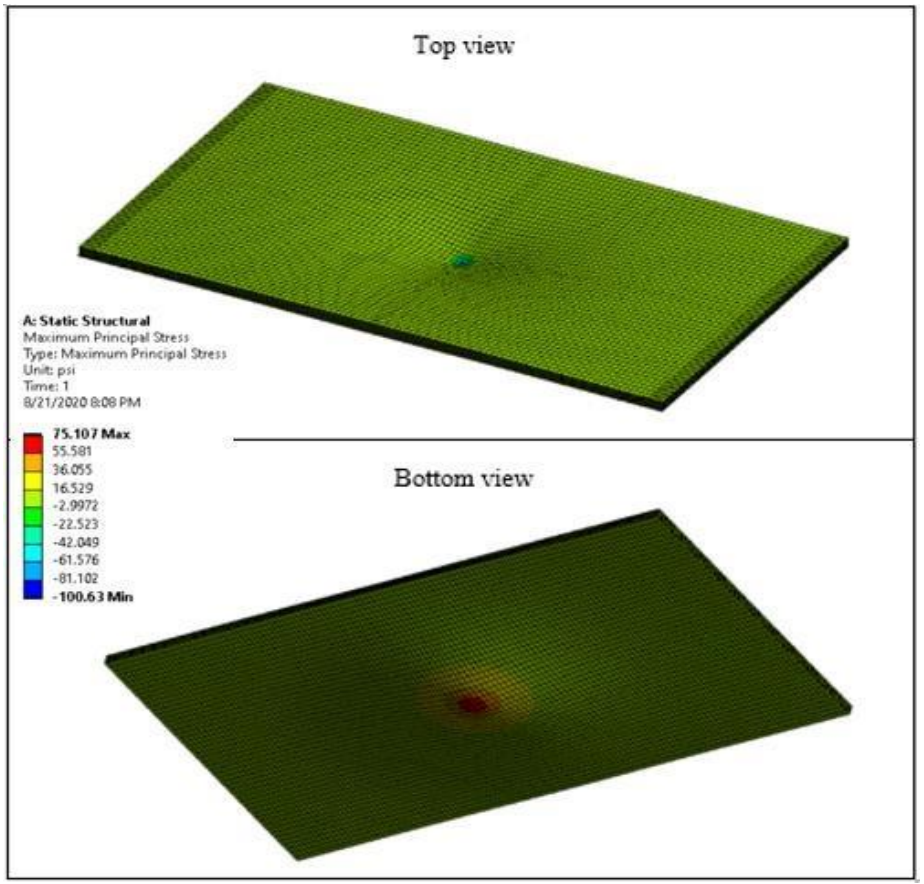

Figure 4.2 Distribution of principal stress

Table 4.1 Comparison of numerical results with Westergaard's solution

	Maximum Principal Stress [psi]		Maximum Surface Deflection [mil]	
Loading Condition	Numerical Result	Westergaard's Solution	Numerical Result	Westergaard's Solution
Interior Loading	75	74	2.3	2.1

4.2.b One-mat CRCP Modelling

To reduce the runtime time of the analysis, a symmetrical CRCP slab model was utilized. In other words, if the loads applied to the structure are symmetric relative to the plane of symmetry, then the full model can be replaced with half the model by applying a symmetric boundary condition. This implies that the displacement normal to the plane of symmetry and rotations about the axes in the plane of symmetry are zero at the plane of symmetry. This technique is universally adapted in FE modeling.

A more conservative modeling, with outside free edge, was used. Even though tied-concrete shoulder is used in Texas, accurate modeling of joint behavior between outside lane and tied concrete shoulder is a challenge. Also, a joint between outside lane and tied concrete shoulder could be construction joint or contraction joint, and their structural behavior could be quite different. In addition, since horizontal cracking as affected by steel depths develops at early ages due to environmental loading (temperature and moisture variations in the concrete), even before the application of wheel loading, the modeling simulates the environmental loading only. Figure 4.3 shows the geometric model – one lane with free edges on both sides. Three different crack spacings were selected for this task – 4, 8 and 12-ft, and the model for 4-ft crack spacing is shown here. The boundary conditions in the model are as follows:

1) Longitudinal steel displacements at transverse cracks in longitudinal direction are zero. In other words, longitudinal steel at transverse cracks do not move in longitudinal direction. This assumption or boundary condition may not be 100 % realistic, as crack spacings in CRCP vary and there might be some movements or displacements of longitudinal steel at cracks in longitudinal direction. However, if crack spacings are uniform, this assumption is not that unrealistic, except at locations near bridge expansion joints.
2) Longitudinal steel at transverse cracks is free to move in vertical direction. This boundary condition is quite realistic, as concrete slab undergoes curling up and curling down, which necessitates the steel movements in vertical direction.

To capture the effects of various variables in a wide range of conditions, a factorial experiment was developed, and Table 4.2 shows the variables and their levels included in the simulations. It is believed that this covers the majority of the possible conditions in Texas.

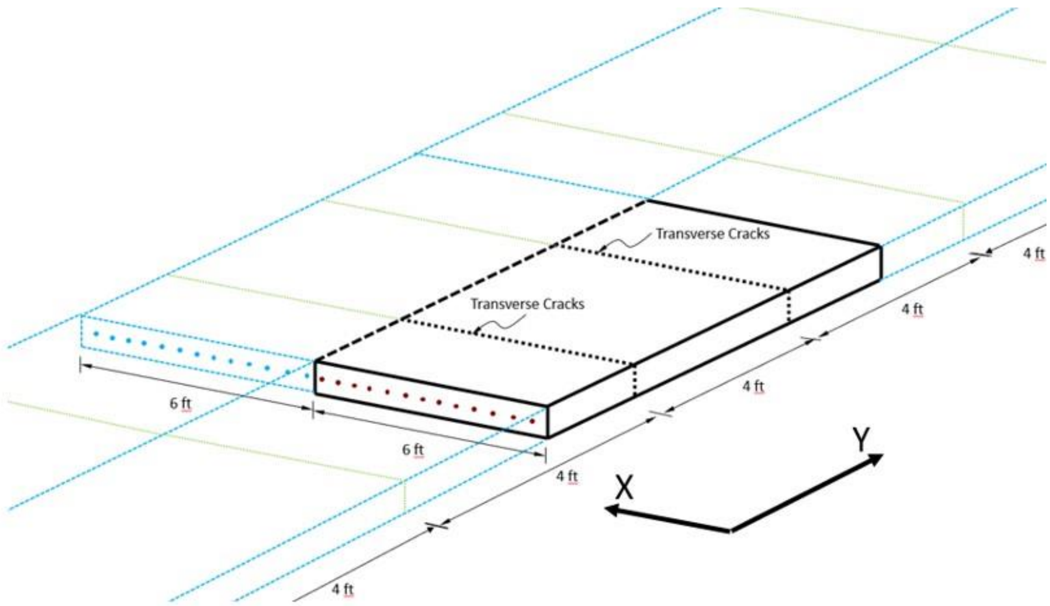

Figure 4.3 Geometry of symmetry model in ANSYS

Table 4.2 Input variables of interest and their levels

Parameters	Level(s)	Values
Slab thickness [in]	1	13
Steel content ratio (%)	1	0.6
Steel depth from the slab surface for one mat [in]	7	3.5, 4, 4.5, 5, 5.5, 6, 6.5
Concrete modulus [million psi]	2	4, 5

Temperature drop from setting to daily minimum temperature [°F]	2	30, 50
Coefficient of thermal expansion [in/in/°F]	3	3.5, 4.5, 5.5
Ultimate drying shrinkage on the concrete surface [μ]	2	400, 700
Temperature variation through slab depth [°F/in]	2	+3, -1.5
Modulus of subgrade reaction [psi/in]	2	300, 500
Crack spacing [ft]	3	4, 8, 12

Figure 4.4 illustrates the finite element mesh model. Twenty-node solid brick elements were used in the mesh representation of concrete and steel. For consistency, equal-sized elements were allocated to the concrete around longitudinal steel. A modulus of subgrade reaction was modeled with a spring element. Elastic supports allow to model the stiffness effects of a distributed support on a surface without specifying actual modeling details of the support.

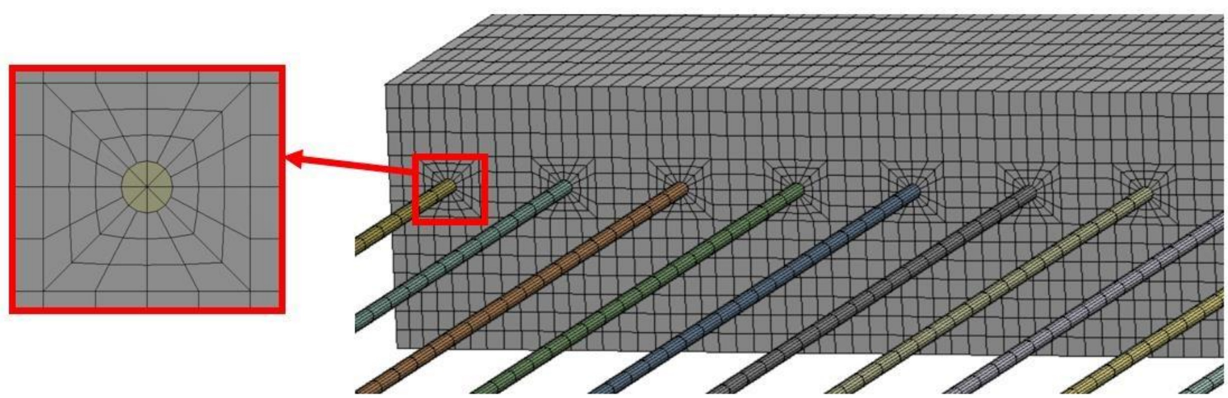

Figure 4.4 Mesh model adopted in the analysis

4.2.b.1 Material properties and constitutive equations

The materials – concrete, steel and base/subgrade – were assumed homogeneous, linear elastic (no creep), and isotropic. In a microscopic level, these assumptions might lead to erroneous results. However, in a macroscopic level, which is the case, it is considered that those assumptions are acceptable, especially investigating overall trend of concrete stresses as affected by longitudinal depths, not necessarily quantifying accurate concrete stresses.

Additional material properties used for this analysis other than those listed in Table 4.2 are as follows:

1) Poisson’s ratio of concrete and steel: 0.15 and 0.3, respectively
2) Elastic modulus and coefficient of thermal expansion of steel: 2.9×10^{7} psi and 6.4×10^{-6} / °F, respectively,
3) Longitudinal steel bar size: 0.75-in (#6 bar)

The interactions between concrete and steel are considered a critical part in CRCP modelling, because it is mostly the stress transfer between concrete and steel that causes high level of concrete stresses and transverse cracks. Traditionally, the stress transfer between steel and concrete is modeled through the bond-slip equation using plane contact elements with the relation between shear traction and shear relative displacement, as shown in Figure 4.5 (Kim et al., 2000). A large stiffness was assigned to the relationship between normal traction and normal relative displacement to keep the debonding between longitudinal steel and surrounding concrete to a minimum. The relationship between bond slip, which is defined as the relative displacements between concrete and steel at the concrete/steel interface, and bond stress as shown in Figure 4.5 has been used in reinforced concrete modeling. However, this information was developed based on macroscopic measurements of displacements in the laboratory. The applicability of this relationship to CRCP has not yet been validated. It is because this relationship implies that there should be bond slip for bond stress (shear stress) to be developed. In other words, bond stress does not develop if concrete and steel are fully bonded and undergoes no relative displacements (slip). However, in the field, it is frequently observed that concrete and steel are fully bonded, and no slip observed at transverse crack areas that are visible on the naked eyes. This implies that, if the relation shown in Figure 4.5 is correct, there should be no stress transfers between steel and concrete, which is not the case. This apparent discrepancy is the result of whether we need to analyze the system in "macroscopic" or "microscopic" scale. In structural engineering, the analysis is based on macroscopic nature since their primary focus is whether structures will fail due to pull-out of reinforcing steel at construction joints or any other discontinuities. The pull-out failure necessarily requires large slip and the general relationship shown in Figure 4.5 has been well accepted and used in structural engineering for mechanistic analysis of reinforced concrete members. Meanwhile, in CRCP, that's not the case. There are no pull-out failures at transverse cracks. Rather, when steel stress is quite high at transverse cracks, in such cases where steel reinforcement rate is much lower than needed, steel stresses could be quite high and longitudinal steel fails by excessive yielding. What is occurring in CRCP at crack areas in stress transfers between steel and concrete is microscopic in nature. It is because bond stresses develop without bond slip and the relationship shown in Figure 4.5 does not represent CRCP behavior; however, because of the absence of proper models that accurately model the stress transfer mechanisms at transverse cracks, researchers in rigid pavement have adopted the relationship shown in Figure 4.5 in their mechanistic analysis. What this implies is that the "quantitative" results of the analysis should be interpreted with caution.

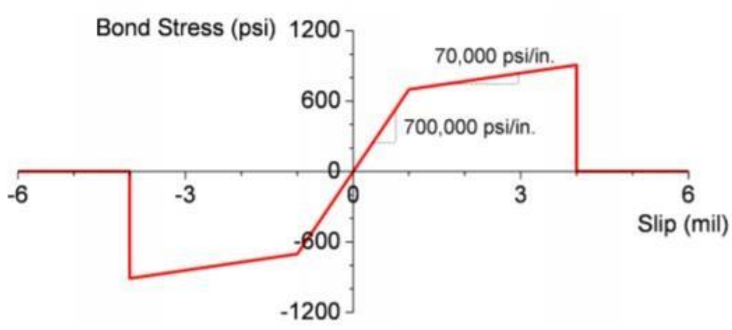

Figure 4.5 Bond-slip behavior between concrete and longitudinal steel

Another assumption made on load transfer at cracks is that aggregate interlock does not exist due to repeated traffic and environmental loading, and therefore the load is transferred only through longitudinal steel across transverse cracks.

For time variations in drying shrinkage of concrete, Equation 1 was used (Dossey and McCullough, 1992):

$$Z_N(t) = N_{256}(2-e^{-Bt}-e^{-Ct}) \qquad \text{Eqn. 1}$$

where:
$Z_N(t)$ = Drying shrinkage at time t
N_{256} = Drying shrinkage at day 256 which was calculated according to the ACI 209 equation. (ACI 209)
t = Time of curing (days)
B, C = Coefficients of curvature specific to a given aggregate, (B=0.0398, C=0.00754 for LS)

For shrinkage variation through the depth of the concrete slab, equation 2 was used (Desai, 2015):

$$\varepsilon_{SH}(Y) = a+b*e^{\lambda Y} \qquad \text{eqn. 2}$$

where:
Y= Slab height (0-in at the bottom and 13-in at the top surface of concrete)
$\varepsilon_{SH}(Y)$ = Drying shrinkage at height Y
λ = 0.518045 and 0.610814 for ultimate drying shrinkage of ultimate drying shrinkage of 400 and 700 micro-strain, respectively
a,b = 24.55357 and 0.446429 respectively, for ultimate drying shrinkage of 400 micro-strain; while, 24.75962 and 0.240385 respectively, for ultimate drying shrinkage of 700 micro-strain

Reviews of several models and experimental data show that the shrinkage strain profiles through the slab depth at a given time are highly nonlinear, and consists of two parts: a constant, low strain at the bottom half of the slab, and an exponential increase of strain from mid-depth to the slab surface. Figure 4.6 and Figure 4.7 show the shrinkage variations through the slab depth at 7 days and infinite days derived from the above 2 equations for 400 μ and 700 μ of ultimate drying shrinkage, respectively.

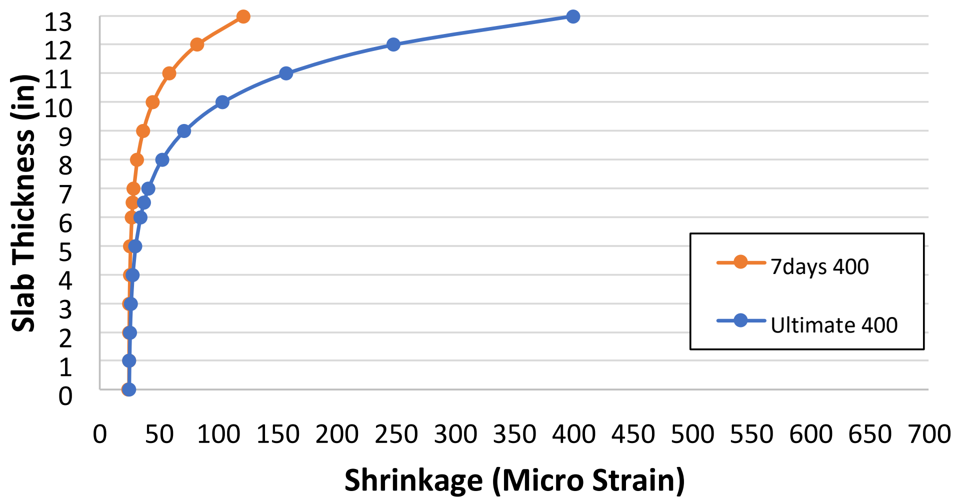

Figure 4.6 Shrinkage changes through the slab depth with ultimate value of 400 μ

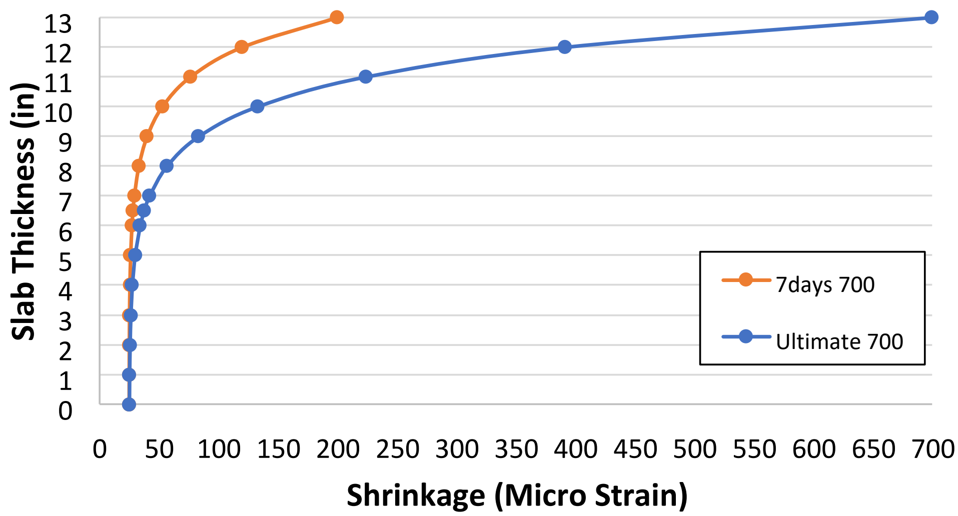

Figure 4.7 Shrinkage changes through the slab depth with ultimate value of 700 μ

4.2.b.2 LTE Evaluations

To evaluate the deflections and LTEs at the transverse cracks of CRCP, a 12 ft-wide and 16 ft long slab with a thickness of 13 in. was analyzed as shown in Figure 4.8. A 9-kip single-wheel loading was applied over a circle with a radius of 6 inches and the loading location is shown with green rectangle in Figure 4.8. The loading is on one-side of a transverse crack and located at a distance of 6 ft. from the slab edge. It was assumed that longitudinal rebar with a diameter of 0.75 in. were placed at 3.5-in from top surface of concrete slab, with 0.6 % of steel ratio. Figure 4.9 a) shows the geometry of the models with loading applied and b) illustrates the path along which deflections were evaluated. Deflections along the path are shown in Figure 4.10. In this figure, distance 0 indicates the top left corner of the slab in Figure 4.8. Deflections and LTE results are summarized in Table 4.3. LTE of 87 % was obtained, which is somewhat lower than the values obtained in the rigid pavement database project, which was about 95 %. The assumption of no aggregate interlock at transverse cracks might be the reason for lower LTE value obtained in the analysis.

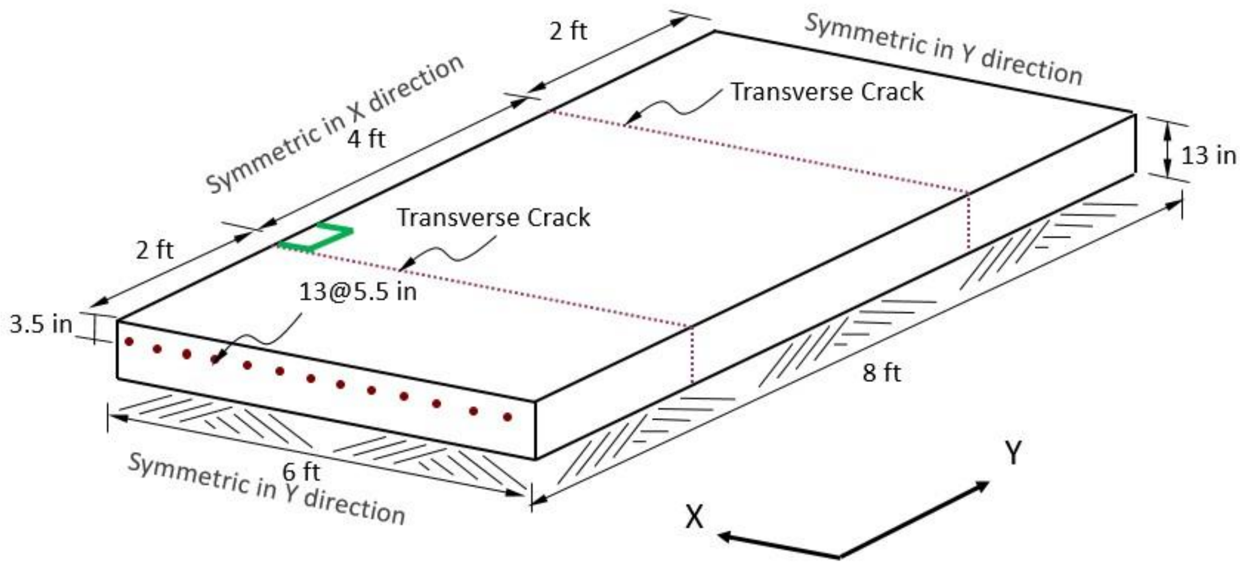

Figure 4.8 Geometry of model of LTE evaluation

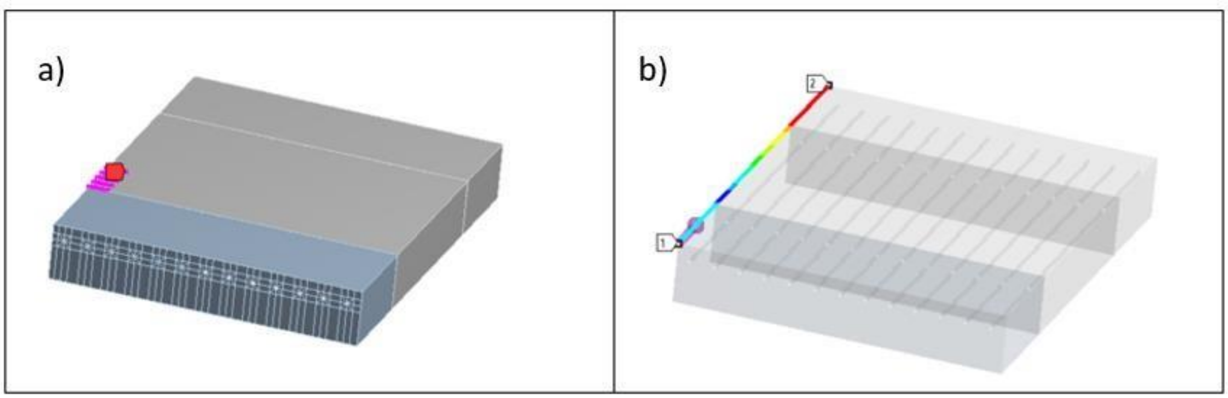

Figure 4.9 a) Loading location in the model, b) the path at loading location along the slabs

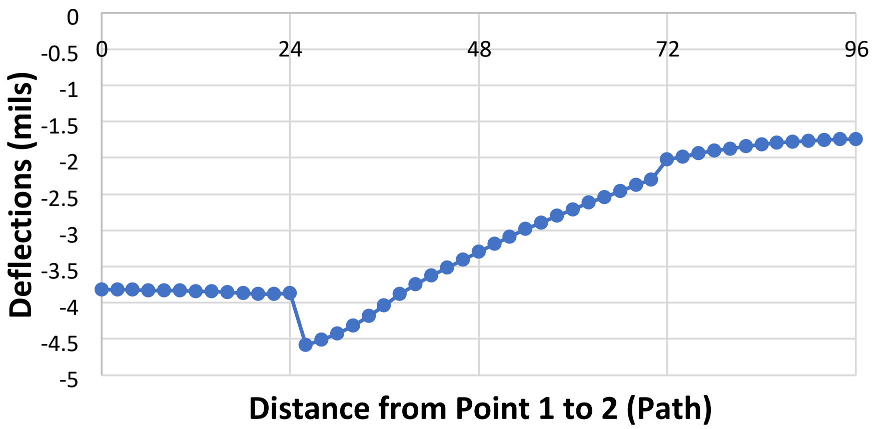

Figure 4.10 Deflections along the path

Table 4.3 LTE result

Rebar depth (in.)	δ_L (mil)	δ_U (mil)	LTE %
3.5	-4.42	-3.86	87

4.2.b.3 Discussion of Numerical Results for one-mat CRCP

One-mat CRCP Modeling

For one-mat CRCP, the total number of combinations covering all different variables and levels (treatment) presented in Table 4.2 was 2,016. As earlier discussed, 3 structural responses were evaluated: (1) maximum concrete stresses at the top (negative temperature gradient) or bottom (positive temperature gradient) of the slab somewhere close to the middle of two adjacent transverse cracks, (2) maximum principal stresses in concrete at the depth of longitudinal steel near transverse cracks, and (3) stresses in longitudinal steel at transverse cracks. These stress values are affected by a number of variables, including stress transfers between concrete to longitudinal steel, especially near transverse cracks.

Stress Results at Top of the Concrete Slab

When there is a negative temperature gradient (temperature at the top of the slab is lower than that at the bottom of the slab, which occurs early in the morning), slabs curl up. In addition, due to the self-equilibrating actions of the uncracked concrete slab, the tensile stresses will develop at the top of the slab, while the compressive stresses at the bottom of the slab. If the tensile stresses at the top of the slab are excessive, a top-down transverse crack could propagate at that location.

The discussion in this section will focus on the concrete stresses at the top of the slab due to negative temperature gradient and drying shrinkage variations through the slab depth, which exerts the same effect as negative temperature gradient. This is more critical than positive temperature gradient, which explains why the majority of transverse cracks in CRCP are top-down having larger crack widths at the top. All the analysis results on maximum principal stresses at concrete slab (at the top due to negative temperature gradient, and at the bottom due to positive temperature gradient) between two adjacent transverse cracks are presented in Appendix A. Selected cases which provide a general trend are presented and discussed.

Effect of modulus of subgrade reaction: Figure 4.11 shows the effect of modulus of subgrade reaction on maximum principal stress at the top of concrete slabs. The results are based on concrete modulus of 4×10^6 psi, CoTE value of 3.5×10^{-6}/˚F, and temperature drop of 30 ˚F. There are 7 lines representing various steel depths for each crack spacing (4-ft, 8-ft, & 12-ft) with a total 21 lines. Each line corresponds to a specific set of input values.

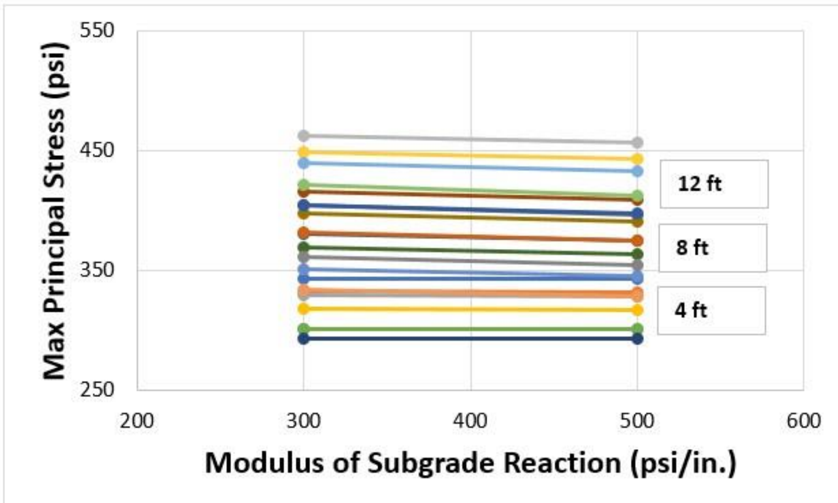

Figure 4.11 Effect of modulus of subgrade reaction

It can be observed that the effect of modulus of subgrade reaction (k-values) on maximum concrete stresses is minimal, which is somewhat unexpected. In jointed concrete pavement (CPCD), k-values are known to have sizable effects on concrete stresses due to environmental loading. However, in CRCP, concrete warping and curling are restrained by longitudinal steel, and accordingly, the effect of k-values is minimal. However, this should not be interpreted as "base stiffness is not important". There is a correlation between k-values and stiffness of stabilized base layer – the stiffer the base layer, the larger the k-values. There is also a good correlation between the durability of the stabilized base and the stiffness or strength of base layer. Since many of the structural failures in CRCP in Texas are due to the deterioration of slab support, base stiffness is still an important aspect of CRCP. This means that the stiffer the stabilized base, the better is the overall performance of CRCP. Another observation in Figure 4.11 is the effects of crack spacing on maximum concrete stresses. It can be further observed that the larger the crack spacing, the larger the concrete stresses, which is expected. The large concrete stresses that develop in CRCP with larger crack spacing will eventually result in additional cracking. This explains why crack spacing in CRCP is large at early ages, but decreases with time until it reaches a stable value of about 4 to 6 ft.

Effect of longitudinal steel depth: The effect of longitudinal steel depth on crack spacing is well known – the smaller the cover depth, the smaller the crack spacing. It is because concrete stresses due to environmental loading are largest near the concrete surface, where temperature and moisture variations are the largest. Accordingly, placing steel closer to the concrete surface will restrain concrete volume changes more effectively, causing larger concrete stresses and more transverse cracking (smaller crack spacing). Figure 4.12 shows the variations in maximum concrete stresses with various steel depths and 2 different ultimate drying shrinkages for 4-ft crack spacing. It can be observed that concrete stresses decrease with the depth of longitudinal steel which is expected. In addition, larger concrete stresses result for concrete with greater ultimate drying shrinkage. Figure 4.13 and Figure 4.14 show 8-ft and 12-ft crack spacing, respectively, and similar trends are observed. However, concrete stress values are higher for CRCP with larger crack spacing as previously discussed.

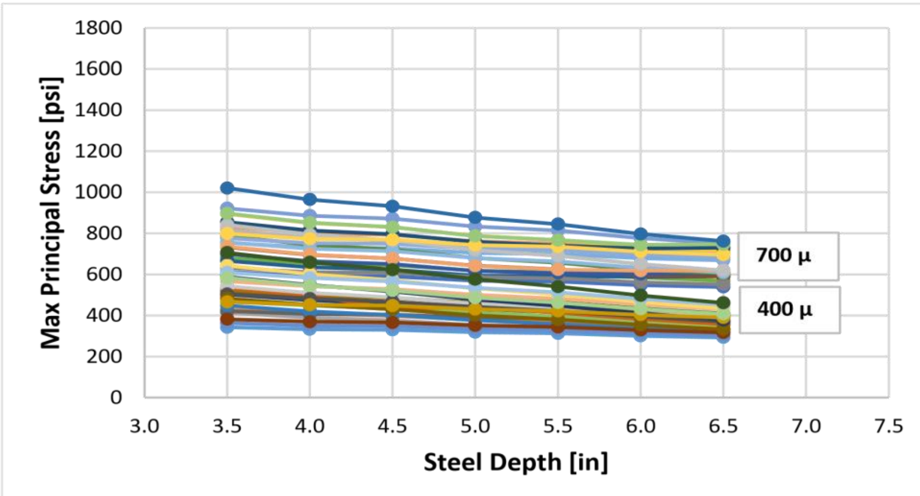

Figure 4.12 Effect of steel depth for 4-ft crack spacing

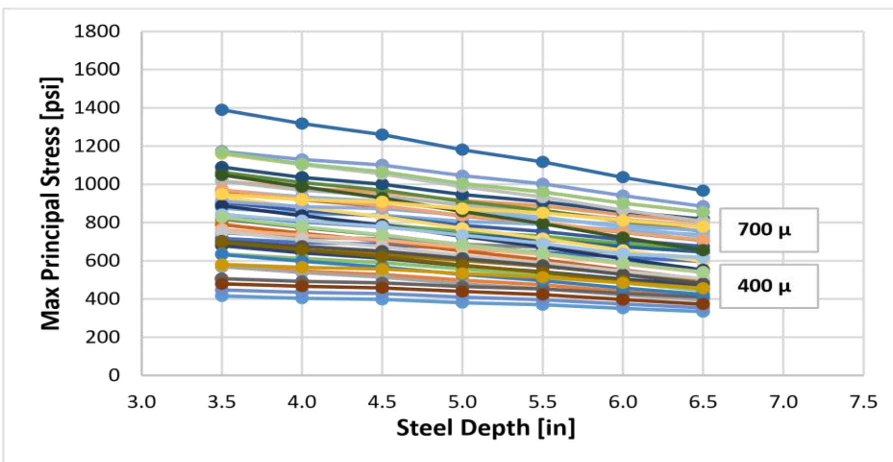

Figure 4.13 Effect of steel depth for 8-ft crack spacing

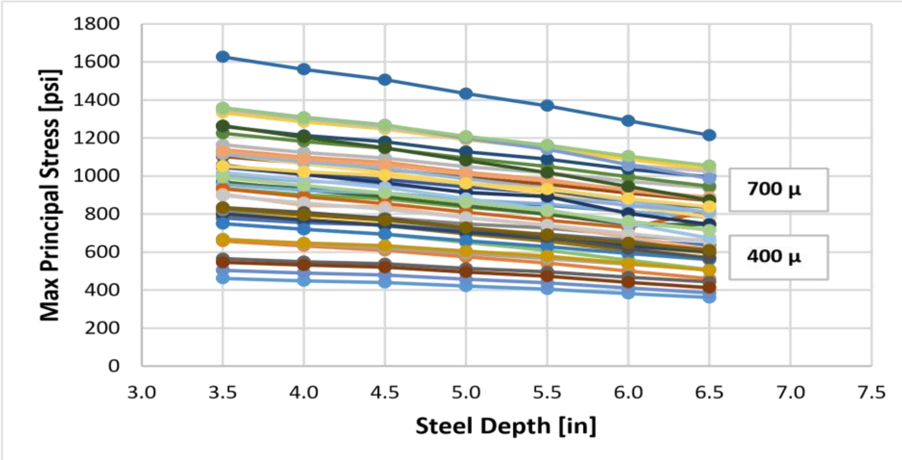

Figure 4.14 Effect of steel depth for 12-ft crack spacing

These observations imply that, as longitudinal steel is placed closer to the slab surface, concrete stresses will increase and more cracks be induced, resulting in shorter transverse crack spacing, which is significant in horizontal cracking development, which will be discussed later.

<u>Concrete Stresses near Steel at Transverse Crack Locations</u>

Field observations indicate that horizontal cracks (HCs) occur at early ages, even before traffic loading is applied, and there is a correlation between crack spacing and HCs – the larger the crack spacing, the higher the probability of HCs. This has two important technical implications. One is that HCs are caused by environmental loading, and the other is that transverse crack spacing affects concrete stresses near longitudinal steel at transverse cracks due to environmental loading. Accordingly, to evaluate the potential for horizontal cracking, assessing concrete stresses around longitudinal steel at transverse crack locations is important. Concrete stresses around longitudinal steel at transverse cracks, which is referred to as "concrete stresses", evaluated in the analysis are discussed. The detailed analysis results on this are presented in Appendix B.

Effect of crack spacing: Figures 4.15 a) to d) illustrate the effects of crack spacing on concrete stresses for various environmental conditions and two ultimate drying shrinkages. Overall, they confirm the discussions previously made, which is, the larger the crack spacing, the larger the concrete stresses and the probability of HCs. Another observation is that the larger the drying shrinkage and temperature drop, the more significant effects of crack spacing on concrete stresses and HCs. However, larger temperature drop, and drying shrinkage will result in smaller crack spacing, which will probably negate the undesirable effect of large crack spacing. However, this should not be interpreted as larger drying shrinkage is not detrimental to HCs. There are several ways to obtain smaller transverse crack spacing, some of which are good, and some are not. Placing steel above the mid-depth of steel is a good way of achieving smaller crack spacing, while poor curing and accompanying larger drying shrinkage is not a way to achieve smaller crack spacing.

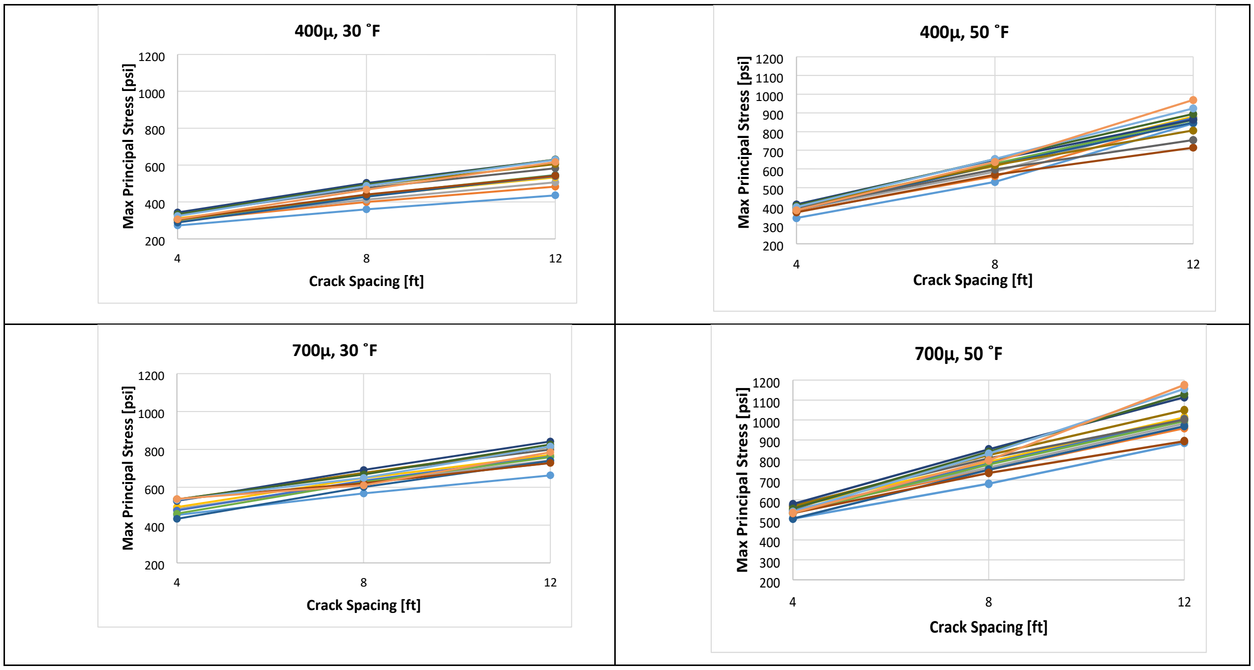

Figure 4.15 Effect of shrinkage on crack spacing

Effect of coefficient of thermal expansion: Figures 4.16 a) to d) show the effects of concrete's coefficient of thermal expansion (CoTE) on concrete stresses for 4-ft crack spacing for various environmental conditions and two ultimate drying shrinkages. It can be observed that the change in CoTE increases the resulting maximum principal stress linearly. In addition, the increase in stresses due to the increase in temperature drop from the setting temperature is about 14%, 25% and 33% with CoTE values of 3.5, 4.5 and 5.5 μ/ºF, respectively. Also, the increase in drying shrinkage from 400μ to 700μ increases the stress by up to 50%. In all conditions presented here, it is shown that the larger the CoTE, the greater the concrete stresses implying a higher probability of HCs. However, concrete with larger CoTE values will have smaller crack spacing, which is supposed to reduce concrete stresses. Based on this, it could be stated that CoTE does not have significant effect on HCs, which has been validated by HCs obtained in CRCP with low CoTE. This may sound counter-intuitive; however, it is not, because if transverse crack spacing can be controlled by placing steel at a right depth, then concrete with low CoTE will have lower probability of HCs than concrete with high CoTE at the same steel content.

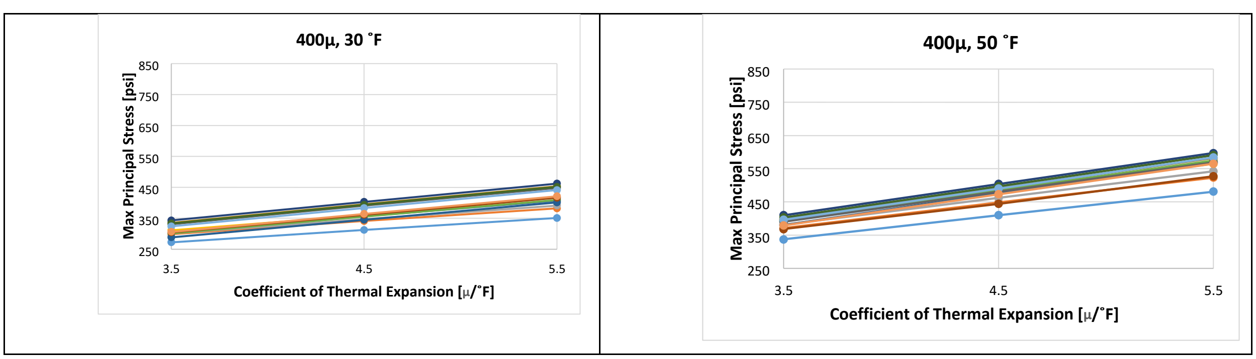

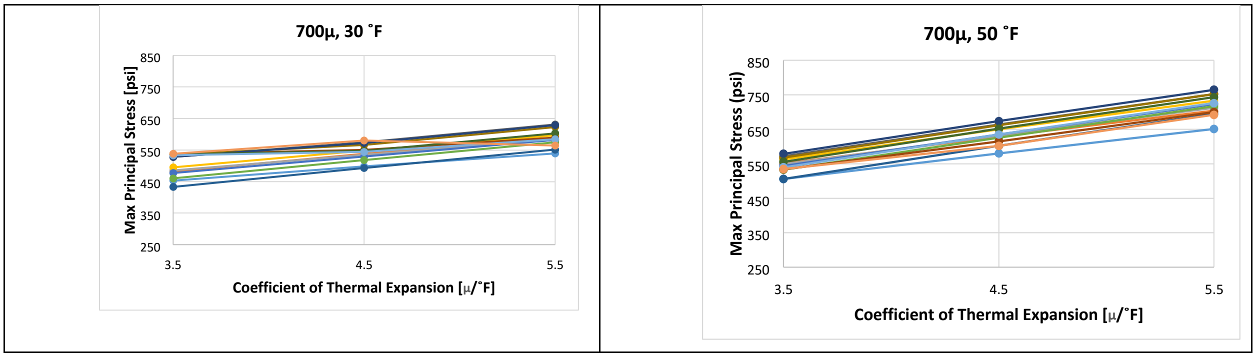

Figure 4.16 Effect of coefficient of thermal expansion on stress at transverse crack for 4-ft crack spacing

Effect of concrete modulus: Figure 4.17 shows the effect of concrete modulus on concrete stresses for 4 ft crack spacing. It shows larger concrete stresses when concrete modulus values increase, which is expected. However, it is to be noted that this analysis was for a fixed crack spacing of 4-ft. Larger concrete modulus will result in, compared with concrete with lower modulus, higher stresses inducing smaller crack spacing to relieve excessive concrete stresses. The information shown in Figure 4.17 indicates the reasonableness of the modeling and analysis program, and not necessarily technical significance.

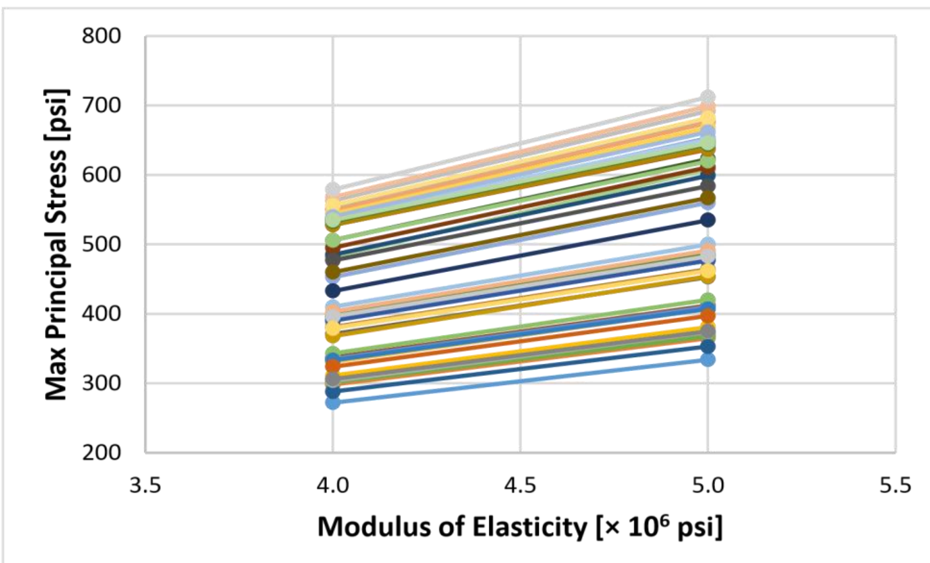

Figure 4.17 Effect of modulus of elasticity on stress at transverse crack for 4-ft crack spacing and α_c=3.5×10^{-6} 1/˚F

Steel Stress at Transverse Cracks

Another aspect in consideration is the stress in longitudinal steel at transverse cracks which is also important, since they would indicate whether the steel stresses are within an elastic range and whether the crack width will be kept tight or not. AASHTO pavement design requires that the steel stresses not to exceed 45 ksi. The analysis results for a specific combination of environmental condition and material properties are presented in Table 4.4. It shows that the larger the crack spacing, the greater the steel stress. For the specific condition selected for the development of this table, steel stresses are exceeding 45 ksi for crack spacing of 8-ft and 12-ft. In actual CRCP projects, it is quite rare to observe steel failures or yielding of steel and resulting large crack widths, unless steel content is quite low. The information in Table 4.4 is contradictory to observations in the field. It is to recall that in this analysis, concrete materials were assumed to be linear elastic, with no creep effects. However, the environmental loading rate is quite slow, about 25 ºF variations at 12-hour duration, which is equivalent to 2 ºF per hour variation. For concrete with 4 million psi and 5 microstrain/ ºF, this environmental loading rate yields 80 psi per hour loading rate (or 1.3 psi per minute), if concrete is fully restrained. This loading rate is quite small, and concrete will undergo creep and stress relaxation, which will reduce the steel stress values at cracks. It is also observed that the steel depth does not have substantial effects on steel stress. It is probably because the crack spacing is fixed at 4-ft. Figure 4.18 illustrates graphical output from ANSYS on steel stress.

Table 4.4 Steel stress at transverse crack location

	Stress Value (psi)		
Steel Depth (in)	4 ft	8 ft	12 ft
3.5	30,737	51,245	66,038
4.0	30,397	51,784	67,494
4.5	29,903	51,765	68,264
5.0	29,531	51,916	69,170
5.5	29,016	51,597	69,415
6.0	28,561	51,267	69,644
6.5	28,026	50,593	70,141

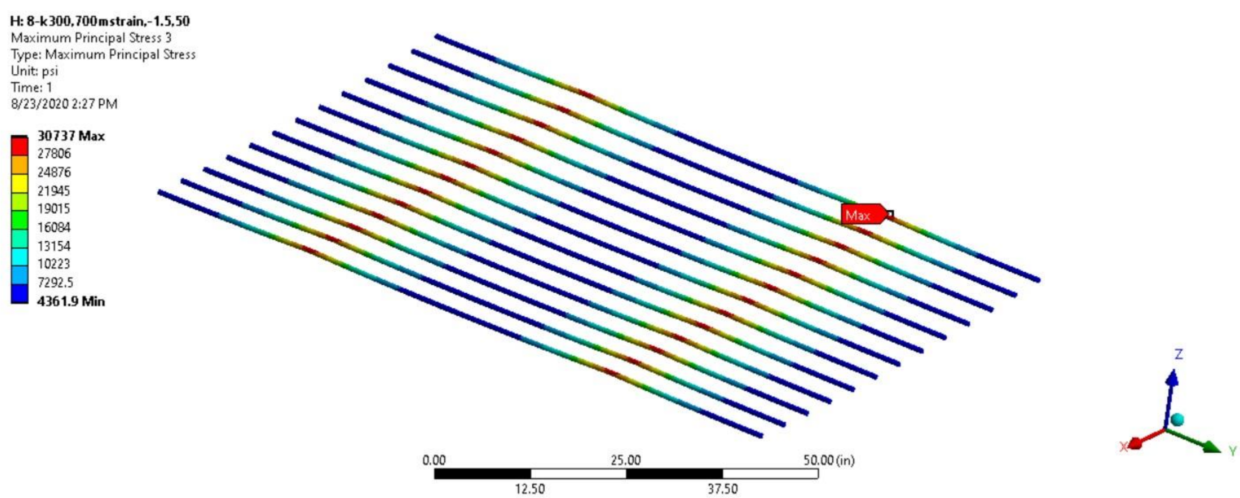

Figure 4.18 Steel stress at transverse crack location

4.2.b.4 Summary of One-mat

The identification of the optimum depth of longitudinal steel in CRCP has become necessary as this appears to be a significant issue pertaining to the performance of the CRCP. In the absence of previous studies which comprehensively discussed this matter, structural responses of CRCP with various steel designs were analyzed through the ANSYS finite element modeling program. Three dimensional (3D) models were developed for the mechanistic analysis. Since the slab thickness for field experiments will be 13-in, one level of slab thickness, the same thickness was also used for all simulations. The factorial design that was developed represented various environmental conditions in Texas. The findings made are summarized as follows:

1) Among variables investigated, transverse crack spacing has the most significant effects on concrete stresses near longitudinal steel at crack locations – the larger the crack spacing, the larger the concrete stresses at the depth of steel at crack locations. This finding supports the observations made in the field, which is that horizontal cracking occurs where transverse crack spacing is large. Accordingly, the optimal steel depth should be able to induce smaller crack spacing, but not too small so that other distress types could develop.
2) Mechanistic responses of CRCP are quite complicated and inter-dependent, i.e., changes in one variable will have effects on mechanistic behavior that will alter the effects of other variables. For example, placing steel near the surface will result in increases in concrete stresses at the top and bottom of the slab, which will reduce crack spacing and concrete stresses near longitudinal steel at crack locations. When interpreting analysis results, the complicated interactions need to be fully understood.
3) Drying shrinkage has substantial effects on concrete stresses near reinforcing steel at crack locations. The importance of drying shrinkage on horizontal cracking development needs to be clearly recognized.
4) Analysis results show CoTE does not have significant effect on concrete stresses near reinforcing steel at crack locations and horizontal cracking (HC), which has been validated by HCs obtained in CRCP with low CoTE. This may sound counter-intuitive; however, it is not, because if transverse crack spacing can be controlled by placing steel at a right depth, then concrete with low CoTE will have lower probability of HCs than concrete with high CoTE.
5) Determining optimum steel depth solely based on mechanistic analysis has limitations. One of them is the assumptions made in the modeling and analysis. Another is the difficulty in incorporating environmental conditions in the analysis, since Texas has large variations in temperatures among regions. Another difficulty is the estimation of actual drying shrinkage at early ages, which is affected by air and concrete temperatures, wind speed, relative humidity of air, and the quality of curing operations. Accordingly, optimum steel depth determination must be aided by field performance of vast amount of CRCP in Texas.
6) Horizontal cracking has rarely been observed in thin CRCPs (8-in through 11-in) with steel placed at mid-depth. On the other hand, horizontal cracking was observed in thick CRCPs with steel placed at mid-depth. It appears that 5.0-in or 5.5-in steel depth for thick CRCPs (thicker than 11-in) induce crack spacing small enough to keep concrete stresses near reinforcing steel at crack locations low enough so that horizontal cracking does not develop.

4.2.c Two-mat CRCP Modelling

Two-mat steel design is also implemented in Texas for CRCP for thicker slabs. Hence, a mechanistic analysis is also implemented for this steel design. The procedure of CRCP modeling is consistent with the one-mat steel design model including the assumptions and boundary conditions unless otherwise stated in this section. Figure 4.19 shows the geometric model adopted for two-mat design – one lane with free edges on both sides. Similar to one-mat steel design, three different crack spacings were also selected for these simulations – 4, 8 and 12-ft, however, only the model for 4-ft crack spacing is shown below.

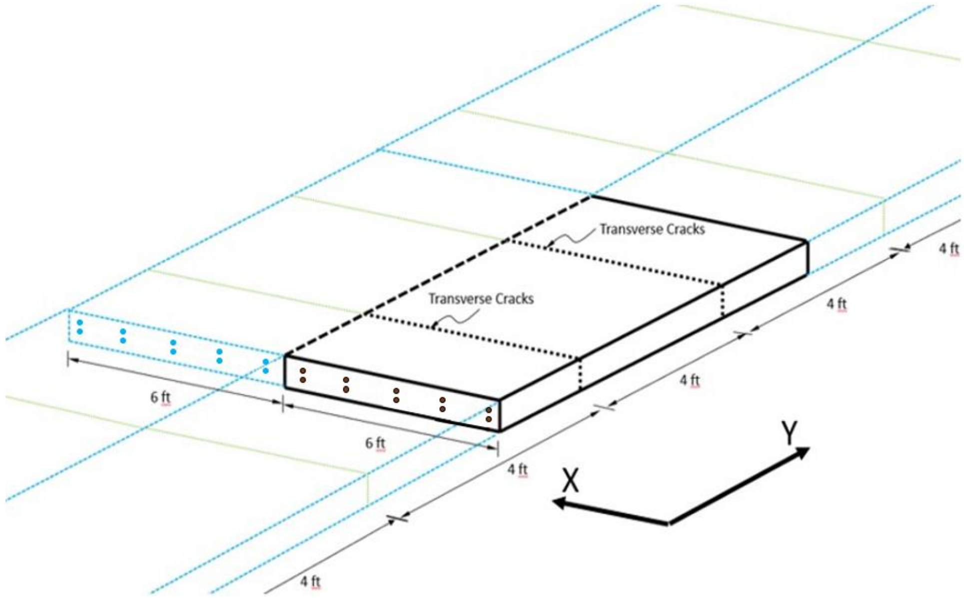

Figure 4.19 Geomtery of symmetry model in ANSYS for two-mat steel design

Table 4.5 shows the variables and their levels included in the simulations. These conditions also represent all possible conditions in Texas as with the one-mat steel design simulations. All the design parameters are the same as one-mat except the steel design, which is two-mat where two layers of steel are installed and have varying depths. Since the longitudinal steel reinforcement is installed in two layers, the distance between rebars have doubled compared to the one-mat steel design

Table 4.5 Variable for two-mat FEM models

Parameters	Level(s)	Values
Slab thickness [in]	1	13
Steel content ratio (%)	1	0.6
Steel depth from the slab surface for first and second layers in a two-mat steel design [in, in]	16	(3.5,6.5), (3.5,7), (3.5,7.5), (3.5,8), (4,6.5), (4,7), (4,7.5), (4,8), (4.5,6.5), (4.5,7), (4.5,7.5), (4.5,8), (5,6.5), (5,7), (5,7.5), (5,8),
Concrete modulus [million psi]	2	4, 5
Temperature drop from setting to daily minimum temperature [ºF]	2	30, 50
Coefficient of thermal expansion [in/in/ºF]	3	3.5, 4.5, 5.5
Ultimate drying shrinkage on the concrete surface [μ]	2	400, 700
Temperature variation through slab depth [ºF/in]	2	+3, -1.5

Modulus of subgrade reaction [psi/in]	2	300, 500
Crack spacing [ft]	3	4, 8, 12

4.2.c.1 Material properties

The materials – concrete, steel and base/subgrade – were assumed homogeneous, linear elastic (no creep), and isotropic. In a microscopic level, these assumptions might lead to erroneous results. However, in a macroscopic level, which is the case, it is considered that those assumptions are acceptable, especially investigating overall trend of concrete stresses as affected by longitudinal depths, not necessarily quantifying accurate concrete stresses.

Additional material properties used for this analysis other than those listed in Table 4.5 are as follows:

1) Poisson's ratio of concrete and steel: 0.15 and 0.3, respectively
2) Elastic modulus and coefficient of thermal expansion of steel: 2.9×10^{7} psi and 6.4×10^{-6} / ^{o}F, respectively.
3) Longitudinal steel bar size: 0.75-in (#6 bar)
4) Longitudinal steel bar spacing: 11-in (twice of one-mat steel design)

4.2.c.2 Discussion of Numerical Results for Two-mat CRCP

The total number of combinations of all different variables and levels (treatment) was 4,608. Similar to the analysis conducted for one-mat steel design, 3 structural responses were also evaluated: (1) maximum concrete stresses at the top (negative temperature gradient) or bottom (positive temperature gradient) of the slab somewhere close to the middle of two adjacent transverse cracks, (2) maximum principal stresses in concrete at the depth of longitudinal steel near transverse cracks, and (3) stresses in longitudinal steel at transverse cracks. All the graphs represent a k-value of 300 psi/in while the data tables for both k-value of 300 and 500 psi/in are presented in Appendix C and D.

<u>Stress Results at Top of the Concrete Slab</u>

The Max Principal Stress results at concrete slab between the two transverse cracks (top of the concrete slab) are all presented as tables in Appendix C.

Effect of longitudinal steel depth: Figure 4.20 shows the effect of depth of the second layer of steel and coefficient of thermal expansion on max principal of concrete at slab location for 4 ft crack spacing for all different conditions. Figure 4.21 and Figure 4.22 show the same results for 8 ft and 12 ft crack spacing. The lines in each figure are made by a combination of the variables other than those specified in the figure. For example, there are 48 lines in Figure 4.20 made by a combination of two levels of modulus of elasticity of concrete, three levels of coefficient of thermal expansion of concrete, two levels of temperature drops, two levels of temperature gradients, and two levels of drying shrinkage strain. It can be observed that concrete stresses decrease with the increase in depth of longitudinal steel for the second layer considering the same depth for the first layer of steel. For example, when the depth of the first steel layer is 3.5 inches, elastic modulus is 5×10^{6} psi, coefficient of thermal expansion of 5.5 μ/°F, ultimate drying shrinkage of shrinkage =700 μ and negative temperature gradient with 50 °F temperature drop, the max concrete stress on top of the slab is 866 psi when the second layer of steel is at depth of 6.5-in and 816 psi when the depth of second layer of steel is 8 inches. Despite the depth of the first steel layer, with increasing the depth of the second layer of steel, the concrete stress on top of the slab will decrease.

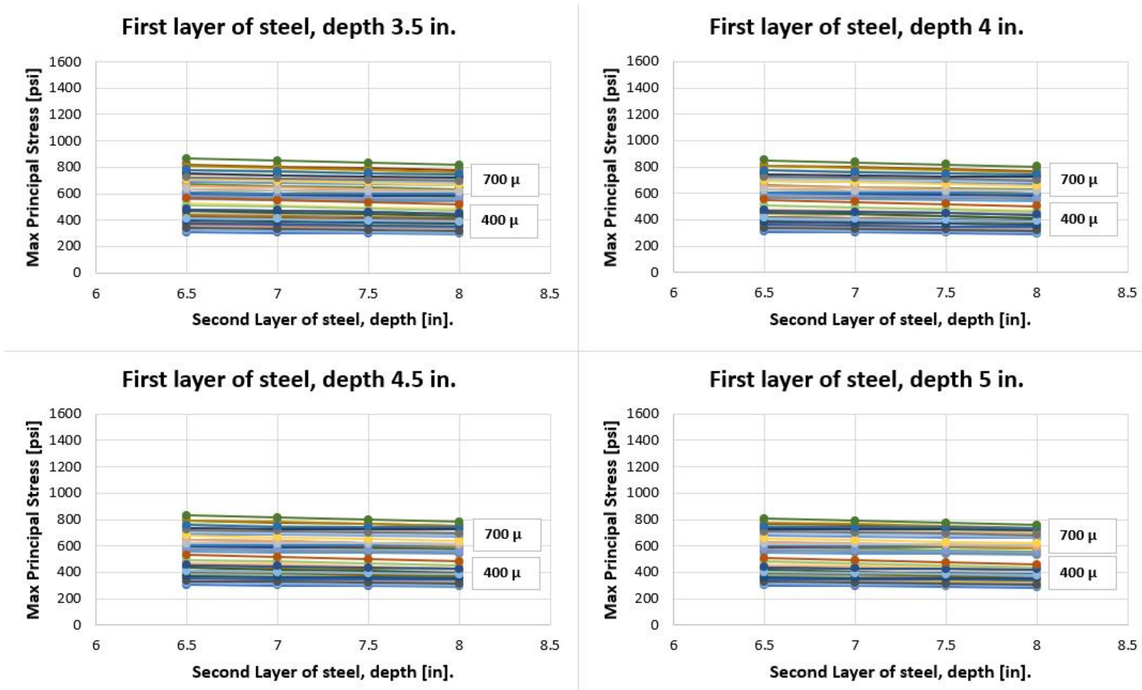

Figure 4.20 Effect of steel depth of second layer for 4-ft crack spacing

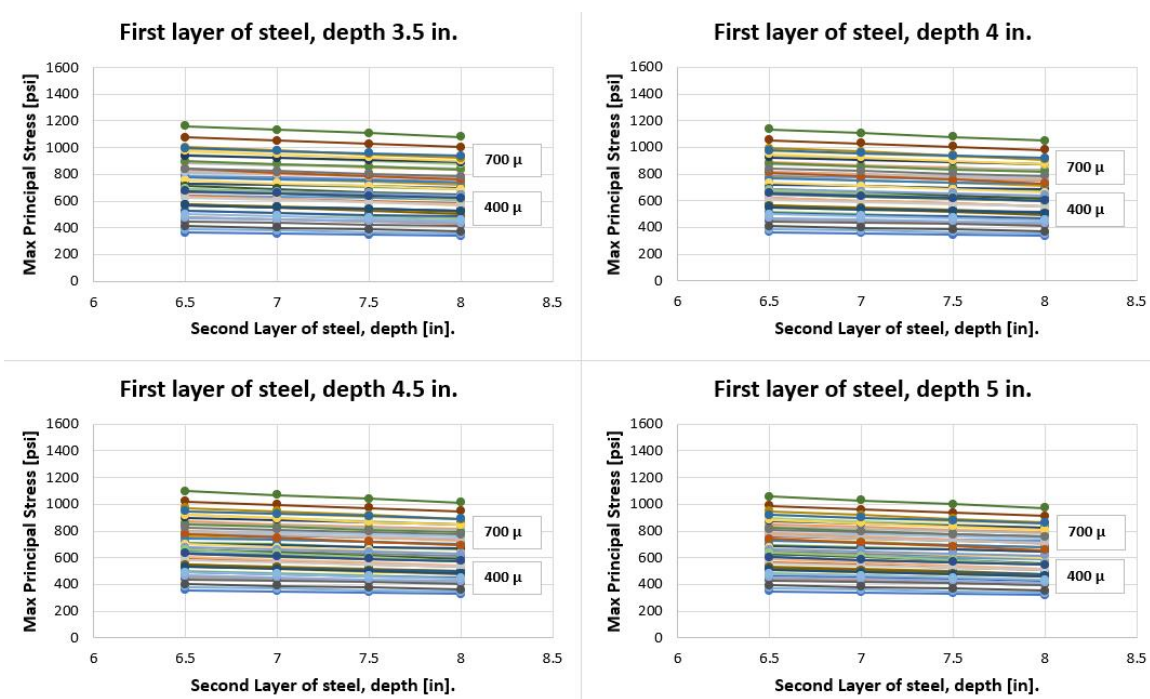

Figure 4.21 Effect of steel depth of second layer for 8-ft crack spacing

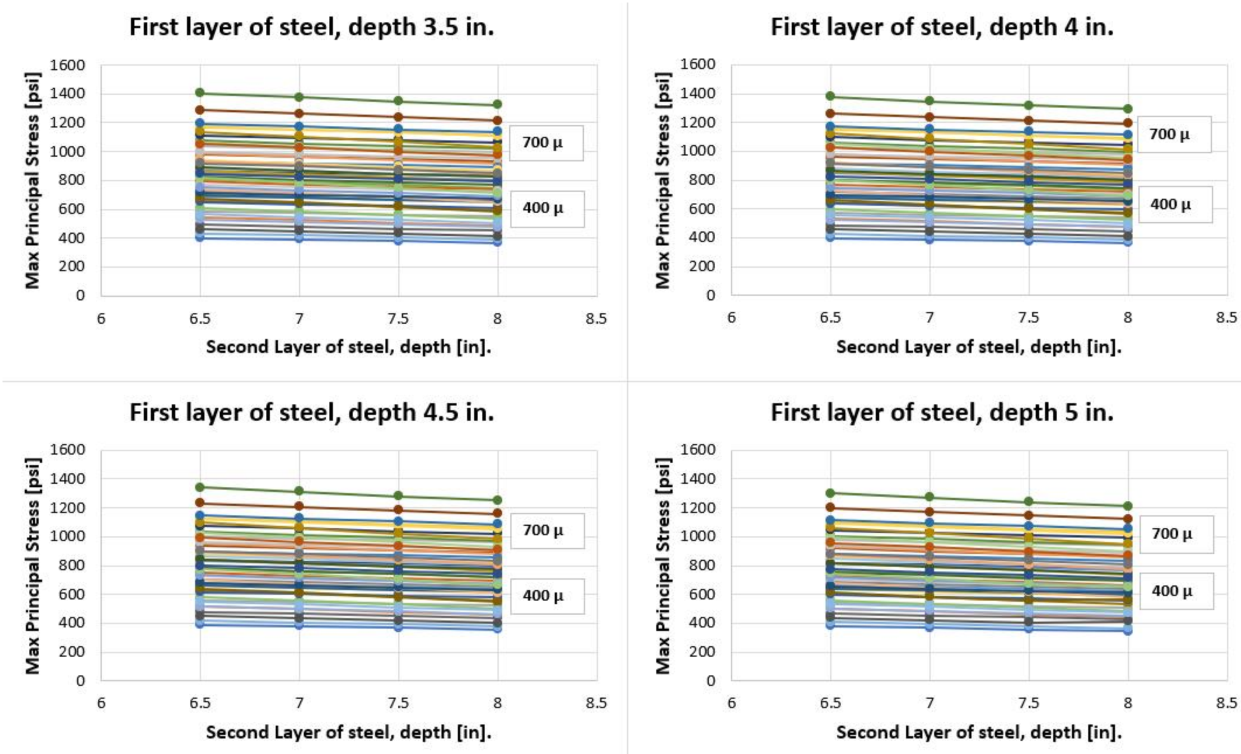

Figure 4.22 Effect of steel depth of second layer for 12-ft crack spacing

To compare the effect of depth of the first layer of steel, Figures 4.23, 4.24 and 4.25 are presented. Figure 4.23 shows the results for 4-ft crack spacing with considering the same depth for the second layer of steel. It can be observed that with increasing the depth of the first layer, the stress on top of the concrete slab will decrease. This means that there would be less restraints and less occurrence of transverse cracks.

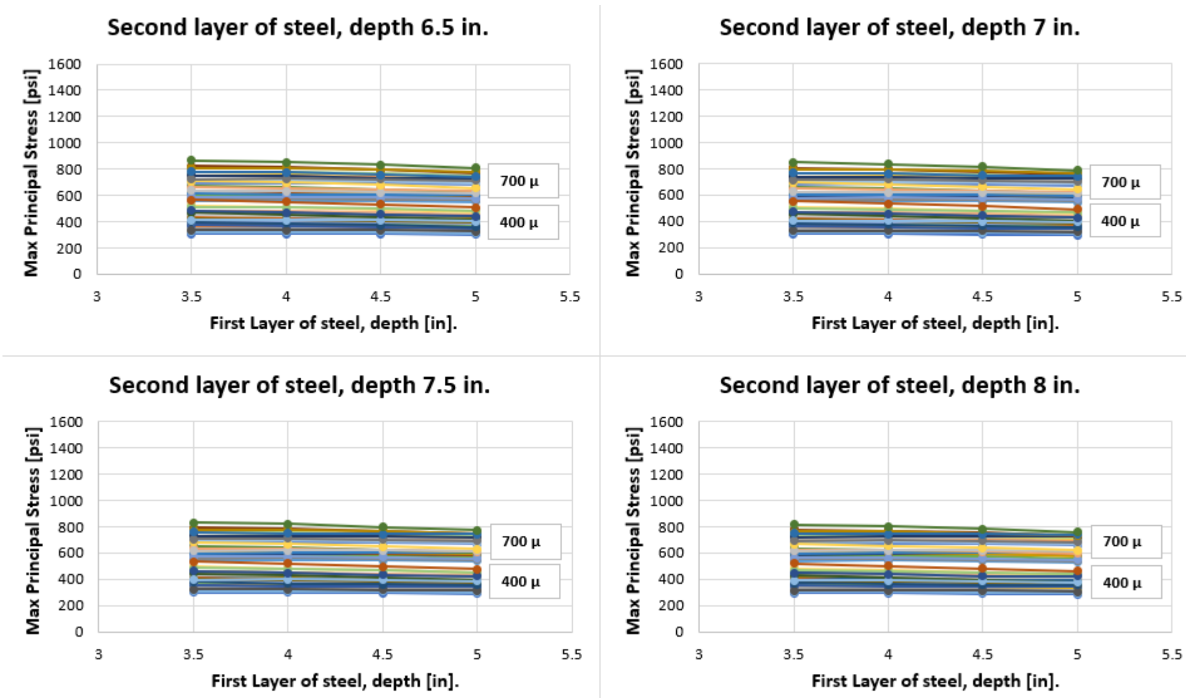

Figure 4.23 Effect of steel depth of first layer for 4-ft crack spacing

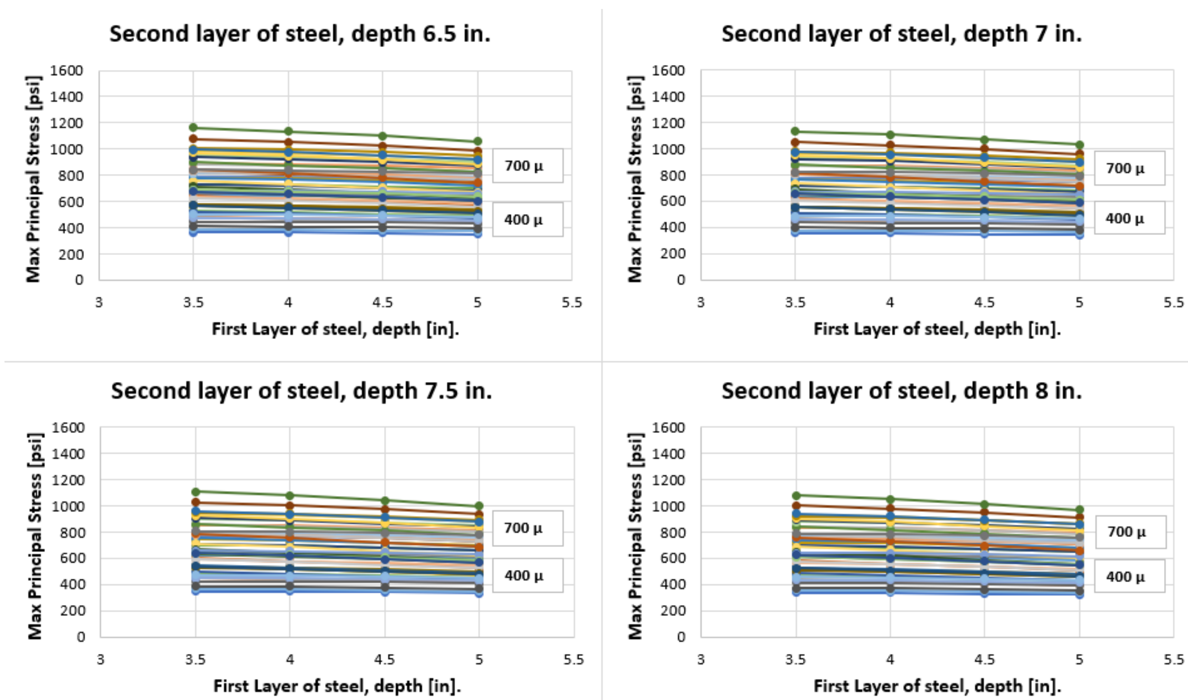

Figure 4.24 Effect of steel depth of first layer for 8-ft crack spacing

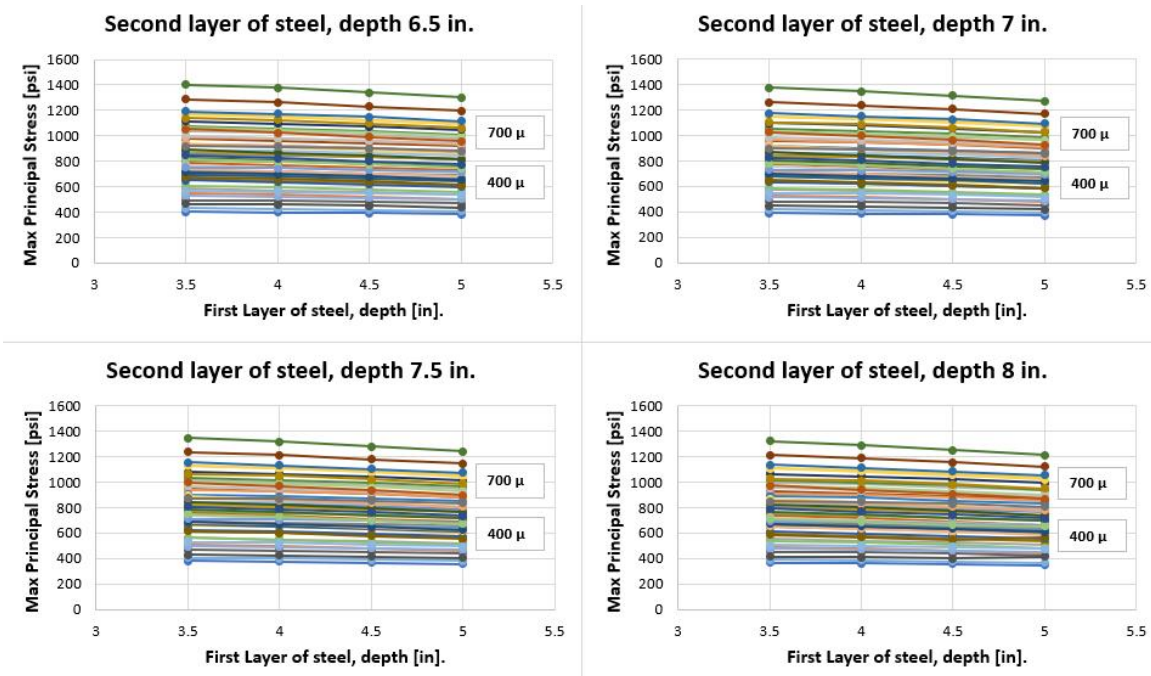

Figure 4.25 Effect of steel depth of first layer for 12-ft crack spacing

In all cases, the increase in steel depth (first or second layer) results to the decrease in the maximum principal stress at the slab which is consistent with previous studies. This signifies that the steel when place at upper depths would increase concrete restraints causing cracks to propagate to release the stress thereby developing shorter crack spacing.

The results also show that with higher ultimate drying shrinkage, the stress at top of the concrete surface will be higher yielding the higher possibility of developing more transverse cracks.

Concrete Stresses near Steel at Transverse Crack Locations for two-mat steel layout

The stresses of concrete close to the reinforcing steel at the transverse crack locations are also investigated. For a 4-ft crack spacing, the maximum principal stress is mostly smaller than the maximum principal stress at the top surface of the concrete slab. This indicates that before any distress happens at transverse crack at the depth of rebar due to the excessive concrete stress, another transverse crack will develop at the mid-slab which prevents distress in concrete. However, this is not the case for crack spacing of 8 ft and 12 ft. The stress in both mid-slab and transverse cracks are quite high and since the models are all within the linear elastic state, it is not clear which part exceeds the concrete strength first and probably there will be distress in transverse crack location. The maximum principal stress results at transverse crack location around the rebar are presented as tables in Appendix D.

Effect of coefficient of thermal expansion: Figure 4.26 shows the effect of coefficient of thermal expansion on maximum principal stress for 4-ft crack spacing having a modulus of elasticity of 4×10^6 psi. The figure includes all steel depths and positive and negative temperature gradient. It can be observed that with increasing CoTE value of concrete, the stress value will proportionally increase for all different conditions. Another observation is that the stress values at transverse crack locations are higher for negative temperature gradient, higher temperature drop, and higher ultimate drying shrinkage conditions.

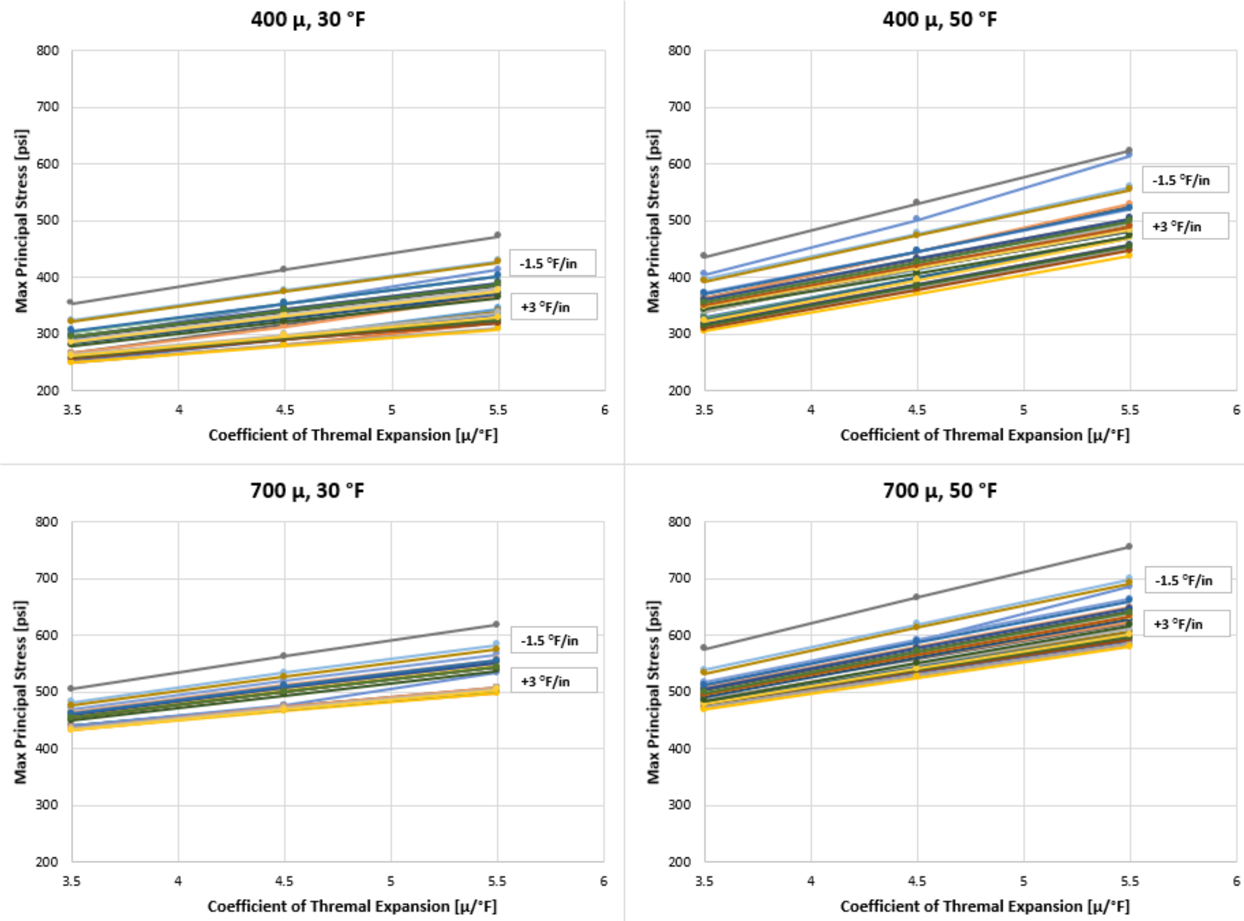

Figure 4.26 Effect of coefficient of thermal expansion on stress at transverse crack for 4-ft crack spacing

Effect of concrete modulus: Figure 4.27 shows the effect of modulus of elasticity on stress value at transverse crack for 4-ft crack spacing which takes into consideration all various temperature gradients, temperature drops, ultimate shrinkage values and steel depths. As shown, higher modulus of elasticity will result in larger stress values and the risk of distress at transverse crack grows higher.

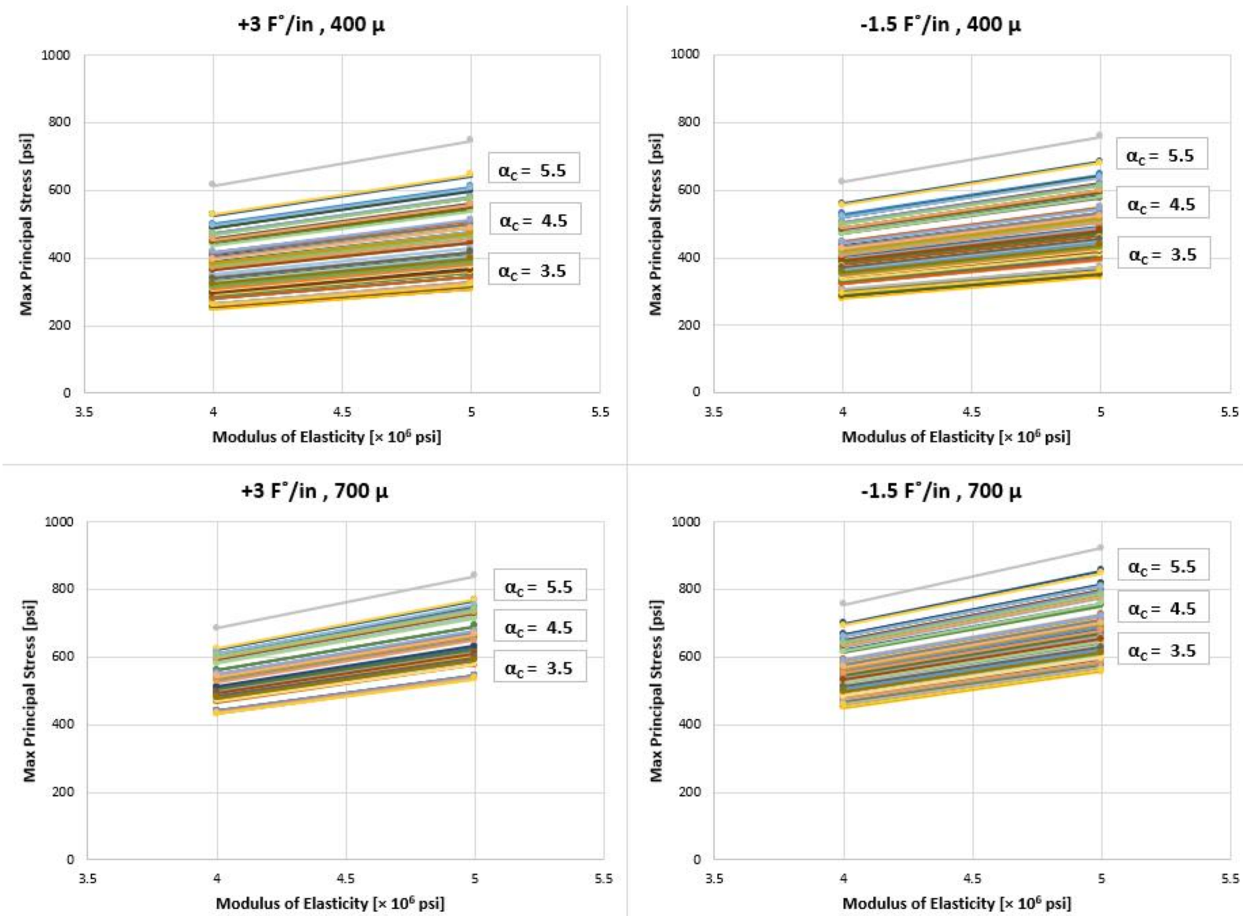

Figure 4.27 Effect of modulus of elasticity on stress at transverse crack for 4-ft crack spacing

Steel Stress at Transverse Cracks

The results show that for 4-ft crack spacing with placing the steel at two different layers (two-mat), the stress results in steel will be in the safe zone but for 8-ft and 12-ft crack spacing stress will be higher than yield stress of the steel. For 8-ft crack spacing, there is no clear trend that was observed. For a worst-case scenario of -1.5 °F/in temperature gradient ,50 °F temperature drop, ultimate drying shrinkage of 700 µ, an elastic modulus of 5 × 10^6 psi, CoTE of 5.5 µ/°F, which creates the highest level of stress condition for steel and concrete, the stress for 4-ft crack spacing remains in the elastic range, however for 12-ft spacing, it goes beyond the elastic range. The results are shown in Table 4.6 and Figure 4.28.

Table 4.6 Steel stress at transverse crack location for two-mat

		Stress Value (psi)		
Steel Depth (in)		4 ft	8 ft	12 ft
3.5	6.5	30,918	55,024	73,714
	7	31,029	55,517	74,702
	7.5	31,124	55,984	75,649
	8	31,224	56,452	76,618
4	6.5	30,162	54,235	73,283
	7	30,267	54,699	74,208

	7.5	30,366	55,153	75,157
	8	30,453	55,573	76,047
4.5	6.5	29,512	53,528	72,901
	7	29,626	53,986	73,837
	7.5	29,721	54,401	74,711
	8	29,809	54,806	75,577
5	6.5	28,884	52,773	72,375
	7	29,006	53,219	73,300
	7.5	29,106	53,626	74,161
	8	29,195	53,996	74,978

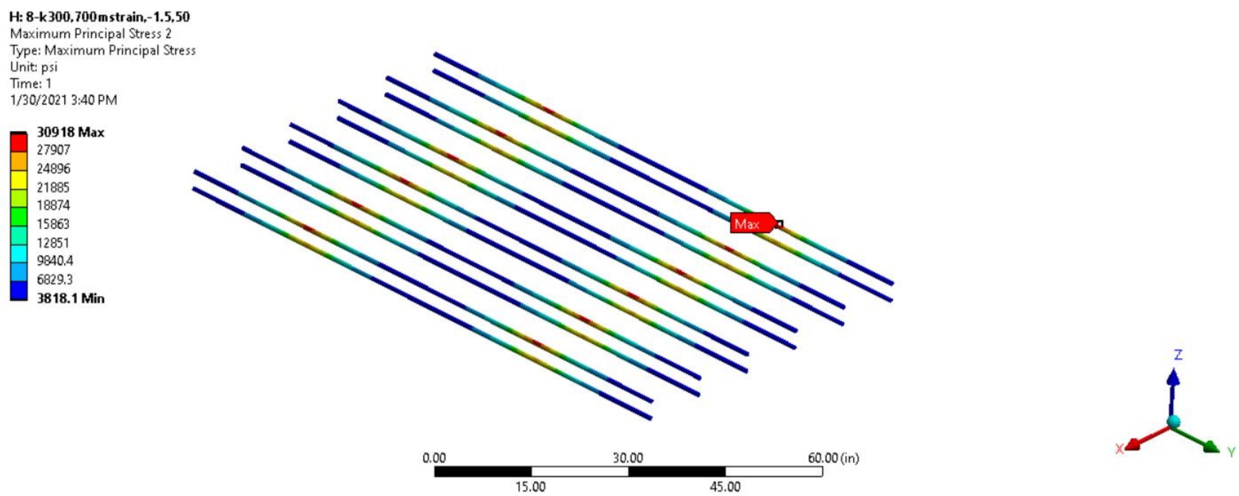

Figure 4.28 Steel stress at transverse crack location

4.2.c.3 Summary of Two-mat

The structural response of a two-mat steel design in CRCP has been mechanistically investigated because it is also one of the current CRCP steel designs in thicker slab. Similar to the one-mat simulations, ANSYS was also used to develop 3D models of a 13-in slab. A factorial design was developed that covers majority of the environmental conditions in Texas. The findings are summarized as follows:

1) Among variables investigated, transverse crack spacing has the most significant effects on concrete stresses near longitudinal steel at crack locations – the larger the crack spacing, the larger the concrete stresses at the depth of steel at crack locations. This finding supports the observations made in the field, which is that horizontal cracking occurs where transverse crack spacing is large. Accordingly, the optimal steel depth should be able to induce smaller crack spacing, but not too small so that other distress types could develop. This is applicable for both one-mat and two-mat steel designs.
2) Mechanistic responses of CRCP are quite complicated and inter-dependent, i.e., changes in one variable will have effects on mechanistic behavior that will alter the effects of other variables. For example, placing steel near the surface will result in increases in concrete stresses at the top and bottom of the slab, which will reduce crack spacing and

concrete stresses near longitudinal steel at crack locations. When interpreting analysis results, there should be a thorough understanding of the interactions of the variables and its corresponding results.

3) Drying shrinkage has substantial effects on concrete stresses near reinforcing steel at crack locations. The importance of drying shrinkage on horizontal cracking development needs to be clearly recognized.
4) CoTE value has significant effect on the concrete stresses near reinforcing steel at crack locations and the potential for horizontal cracking (HC). As the CoTE value increases, the stress at steel depth gets larger.
5) Comparing the one-mat steel design with two-mat steel design shows that as we place in two-mat layout, the stress at concrete surface and at steel depth at transverse crack location will decrease. The reason for decreasing the stress at concrete top surface is that since we removed some rebars from the top layer, the concrete at that depth is less restrained and it will cause less stress. For the stress at steel depth at transverse crack, we can say because there is another layer of steel at different depth, each layer of steel needs to just overcome to the less restrains and therefore, there would be less stress, which results in less possibility for HC in CRCP.

4.3 Comparison of One-mat and Two-mat

To compare the results between one-mat and two-mat reinforcement design, Figures 4.29, 4.30, 4.31, 4.32, 4.33, 4.34 are shown, which are for negative temperature gradient (-1.5 °F/in.), 50 °F temperature drop, 4×10^{6} psi elastic modulus, 3.5×10^{-6} 1/°F coefficient of thermal expansion, 400 με and 700 με ultimate drying shrinkage, and 4 ft. crack spacing. Other crack spacings show similar results. Figures 4.29 and 4.30 show the effect of reinforcement depth for one-mat and two-mat designs with four different top reinforcement depths on vertical tensile concrete stress. The reason for the reduction of vertical tensile concrete stress in two-mat compared with one-mat, considering the same concrete cover on top of the rebars for both designs, is that for two-mat, half of the reinforcements are moved from the top reinforcement layer to the bottom reinforcement layer with a greater depth. Therefore, the concrete top surface is less restrained and creates fewer transverse cracks. According to Figure 4.29 and Figure 4.30, for one-mat design, placing the reinforcement closer to the top surface results in higher vertical tensile concrete stress, and there is a higher chance of more transverse cracks. Comparing the one-mat design with 6.5 in. reinforcement depth with the two-mat designs shows that there is a higher chance of more transverse crack on the top surface of the concrete slab, (i.e., shorter crack spacing) for two-mat design in almost all cases, because the stresses in all two-mat designs are equal or higher than the stress resulted by 6.5 in. reinforcement depth (mid-depth) in one-mat. The stresses in one-mat design with 5 in. to 5.5 in. reinforcement depth are almost identical to those in the two-mat design with 3.5 in. top reinforcement depth: it could be inferred that both designs would exhibit similar transverse crack spacing.

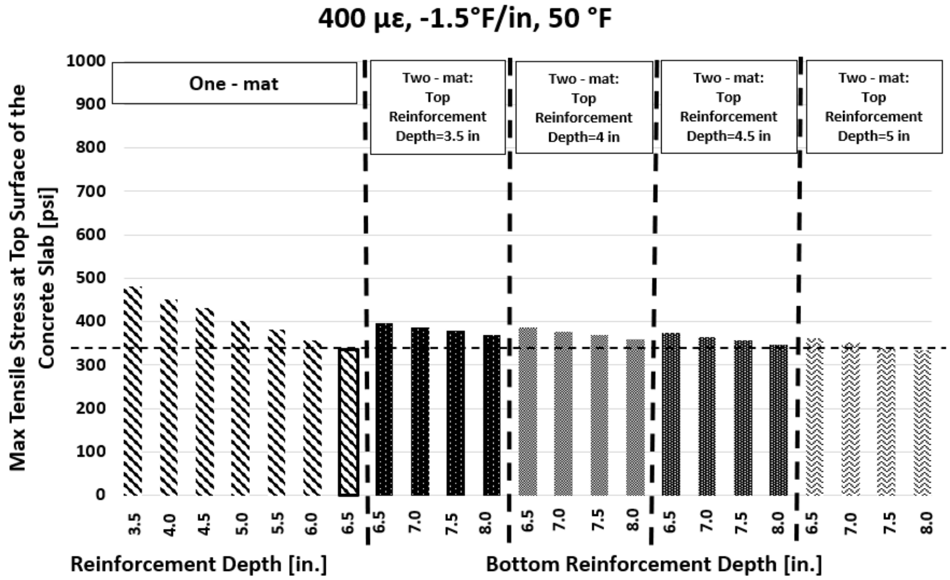

Figure 4.29 Comparison of concrete vertical stress in one-mat and two-mat for 400 με ultimate drying shrinkage

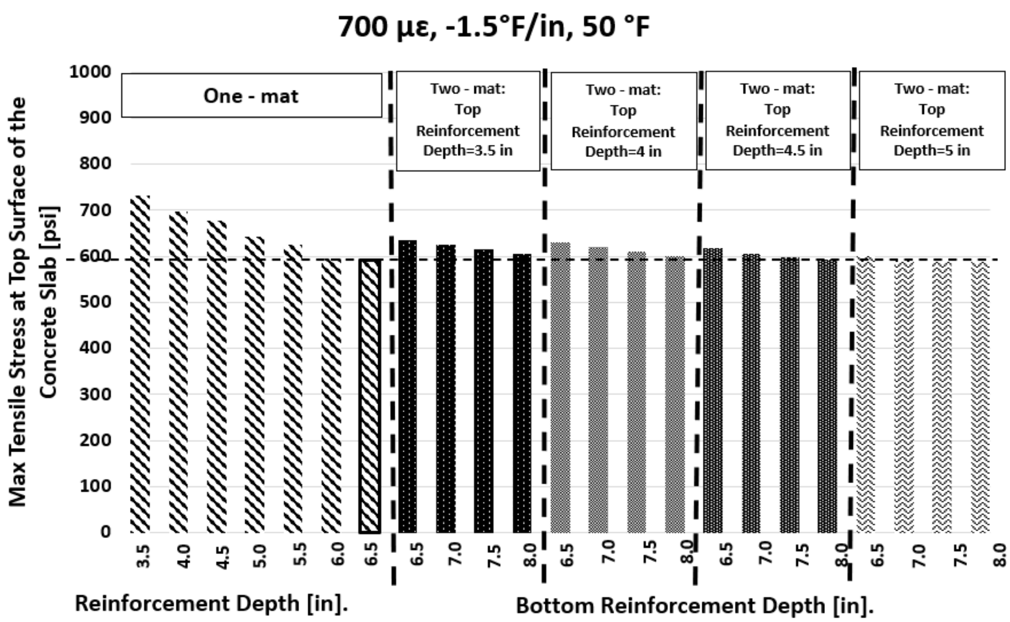

Figure 4.30 Comparison of concrete vertical stress in one-mat and two-mat for 700 με ultimate drying shrinkage

Figure 4.31 and Figure 4.32 show the effect of reinforcement depth for one-mat and two-mat design on concrete stress on top surface of the slab for 400 με and 700 με ultimate drying shrinkage respectively. The figures show the higher stress values in the one-mat design than the stress in the two-mat for most cases, this could imply that the chance of horizontal cracking for two-mat design is lower than one-mat design. According to Figures 4.29, 4.30, 4.31, and 4.32, it appears that 5 in. or 5.5 in. reinforcement depth for one-mat design induces crack spacing small enough to keep concrete stress on top surface of the slab low enough so that horizontal cracking does not develop.

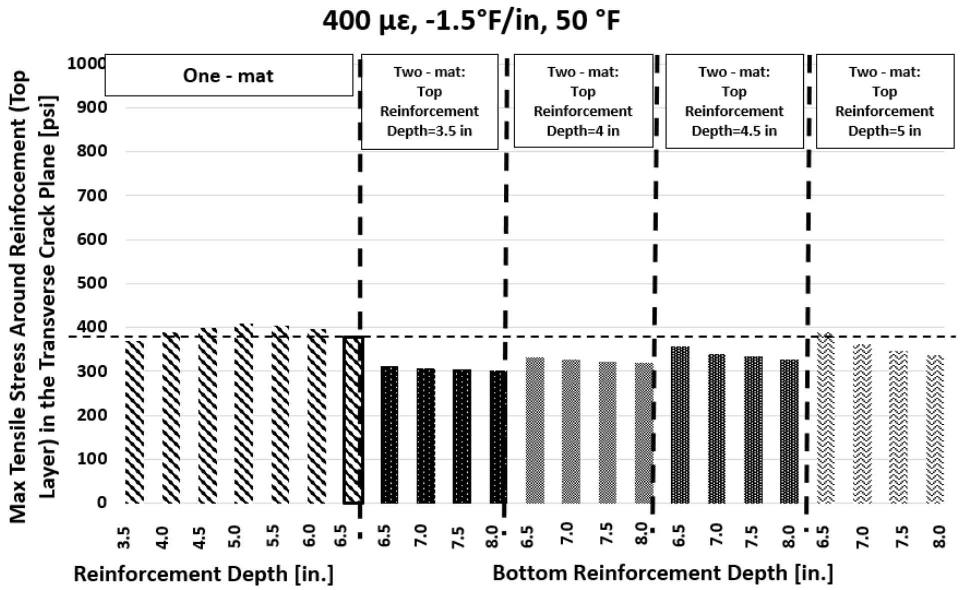

Figure 4.31 Comparison of concrete stress on top surface in one-mat and two-mat for 400 με ultimate drying shrinkage

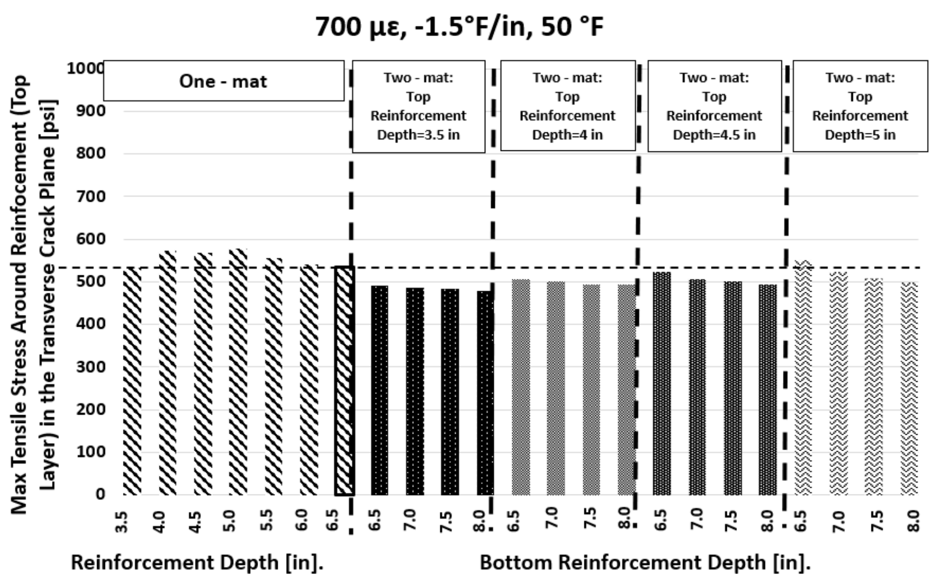

Figure 4.32 Comparison of concrete stress on top surface in one-mat and two-mat for 700 με ultimate drying shrinkage

Figure 4.33 and Figure 4.34 show the concrete stress on top surface of the slab between top and bottom reinforcement layers in the two-mat design with 400 με and 700 με ultimate drying shrinkage, respectively. Since the results for the negative temperature gradient (-1.5 °F/in.) are being compared, the slab is curling up and the stress values are higher around the top reinforcement compared with the bottom reinforcement. According to Figure 4.33 and 4.34, among all different two-mat reinforcement layouts, concrete stress on top surface of the slab is lowest when the top reinforcement and the bottom reinforcement depths are 3.5 in. and 8 in., respectively. Note that the chance of horizontal cracking is the lowest when concrete stress on top surface of the slab is smaller.

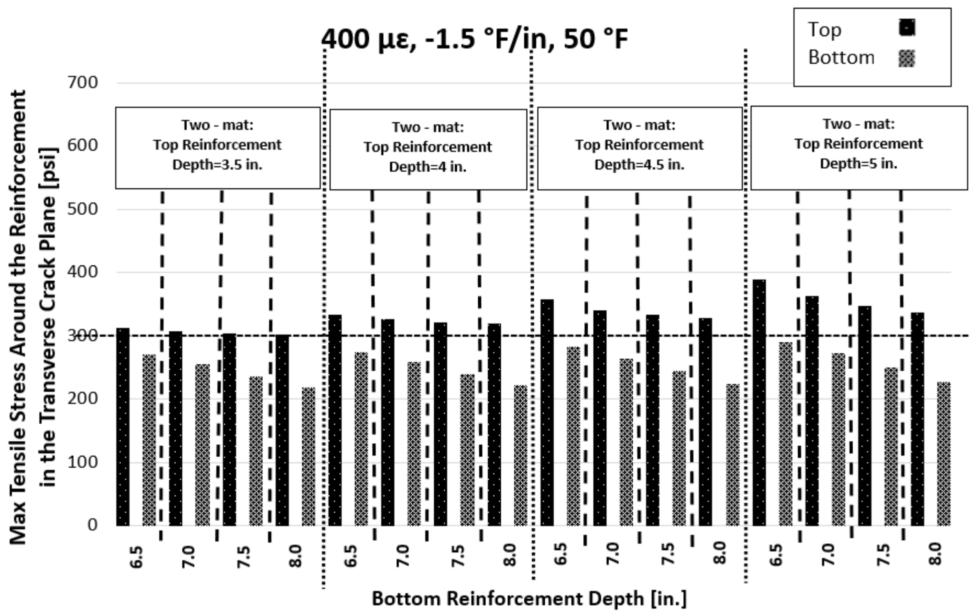

Figure 4.33 Comparison of concrete stress on top surface between top and bottom reinforcement layer in two-mat design for 400 με ultimate drying shrinkage

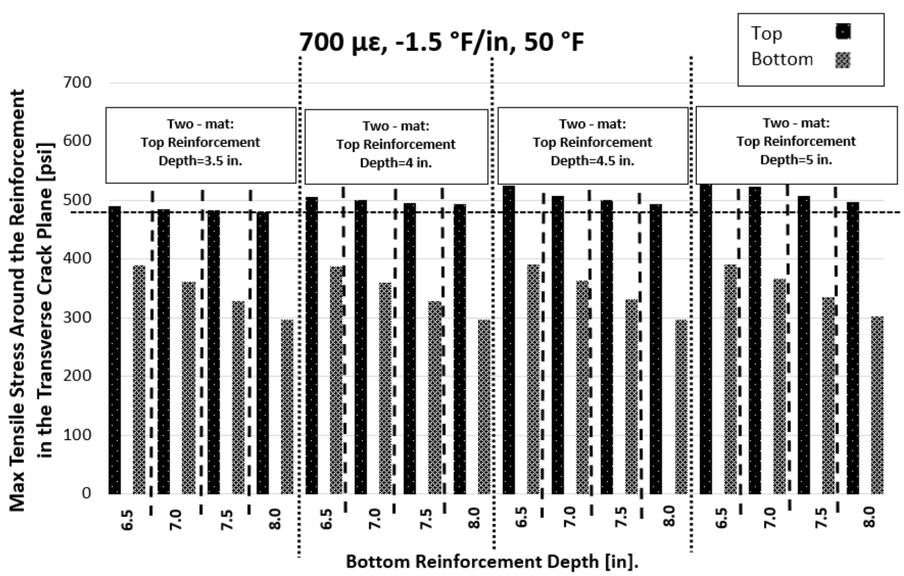

Figure 4.34 Comparison of concrete stress on top surface between top and bottom reinforcement layer in two-mat design for 700 με ultimate drying shrinkage

4.4 Summary of Findings

In this chapter, structural responses of CRCP with various reinforcement depths on both one-mat and two-mat steel reinforcement configuration were analyzed. The findings are summarized as follows:

1) Among variables investigated, transverse crack spacing has the most significant effects on concrete stress near longitudinal reinforcement at crack location: the larger the crack spacing, the greater these vertical concrete stresses.
2) Drying shrinkage has substantial effects on concrete stresses around reinforcement at transverse crack locations. Higher drying shrinkage will result in higher stress at the top surface of the concrete and around reinforcement in the transverse crack plane. As a result, the chance of horizontal cracking increases. The stress around the reinforcements due to the ultimate drying shrinkage of 700 $\mu\varepsilon$ is almost 50% higher than the stress due to the 400$\mu\varepsilon$ ultimate drying shrinkage.
3) Coefficient of thermal expansion has a significant effect on concrete stresses around reinforcement at transverse crack plane and horizontal cracking. As the coefficient of thermal expansion increases, the concrete stress around reinforcement increases.
4) Reinforcement configurations in CRCP have substantial effects on cracking, both transverse and horizontal. In all two-mat designs considered in this chapter, concrete stresses at the top surface of the concrete are greater than those in the one-mat with mid-depth reinforcement. Therefore, it could be assumed that the two-mat design would develop shorter transverse crack spacing than the one-mat design.
5) Comparing the same concrete cover depth for both designs, where the depth of the top layer in the two-mat design is the same as the depth of the one-mat design, the stress at the top surface of the concrete and the stress around reinforcement at the transverse crack plane appears to be smaller in the two-mat design than the one-mat design.
6) For the two-mat design considered in this chapter, since there are two layers of reinforcement at different depths, each layer needs to restrain less volume of concrete in terms of warping and curing. Therefore, it creates less stress, which results in less possibility for horizontal cracking in CRCP.
7) Based on the work conducted in this chapter, the optimal reinforcement depths are suggested as follows.
    a. One-mat design: 5 in. to 5.5 in.
    b. Two-mat design: 3.5 in. for the top reinforcement and 8 in. for the bottom reinforcement.

Chapter 5 Field Testing Program

5.1 Overview of Field-Testing Sites

Three different CRCP sections were identified, and a series of field experiments were carried out. The summarized information of the test sites is presented in Table 5.1, while Figure 5.1 shows geographical location of the field test sections.

Waxahachie field test section located in IH35E southbound was placed on April 26th to May 4th, 2021. OHL of Texas was the contractor and HTNB was the CEI of the project. The El Paso test section located in US62/180 was placed on July 28th to July 29th, 2021. Jordan Foster Construction was the contractor of the project. The San Antonio test section located at the eastbound of IH10 was placed on March 30th to April 4th, 2022. Jordan Foster Construction was also the contractor of the project and Raba Kistner was the project management team. Hillsboro test section located in IH35E was placed on August 2nd to 3rd, 2022. Sacyr S.A. was the contractor and HNTB was the CEI for the construction.

Table 5.1 Detailed information of testing sites

Locations	**Waxahachie**	**El Paso**	**San Antonio**	**Hillsboro**
Highway	IH35E	US62/180	IH10	IH35E
CSJ	0048-04-079	0374-02-097	0025-02-219	0048-09-029
Date of construction	Apr 26th, 2021 to May 04th, 2021	Jul 28th, 2021 to Jul 29th, 2021	Mar 30th, 2022 to Apr 04th, 2022	Aug 2nd, 2022 to Aug 3rd, 2022
Pavement Structure	13-in. CRCP 4-in ASB + 10-in flexible base	12-in. CRCP + 6-in TY-D HMA	13-in. CRCP + 4-in HMA	13-in. CRCP + 4-in HMA
Steel Design	#6 longitudinal steel with a 5.5-in spacing (for low CoTE section #6 longitudinal steel with a 6-in spacing)	#6 longitudinal steel with a 6-in spacing (for low CoTE section #6 longitudinal steel with a 6.5-in spacing)	#6 longitudinal steel with a 5.5-in spacing	#6 longitudinal steel with a 5.5-in spacing

The Waxahachie field test section has a pavement structure of 13-in CRCP + 4-in ASB + 10-in flexible base. Typical Section sheets in the plan set do not provide information on what treatment, if any, was made to the subgrade. The steel design was in accordance with TxDOT CRCP Design Standards CRCP (1)-17, with a 5.5-in spacing with #6 longitudinal steel. Meanwhile, El Paso field test section has pavement structure of 12-in slab + 6-in TY-D HMA. Subgrade soil was not treated with either lime or cement; rather, it was built with a Type A density control. The section was relatively flat having a slope of 0.641 %. The steel design was in accordance with TxDOT CRCP Design Standards CRCP (1)-17, with a 6.0-in spacing with #6 longitudinal steel. For the low CTE section, the steel spacing with #6 bars was 6.5-in. The 3rd field test section in San Antonio field has a pavement structure of 13-inch CRCP + 4-in HMA base. Typical Section sheets in the plan set do not provide information on what treatment was made to the subgrade. The steel design was in accordance with TxDOT CRCP Design Standards CRCP (1)-17, with 5.5-in spacing with #6 bars for longitudinal steel. Lastly, the Hillsboro field test section has a pavement structure of 13-in slab + 4-in HMA base. The steel design was in accordance with TxDOT CRCP Design Standards CRCP (1)-17, with a 5.5-in spacing with #6 longitudinal steel.

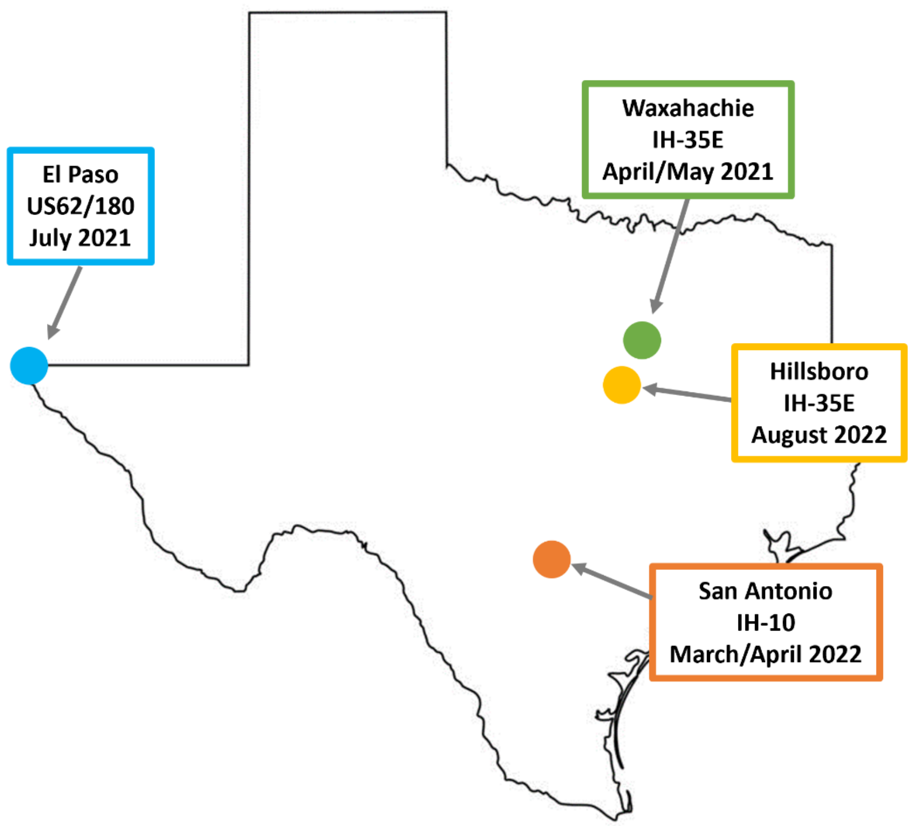

Figure 5.1 Field test sections in the State of Texas

5.2 Material Properties

Class P concrete was used in all four test sections. A Class F fly ash replacement of 30%, 20%, 25%, and 25% of cement was carried out in Waxahachie, El Paso, San Antonio, and Hillsboro test sections, respectively. The water-cement ratio for Waxahachie and San Antonio was 0.45, while 0.5 for El Paso and Hillsboro. The detailed mixture proportions and material properties of the concrete are summarized in Table 5.2.

Table 5.2 Mixture proportion of materials used in the field tests

Mix component	Waxahachie	El Paso	San Antonio	Hillsboro	Unit
Cement (Type I/II)	361	416	386	335	lbs/yd^3
Fly ash (Replacement rate)	155 (30%)	104 (20%)	129 (25%)	112 (25%)	lbs/yd^3
Coarse aggregate	1943	1938	1819	1850	lbs/yd^3
Fine aggregate	1380	1251	1422	1413	lbs/yd^3
Water	230	260	231	224	fl oz/yd^3
W/C	0.45	0.5	0.45	0.5	-
Slump	1.5	1.5	2	3	in.
7-day compressive strength		4340	3200	4230	psi
28-day compressive strength		-	4270	5920	psi

5.3 Field Instrumentation

5.3.a Weather Station

Air temperature helps in the better understanding of the CRCP. Since the temperature of the concrete has a substantial effect on the temperature of the concrete, collecting actual air temperature is necessary. However, the National Weather Service is accessed to obtain air temperature data in the absence of the weather station. The air temperature collected from the National Weather Service has a limitation as the station is distant from the test site which may have effects on the accuracy. As such, a wireless weather station was installed in San Antonio test section to obtain local air temperature data using the wireless weather station from Davis as shown in Figure 5.2.

Figure 5.2 Davis Weather Station installed in field test site

5.3.b Datalogger

The data collection from all the gauges installed in the field test section was done using data logger. CR1000X from Campbell Scientific was used for this purpose. The data logger was assembled according to field requirement. Figure 5.3 shows the image of the datalogger installed in the field.

Figure 5.3 Datalogger (CR1000X; Campbell Scientific)

5.3.c Thermocouple (TC)

Concrete temperature plays an important role in understanding concrete. Being one of the environmental loadings, it is considered a major factor that affects the behavior of concrete. Higher variations of the temperature in the concrete may generate higher stresses leading to crack development. Thus, to understand temperature variation effect on behavior of concrete, thermocouples were installed at various depths in the slab. Type T thermocouple was used for the test sections to measure the concrete temperature variation through the concrete slab depth.

Figure 5.4(a) shows the typical installation of thermocouple with various depths from the surface of the slab.

5.3.d Vibrating Wire Strain Gauge (VWSG)

Two types of VWSG were used to measure the strain of the concrete. The strain of concrete is a critical factor for evaluating the behavior of concrete. The deformation caused by concrete change when it is under the environmental load is a continuous process. So, measuring the strain in short intervals will aid to understand the concrete behaviors. For this purpose, a Vibrating Wire strain gauge (VWSG) from Geokon was used. As this instrument is designed for direct embedment in the concrete, we used 6-in VWSG and 2-in VWSG for the measurement attaching it to rods or steel and placing it directly into concrete. The strain measured with this instrument works using the vibrating wire principle. According to the vibrating wire principle, when there is deformation in the concrete it will lead to the movements of the VWSG flanges. When there is movement of the VWSG flanges, a tensioned wire vibrates at a frequency that is proportional to the strain in the wire. The strain is then calculated by squaring the frequency value and applying manufacturer (Geokon) constant. In all test sections, 2 in. VWSG was placed vertically. It was used to measure the vertical strain of the concrete slab. Similarly, 6 in. VWSG was used to measure the strain in the horizontal (longitudinal) direction. Figure 5.4(b)(c) shows the typical setup of the VWSGs in the field.

5.3.e Steel Strain Gauge (SSG)

In CRCP, the movement of the concrete is restrained because of the reinforcement. Thus, the behavior of the rebar becomes critical while understanding CRCP behavior. Steel strain gauge also known as SSG is used for evaluating behavior of the reinforcement to measure the strain. SSG is an attachment type, and it is directly attached to the reinforcement to measure the strain of the steel. For this we grind the surface, prepare, bond, and protect the surface and gauge using appropriate treatments. Figure5.4(d) shows the shape and typical installation of the SSG.

Figure 5.4 (a) Typical Installation of Thermocouple, (b) 6-in Vertical VWSG, (c) 2-in Horizontal VWSG, (d) SSG installed in the field

5.3.f Crackmeter

To evaluate the concrete displacements, crack meters were installed on the side of the slab. This was used for measuring both the horizontal and vertical displacement of the concrete. The crack meter operates on principle similar to VWSG. It can measure the movement of concrete in mils. The measured displacement is used to compare with the internal behavior of concrete and steel. Figure 5.5 shows the typical installation of the crack meter in the field test. During the installation, we use anchor bolts and fix it using epoxy on the exposed side of the concrete slab. Concrete displacements were recorded at specific time intervals and collected through the data logger.

Figure 5.5 Typical Installation of Crackmeter in the field

5.3.g REBEL Sensor

The REBEL sensor is developed by the Purdue University research team under Dr. Lu. This sensor will provide real-time information of the elastic modulus development of the concrete pavement. The elastic modulus is measured by the REBEL sensor based on the acoustic and ultrasonic resonant behavior of the concrete. REBEL sensor is specially designed to be embedded in concrete and to generate high quality resonance spectrum of concrete, which is an intrinsic indicator of the elastic modulus of concrete. The sensor is excited by a series of electric signals with various frequencies. The sensor then drives itself along with the concrete to mechanically vibrate in the frequency of interest range, and such vibration's resonant frequency is correlated to the elastic modulus of concrete. The detailed first principle based physical modeling and mathematical equations has been discussed in Kong and Lu's research (Kong and Lu, 2020).

Figure 5.6 REBEL Sensor and its typical installation

5.4 Testing Plan and Gauge Setup

5.4.a IH 35E in Waxahachie

Figure 5.7 shows the overall layout of the test section. Concrete was placed on April 26, 2021, at about 2:30 in the afternoon for the first segment covering 330-ft. The reason for placing only

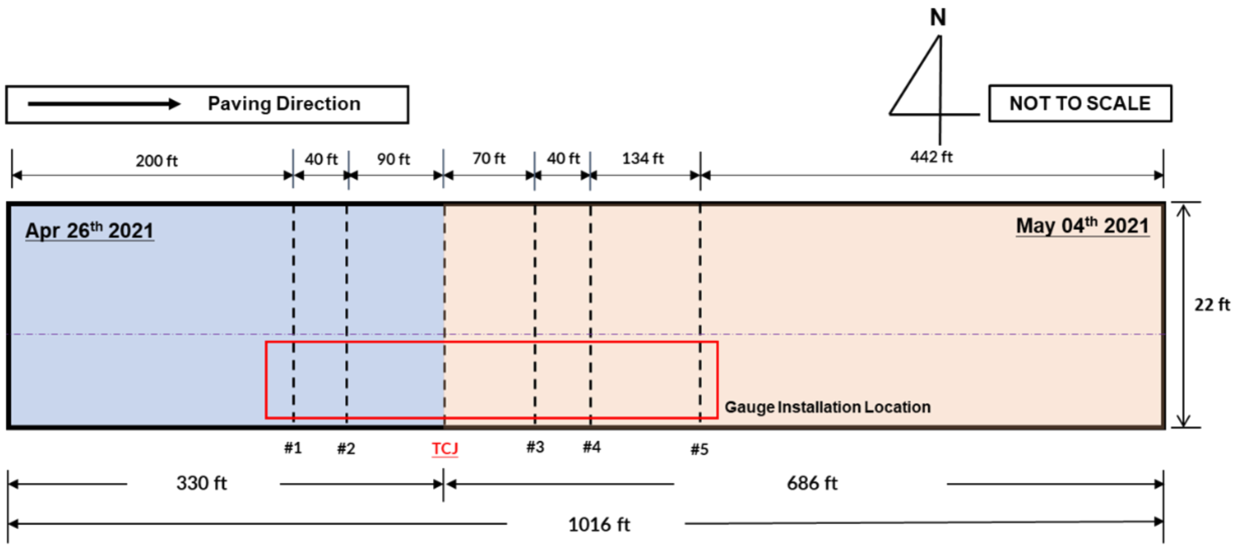

Figure 5.7 Layout of test Section in Waxahachie

330-ft was the issue with the concrete plant. The first segment covered only 2-gauge installations locations. The construction crew finished the formation of a transverse construction joint at about 6:30pm. Later the research team was informed about the uncertainty of the concrete plant operation. Next day, it was announced that the remaining section concrete placement wouldn't be placed until May 1st. Since datalogger were already placed, the research team decided on collecting the data from the first segment. However, it was remarked that the data collected from the CRCP section will not provide valuable information on the effects of steel placements at different depths. The reason behind this is the concrete and steel behavior with short (330-ft) lengths would be quite different from Normal CRCP. Meanwhile, the vibrating wire strain gauges (VWSGs) pre-installed in the second segment were removed as it would be placed after May 1st. The second segment was placed on 4th May 2021 at about 8:30 in the morning covering 686-ft in length. Table 5.3 summarizes date and time, location (GPS coordinates and length) of the field section.

Table 5.3 Date and Time, location (GPS coordinates), and length of Waxahachie test field section

<table>
<tr><th>Segment No.</th><th colspan="2">Date & Time (Start, Finish)</th><th>GPS Coordinates</th><th colspan="2">Length (ft.)</th></tr>
<tr><td rowspan="2">1</td><td rowspan="2">Apr 26th, 2021</td><td>14:30</td><td>32.420623, -96.867895</td><td rowspan="2">330</td><td rowspan="4">1016</td></tr>
<tr><td>18:30</td><td>32.420623, -96.867895</td></tr>
<tr><td rowspan="2">2</td><td rowspan="2">May 04th, 2021</td><td>08:30</td><td>32.419845, -96.868434</td><td rowspan="2">686</td></tr>
<tr><td>15:00</td><td>32.418297, -96.86971</td></tr>
</table>

Figure 5.8 illustrates gauge installation plan and a picture of installed gages. For each gauge installation location 14 SSG, 4 Vertical VWSG's, 1 Horizontal VWSG's and 1 Thermocouple were installed.

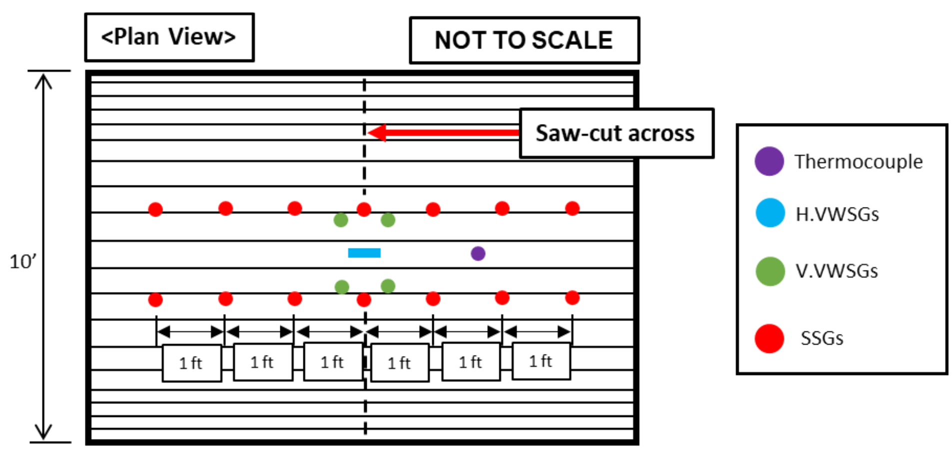

Figure 5.8 Plan view of typical gauge installation location in Waxahachie

Once all the concrete placement was completed, data was observed for 10 days. Due to the reason mentioned earlier the short length CRCP behavior wouldn't represent Normal CRCP behavior' datalogger were removed 10 days after the concrete placement and the data obtained from this section was not included in this report.

5.4.b US 62 in El Paso

Figure 5.9 shows the overall layout of the test section. Three different steel depth sections were placed. The first three-gauge installation locations 1-1, 1-2 and 1-3 fall under Section 1, which is normal steel depth (mid-depth) section. Similarly, gauge installation location 2-1, 2-2 and 2-3 falls under Section 2, which is Upper-depth steel section. Lastly, gauge installation location 3-1, 3-2 and 3-3 falls under Section 3, which is upper-depth and low CoTE steel section. The chairs used for upper-depth steel section were 6.5-in tall. Accordingly, the depth of the longitudinal steel for upper-depth steel section was 7.5-in from the bottom of the slab (6.5-in + 0.625-in (transverse steel) + 0.75-in/2), or 4.5-in from the slab surface.

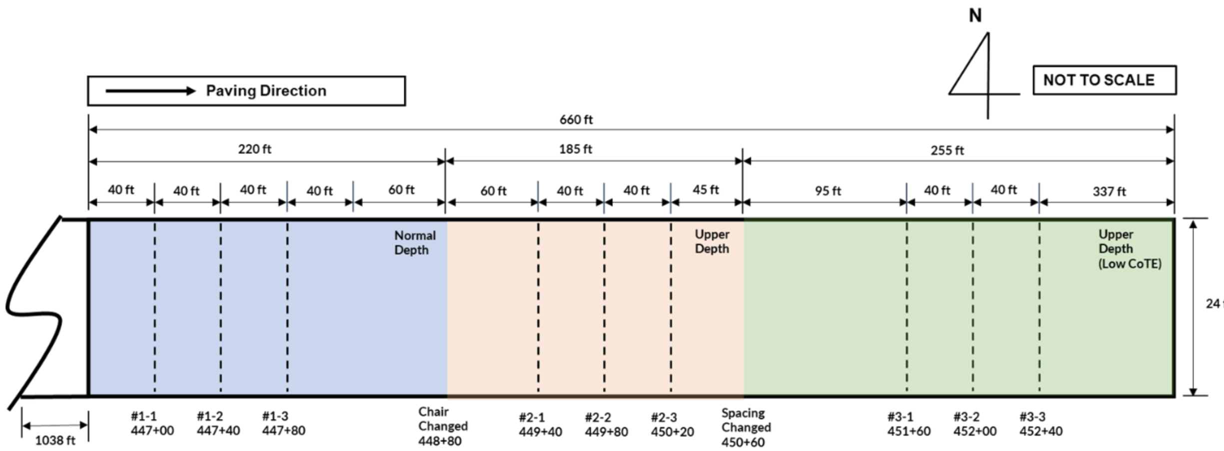

Figure 5.9 Layout of test Section in El Paso

Concrete was placed on July 28, 2021, at about 10:20 in the evening over the length of 2,185-ft, from STA 434+77 eastbound to STA 456+62. The concrete placement was completed at about 9:10 in the morning on the following day. The paving operation proceeded without any hurdles. The average paving speed was noted to be about 3.4ft/min, which is considered in line with the average paving speed in concrete paving. The width of the paving was 24-ft, with two 12-ft lanes and the test section was located at the outer 12-ft lane. The concrete at the first saw-cut area at mid-depth steel was placed at about 4:00 am on July 29, and the last saw-cut area at around 8:00 in the morning. Saw-cuts were made on the same day of the concrete placement (July 29) at around 1:30 in the afternoon. Saw-cuts were made throughout 24-ft width. Initially, the saw-cuts were made at each location at 2 ¼-in deep. Additional saw-cuts were made up to 3-in deep on the morning of July 30 at around 9:00. Detailed information on the saw-cut timing and locations (GPS Coordinates and STA) is presented in Table 5.4.

Table 5.4 Information of section ID, Date and Time, location (GPS coordinates), and length of El Paso test field section

Section I.D.	Date & Time (Start, Finish)		GPS Coordinates	STA	Length (ft.)
Start	Jul 28th, 2021	22:20	31.802227, -106.301265	434+77	2185
1-1	Jul 29th, 2021	04:23	31.802711, -106.298077	447+00	
1-2		04:40	31.802713, -106.297915	447+40	
1-3		04:55	31.802722, -106.297815	447+80	
2-1		06:10	31.802768, -106.297288	449+40	
2-2		06:25	31.802778, -106.297155	449+80	
2-3		06:45	31.802813, -106.297048	450+20	
3-1		07:25	31.802902, -106.296622	451+60	
3-2		07:35	31.802926, -106.296495	452+00	
3-3		07:48	31.802935, -106.296335	452+40	
End		09:10	31.80314, -106.295018	456+62	

The details of the gage installations are the same as the Waxahachie section as shown in Figure 5.10. For each gauge installation location 14 SSG, 4 Vertical VWSG's, 1 Horizontal VWSG's and 1 Thermocouple were installed.

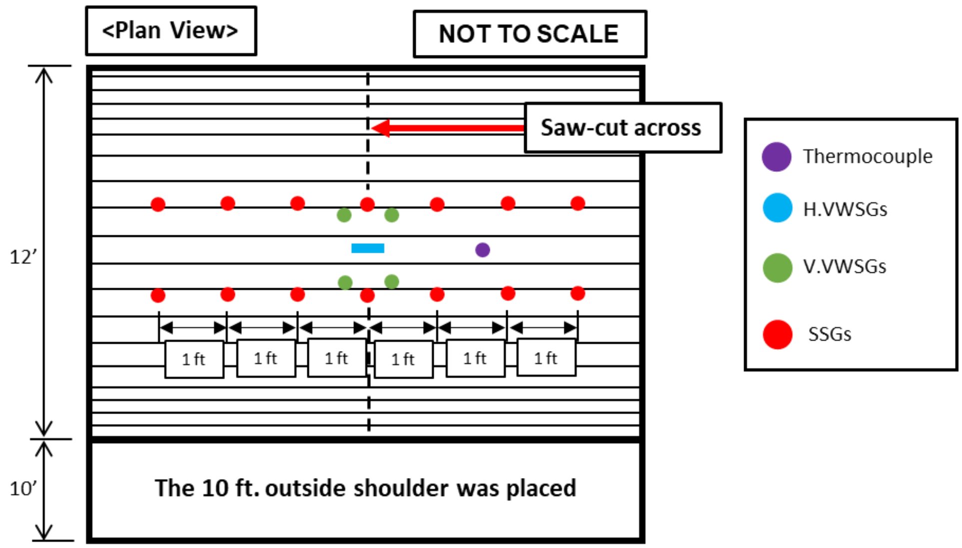

Figure 5.10 Plan view of typical gauge installation location in El Paso

5.4.c IH 10 in San Antonio

Figure 5.11 shows the overall layout of the test section. Two different steel depth sections were placed. The first gauge installation locations #1 falls under Section 1, which is normal steel depth (Mid-depth) section. Similarly, gauge installation location #2 falls under Section 2, which is upper steel depth (upper-depth) section.

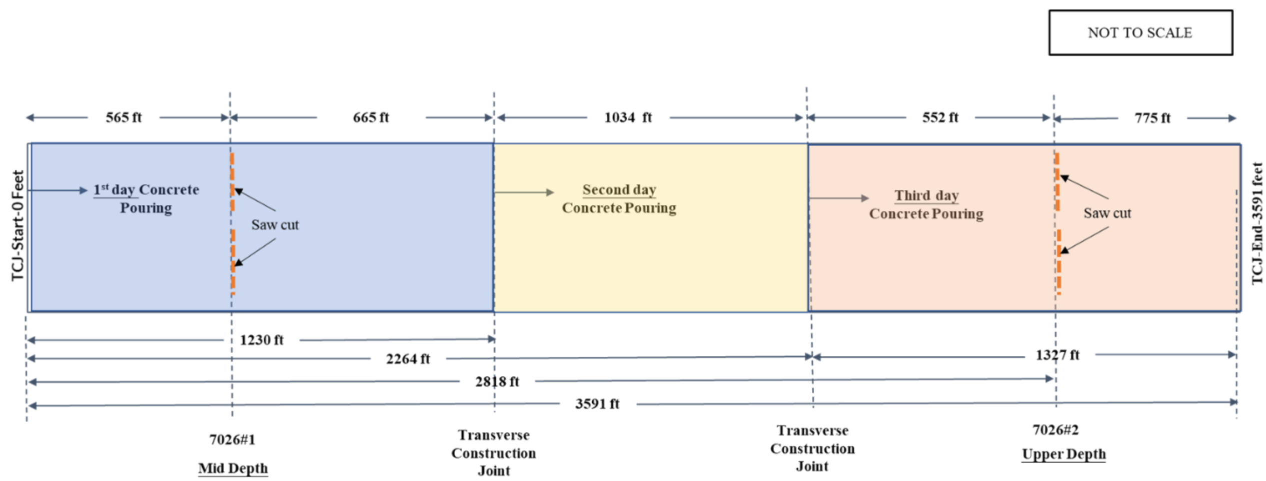

Figure 5.11 Layout of test Section in San Antonio

The first day of the concrete placement was done on March 30, 2022, from 7:30 in the morning until 4:30 in the afternoon covering 1,230 feet. The second day placement continued the following day from 7:30 in the morning until 4:30 in the afternoon covering 1,034 feet. The third day placement was postponed to 4 days due to logistics issues, specifically on the delivery of the expansion board. It was done on April 4 from 7:30 in the morning until 4:30 in the afternoon covering 1,327 feet. The remaining 186-feet before the bridge deck was done through hand placement. After the concrete placement was done, 2 active crack control saw-cuts were made on the following day: 1 edge active crack control saw-cut at the mid-depth steel section (#1), and 1 edge active crack control saw-cut at the upper-depth steel section (#2). Table 5.5 summarizes data and Time, location (GPS Coordinates and STA) of the concrete placement.

Table 5.5 Information of section ID, Date and Time, location (GPS coordinates), and length of San Antonio test field section

ID	Time		GPS	STA	Length (ft.)
Start (Day 1)	Mar 30th, 2022	07:30	29.46874, -98.28137	1418+75	1230
Mid-depth Section		11:00	29.46923, -98.27969	1424+40	
End (Day 1)		16:30	29.46993, -98.27769	1431+05	
Start (Day 2)	Mar 31st, 2022	07:30	29.46993, -98.2777	1431+05	1036
Transition		10:30	29.47175, -98.2728	1436+00	
End (Day 2)		16:30	29.46993, -98.2742	1441+41	
Start (Day 3)	Apr 04th, 2022	07:00	29.46993, -98.2742	1441+41	1328
Upper-depth Section		11:00	29.47144, -98.27305	1446+93	
End (Day 3)		16:30	29.47208, -98.27050	1454+69	

The test section consisted of two different steel sections (mid-depth & upper-depth). In this test section, 2 locations (#1, and #2) were used for gauges installation. Each location consisted of 2 numbers of 6 in. VWSGs, 6 number of 2 in. VWSG, 4 number of Steel strain gauge and thermocouple. The details of the gage installations are shown in Figure 5.12.

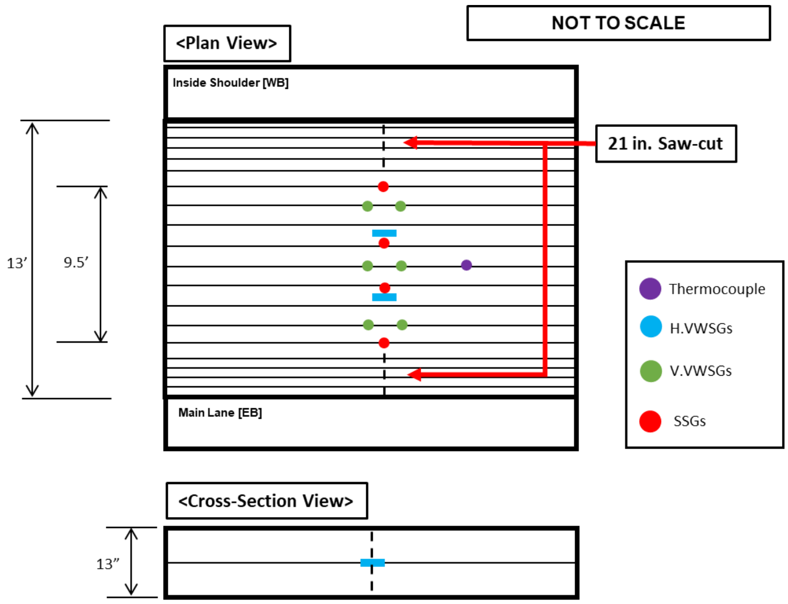

Figure 5.12 Plan view of typical gauge installation location in San Antonio

5.4.d IH 35E in Hillsboro

Figure 5.13 shows the overall layout of the test section. Two different steel depth sections were placed. The first gauge installation locations #1 is normal steel depth (mid-depth) section. Another gauge installation at #2 is the upper-depth steel section.

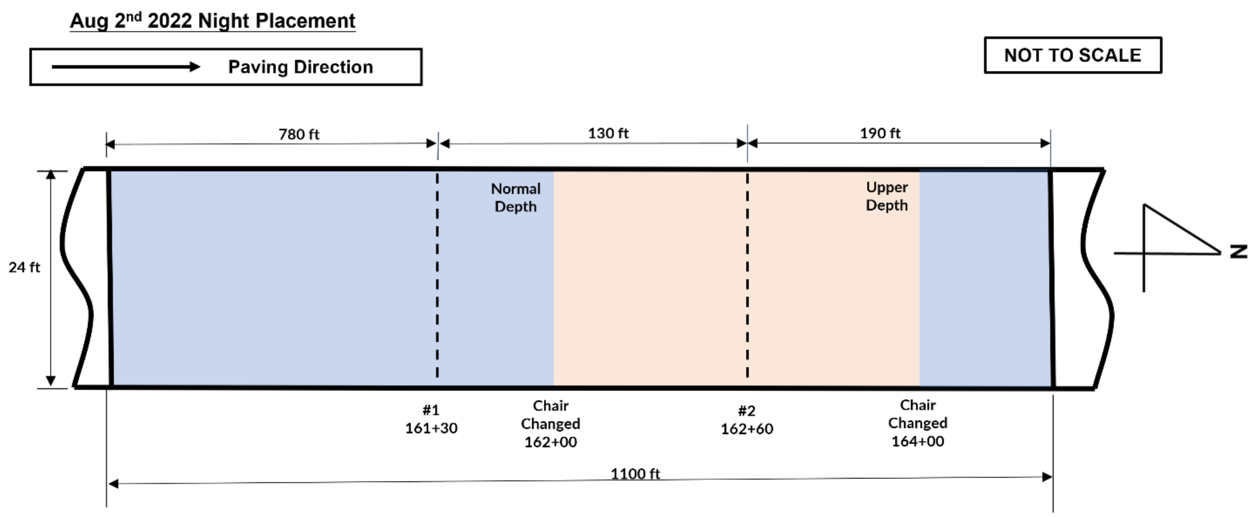

Figure 5.13 Layout of test Section in Hillsboro

Concrete placement started from 6:00 in the evening on August 2nd, 2022, until 3:00 in the morning of the following day covering 1,100 feet. The #1 location was placed around 11:30pm on August 2nd, 2022, followed by #2 location which was placed around 12:25am on August 3rd, 2022. After the concrete placement was done, 2 active crack control saw-cuts were made in the morning of August 3rd, 2022: 1 saw-cut at the mid-depth steel section (#1), and 1 saw-cut at the upper-depth steel section (#2). The Table 5.6 summarizes data and Time, location (GPS Coordinates and STA) of the concrete placement.

Table 5.6 Date and Time, location (GPS coordinates), and length of Hillsboro test field section

Segment No.	Date & Time (Start, Finish)		GPS Coordinates	Length (ft.)
1	August 2nd, 2022	18:00	32.065594, -97.076253	1100
	August 3rd, 2022	2:00	32.067253, -97.073198	

Figure 5.14 illustrates gauge installation layout. For each gauge installation location 4 SSG, 4 Vertical VWSG's, 4 Horizontal VWSG's and 1 Thermocouple were installed.

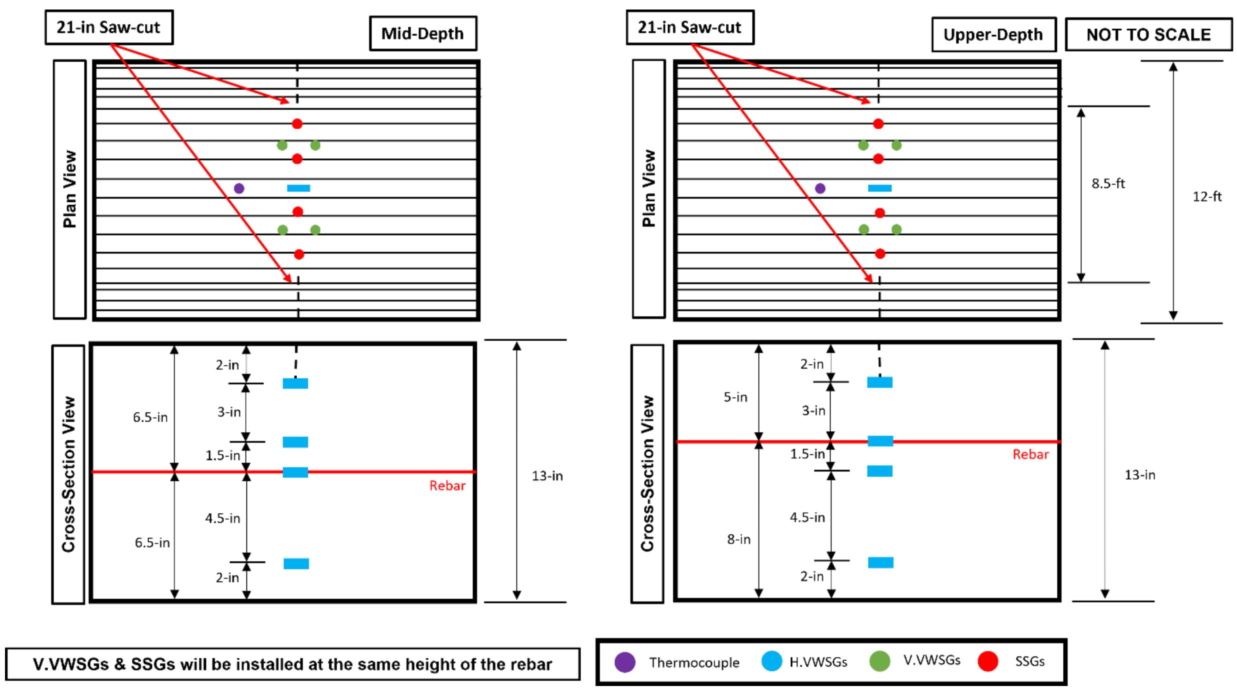

Figure 5.14 Plan view of typical gauge installation location in Hillsboro

Meanwhile, another section was also instrumented with the REBEL sensors from Purdue University research team. The location of the section was at STA 212+00 where the location of the reinforcing steel was located at the upper depth (5-in from the surface). 6 REBEL sensors were installed at various locations on the north and south side of the active crack control sawcut and 4 VWSG strain gauges are various depths like the previous section's configuration as shown in the figures below.

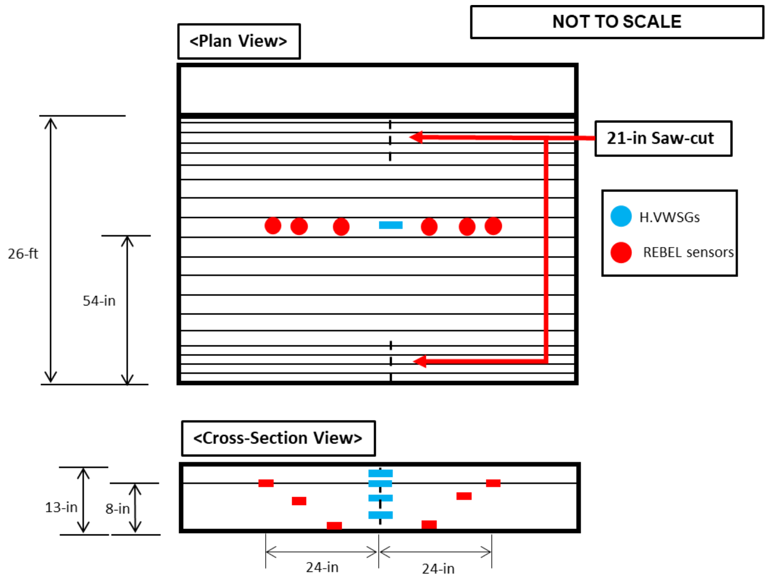

Figure 5.15 Plan and cross-section views of typical gauge installation location at STA 212+00 in Hillsboro

Figure 5.16 Actual gauge installation location at STA 212+00 in Hillsboro

5.5 Temperature and Strain Analysis

5.5.a IH 35E in Waxahachie

Since the length of the section is only 330-ft, a transverse crack did not occur until the morning of April 30, 3rd morning after the concrete placement. The crack occurred at the saw-cut location, which is as expected and at the same time fortunate.

5.5.a.1 Vertical concrete Strains

Horizontal cracking is caused by excessive stresses in concrete in the vertical direction. Therefore, accurately evaluating the effects of steel depths on vertical concrete stresses is one of the major objectives of this project and field experimentation. Since 330-ft length of concrete contains only one steel depth (mid-depth), the primary objectives of this research – evaluating the effects of steel depths on horizontal cracking potential – could not be achieved. However, the data obtained provided convincing evidence that the testing plan developed in this study has great merit.

Figure 5.17 illustrates vertical VWSGs installed. As noted, 4 gages were installed, and an early saw-cut was made in the middle of the two sets of 4 gages. The intent was to estimate concrete tensile strains and stresses in the vertical direction as close to a transverse crack as possible.

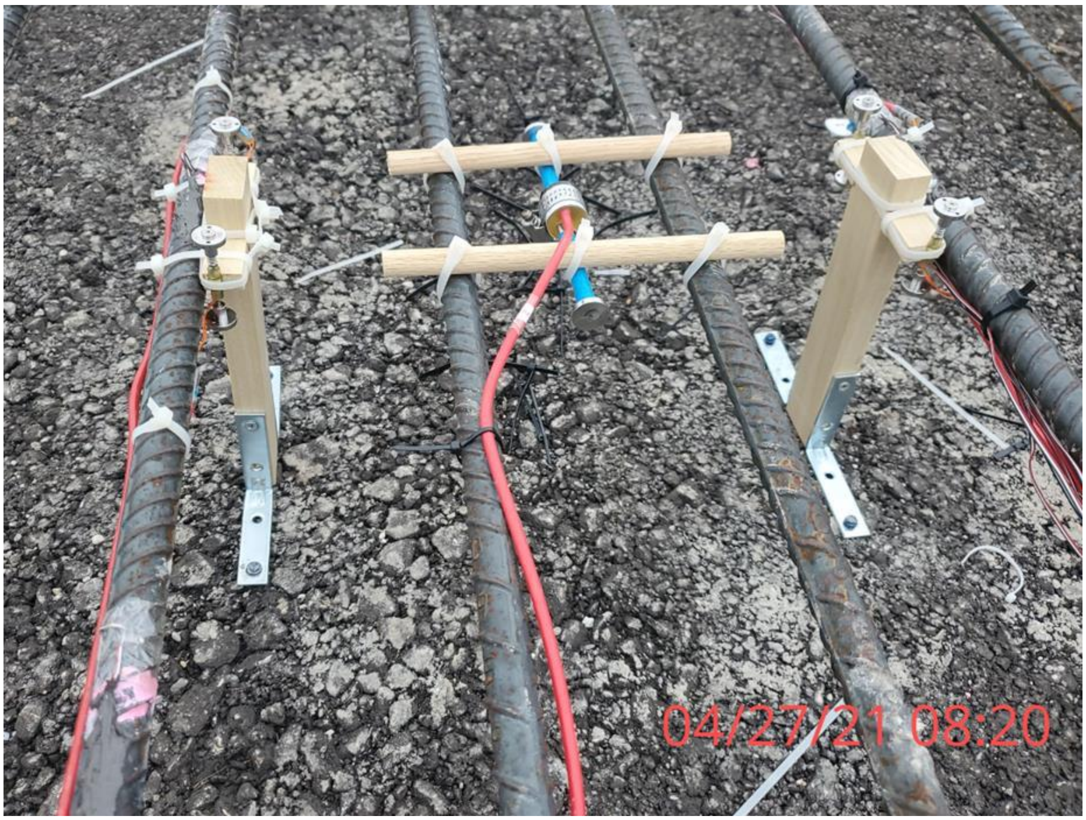

Figure 5.17 vertical VWSGs and Horizontal VWSGs installed in the Waxahachie

Figure 5.18 shows numbering of vertical VWSGs (V.VWSG). V.VWSG 1 and V.VWSG 2 are gages placed inside of the slab, while V.VWSG 3 and V.VWSG 4 are those located on the outside of the slab, or closer to the outside shoulder. Accordingly, V. VWSGs 1 and 3 are on the same side of the saw cut, while V. VWSGs 2 and 4 are in the other side of the saw cut.
Figure 5.19 shows saw cut operations at 8 in the morning the next day, about 15 hours of concrete placement. Since the spacing between two sets of vertical VWSGs is only 4 inches, a saw-cut had to be made as precisely as possible and the data shows that the saw cut was made indeed in the middle of the two sets of vertical VWSGs.

Saw cuts were made at 2 locations in the concrete segment placed on April 26. An additional 3 saw cuts were made in the concrete segment placed on May 4. Figure 5.20 shows the locations of saw cuts in both concrete segments. The first crack occurred in saw cut location 1, which is 130-ft away from the free edge (or TCJ). The second crack occurred at saw cut location 2, after the second segment of the concrete was placed on May 4. Other than these 2 cracks, by the time the research team left the section on May 6, which is 10 days after the concrete placement of the first segment, no other cracks were observed in the concrete segment placed on April 26.

Accordingly, the average crack spacing in the first segment is 110-ft, even with the aid of saw cuts. In other words, the data obtained in this experiment does not accurately represent CRCP behavior.

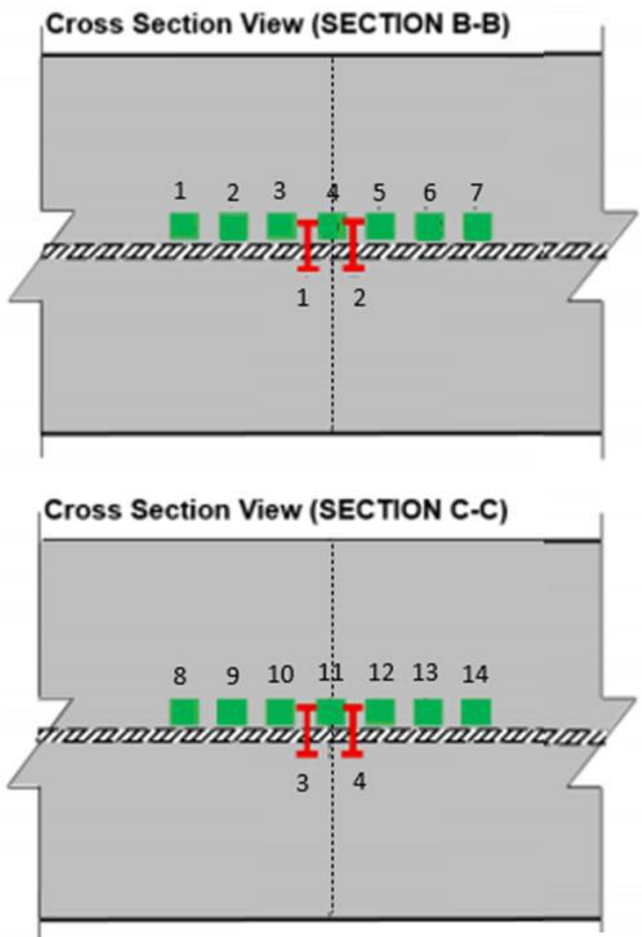

Figure 5.18 IDs of vertical VWSGs

Figure 5.19 Sawcut operation

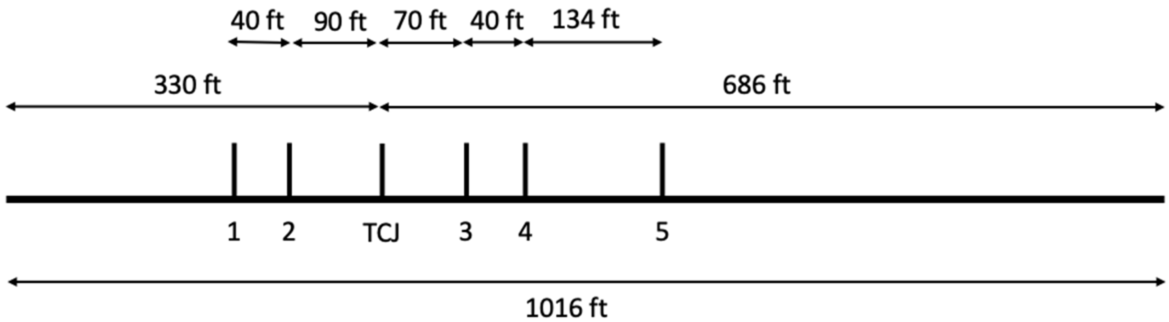

Figure 5.20 Sawcut locations

Figure 5.21 illustrates the variations in the vertical strains measured. X-axis is time, and the whole date indicates the midnight of the specific date. Also, positive strain means tension, while negative indicates compression.

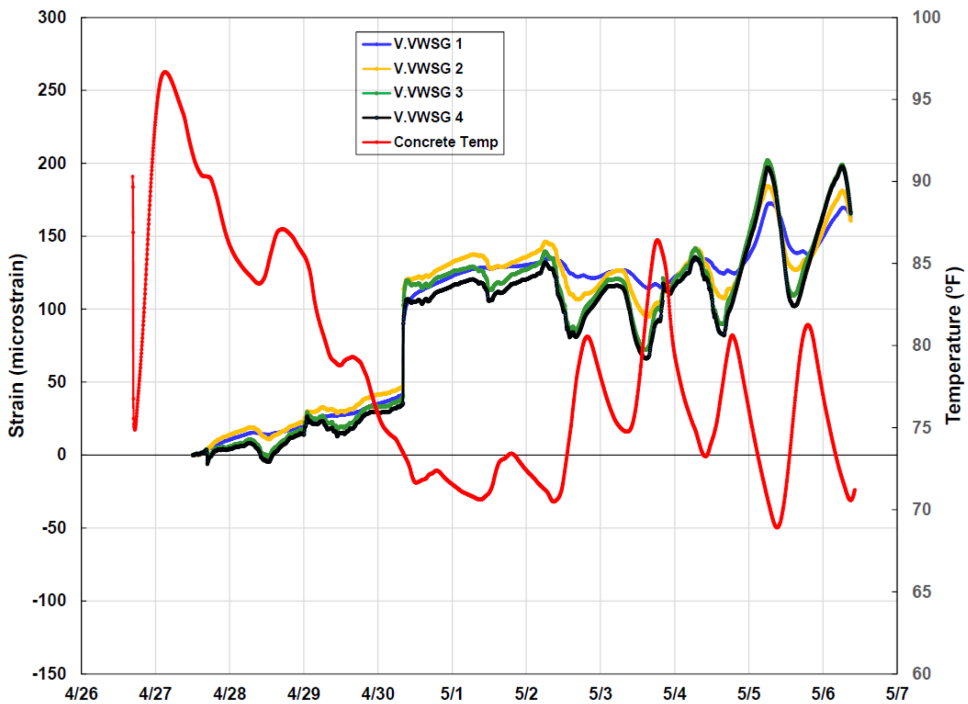

Figure 5.21 Vertical concrete strain variations in IH35 Waxahachie

It shows that as the concrete temperature went down, vertical strains increased in the tension direction. Also, all four VWSGs illustrate similar behavior (when temperature decreases, they move to the tension direction, while when temperature increases, they move to the compression direction). Also noted is that strains at V.VWSGs 3 and 4 are quite close to each other, with larger strains than V.VWSGs 1 and 2. Recall that V.VWSGs 3 and 4 are on the other sides from the saw cut, or induced crack, which indicates a saw cut was made in between the two sets of vertical VWSGs. It is also noted that the variations in concrete strains in V.VWSGs 1 and 2 are smaller than those in V.VWSGs 3 and 4. The reason for these differences needs to be identified. When a crack occurred in the morning of April 30, vertical strain increased substantially, more than 80 microstrains for V.VWSG 3. If the concrete modulus is 3 million psi at the time of cracking, the instantaneous increase in concrete stress in the vertical direction would be 240 psi. This value is a pure increase in concrete tensile stress, not the total tensile stress. The actual concrete tensile stress in the vertical direction needs to be added to whatever the existing tensile stress. If drying shrinkage of the concrete at the location of the gages is known, then actual concrete tensile stress could be estimated. During the field testing, molds were made to evaluate concrete drying shrinkage; however, due to the discontinuity of concrete placement, drying shrinkage testing was not conducted to save VWSGs. Regardless, 240 psi increase in concrete tensile stress is quite substantial, considering concrete tensile strength at early ages might be in the range of 300 psi to 400 psi. From a strain standpoint, ultimate concrete tensile strain is in the range between 120 and 150 microstrains. Increase of 80 microstrain instantaneously due to a crack formation represents more than a half of ultimate tensile strain capacity or 2/3 of the ultimate tensile strain capacity. Any further increase in tensile strain or stress due to continued drying shrinkage of concrete or temperature drop could induce horizontal cracking. It is to be noted that the behavior obtained in this experiment does not represent real CRCP, since both ends of the slab were free and far from fully restrained.

Even though the value of the information presented above is quite diminished due to little restraint on concrete volume changes, a substantial increase in vertical strains due to the development of a transverse crack illustrates the vulnerability of CRCP system to horizontal cracking. Also demonstrated above are the soundness and the feasibility of vertical strain measurements, which is really encouraging.

5.5.a.2 Horizontal concrete Strains

Figure 5.22 shows concrete strain variations in a VWSG placed longitudinally. It is noted that, as concrete temperature continued to decrease, concrete strain in the longitudinal direction also moved to the compression side. However, the strains shown here are total strains. Since total strains are made up of strains due to temperature variations, drying shrinkage, and stresses, actual concrete stress would be in tension during the time period prior to the cracking. If drying shrinkage is accurately estimated and zero-stress temperature can be quantified, concrete tensile strength can be estimated with a reasonable precision, as long as accurate estimation of concrete modulus is made at the time of cracking.

Figure 5.22 illustrates that the rate of concrete strain across the crack is about 36 microstrain per ºF, which is obviously much larger than the CoTE of this concrete. In this experiment, only one crack developed, and because of that, the effect of crack spacing on the rate of concrete strain across crack could not be evaluated. In the next field testing, since different crack spacings will result at saw cut locations, the effect of crack spacing on the rate of concrete strain across the crack could be identified. This information will be compared with vertical strain rates, which will further enhance our understanding of CRCP behavior, especially due to various steel depths. Ultimately, this understanding will help identify an optimum steel depth to minimize the horizontal cracking potential.

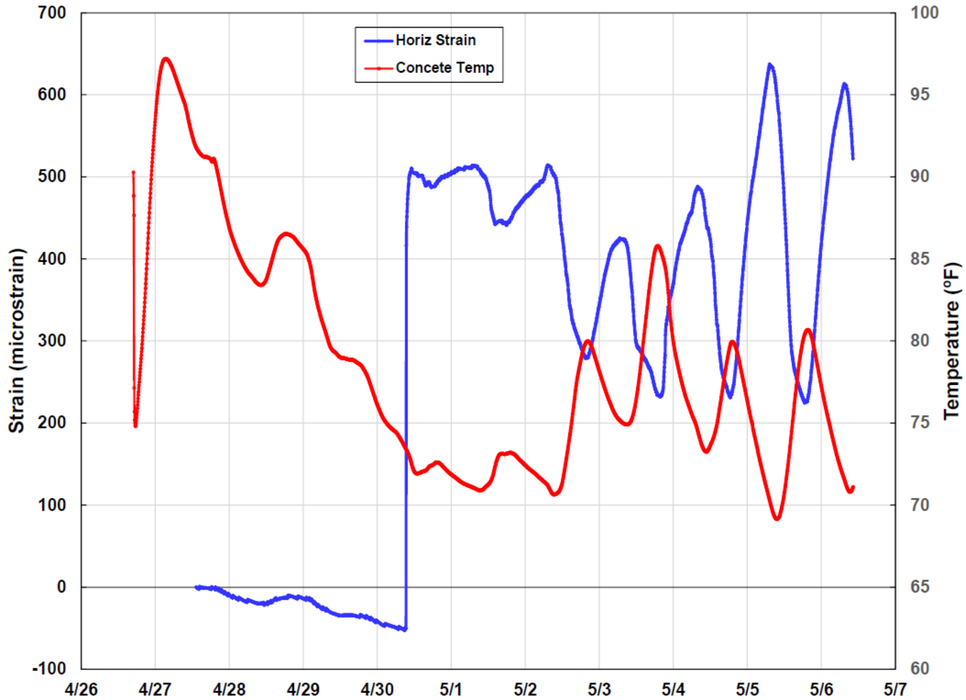

Figure 5.22 Longitudinal concrete strain variations across the sawcut in IH35 Waxahachie

5.5.b US 62 in El Paso

5.5.b.1 Early-age strain behaviors of concrete and steel at varying depths

5.5.b.1.1 <u>Longitudinal steel strains at sawcut sections</u>

The electrical resistance foil type strain gages were installed on the longitudinal steel bars to investigate the behavior of the reinforcement nearby and at the location of the sawcut. It was found out that the gages installed at the "inside" location of the slab were defective and failed to acquire strain data shortly after the concrete was placed. However, the gages installed at the "outside" location of the slab were functioning normally. In Figure 5.23 where the longitudinal steel was located at the mid-depth, it can be observed that the steel strains on all 3 saw-cut sections were behaving similarly until the temperature significantly dropped on August 11. When the temperature dropped, the steel strain at section 1-1 significantly jumped higher than the strains at 1-2 and 1-3. This might be attributed to the crack interval at section 1-1 (29-ft west, 16-ft east) which is higher than section 1-2 (14-ft west, 12-ft east) and 1-3 (15-ft west, 18-ft east). However, the steel strain at section 1-1 suddenly dropped significantly to the compression side on August 15 when the temperature begins to go up. This may be attributed to the crack the propagated at 16-ft on the west side which was observed during the survey conducted on August 20 while there were no additional cracks recorded in between the previously recorded crack interval near sections 1-2 and 1-3. Although, the sudden drop in steel strain to the compression side doesn't have physical evidence to support this behavior other than a possibility that the gages began to fail after being subjected to high tensile strain.

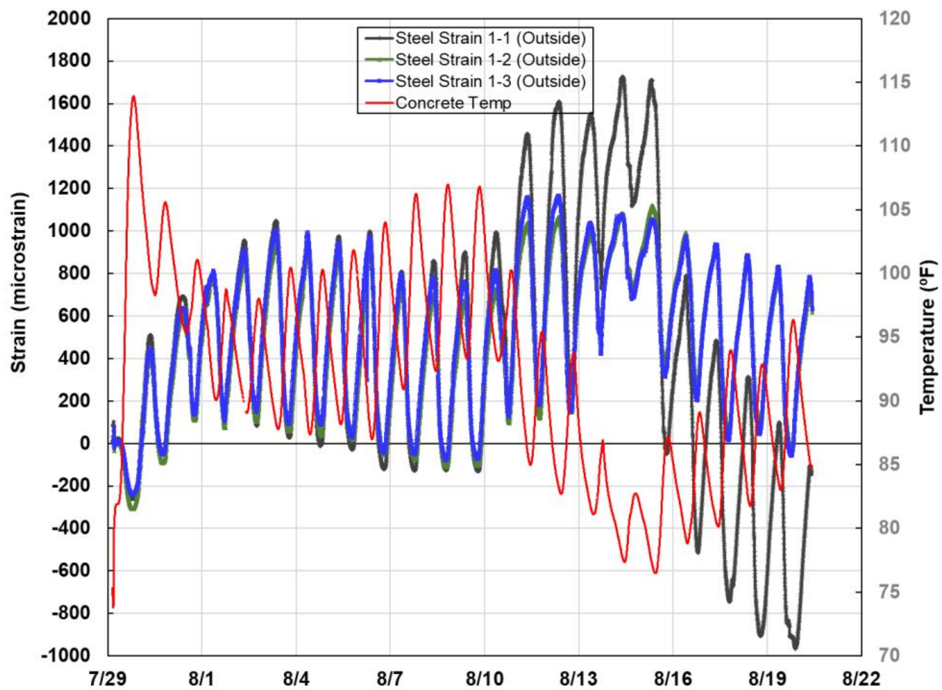

Figure 5.23 Early-age steel strains at the mid-depth section in US62/180 El Paso

Meanwhile in Figure 5.24 where the longitudinal steel was located at the upper-depth, the steel strains at sections 2-1 and 2-2 have similar behaviors. The recorded strains were similar to the strains obtained from the section where the reinforcing steel is at mid-depth. However, the strain gages at 2-2 (outside) have recorded a lower strain reading than the other gage at 2-2 (inside). A possible explanation is that the crack did not propagate directly to the location of the gage. As shown in Figure 5.25, it appears that the crack did not propagate vertically from the induced saw-cut indicating that it may have skewed slightly away from the center of the location of the gage. Meanwhile, the recorded strain at section 2-3 is lower compared to section 2-1 and 2-2 because it was the location of the reinforcement steel splices. The presence of the additional steel reinforcements at the sawcut may have influenced the reduction of the tensile strain acting on the longitudinal steel.

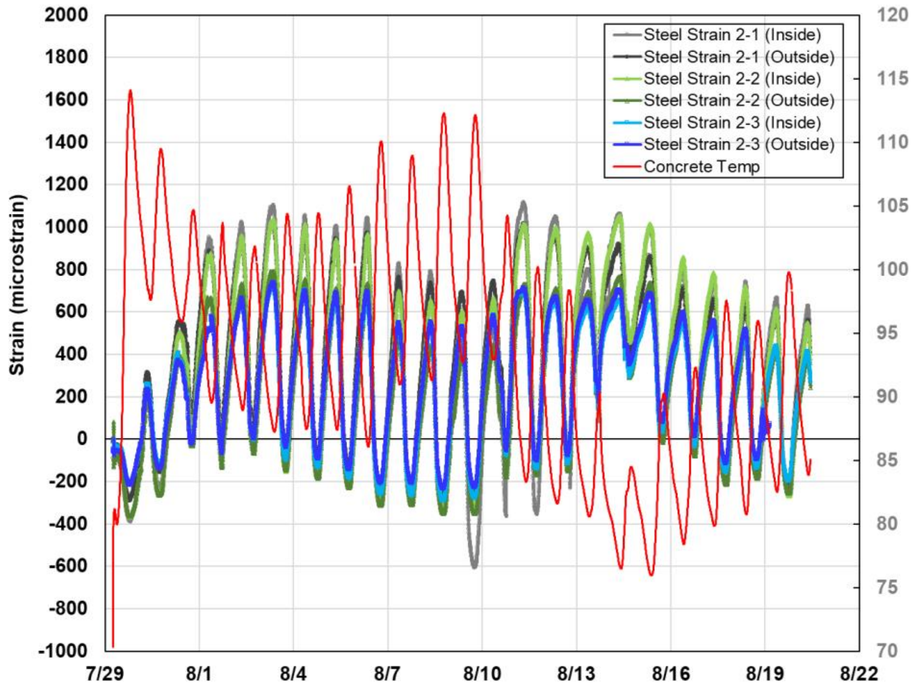

Figure 5.24 Early-age steel strains at the upper-depth section in US62/180 El Paso

Figure 5.25 Crack propagation at the upper-depth section (2-2) in US62/180 El Paso

In Figure 5.26 where the longitudinal steel is located at the upper-depth and the steel spacing is 1/2-in wider than section 2 (low CoTE), it can be observed that the steel strains recorded are generally the largest among the 3 sections. This is attributed to the reduction of the percentage of steel which generated an increase in tensile strain. The low strain recorded at section 3-2 may be attributed to the additional transverse crack that propagated 1-ft west of the saw-cut 6 days after concrete placement slightly relieved the stress acting on the reinforcing steel.

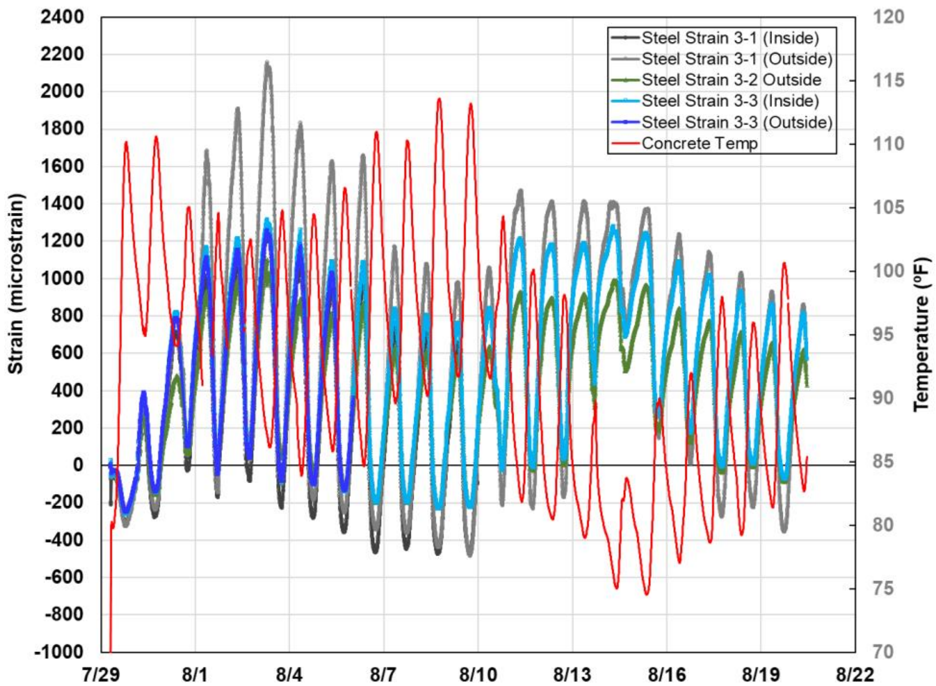

Figure 5.26 Early-age steel strains at the upper-depth low CoTE section in US62/180 El Paso

Meanwhile, the location of the strain gages at a distance from the saw-cut significantly affects the recorded strains. In Figure 5.27, it can be observed at section 2-2 that only the strain gages located at the saw-cut were subjected to significant tensile strains while the strains away from the saw-cut were generally under compression. However, in Figure 5.28, it can be noticed that at section 3-2 there was a sudden jump in steel strain of the gages located 1-ft west of the sawcut. This was due to the transverse crack that was observed, during the crack survey, to have propagated at that location. It can also be noticed that the 2-ft west (in) gage has also been affected by the crack propagation and has recorded a spike in tensile strain. The gages at 1-ft east of the sawcut have been observed to have developed a degree of tensile strain at the early ages but there was no jump observed when the additional transverse crack propagated. This implies that the steel strain away from the location of the crack is bonded with the concrete and are not affected by the steel strain behavior at the saw-cut.

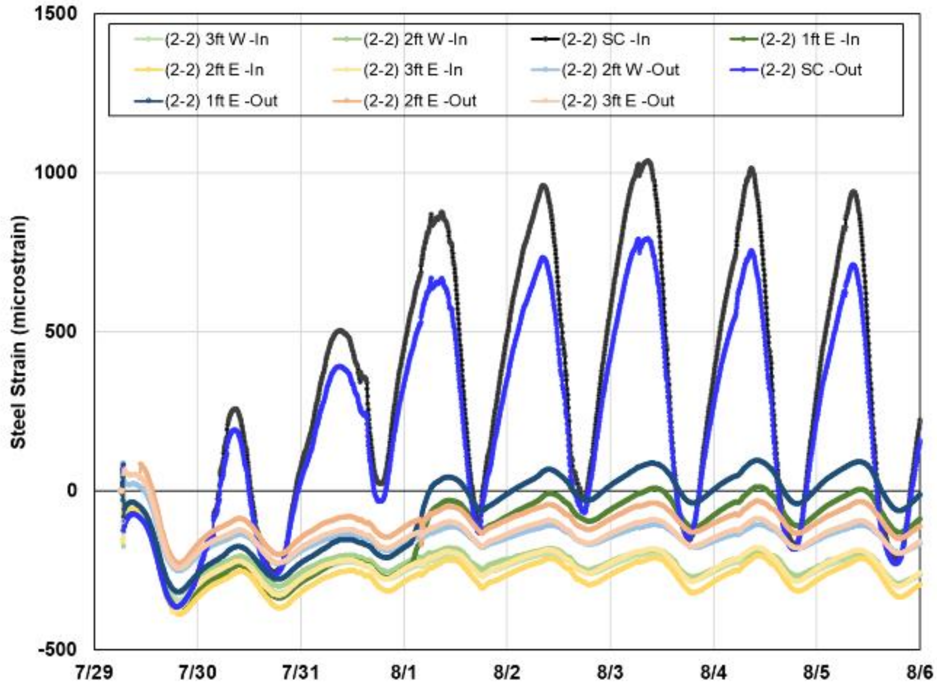

Figure 5.27 Early-age steel strains at a distance from the sawcut in section 2-2 in US62/180 El Paso

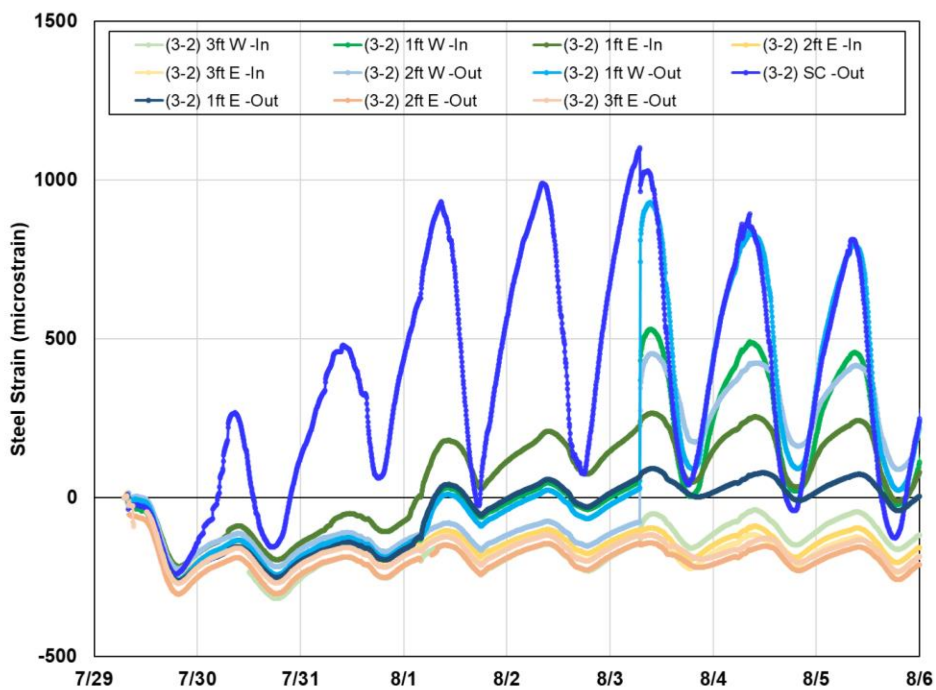

Figure 5.28 Early-age steel strains at a distance from the sawcut in section 3-2 in US62/180 El Paso

5.5.b.1.2 Longitudinal concrete strains at sawcut sections

Figure 5.29 illustrates the concrete strains at Section 1 (mid-depth). It shows that there is an inverse relationship between concrete temperatures and concrete strains – the higher the temperature, the smaller the concrete strain, which is as expected. What is interesting over here is that, on Aug 11, concrete temperature went down significantly, and longitudinal concrete strains at three saw-cuts reacted differently – more specifically, the largest variations were observed at 1-1 (first saw-cut in the mid-depth section). This behavior is consistent with the recorded steel strains which indicates that the crack interval may have caused the spike at 1-1 when the temperature suddenly went down.

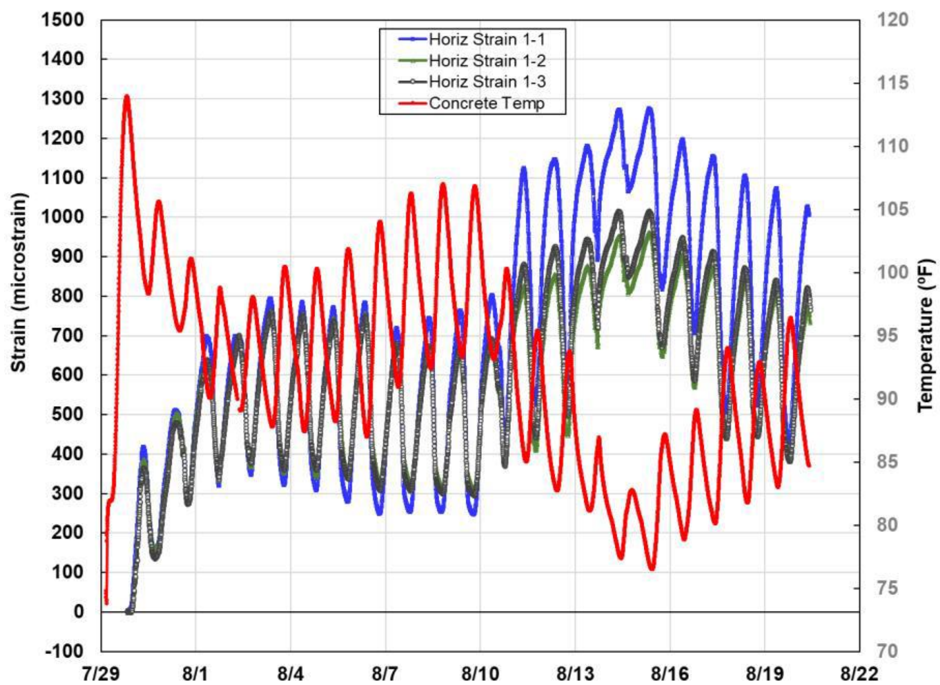

Figure 5.29 Early-age longitudinal concrete strains at the mid-depth section in US62/180 El Paso

Figure 5.30 illustrates the concrete strains at Section 2 (upper-depth steel placement). Similar trends are observed to those in Figure 5.24 earlier, except that concrete temperature variations are larger than in Section 1, because the gages were installed closer to the surface in this section. Because of the larger temperature variations as well as the location of the gages, daily variations in concrete strains are larger than those in Section 1, which is also as expected.

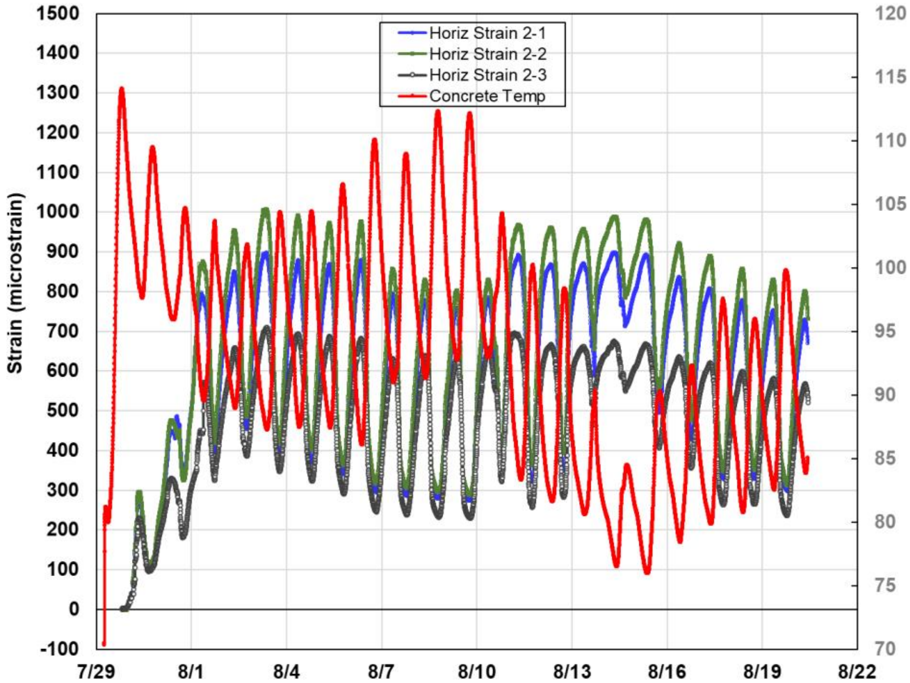

Figure 5.30 Early-age longitudinal concrete strains at the upper-depth section in US62/180 El Paso

Figure 5.31 shows the concrete strains at Section 3 (upper-depth, low CoTE). Overall behavior is quite similar to those in the other 2 sections. However, the concrete strains that were recorded in these sections are the highest compared to the previous 2. This is aligned with the steel strains behaviors which indicates that the reduction of steel reinforcement reduces the restraint and increases the tensile strain acting on the steel. Also, the lower concrete strains recorded at section 3-2 are attributed to the additional transverse crack that propagated 1-ft west of the saw-cut which was observed on the 6th day from concrete placement.

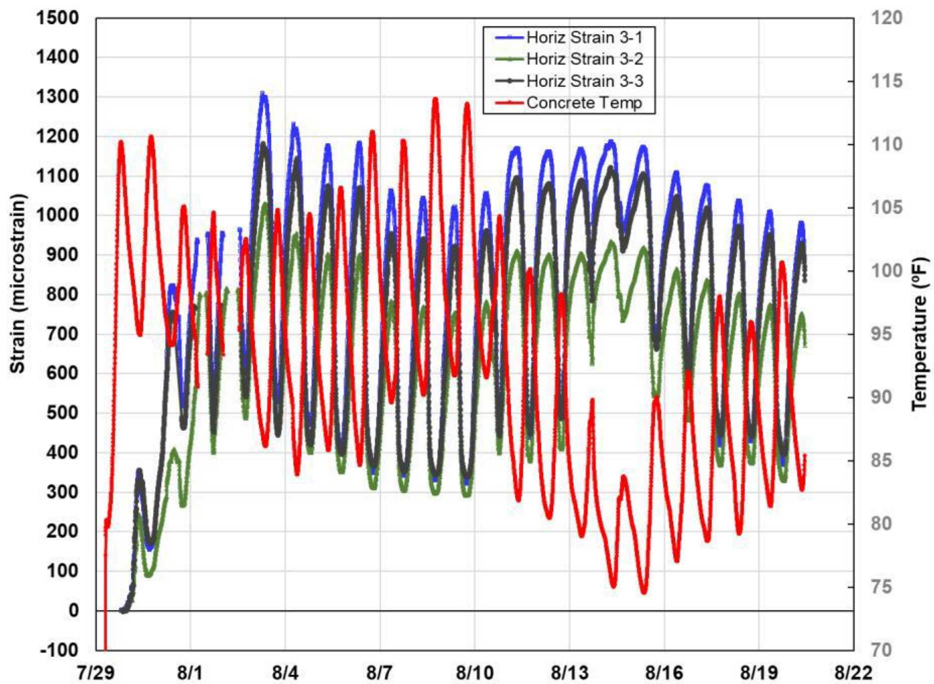

Figure 5.31 Early-age longitudinal concrete strains at the upper-depth low CoTE section in US62/180 El Paso

5.5.b.1.3 <u>Vertical concrete strains at sawcut sections</u>

Figure 5.32 shows vertical concrete strains at saw-cut 1-1 (mid-depth). For some reason, 3 gages did not provide any data points. The data from one gage illustrates large variations of vertical concrete strains. On Aug 10 and 11, concrete temperature dropped from 100 °F to 85 °F, which resulted in the increase of vertical concrete strain of 180 microstrains. Assuming 5.5 microstrains/°F for the concrete CoTE, the increase in tensile strain in concrete was 97.5 microstrains, which is not small considering the ultimate concrete tensile strain capacity of about 120 to 150 microstrains. Even though horizontal concrete strain increased quite substantially on Aug 11 at 1-1, the increase in vertical strain on Aug 11 is not that much different from previous days. Accordingly, it is considered that the large increase in horizontal concrete strain at 1-1 on Aug 11 is not due to horizontal cracking.

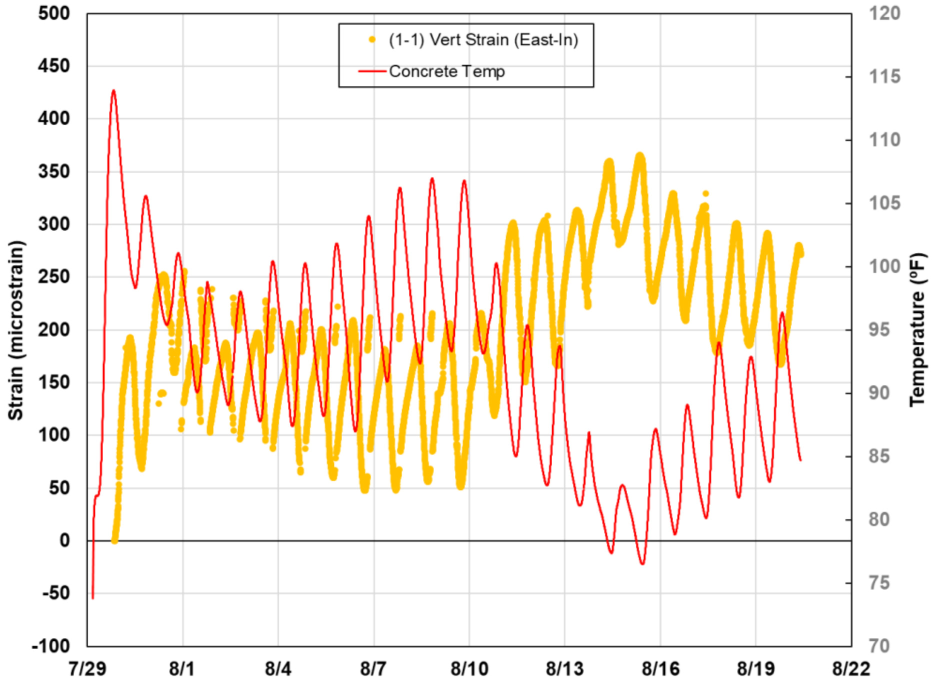

Figure 5.32 Early-age vertical concrete strains at section 1-1 in US62/180 El Paso

Figure 5.33 shows the concrete vertical strains at saw-cut 1-2 (mid-depth). In this location, all 4 vertical VWSGs are working properly. It is noted that two groups of gages – west side and east side of the saw-cut) – produced quite different strain values. In the west side, the variations are much larger than those in the east side of the saw-cut.

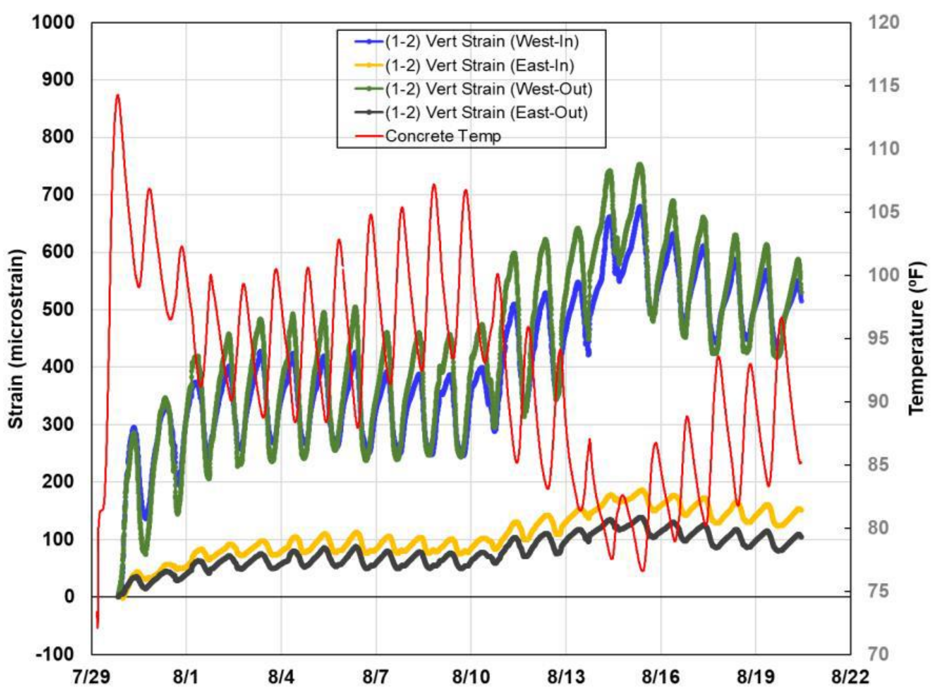

Figure 5.33 Early-age vertical concrete strains at section 1-2 in US62/180 El Paso

As a matter of fact, the variations in the east side are quite small – less than 50 microstrains per day. On the other hand, in the west side, daily variations large than 300 microstrains are observed (from afternoon of Aug 10 to the morning of Aug 11), even though the temperature variations were 15 °F, as in saw-cut 1-1. With the assumption of 5.5 microstrains/°F for CoTE, concrete strains due to stresses would be 217.5 microstrains, which far exceeds the ultimate concrete tensile strain capacity. A coring activity was conducted to investigate horizontal cracking in the instrumented sections, but coring samples have shown that there was no horizontal cracking that took place in the section with higher concrete vertical strains.

Figure 5.34 illustrates concrete vertical strains at saw-cut 1-3 (mid-depth steel). Compared with 1-2, daily variations in vertical concrete strains are smaller; however, as in 1-3, those in the west side of the saw-cut are much larger than those in the east side.

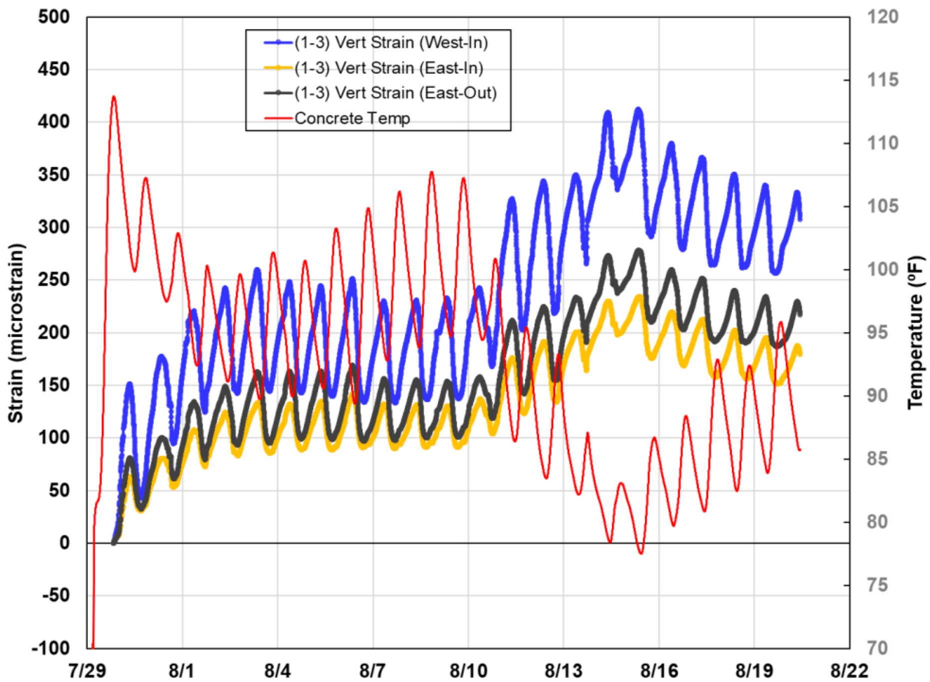

Figure 5.34 Early-age vertical concrete strains at section 1-3 in US62/180 El Paso

Figures 5.35, 5.36 and 5.37 show concrete vertical strains at saw-cut 2-1, 2-2 and 2-3 (upper depth steel), respectively. It is observed that, compared with mid-depth steel saw-cuts, the daily variations of concrete vertical strains are substantially smaller, which implies that the probability of horizontal cracking is reduced when the steel is placed closer to the top of the slab.

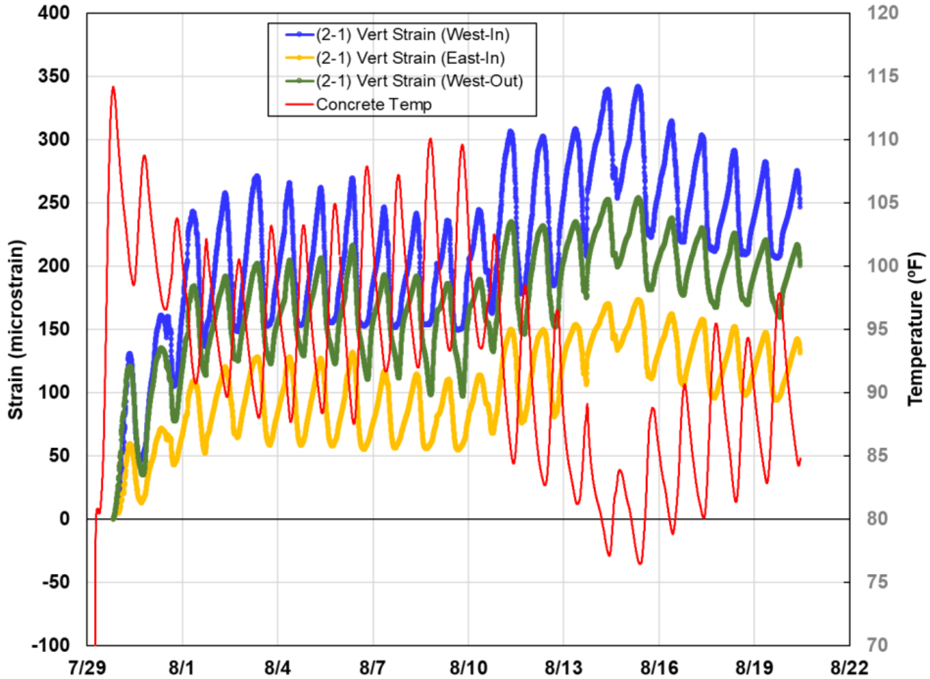

Figure 5.35 Early-age vertical concrete strains at section 2-1 in US62/180 El Paso

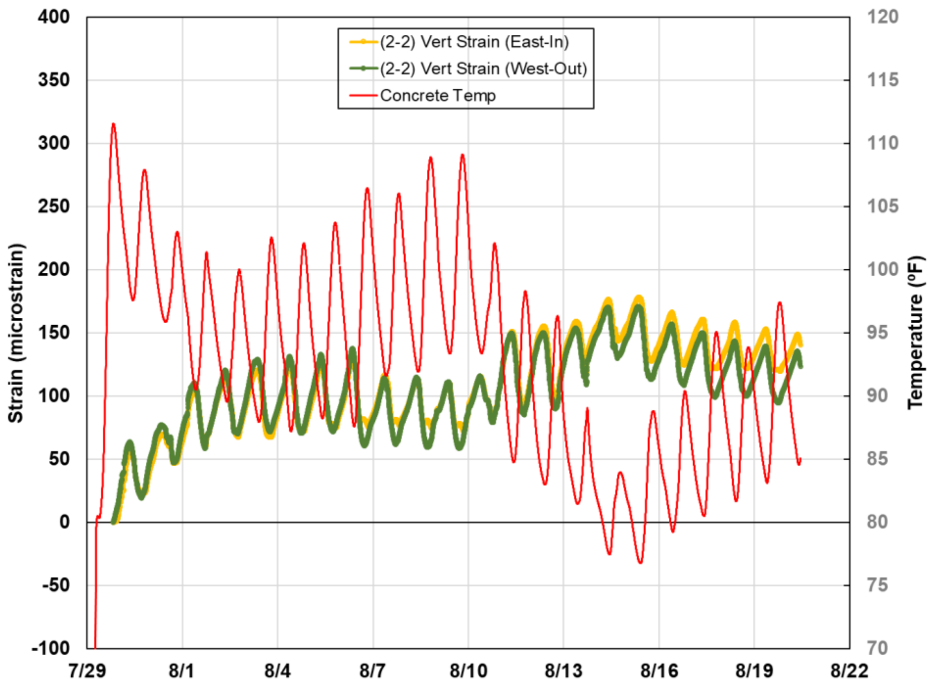

Figure 5.36 Early-age vertical concrete strains at section 2-2 in US62/180 El Paso

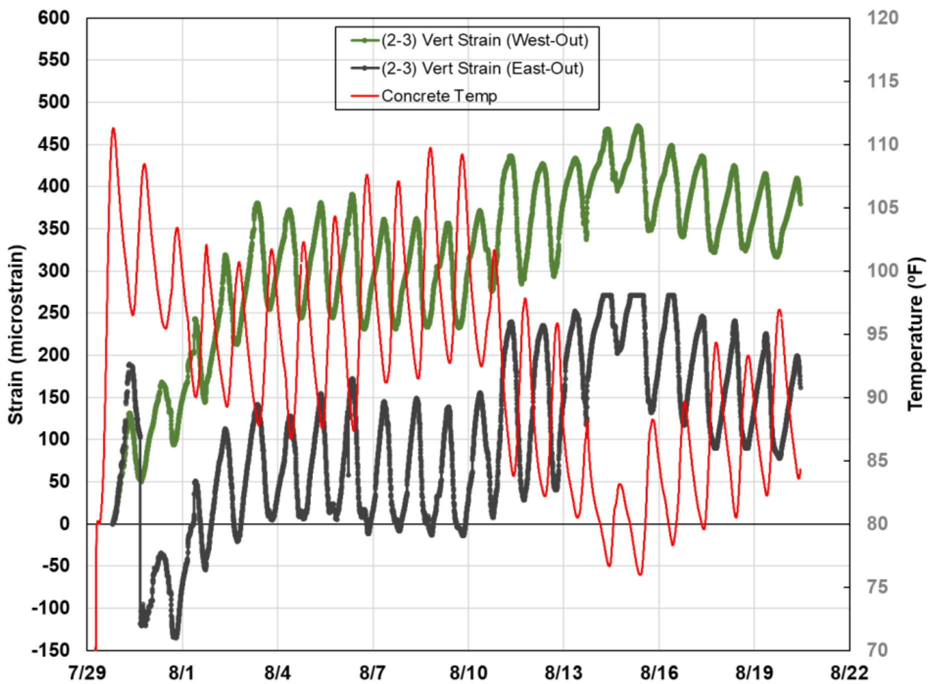

Figure 5.37 Early-age vertical concrete strains at section 2-3 in US62/180 El Paso

Figures 5.38, 5.39 and 5.40 present concrete vertical strains at saw-cut 3-1, 3-2 and 3-3 (upper depth steel with low CoTE), respectively. It is also observed that the daily variations of concrete vertical strains are somewhat comparable to those in upper-depth steel and substantially smaller than those in the mid-depth steel section. This implies that the use of longitudinal steel for low CoTE might mitigate horizontal cracking as long as the steel is placed closer to the surface. A discussion is presented in the next section to analyze these behaviors further using the long-term performance data.

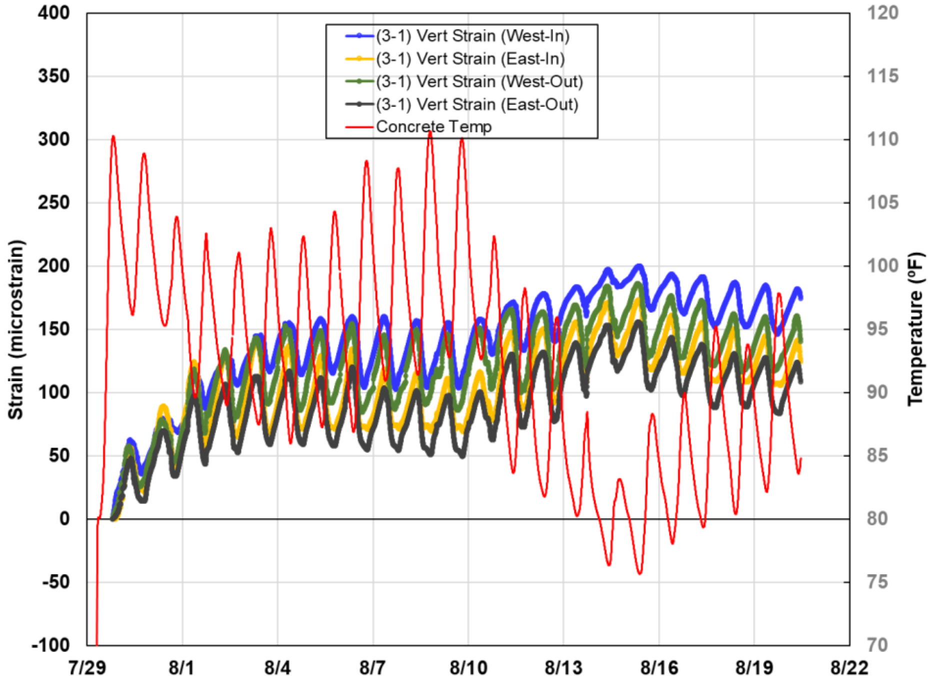

Figure 5.38 Early-age vertical concrete strains at section 3-1 in US62/180 El Paso

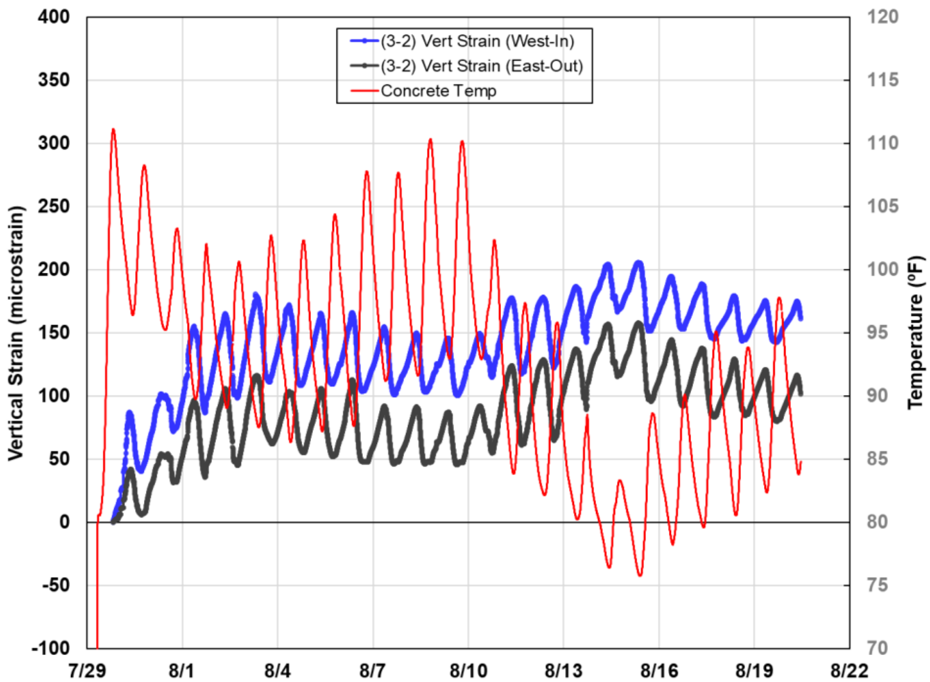

Figure 5.39 Early-age vertical concrete strains at section 3-2 in US62/180 El Paso

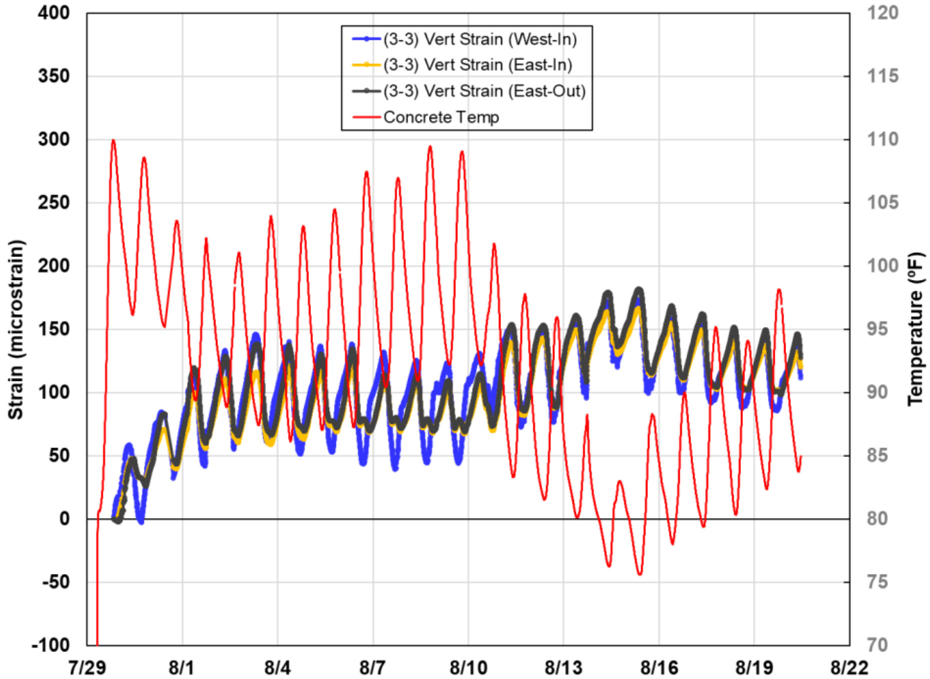

Figure 5.40 Early-age vertical concrete strains at section 3-3 in US62/180 El Paso

5.5.b.2 Long-term concrete pavement behavior

5.5.b.2.1 Thermal behavior in concrete slabs

Since concrete responses to temperature variations in CRCP and their interactions with longitudinal steel are the major cause of cracking and responsible for the magnitudes of crack widths, understanding temperature variations in concrete slab is quite important. Extensive concrete temperature data was obtained from the El Paso test section and a detailed analysis was conducted. It is well known that transverse cracking in CRCP is due to warping and curling, not necessarily due to axial strains in concrete. Theoretically, warping indicates concrete flexural behavior due to variations in moisture contents in concrete slab through the slab depth, while curling is due to temperature variations through slab depth. Measuring moisture variations through the slab depth and resulting shrinkage variations through slab depth is a real challenge, and in concrete pavement research, warping of the slab is quite often ignored or equivalent curling is estimated and included in the total curling estimation. Figure 5.41 shows the slab temperature in the El Paso test section. Seasonal variations as well as daily variations in concrete temperature are investigated. It is observed that temperature variations are largest near the slab surface, while smallest near the bottom, which is as expected. The range of daily temperature variation at 1-in from the surface of the slab (called "surface temperature" in this section) between July 2021 and March 2022 was from 21 to 37 °F, with an average of 31 °F while, at 1-in from the bottom of the slab (called "bottom temperature" in this section), it was 8 to 17 °F, with an average of 13 °F.

Temperature gradients throughout the duration of the measurement period were investigated. Figure 5.42 shows the temperature gradients through the slab depth at specific periods between July 2021 and March 2022. From August to November 2021, the daily surface temperature range was between 30 and 37 °F, while the daily bottom temperature range was between 12 to 17 °F.

From December 2021 to January 2022, the daily surface temperature range was between 21 to 23 °F and about degrees 8 to 10 °F for bottom temperature. From February to March 2022, the daily surface temperature range went up to 35 °F and about 15 °F for the bottom temperature. The point here is that the temperature ranges at the top or at the bottom of the slab vary from month to month. It can also be seen that the temperature at the surface is generally higher than that at the bottom between noon to 6 pm and the other way around for the rest of the day, except during colder seasons, there is minimal difference in temperature between surface and bottom of the slab at noon. It is also observed that generally, the slab temperature at the surface and at the bottom is the lowest at 9 am and the highest at 6 pm. Another interesting observation is that concrete temperature profiles below the mid-depth of the slab are linear, implying that the slab behavior would be more of axial than curling, even though “actual” behavior would be that of curling due to the curling behavior of the upper part of the concrete slab. This “curling” and “axial” behavior of the concrete slab at the top and bottom portions of the slab, respectively, has important implications for the determination of an optimum longitudinal steel depth. The idea of placing longitudinal steel at the mid-depth of the slab was based on the idea that a neutral axis in the slab due to warping and curling would be at mid-depth. The observations in Figure 5.42 do not support the idea of “Let’s place longitudinal steel at a neutral axis.” Since the moisture variations in the concrete slab below the mid-depth is almost minimal, including the effect of moisture variations through the slab depth will further invalidate the idea of “Let’s place longitudinal steel at a neutral axis.”

Westergaard (1927) assumed a linear temperature gradient thru the slab depth, simply to make the analysis less demanding, even though Teller and Sutherland (1935) later on measured temperature profiles in the slab and proved that the linear temperature gradient is not realistic. The nonlinearity of the temperature gradient from the El Paso test section is consistent with the Teller and Sutherland findings. The bottom line here is that concrete volume changes, especially in flexural behavior, are much larger in the top half of the slab than those at the bottom half. Observations of top-down and bottom-up cracking, as well as those cracking not taking place at the same location, clearly illustrate (1) top-down cracking occurs due to curl-up of the slab early in the morning, while (2) bottom-up cracking does not necessarily due to curl-down of the slab in the afternoon. If bottom-up cracking is primarily due to curl-down of the slab, then the bottom-up crack must be located near the top-down crack; however, that is not always the case. In other words, bottom-up crack occurs where the sum of “axial” tensile stress and “curling” tensile stress becomes largest, if longitudinal steel is placed at a mid-depth. If longitudinal steel is placed near the surface, the “curling” tensile stress at the bottom of the slab will become smaller and the “axial’ tensile stress will dominate in inducing bottom-up cracking. It is concluded that (1) the interactions between longitudinal steel and concrete volume changes in CRCP are quite complicated, (2) placing longitudinal steel at various depths will have definite effects on transverse cracking behavior, and (3) accordingly, it appears that there should be an optimum depth of longitudinal steel in order to minimize the development of horizontal cracking. Another point is that, in a 2-mat steel placement, the current practice of placing the same amount of longitudinal steel at both layers may not be the best practice. Since the bottom half of the concrete experiences least temperature variations and also no curling on its own (obviously, there will be curling component in concrete stresses due to the curling behavior of the top half of the slab), it is expected that steel stresses at the bottom layer of the steel will be lower and the amount of steel at the bottom layer could be reduced, possibly by a large amount.

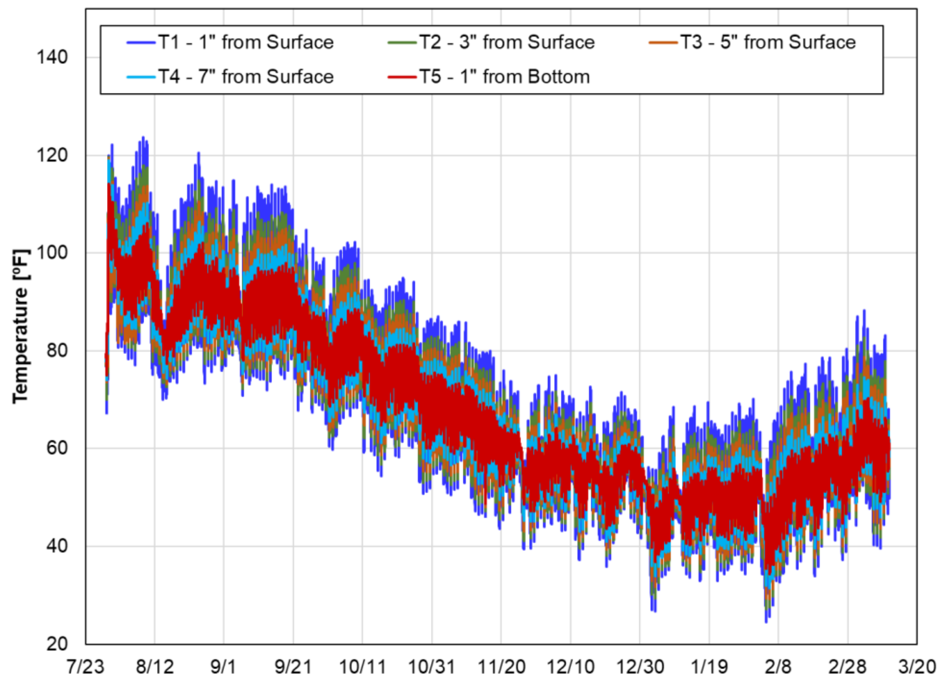

Figure 5.41 Pavement temperature profile in US62/180 El Paso test section

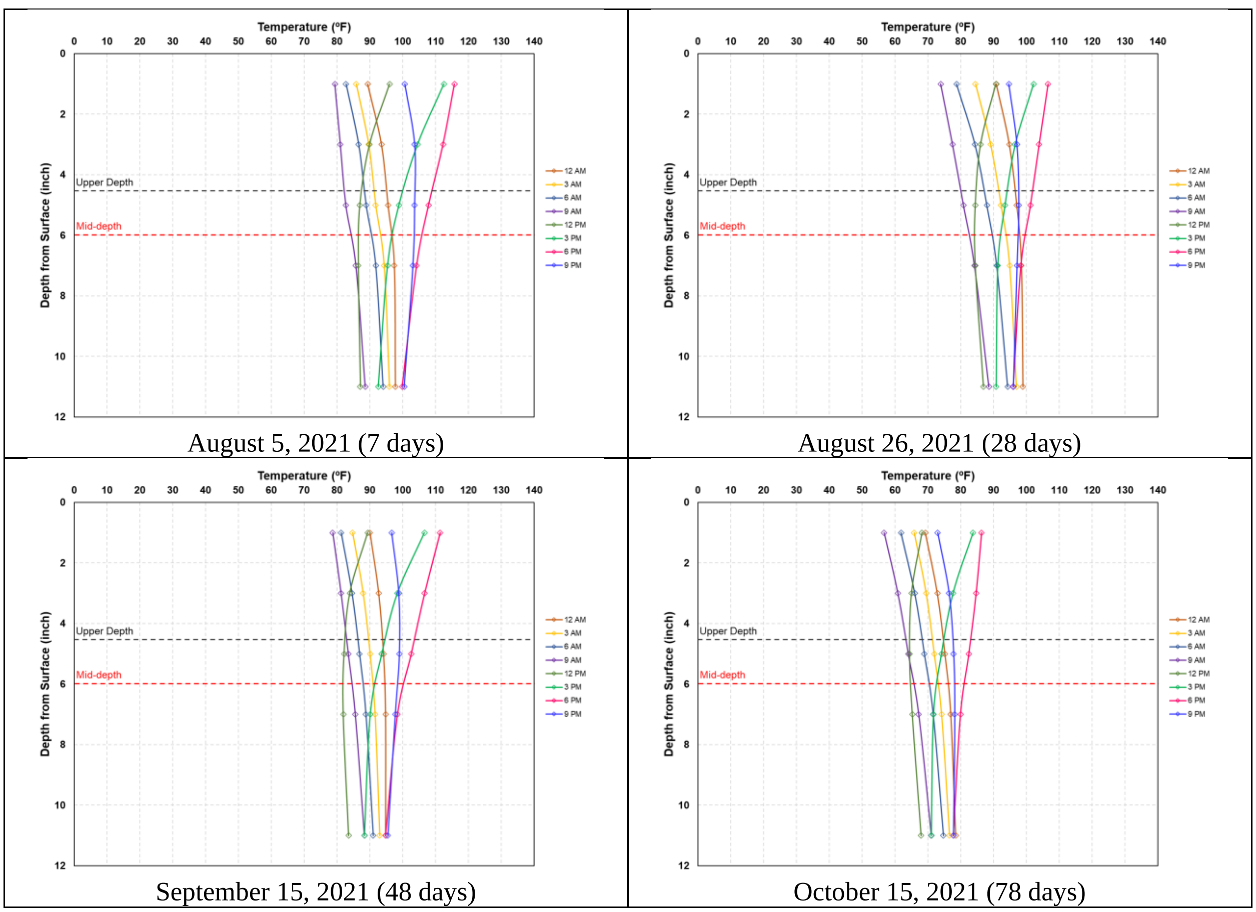

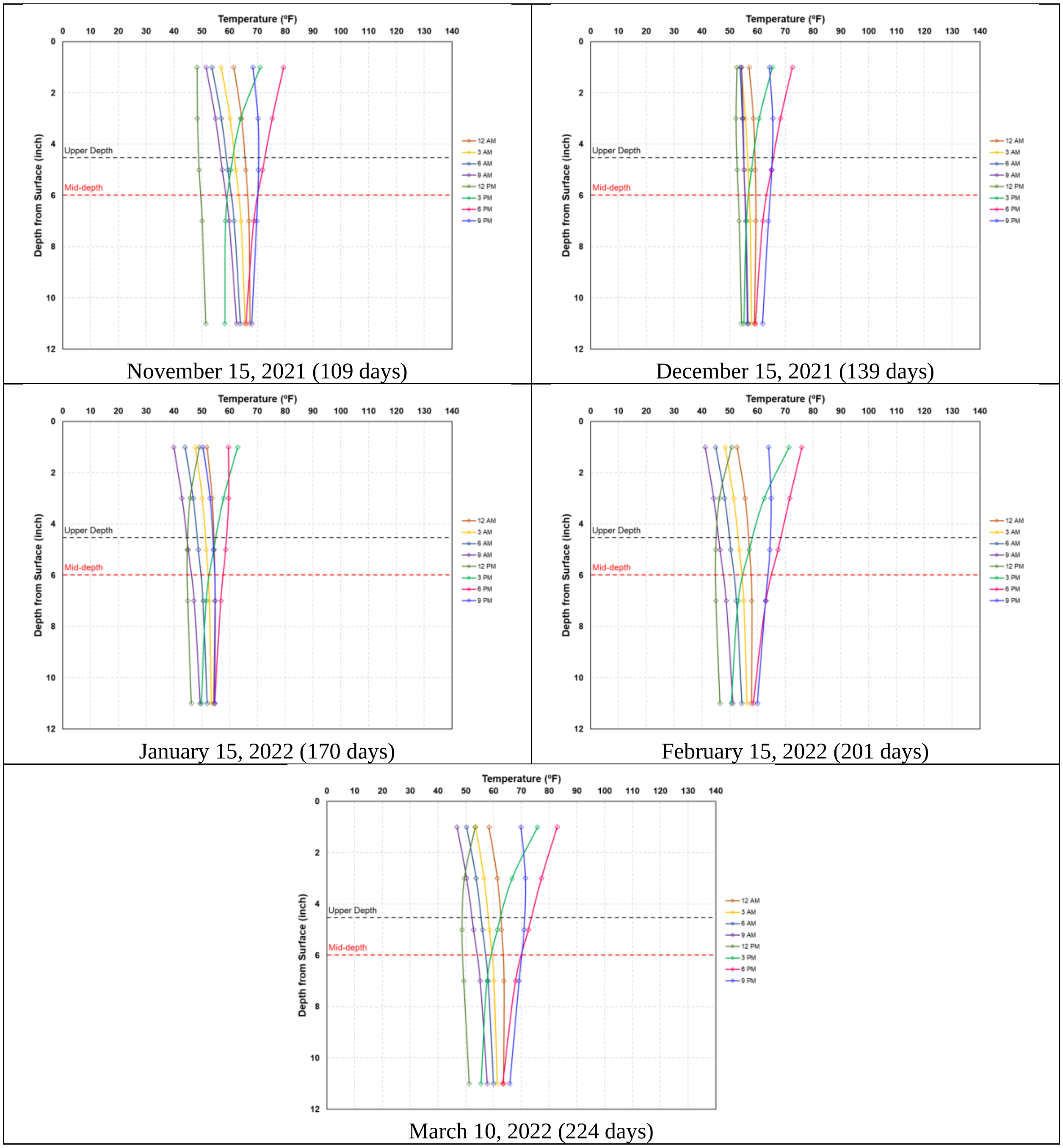

Figure 5.42 US62/180 El Paso test section temperature gradient at 7, 28, 48, 78, 109, 139, 170, 201, and 224 days from concrete placement

5.5.b.2.2 <u>Longitudinal steel strain behaviors in concrete slabs</u>

Past research studies have shown that longitudinal steel has significant effects on the cracking behavior in CRCP. This is due to the environmental load acting on the concrete slab and the restraint that is provided by the steel (Hall, et. al, 2007; Kim, et. al, 2000). This section investigates the behavior of the steel strains at induced crack locations in three steel placements:

at middle of the slab (mid-depth), steel at 1.5-in above the middle of the slab (upper-depth) and steel at 1.5-in above the middle of the slab with a spacing ½-inch wider (upper-depth low CoTE).

Figures 5.43 to 5.45 show the steel strains recorded at the sawcut locations of the mid-depth, upper-depth and upper-depth low CoTE sections. It is observed that the strains at the upper-depth low CoTE sections are the largest, followed by the steel strains at the upper-depth and at the mid-depth, which is as expected. Also observed is that when concrete temperature goes up, the steel strains go down and vice versa.

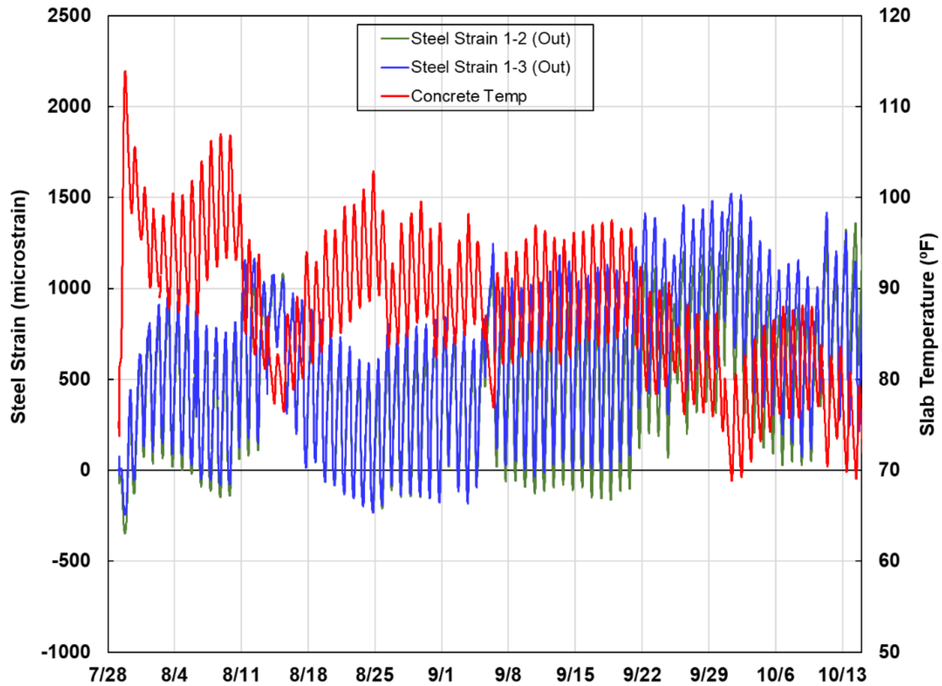

Figure 5.43 Long-term steel strains at the mid-depth section in US62/180 El Paso

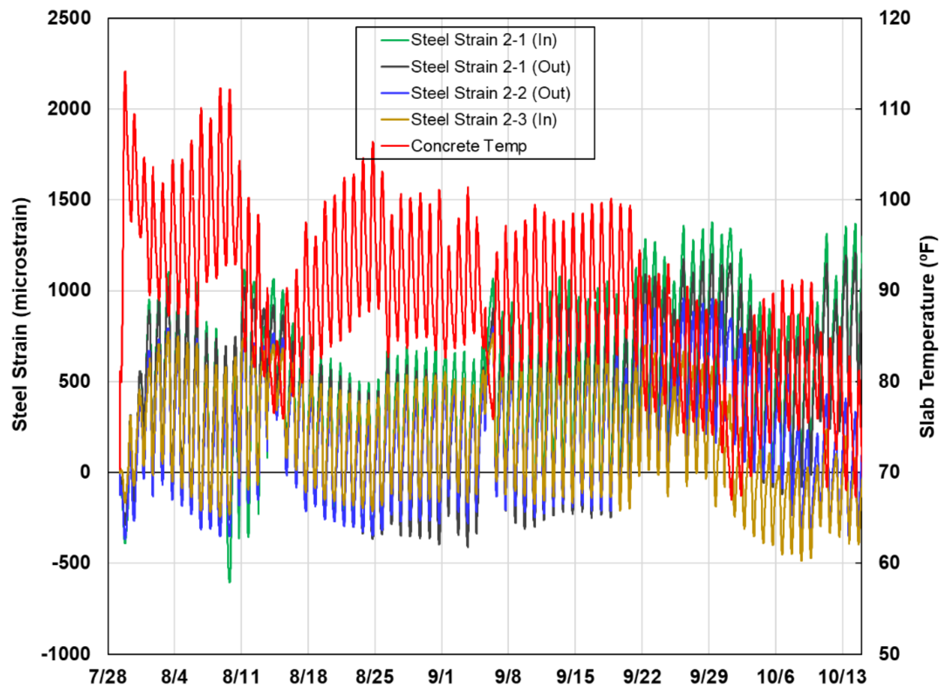

Figure 5.44 Long-term steel strains at the upper-depth section in US62/180 El Paso

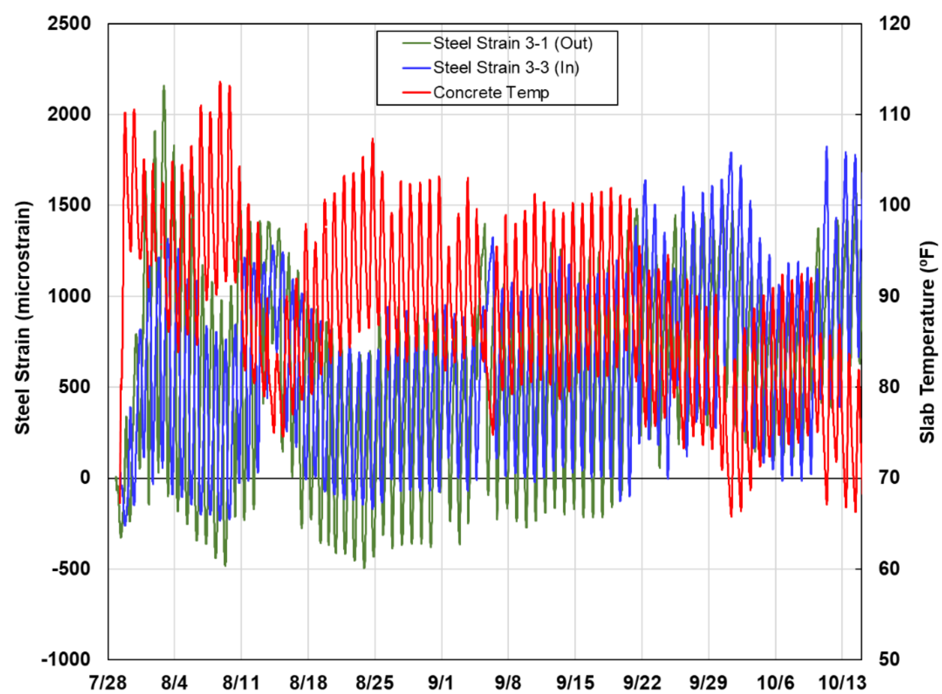

Figure 5.45 Long-term steel strains at the upper-depth low CoTE section in US62/180 El Paso

In order to fully comprehend the steel strain behaviors affected by the three longitudinal steel configurations, the steel strains of a fully day cycle were plotted versus the recorded temperature at a specific concrete age. Data were analyzed at 7, 28, and 48 days from the concrete placement. Figure 5.46 shows that temperature variations at the mid-depth are lower than other steel depths, and corresponding steel strains are comparable to temperatures. This is somewhat unexpected, since concrete volume changes are the largest near the slab surface, which will be discussed later, and it was expected that steel strains at upper-depth would be much larger than those at mid-depth. The data in Figure 5.46 implies that placing longitudinal steel at where concrete volume changes are larger does not necessarily increase steel strains to a great extent. It could be because, under negative temperature gradient (top temperature lower than bottom temperature), steel placed at upper-depth restrains concrete volume changes more effectively, resulting in a smaller crack width and lower steel stress, compared with when the steel is placed at mid-depth. When the steel is placed at mid-depth, concrete above the steel is relatively free to move, causing larger curling-up and resulting crack width on the surface, which increases steel strains. What is presented in Figure 5.46 shows the "net" effects of these different behaviors of the slab when steel is placed at different depths.

The direction of the hysteresis loop of the steel strains versus temperature is counterclockwise. This means that, for a given temperature, there are 2 different steel strains. While temperature is going down at the depth of the steel (generally during negative temperature gradient), the slab curls up and crack width on the surface increases. During this phase, steel strains will be larger. Meanwhile, during positive temperature gradient, or while temperature at the depth of the steel is increasing, the slab curls down and crack width on the surface closes, resulting in lower steel strains. This hysteresis loop type behavior of the steel strains is another indication of the curling behavior of CRCP slab. If the slab behaves only axially, then there will be no loop, and there will be one-on-one correlation between temperature and steel strains. What is encouraging here is that placing steel closer to the surface did not increase steel strains or stresses substantially.

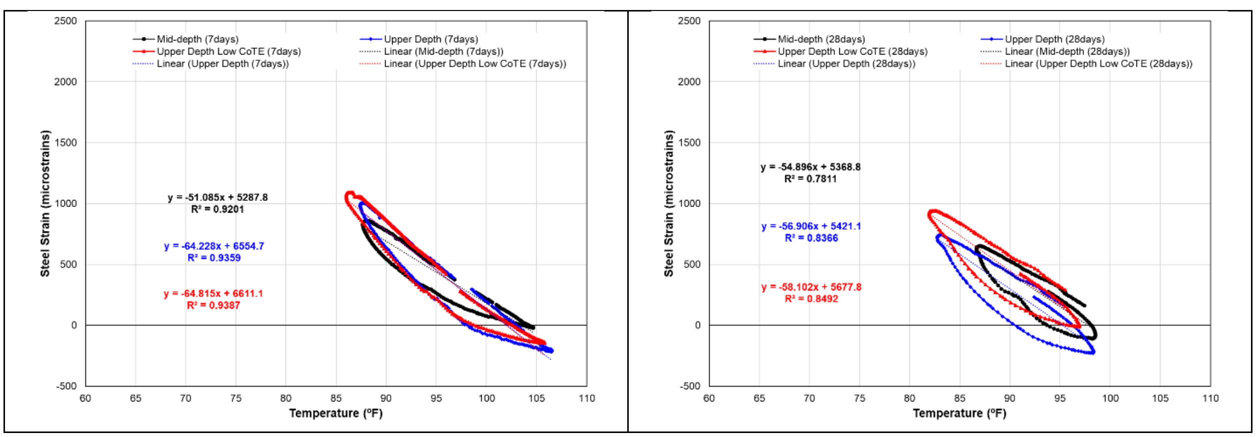

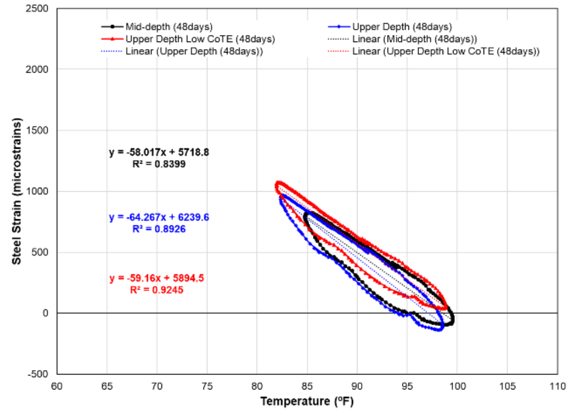

Figure 5.46 Steel strains versus temperature of mid-depth, upper depth and upper depth low CoTE sections at 7, 28, and 48 days from concrete placement in US62/180 El Paso

5.5.b.2.3 <u>Concrete strain behaviors in slabs</u>

This section investigates the behavior of concrete slabs at induced crack areas. VWSGs were installed at intended crack locations and saw-cuts were made at those locations across the width of the slab. Figures 5.47 to 5.49 show the concrete longitudinal (horizontal) strains recorded at the sawcut locations in the mid-depth, upper-depth and upper-depth low CoTE sections, respectively. It is observed that there was a rather large temperature drop within 2 weeks or so after concrete placement, and concrete strains increased by a large amount. However, with time, the temperature dropped continuously until the end of 2011. However, concrete horizontal strains remained relatively unchanged. This has significant implications on CRCP behavior and performance. Current theories on CRCP state that crack widths are almost linearly proportional to concrete temperature. Also, it is stated that crack widths or steel stress values are larger during the initial cracking of the CRCP but decrease with time as additional transverse cracks develop (Kashif et al., 2021). The findings made in this experiment and in previous studies by the research team indicate that crack widths decrease over time and seasonal values do not correlate well with temperature, even though a good correlation has been observed on daily crack width variations vs temperature.

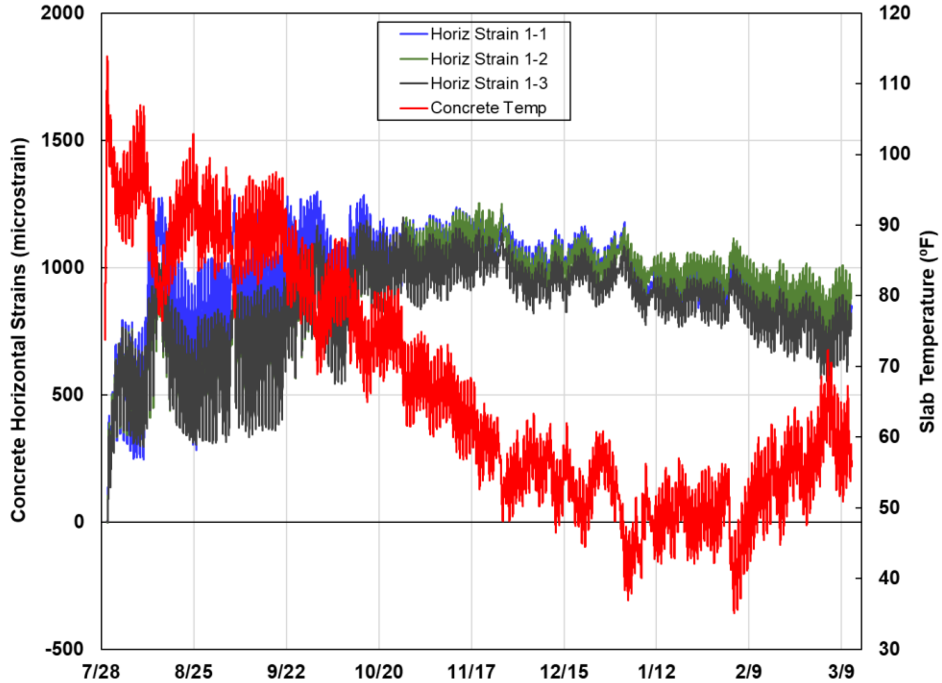

Figure 5.47 Long-term concrete horizontal strains at the mid-depth section in US62/180 El Paso

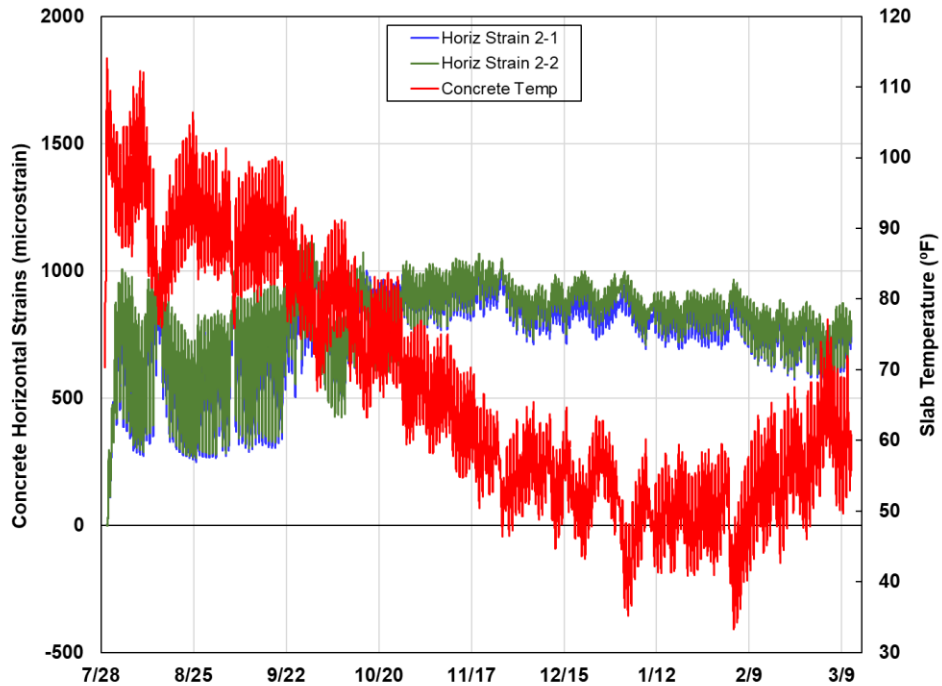

Figure 5.48 Long-term concrete horizontal strains at the upper-depth section in US62/180 El Paso

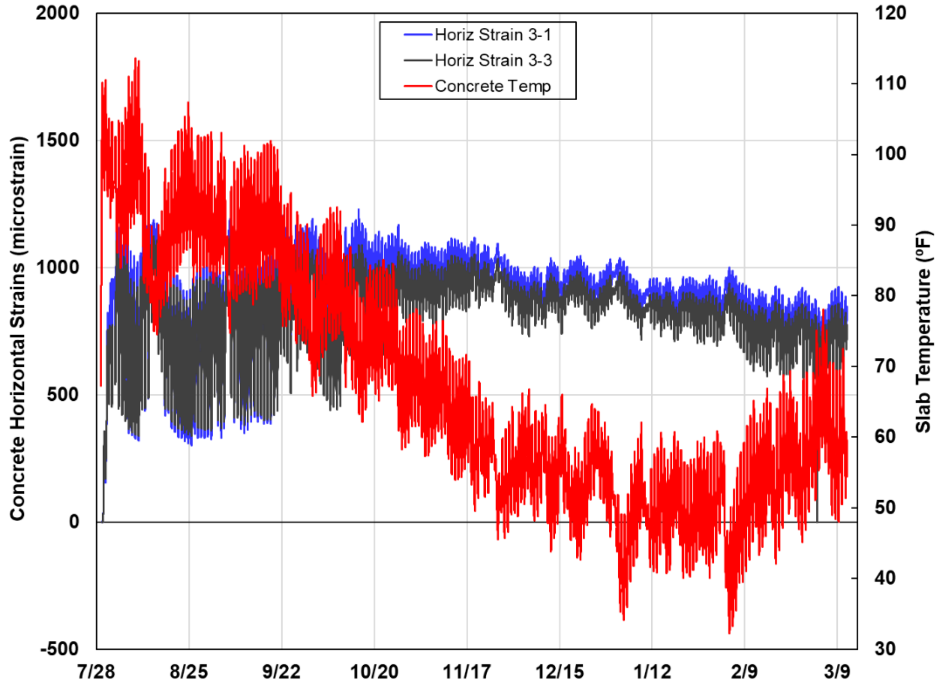

Figure 5.49 Long-term concrete horizontal strains at the upper-depth low CoTE section in US62/180 El Paso

The variations of crack widths over time were estimated using the dataset. 6-in VWSGs were installed horizontally in a longitudinal direction at the depth of the steel. Also, a transverse saw-cut was made right at the middle of these VWSGs. Accordingly, the strains recorded after a crack propagation are predominantly due to the movement of the crack. If the stresses in concrete within 3-in from the crack at both sides are assumed negligible, which is a reasonable assumption, then crack widths could be estimated by summing the concrete strains within 6-in length. The resulting values were converted into mils and the movement of the crack was plotted versus the recorded temperature at the depth of the installed sensor.

Figure 5.50 shows calculated crack movements at the mid-depth, upper-depth and upper-depth low CoTE sections at 7, 28, 48, 78, 109, 139, 170, 201, and 224 days from concrete placement. It is observed that, at early ages, crack widths at upper-depth low CoTE are the largest, which is as expected; however, after 78 days, crack widths at mid-depth became the largest and continued that way. It is postulated that, at early ages, restraints provided by longitudinal steel on concrete volume changes dominate slab movements and crack widths, and lower amount of steel with low CoTE section resulted in larger crack widths. The effect of subsequently developed cracks and crack spacing does not appear to have meaningful effects on crack widths. With time, concrete above the mid-depth undergoes volume contraction due to drying shrinkage and it appears that steel location plays an important role on crack width. At mid-depth section, with longitudinal steel placed 6-in from the surface, the steel has limited influence on concrete volume changes, which resulted in larger crack width. This has important implications. If there is a large temperature drop at early ages, if steel is placed at mid-depth, concrete above the mid-depth will try to shrink and the steel may not be able to effectively restrain the concrete shrinkage, resulting in large crack width as well as large upward curling of concrete, which could result in horizontal cracking at the depth of the steel (mid-depth). On the other hand, if the steel is placed closer to the surface, the steel could restrain concrete shrinkage, which reduces upward curling and vertical concrete stress at the depth of the steel. This could reduce horizontal cracking potential.

Another observation is that crack width actually decreases over time. This finding is consistent with the previous findings made by the research team, as well as field observations. In other words, for unknown reasons, concrete in CRCP appears to be in compression, unless temperature is quite low. Figure 5.51 shows what happened to CRCP on IH 45 in Houston. A portion of 2 lanes of CRCP were removed near the bridge. It was reported that the remaining CRCP slabs expanded, causing failures at stapling repairs. The expansion was about 3.5-in, which is quite substantial. These pictures were taken on Oct 3, 2008. Ambient temperature conditions prior to this occurrence were within normal range, and this example indicates that the concrete in CRCP was in tremendous compression. This finding is somewhat contrary to what's been advocated in CRCP research, where concrete is in tension and crack widths keep increasing with time due to continued drying shrinkage of concrete, which will result in decrease in load transfer efficiency at cracks, and eventually punchouts. What happened here does not support the above hypothesis. Rather, it supports the data presented in Figure 5.50.

The direction of the hysteresis loop observed is also counterclockwise. Crack width is larger during negative temperature gradient than positive gradient, which as discussed previously, indicates that curling behavior is more dominant than axial behavior.

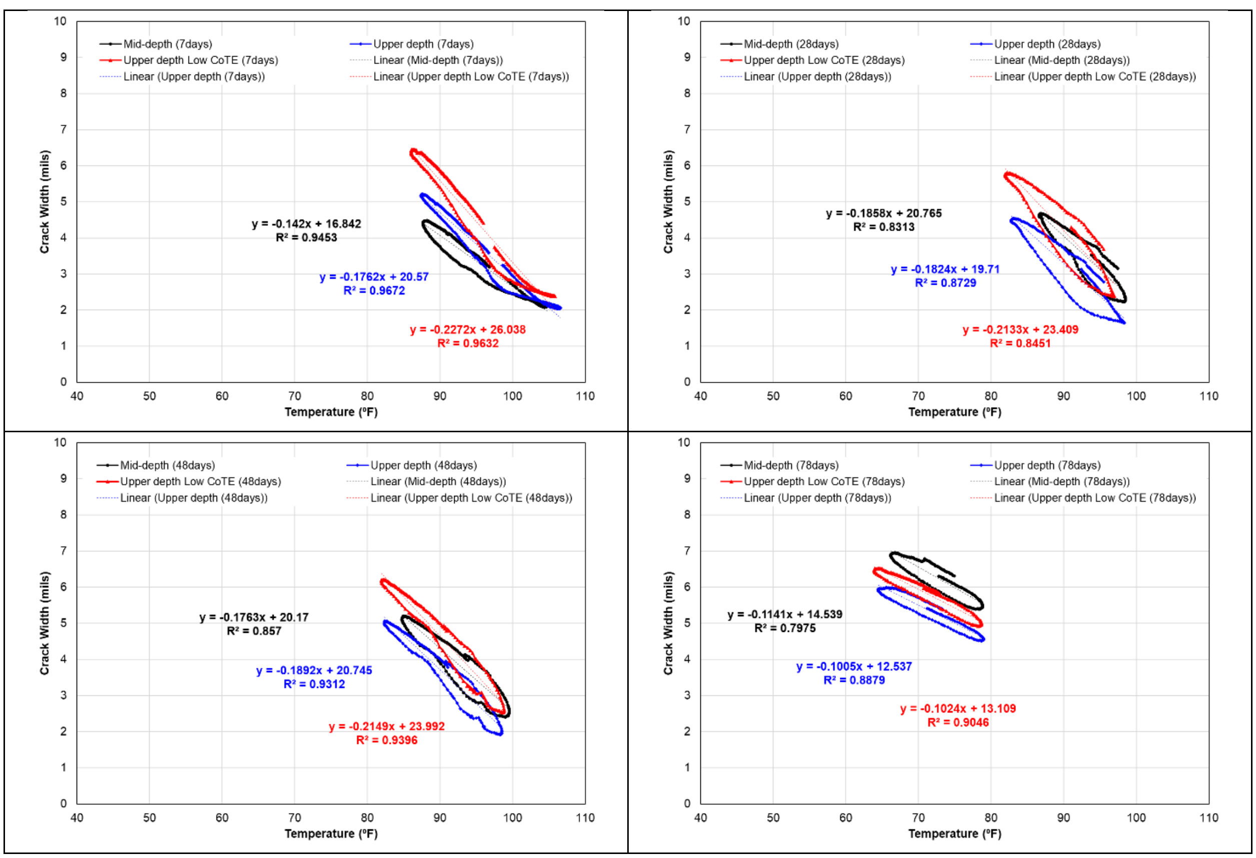

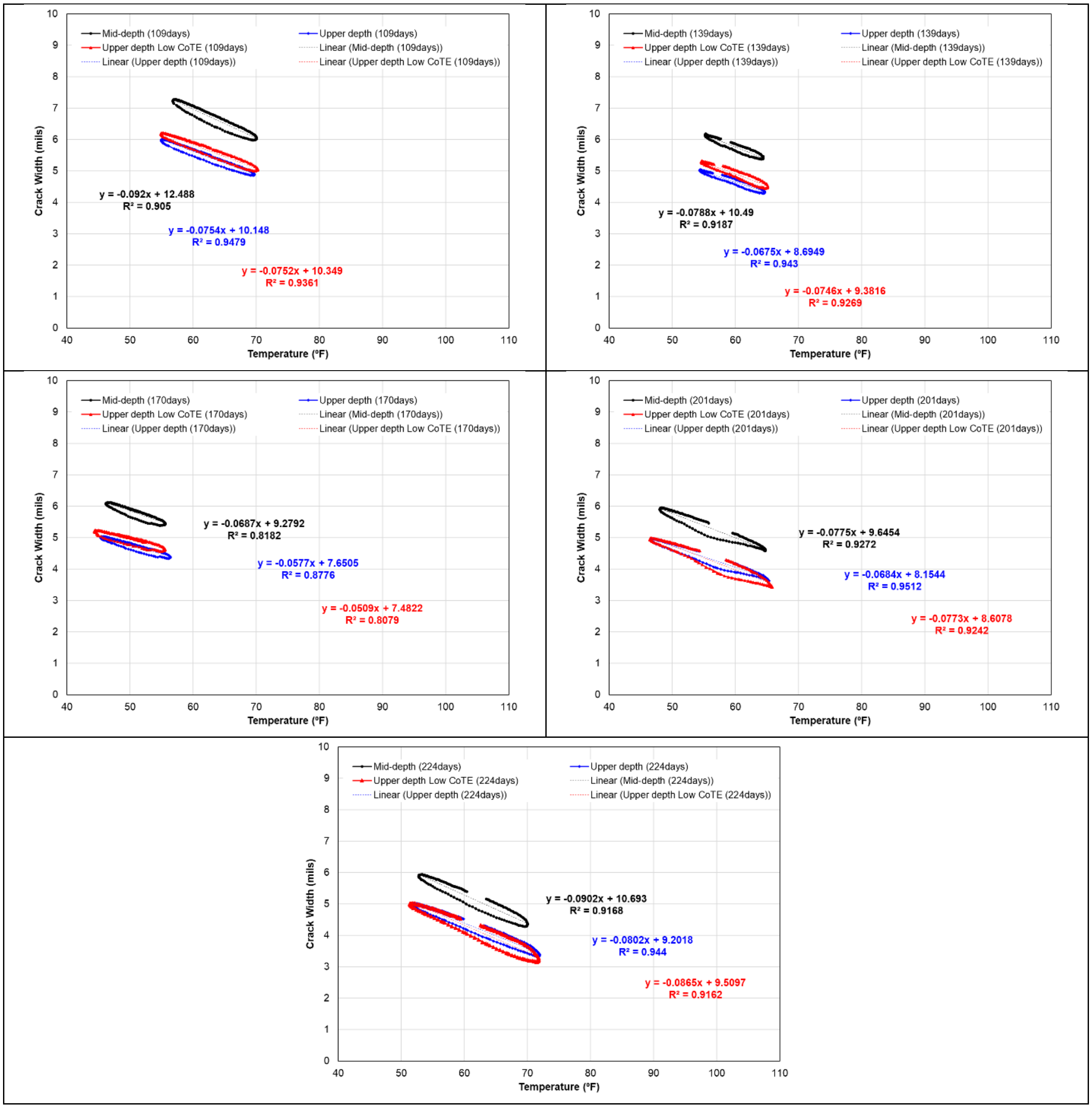

Figure 5.50 Crack width versus temperature of mid-depth, upper depth and upper depth low CoTE sections at 7, 28, 48, 78, 109, 139, 170, 201, and 224 days from concrete placement in US62/180 El Paso

Figure 5.51 CRCP expansion and resulting stapling failure

Another type of VWSGs (2-inch sensor) were installed vertically on both sides of the crack (i.e., west side and east side) to measure the concrete vertical strains at the location of the longitudinal steel throughout the duration of the measurement period. Figures 5.52 to 5.54 illustrate concrete vertical strains recorded throughout the measurement period. Firstly, it is observed that vertical strains at the mid-depth sections are larger than those of the upper-depth sections. Another observation is that, for the mid-depth and upper-depth sections, vertical strains at the west side are larger than those at the east side while, at the upper-depth low CoTE section, the vertical strains are similar between the west and the east side. The paving direction for this test section was eastbound and it was observed that most of the vertical strains at the west side of the sawcut are higher than those at the east side of the crack. It was initially thought that paving direction might have an effect on the vertical strains; however, no positive consistency was observed in the dataset and, unless further convincing evidence shows up, the paving direction effect may not exist.

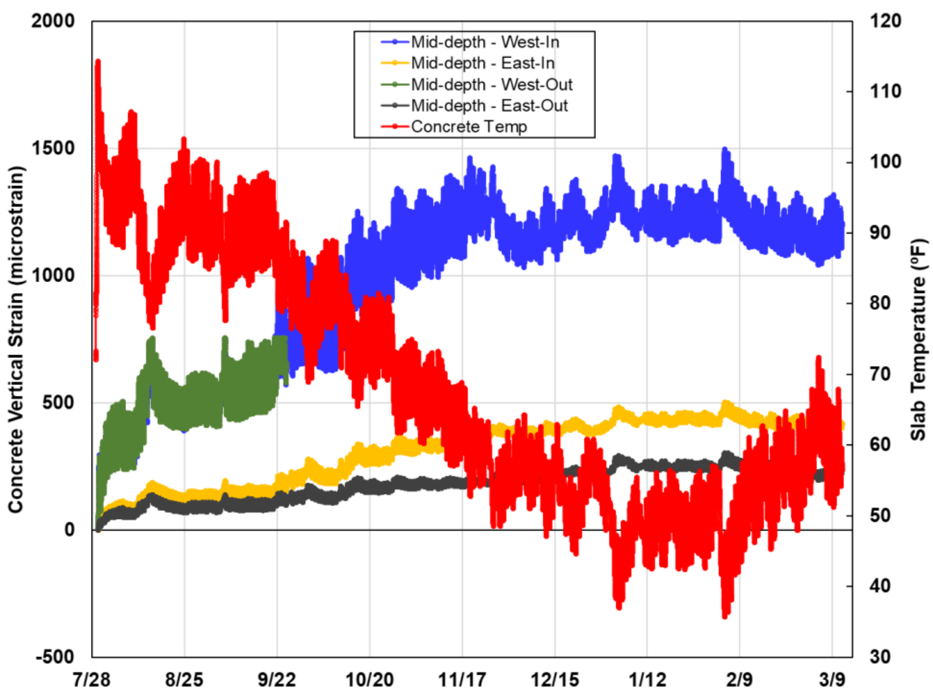

Figure 5.52 Long-term concrete vertical strains at the mid-depth section in US62/180 El Paso

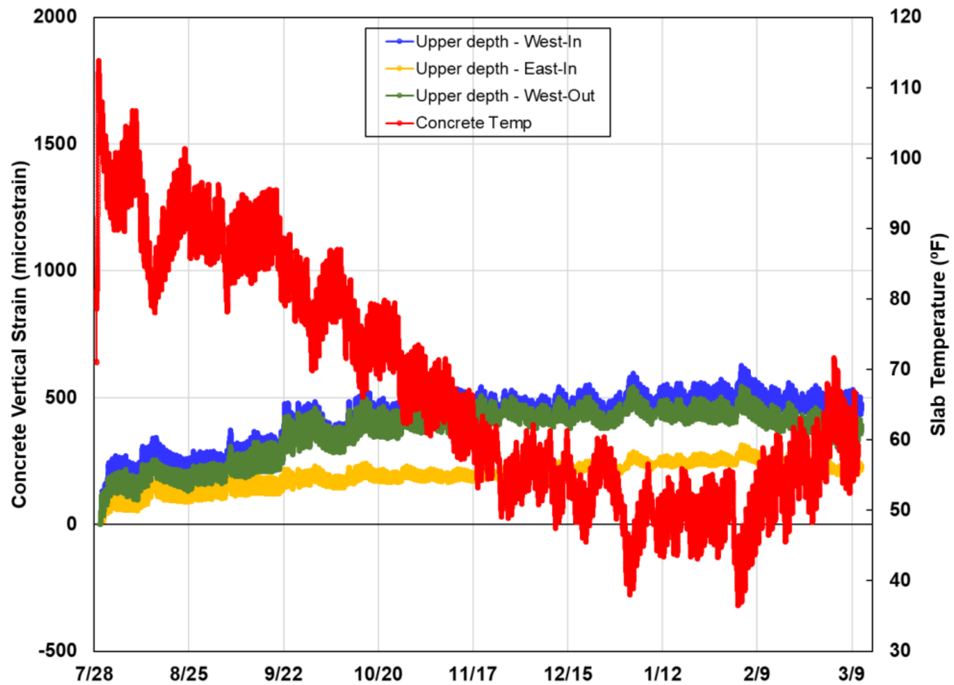

Figure 5.53 Long-term concrete vertical strains at the upper-depth section in US62/180 El Paso

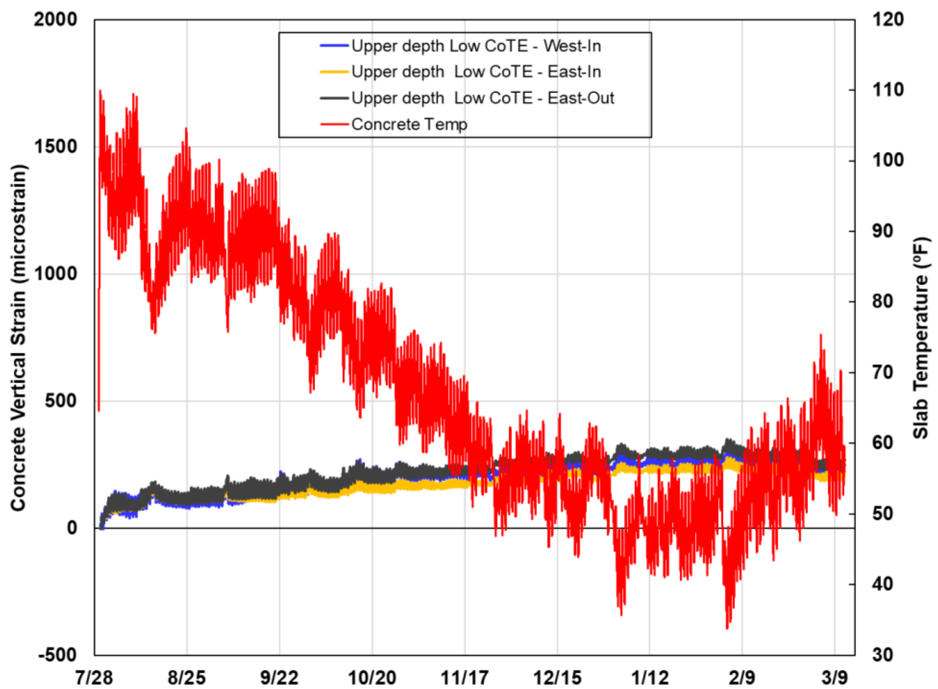

Figure 5.54 Long-term concrete vertical strains at the upper-depth low CoTE section in US62/180 El Paso

A relationship between the concrete vertical strains and temperature is presented in Figure 5.55 to describe the strain behavior of the concrete slab at the transverse crack during changes in temperature at 7, 28, 48, 78, 109, 139, 170, 201, and 224 days from concrete placement. Since the difference in strain magnitude at the west is greater than the east side of the crack, separate figures were presented. At first glance, it can be observed that the strain magnitudes at the mid-depth section are already higher compared to the upper depth sections as early as 7 days from concrete placement. The daily hysteresis loop that is formed by plotting the vertical strains with temperature follows are counterclockwise direction through time from 12AM to 11:59PM. It was also observed that the area bounded by the hysteresis loop at the mid-depth section is greater than the upper depth sections implying that the difference of strain magnitude within the same temperature at the early time of the day is significantly higher than the strain at the same temperature recorded later in the day. In addition, when a regression line is generated, the slope of the line which corresponds to the rate of change of vertical strains with respect to temperature is higher at the mid-depth section than at the upper depth sections. In addition, as the weather gets colder, it is noticeable that the increase in vertical strains at the mid-depth has increased significantly compared to the increase in strain at the upper depth.

The physical implications of the trend in concrete vertical strains have been investigated. In the temperature profile section, it was discussed that the surface temperature is lower than the temperature at the bottom of the slab during early morning which induces the slab to curl up. At the later time of the day, the surface temperature increases and becomes higher than the temperature at the bottom of the slab which makes the slab curl down. This means that there is the same temperature in a day where one condition is that the slab curls up and the other condition is when the slab curls down which occurs in the early morning and later in the day, respectively. When the slab curls up, the contraction at the surface of the slab is high that it tends to widen the crack width. However, the transverse crack has been restrained by the longitudinal steel that prevents the crack from further separating. Meanwhile, at this condition, the crack width at the bottom of the slab which already narrower due to the higher temperature at this condition is being pushed against each other producing surface contact at the bottom slab which creates a “pivot” which generates additional restraint. Because of this additional restraint and the continuous contraction at the surface of the slab, the slab begins to move in the upward direction because of the moment induced at the “pivot” point which explains why the vertical strain at the mid-depth is high. However, when the longitudinal steel is located above the middle of the slab, it increases the contact area between adjacent slabs and reduces the magnitude of moment induced at the “pivot’ point when the surface begins to contract and, thereby, reduces the volume above the longitudinal steel to be subjected to contraction due to lower temperature. As a result, the vertical strains at the upper depth sections are reduced. Meanwhile, when the slab curls down, the surface of the slab expands but will not be in contact with each other and thus there will be no “pivot” that will provide additional restraint in the slab to cause significant vertical movement that is why the vertical strains in the afternoon as lower. It can be noticed that the vertical strain variations for mid-depth section is higher compared to the upper depth sections. This implies that, when the longitudinal steel is placed above the middle of the slab, it does not only provide better horizontal restraint to the high variations upper portion of the slab, but it also provides better restraint in vertical movements at the location where volume changes are high which is at the upper depth of the slab.

However, it can be observed that the east side of the crack does exhibit the same trend. In fact, the vertical strain magnitude and behavior at the east side are relatively similar for all mid-depth, upper depth and upper depth low CoTE sections. This implies that the slab on the east side of the crack has minimal movements across. Although, it can be observed that when the temperature went down the vertical strain at the mid-depth have significant increase over the upper depth sections. This behavior implies that both slabs adjacent to the crack do not behave the same. It is possible that the movement of one side of the slab is high while the other side of the slab is minimal.

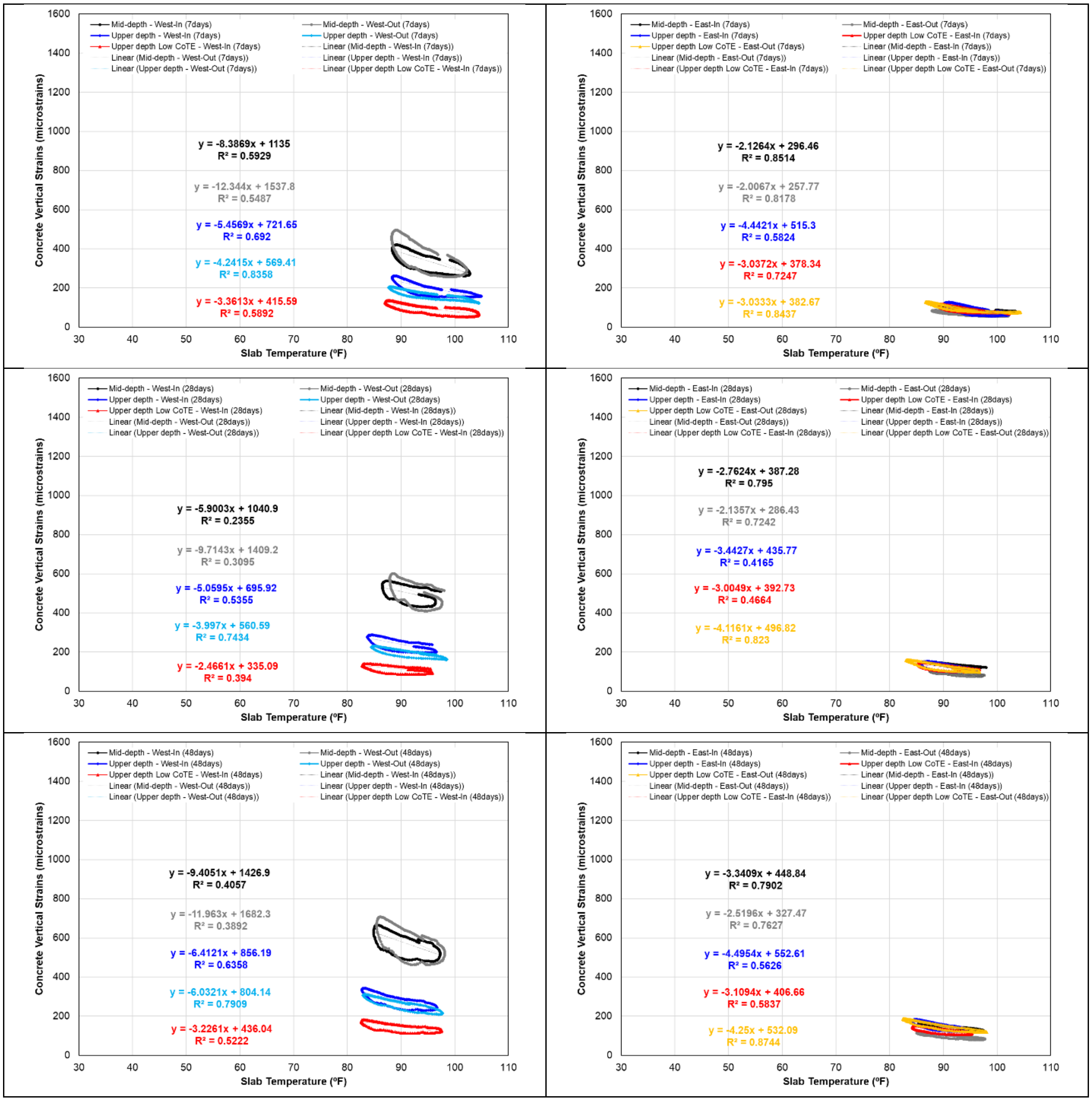

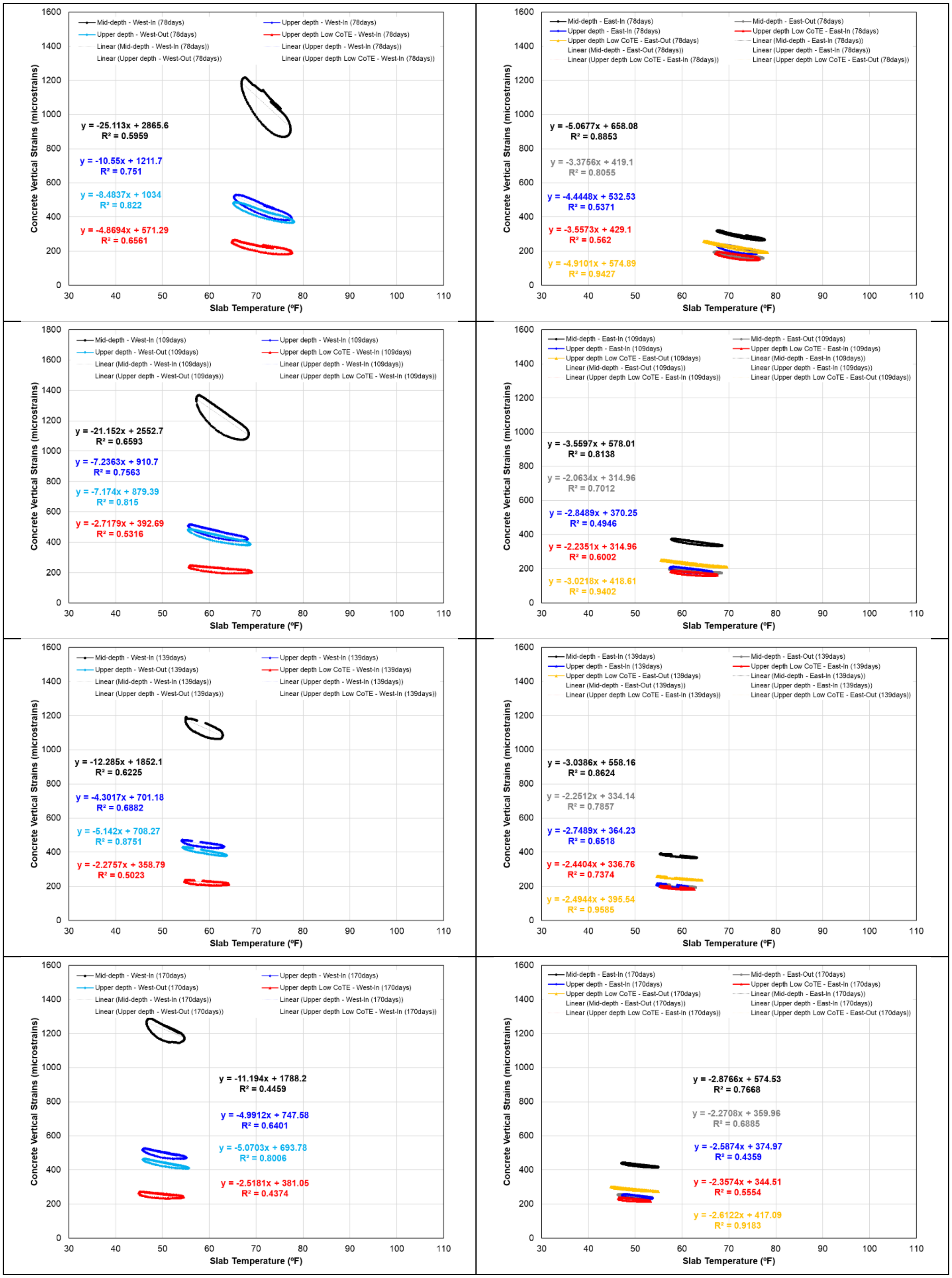
Mid-depth - West-In (78days)
Upper depth - West-In (78days)
Upper depth - West-Out (78days)
Upper depth Low CoTE - West-In (78days)
y = -25.113x + 2865.6
R² = 0.5959
y = -10.55x + 1211.7
R² = 0.751
y = -8.4837x + 1034
R² = 0.822
y = -4.8694x + 571.29
R² = 0.6561
Mid-depth - East-In (78days)
Mid-depth - East-Out (78days)
Upper depth - East-In (78days)
Upper depth Low CoTE - East-In (78days)
Upper depth Low CoTE - East-Out (78days)
y = -5.0677x + 658.08
R² = 0.8853
y = -3.3756x + 419.1
R² = 0.8055
y = -4.4448x + 532.53
R² = 0.5371
y = -3.5573x + 429.1
R² = 0.562
y = -4.9101x + 574.89
R² = 0.9427
y = -21.152x + 2552.7
R² = 0.6593
y = -7.2363x + 910.7
R² = 0.7563
y = -7.174x + 879.39
R² = 0.815
y = -2.7179x + 392.69
R² = 0.5316
y = -3.5597x + 578.01
R² = 0.8138
y = -2.0634x + 314.96
R² = 0.7012
y = -2.8489x + 370.25
R² = 0.4946
y = -2.2351x + 314.96
R² = 0.6002
y = -3.0218x + 418.61
R² = 0.9402
y = -12.285x + 1852.1
R² = 0.6225
y = -4.3017x + 701.18
R² = 0.6882
y = -5.142x + 708.27
R² = 0.8751
y = -2.2757x + 358.79
R² = 0.5023
y = -3.0386x + 558.16
R² = 0.8624
y = -2.2512x + 334.14
R² = 0.7857
y = -2.7489x + 364.23
R² = 0.6518
y = -2.4404x + 336.76
R² = 0.7374
y = -2.4944x + 395.54
R² = 0.9585
y = -11.194x + 1788.2
R² = 0.4459
y = -4.9912x + 747.58
R² = 0.6401
y = -5.0703x + 693.78
R² = 0.8006
y = -2.5181x + 381.05
R² = 0.4374
y = -2.8766x + 574.53
R² = 0.7668
y = -2.2708x + 359.96
R² = 0.6885
y = -2.5874x + 374.97
R² = 0.4359
y = -2.3574x + 344.51
R² = 0.5554
y = -2.6122x + 417.09
R² = 0.9183
Concrete Vertical Strains (microstrains)
Slab Temperature (ºF)

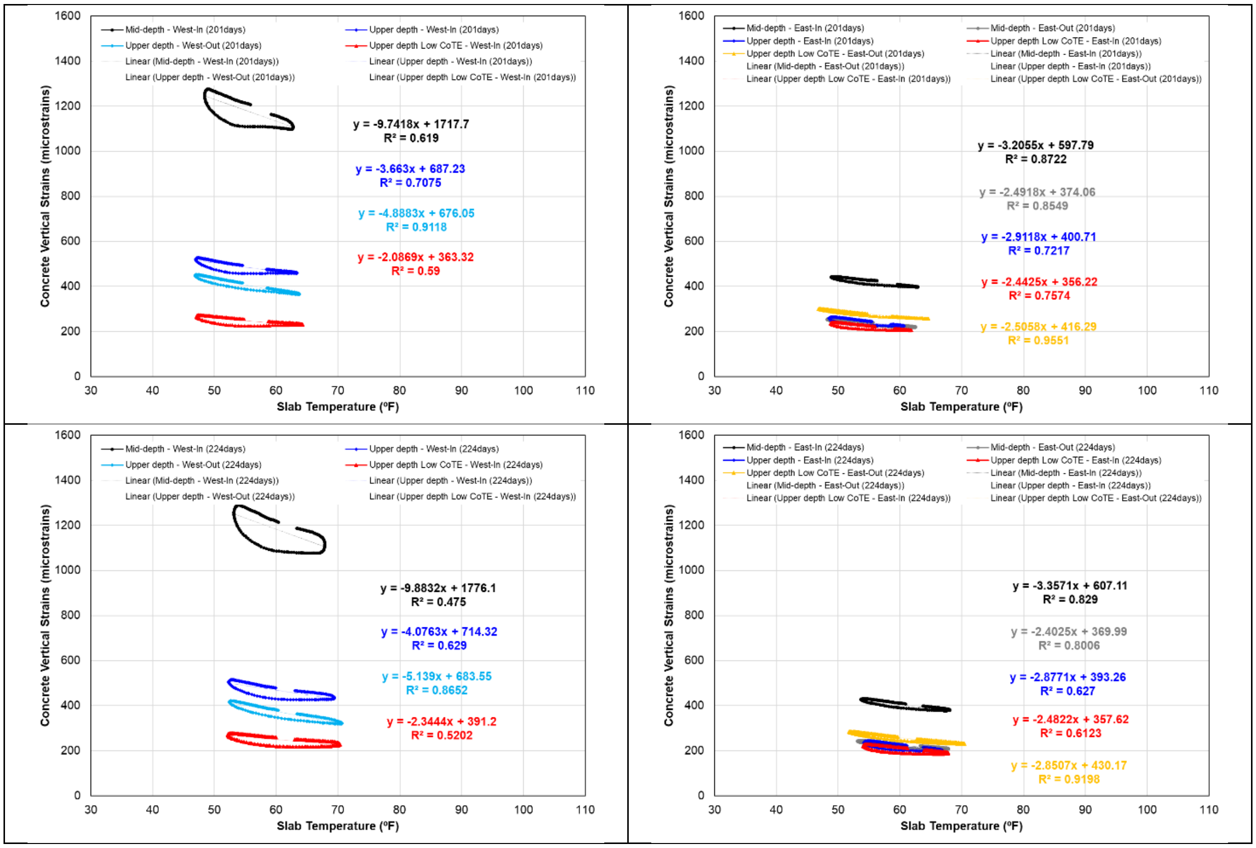

Figure 5.55 Concrete vertical strains versus temperature of mid-depth, upper depth and upper depth low CoTE sections at 7, 28, 48, 78, 109, 139, 170, 201, and 224 days from concrete placement in US62/180 El Paso

The research team were looking for evidence to support this case. In one of the previous distress investigations in IH45 in Dallas District in February 2010, it was observed that one side of the crack moved vertically as shown in Figure 5.56. The slab where horizontal cracking has propagated generated faulting at the surface of the slab. It was also observed that the crack propagation was diagonal and not vertical. This implies that the vertical strains on one side of the crack may be higher than the other and that the excessive stress acting on the slab may initiate horizontal cracking. This also supports the finding that when the longitudinal steel is placed at the upper depth of the slab then it reduces the stress acting on the concrete and thus preventing the propagation of horizontal crack.

Figure 5.56 CRCP horizontal cracking observed in IH45 Dallas

5.5.c IH 10 in San Antonio

5.5.c.1 Air and slab temperature behaviors

The air temperature was monitored from the weather station installed at the testing site and Figure 5.57 shows the air temperature throughout the measurement period. It can be observed that the minimum and maximum daily air temperature was 44 and 95°F in April 2022 which went up between 60 and 100°F in May 2022. It can also be noted that, on April 8, there was a significant drop in temperature. Due to memory constraints of the weather station, it failed to store the temperature information between April 8 and April 14.

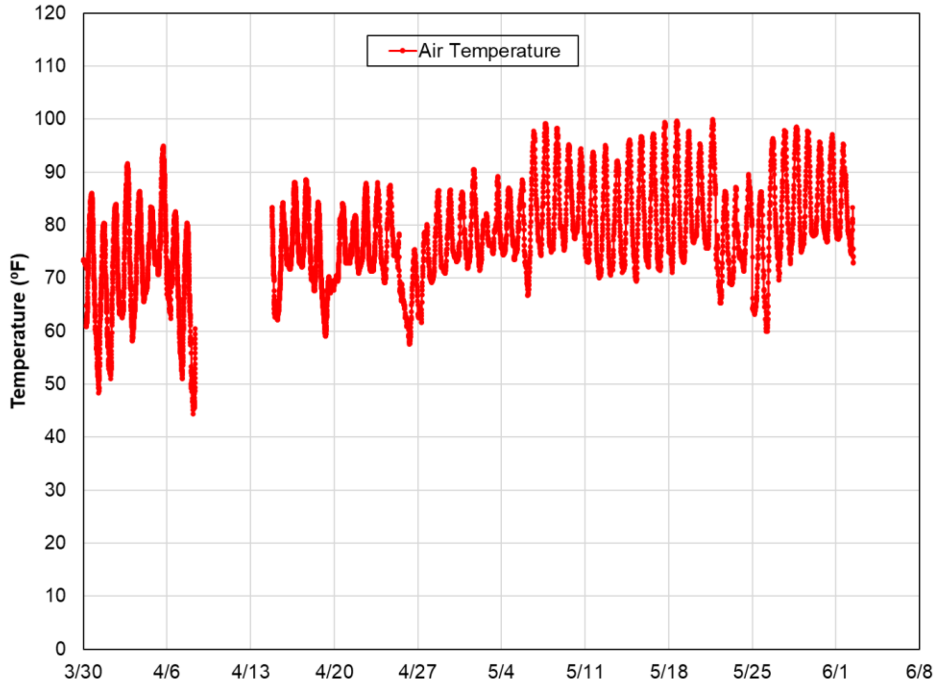

Figure 5.57 Air temperature profile in IH10 San Antonio

The slab temperatures relative to depth throughout the duration of the measurement period were investigated as shown in Figure 5.58. It can be observed that the slab temperatures are generally higher than the recorded air temperature. The surface temperature having the highest temperature variation is consistent with the El Paso data. Figure 5.59 shows the temperature gradients through the slab depth at specific periods between July 2021 and March 2022. Because of the time interval between the placement date of the mid-depth section and the upper depth section, there is a challenge to compare the temperature profile of the slab between both sections. In the first 7 days from concrete placement on both sections, the temperature profiles are different due to the difference in temperature condition in both sections. Also, it is the 2nd day from placement on the upper-depth section which means that the concrete hydration might have effect on the slab temperature. However, on April 14, which is 14 days from mid-depth concrete placement and 9 days from upper-depth concrete placement, it can be observed that the temperature profiles on both sections are similar. This means that, beyond April 14, the temperature profiles on both mid-depth and upper-depth sections uses the date of measurement and not the age of concrete in the analysis.

From end March to June 2022, the daily surface temperature range was between 10 and 47 °F, while the daily bottom temperature range was between 2 to 10 °F. In April 2022, the daily surface temperature range was between 10 to 40 °F and about degrees 2 to 9 °F for bottom temperature. In May 2022, the daily surface temperature range went slightly up between 18 to 47 °F and between 4 to 10 °F for the bottom temperature. The month-to-month variation of daily temperature ranges are consistent with the results from the El Paso test section. It can also be seen that the temperature at the surface is higher than that at the bottom between noon to 6pm and the other way around for the rest of the day throughout the measurement period. Also, the slab temperature at the surface is lowest at 6am, however, the highest slab temperature occurs at 3pm with instances at 12 noon on April 27 and 6pm on April 20. It is also notable that the temperature variation from the middle to the bottom of the slab is minimal compared to the nonlinear variation from the surface to the middle of the slab. This observation is also consistent with the El Paso test section.

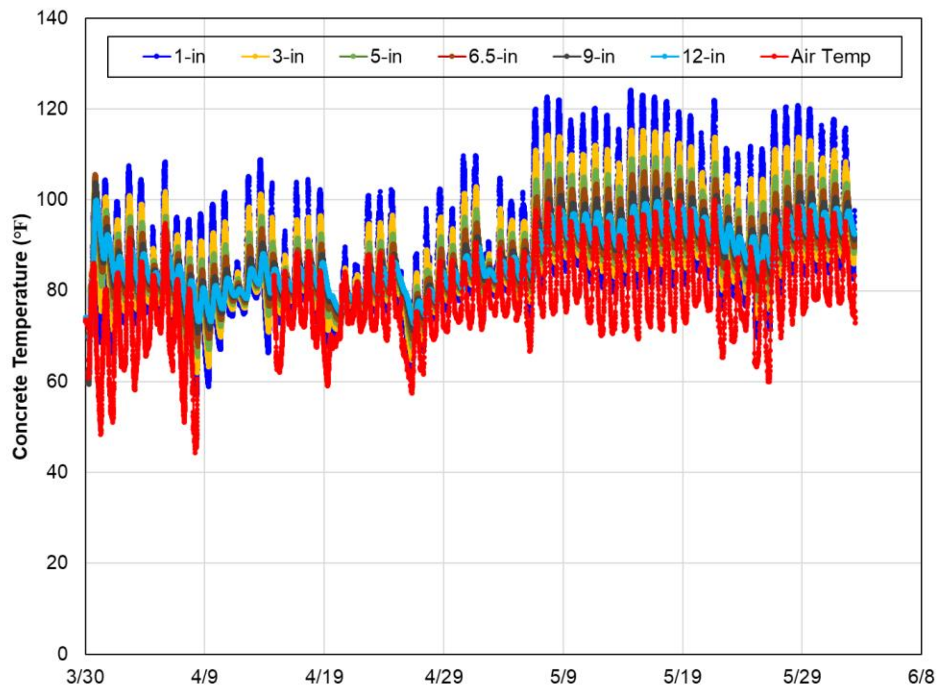

Figure 5.58 Pavement temperature profile in IH10 San Antonio test section

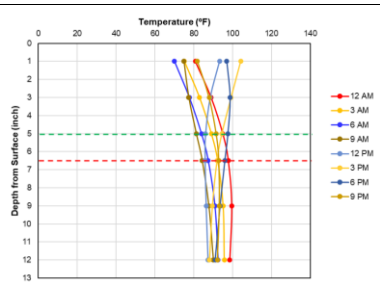 Day 1 (March 31) – mid-depth section	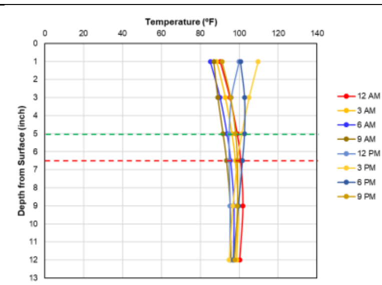 Day 1 (April 5) – upper-depth section
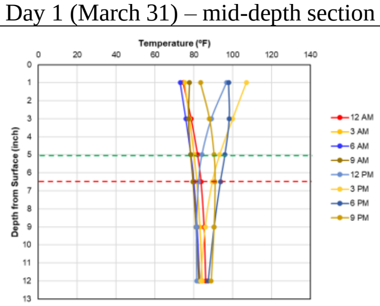 Day 3 (April 2) – mid-depth section	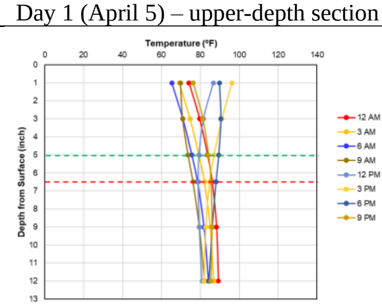 Day 3 (April 7) – upper-depth section

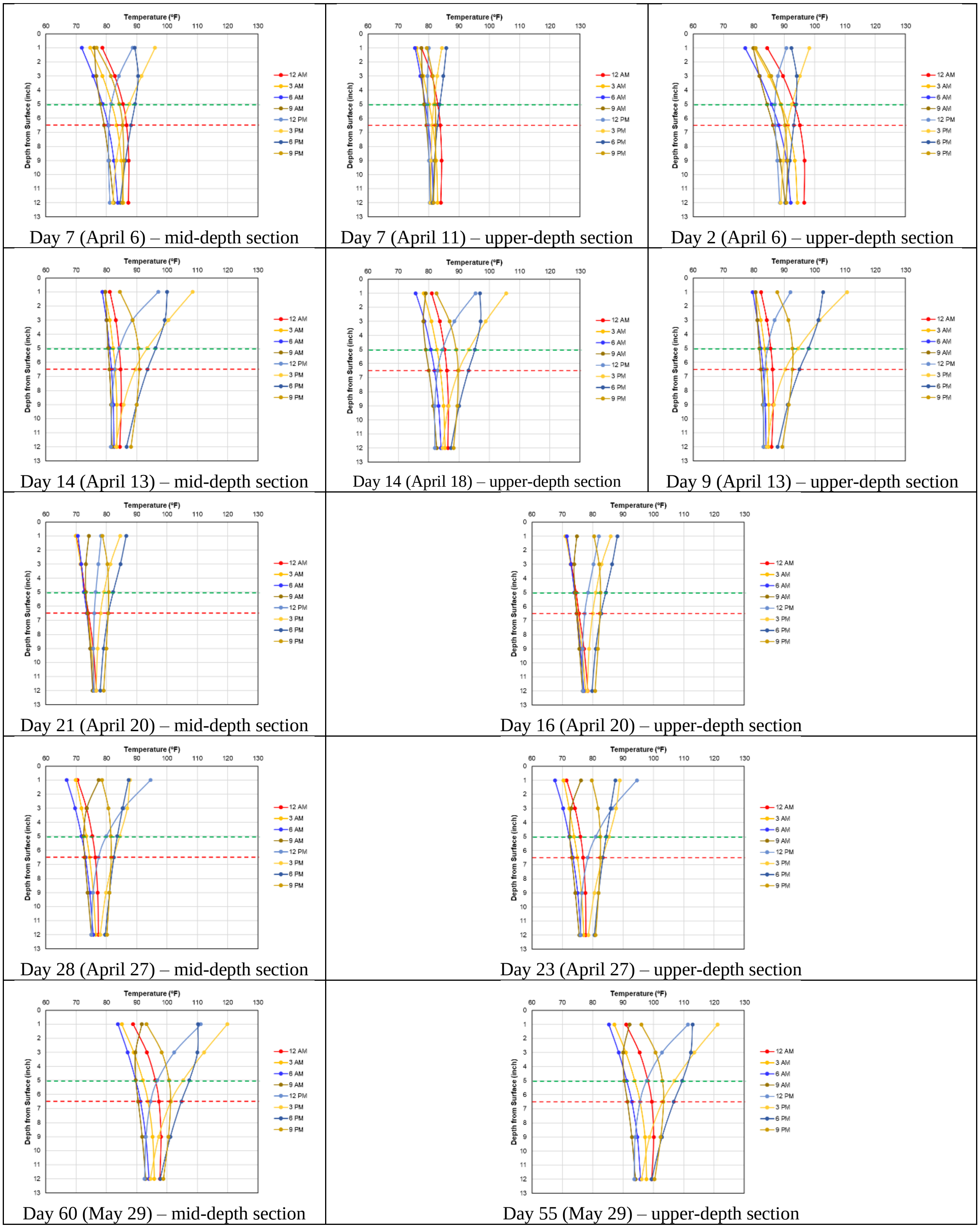

Day 7 (April 6) – mid-depth section

Day 7 (April 11) – upper-depth section

Day 2 (April 6) – upper-depth section

Day 14 (April 13) – mid-depth section

Day 14 (April 18) – upper-depth section

Day 9 (April 13) – upper-depth section

Day 21 (April 20) – mid-depth section

Day 16 (April 20) – upper-depth section

Day 28 (April 27) – mid-depth section

Day 23 (April 27) – upper-depth section

Day 60 (May 29) – mid-depth section

Day 55 (May 29) – upper-depth section

Figure 5.59 IH10 San Antonio test section temperature gradient at specific days from concrete placement

5.5.c.2 Longitudinal steel strain behaviors

Figures 5.60 and 5.61 show the steel strains recorded at the induced sawcut locations of the mid-depth and upper-depth sections, respectively. It is observed that the strains at the upper-depth low CoTE sections are higher than at the mid-depth, which is also consistent with the El Paso test section data. It is also observed that as the concrete temperature goes up, the steel strains go down and vice versa. Another thing noticeable is the sudden spike in steel strain at the upper-depth section on April 26 when the temperature went below 70°F. This may be attributed to the increased crack opening at the induced sawcut location of the upper-depth section. This will be verified by the concrete strain behavior obtained and will be discussed in the next section.

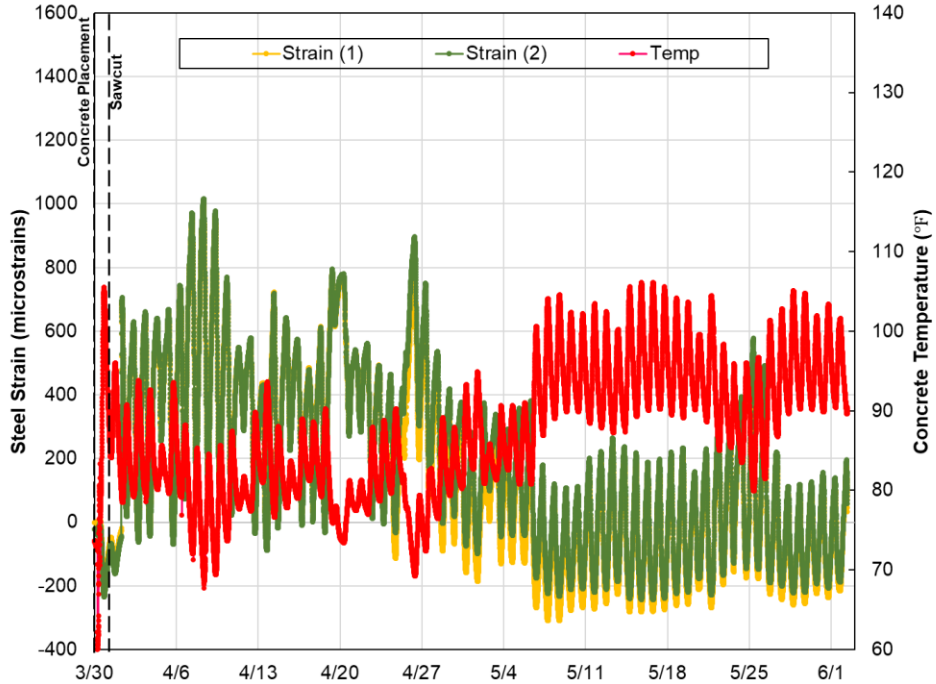

Figure 5.60 Steel strains at the mid-depth section in IH10 San Antonio

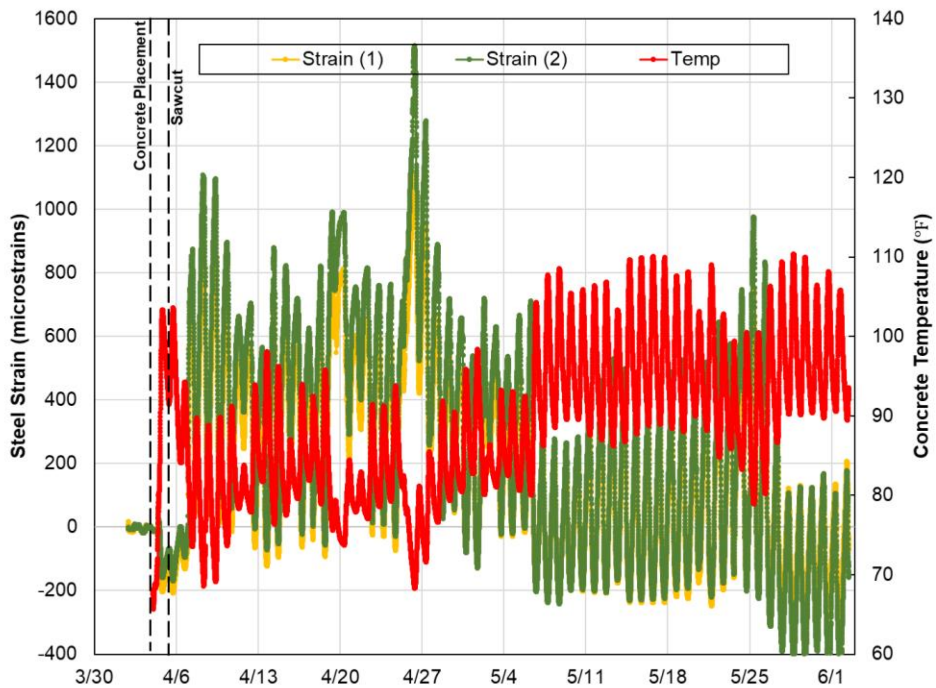

Figure 5.61 Steel strains at the upper-depth section in IH10 San Antonio

Steel strains on a full day cycle were also plotted with respect to the slab temperature at the location of the steel. Data were analyzed at 3, 7, 14, 21, 28 and 60 days from concrete placement at the mid-depth section and 3, 7, 9, 16, 23 and 55 days from concrete placement at the upper-depth section. It should be noted that, for 3 and 7 days, strain data used have different dates and the temperature profiles. For the rest, the data used are the strain recorded on the same date which means that the temperature profiles on both sections are similar.

Figure 5.62 shows the hysteresis loop generated by plotting the full day strain versus temperature. It can be observed that, generally, the steel strains are similar even when the location of the steel is different except when the temperature fell lower than 80°F where the steel strain at the upper depth section is higher than at the mid-depth section. This implies that, even when the location of the longitudinal steel is moved above mid-depth, the tensile strain acting on the steel does not significantly change. The direction of the hysteresis loop remained to be counterclockwise, having the same trend as the previous test section.

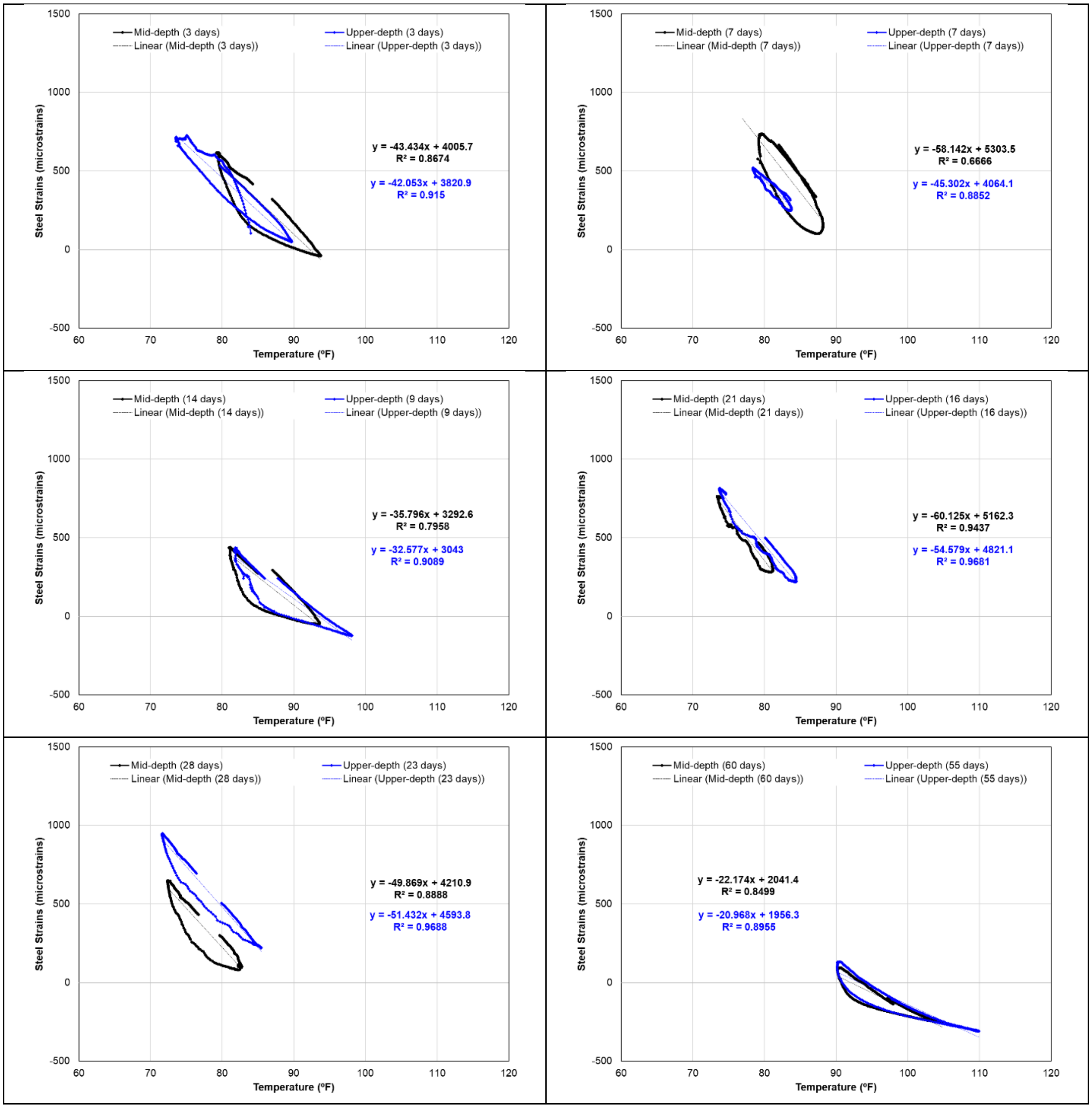

Figure 5.62 Steel strains versus temperature of mid-depth and upper depth sections in IH10 San Antonio

5.5.c.3 Concrete strain behaviors

Figures 5.63 and 5.64 show the concrete strain behavior at the mid-depth and upper depth sections, respectively. Firstly, it can be observed that the temperature at the upper depth section has larger variations compared to the mid-depth section. This is consistent with the results from the temperature profiles discussed above where the temperature variation increases significantly as the depth gets closer to the surface. Another observation is the sudden jump in concrete strain on April 26. This is due to the sudden drop in temperature. However, the upper-depth section has a higher surge in strain compared to the mid-depth section. This implies that there is a sudden increase in crack opening at the upper-depth location.

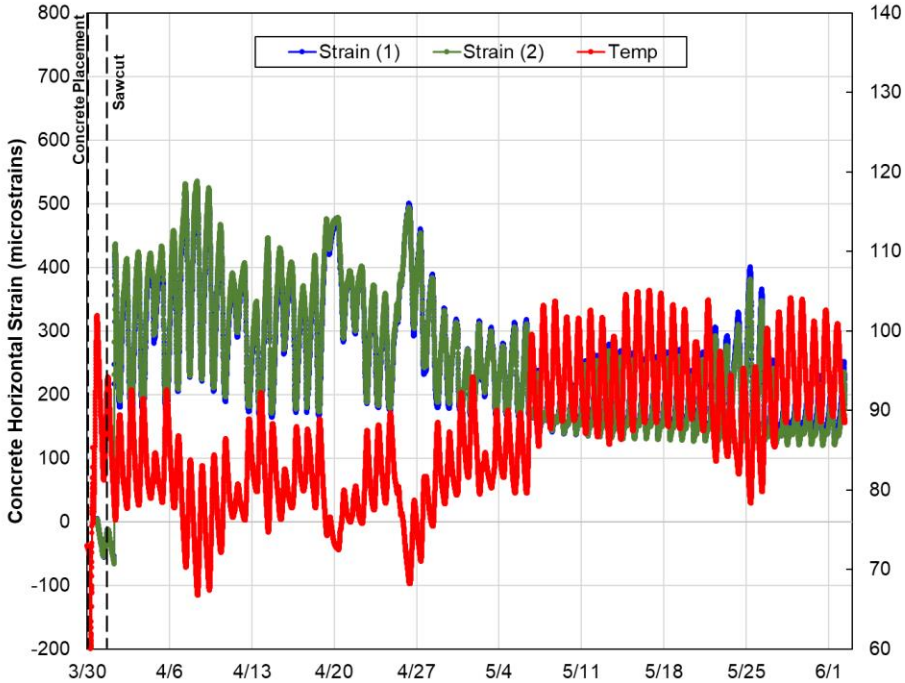

Figure 5.63 Longitudinal concrete strains at the mid-depth section in IH10 San Antonio

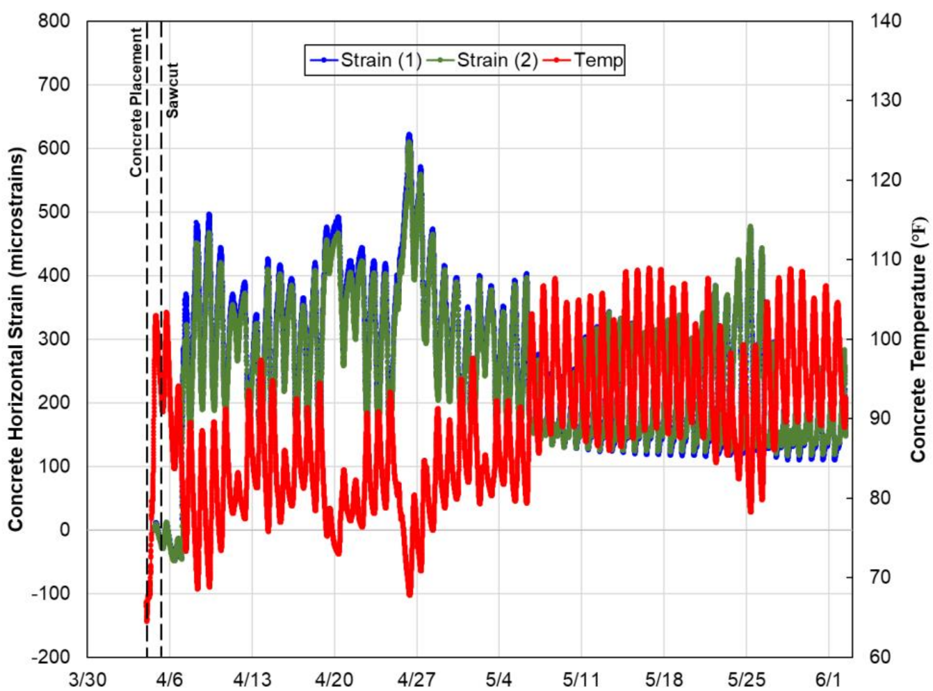

Figure 5.64 Longitudinal concrete strains at the upper-depth section in IH10 San Antonio

The variations of crack widths over time were also estimated using the dataset. 6-in VWSGs were installed horizontally in a longitudinal direction at the depth of the steel. An active crack control saw-cut was made at the edge of the pavement such that, when the transverse crack propagates, it will pass though the location of these VWSGs. As previously discussed, the strains recorded after crack propagation are predominantly due to the movement of the crack. If the stresses in concrete within 3-in from the crack at both sides are assumed negligible, which is a reasonable assumption, then crack widths could be estimated by summing the concrete strains within 6-in length. The resulting values were converted into mils and the movement of the crack was plotted versus the recorded temperature at the depth of the installed sensor.

Figure 5.65 shows calculated crack movements at 7, 14, 21, 28, and 60 days from concrete placement for the mid-depth section and 7, 9, 16, 23 and 55 days from concrete placement for the upper-depth section. Similar to the steel strain behaviors, it appears that the crack width at the mid-depth and upper depth sections have similar trends and magnitudes except when the temperature dropped below 80°F. It can also be observed that when the temperature goes beyond 90°F the crack widths remain the same at about 1 mil. It may be attributed to the gage limitation to record crack width movement in the compressive direction such that it cannot go down from 1 mil to zero when the crack is tightly closed due to thermal expansion.

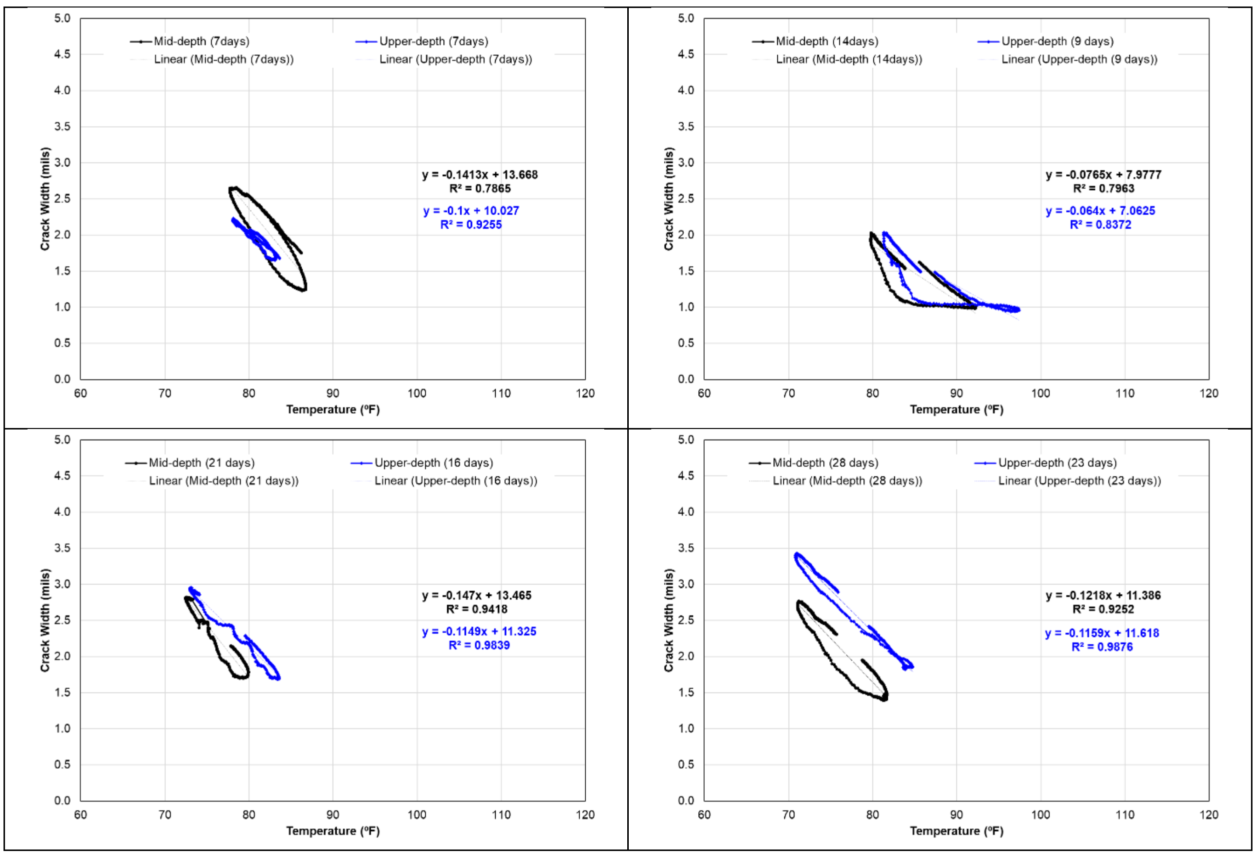

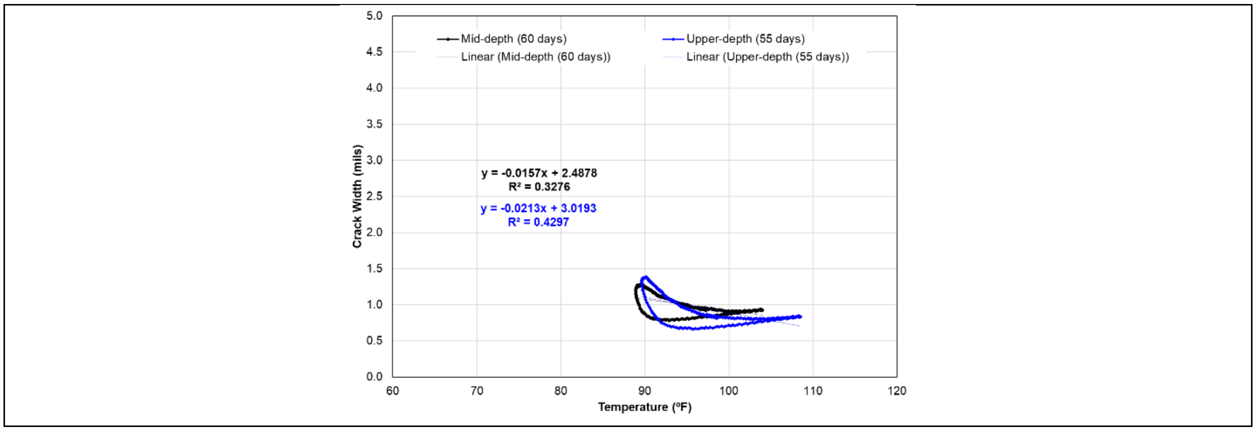

Figure 5.65 Crack width versus temperature of mid-depth and upper depth sections in IH10 San Antonio

Meanwhile, Figures 5.66 and 5.67 illustrate concrete vertical strains recorded throughout the measurement period. Firstly, it is observed that vertical strains at the mid-depth sections are larger than the upper-depth section. This pattern is the same as the El Paso test section. However, it can be observed that, unlike the El Paso where there is a huge strain difference between the west side and the east side of the crack, the difference here is lower. The paving direction for this test section was eastbound, however, unlike the results of the El Paso test section in which the west side of the crack has a larger strain, it can be observed that the east side of the crack has a vertical strain higher than the opposite side considering the paving direction is the same. As mentioned earlier, it was initially thought that the paving direction might influence the vertical strains; however, with this results in this test section, the paving direction has no effect on which side of the crack is subjected to higher vertical strain.

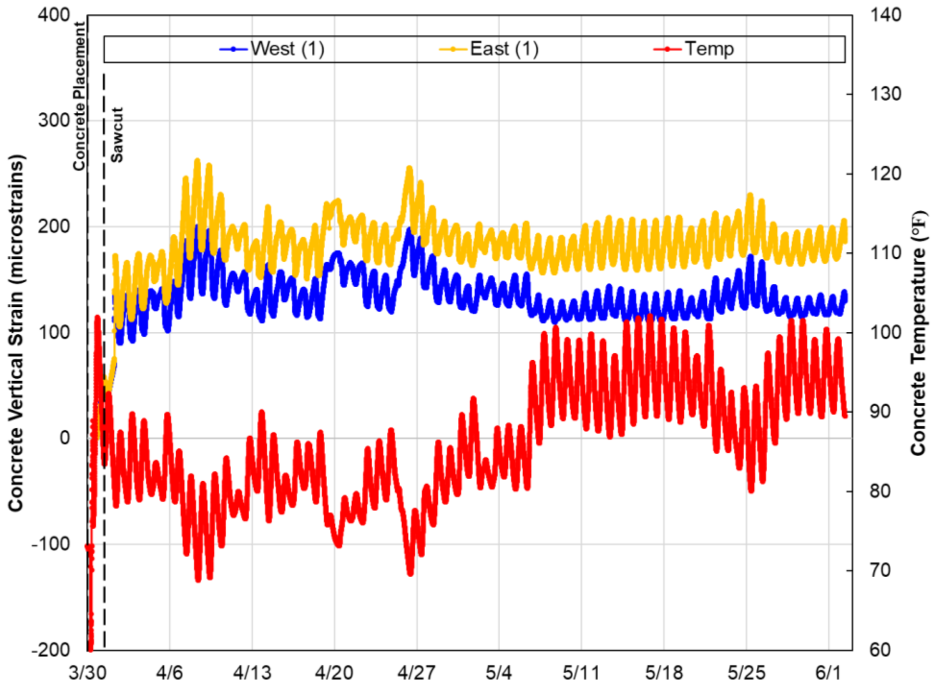

Figure 5.66 Vertical concrete strains at the mid-depth section in IH10 San Antonio

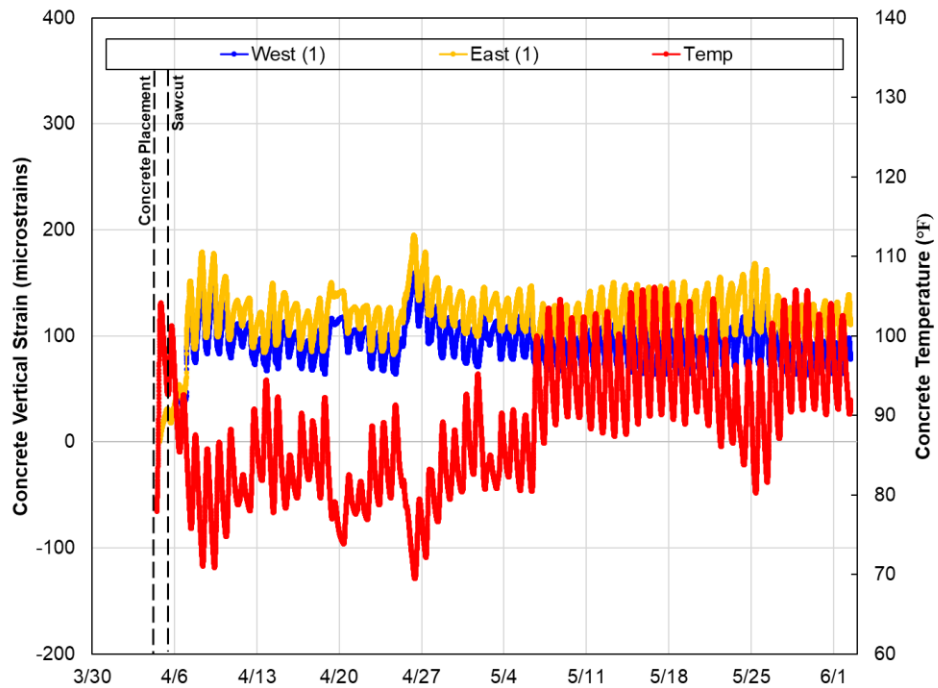

Figure 5.67 Vertical concrete strains at the upper-depth section in IH10 San Antonio

Figure 5.68 shows the hysteresis loop obtained by plotting the full day cycle of vertical strain with respect to temperature. A relationship between the vertical concrete strains and temperature has been generated at 7, 14, 21, 28, and 60 days from concrete placement for the mid-depth section and 7, 9, 16, 23 and 55 days from concrete placement for the upper-depth section. It is obvious that the vertical strain at mid-depth is higher than the upper-depth vertical concrete strain. The physical implication of this trend is consistent with the results of the El Paso test section which provides additional evidence to demonstrate that by placing the steel above the mid-depth would reduce the vertical movement of the concrete slab at the location of the crack due to curling and thereby reduce the potential for horizontal cracking.

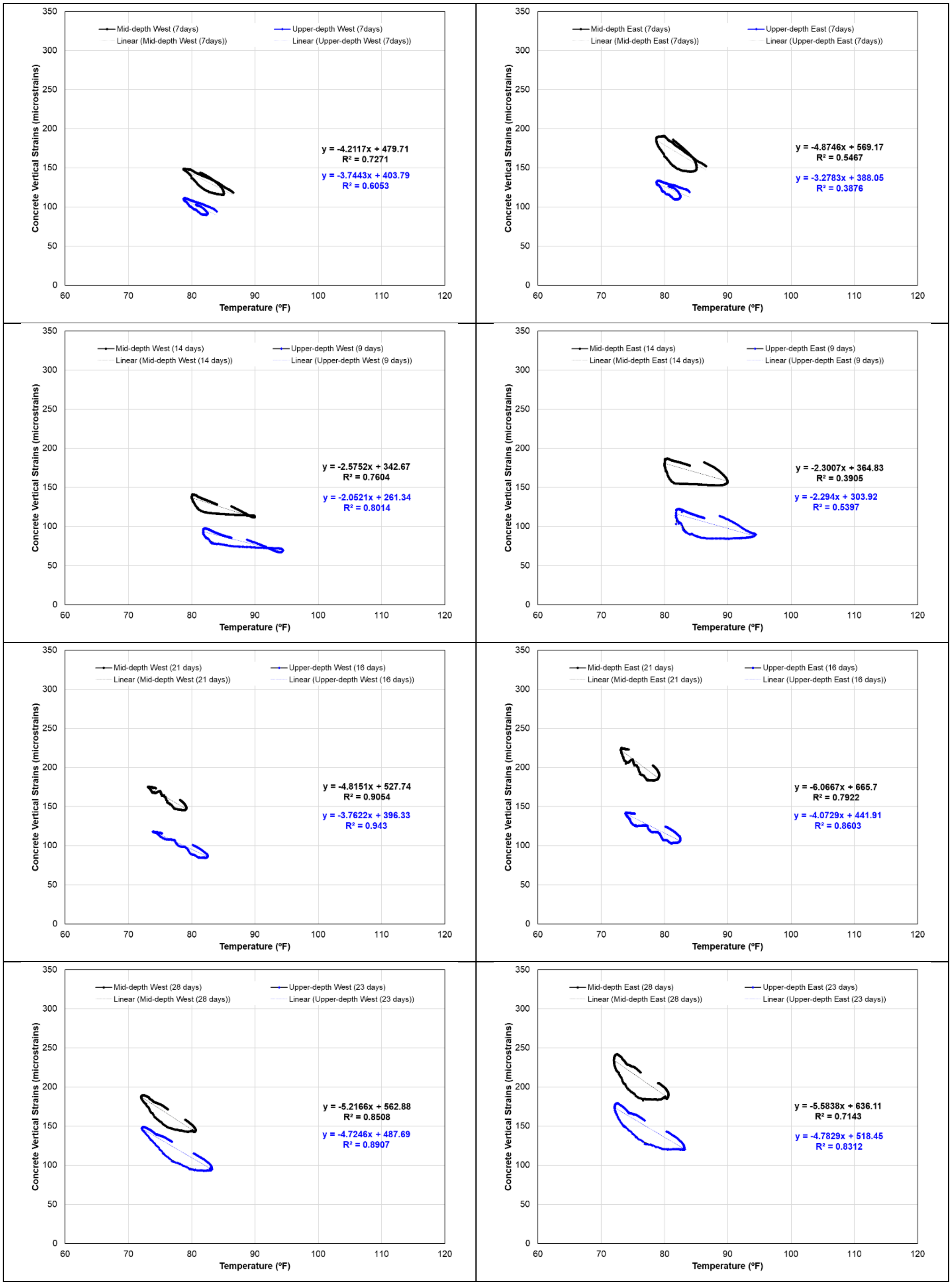
Mid-depth West (7days)
Upper-depth West (7days)
Linear (Mid-depth West (7days))
Linear (Upper-depth West (7days))
y = -4.2117x + 479.71
R² = 0.7271
y = -3.7443x + 403.79
R² = 0.6053
Mid-depth East (7days)
Upper-depth East (7days)
Linear (Mid-depth East (7days))
Linear (Upper-depth East (7days))
y = -4.8746x + 569.17
R² = 0.5467
y = -3.2783x + 388.05
R² = 0.3876
Mid-depth West (14 days)
Upper-depth West (9 days)
Linear (Mid-depth West (14 days))
Linear (Upper-depth West (9 days))
y = -2.5752x + 342.67
R² = 0.7604
y = -2.0521x + 261.34
R² = 0.8014
Mid-depth East (14 days)
Upper-depth East (9 days)
Linear (Mid-depth East (14 days))
Linear (Upper-depth East (9 days))
y = -2.3007x + 364.83
R² = 0.3905
y = -2.294x + 303.92
R² = 0.5397
Mid-depth West (21 days)
Upper-depth West (16 days)
Linear (Mid-depth West (21 days))
Linear (Upper-depth West (16 days))
y = -4.8151x + 527.74
R² = 0.9054
y = -3.7622x + 396.33
R² = 0.943
Mid-depth East (21 days)
Upper-depth East (16 days)
Linear (Mid-depth East (21 days))
Linear (Upper-depth East (16 days))
y = -6.0667x + 665.7
R² = 0.7922
y = -4.0729x + 441.91
R² = 0.8603
Mid-depth West (28 days)
Upper-depth West (23 days)
Linear (Mid-depth West (28 days))
Linear (Upper-depth West (23 days))
y = -5.2166x + 562.88
R² = 0.8508
y = -4.7246x + 487.69
R² = 0.8907
Mid-depth East (28 days)
Upper-depth East (23 days)
Linear (Mid-depth East (28 days))
Linear (Upper-depth East (23 days))
y = -5.5838x + 636.11
R² = 0.7143
y = -4.7829x + 518.45
R² = 0.8312
Concrete Vertical Strains (microstrains)
Temperature (ºF)
0
50
100
150
200
250
300
350
60
70
80
90
100
110
120

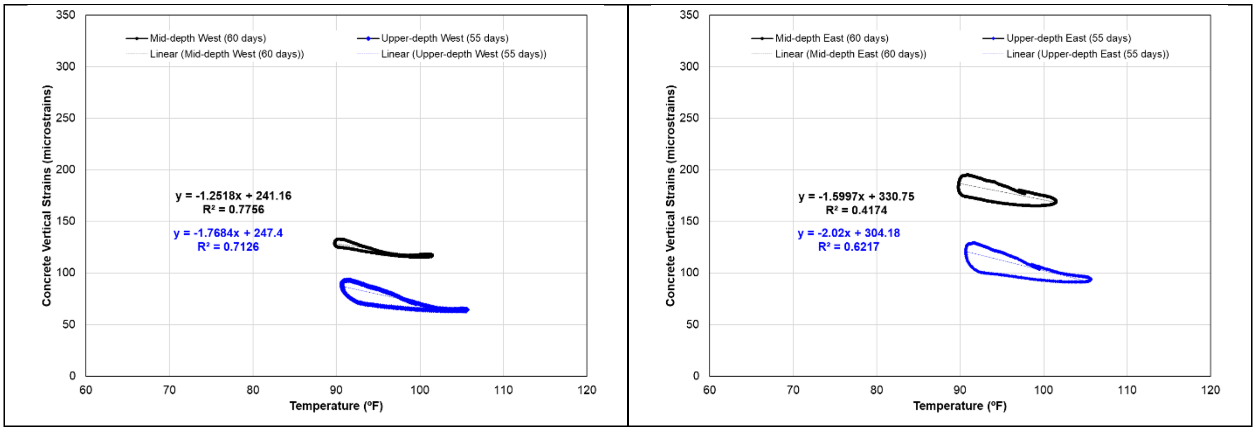

Figure 5.68 Vertical concrete strains versus temperature of mid-depth and upper depth sections in IH10 San Antonio

5.5.d IH 35E in Hillsboro

5.5.d.1 Slab temperature profile

The section was paved at night to avoid extreme weather conditions. Figure 5.69 shows the temperature profile of the slab at various depths. It can be observed that the maximum temperature at the surface was about 120°F during hydration and about 114°F after one week from placement. There was a period of low temperature on the 3rd week from placement due to the heavy rains that occurred in the area where the temperature fell below 80°F.

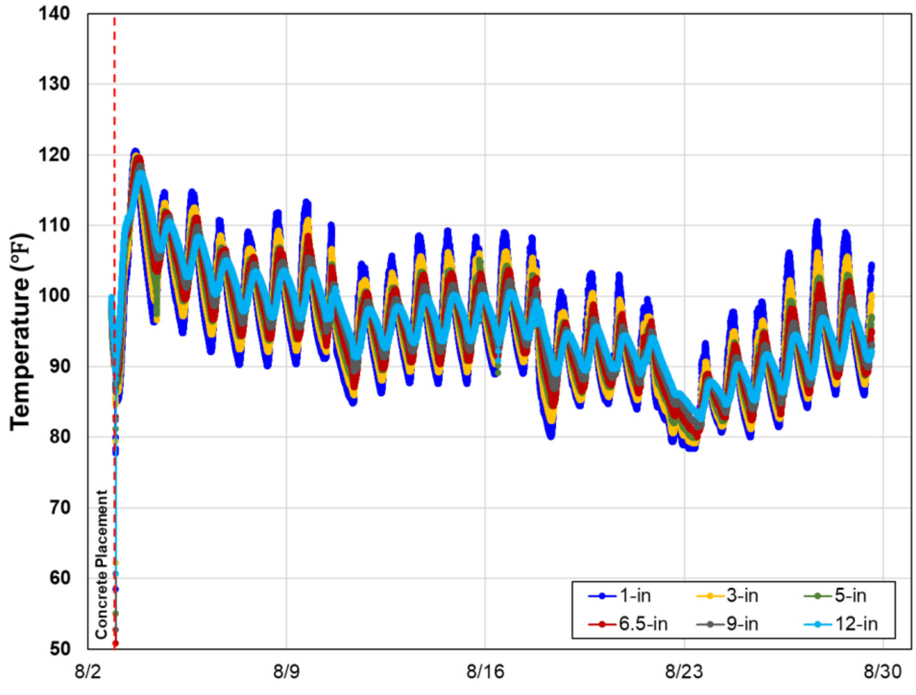

Figure 5.69 Pavement temperature profile in IH35E Hillsboro test section

Figures 5.70 show the temperature gradients of the slab on the 7th, 14th and 21st day after concrete placement. The range of temperature variation at the surface of the slab is 14°F (90 to 104°F), 19°F (88 to

107°F), and 14°F (81 to 96°F) on the 7th, 14th, and 21st day after placement, respectively. Meanwhile the range of temperature variation at the bottom of the slab is 6°F (96 to 102°F), 5°F (94 to 99°F) and 6°F (84 to 90°F) on the 7th, 14th and 21st day after placement, respectively. This means that the range of the temperature at the surface of the slab is more than twice the range at the bottom of the slab which is consistent with the trend observed in the previous field-testing activities. The higher temperature variation of the upper half of the slab compared to the lower half is consistent with the previous field test findings.

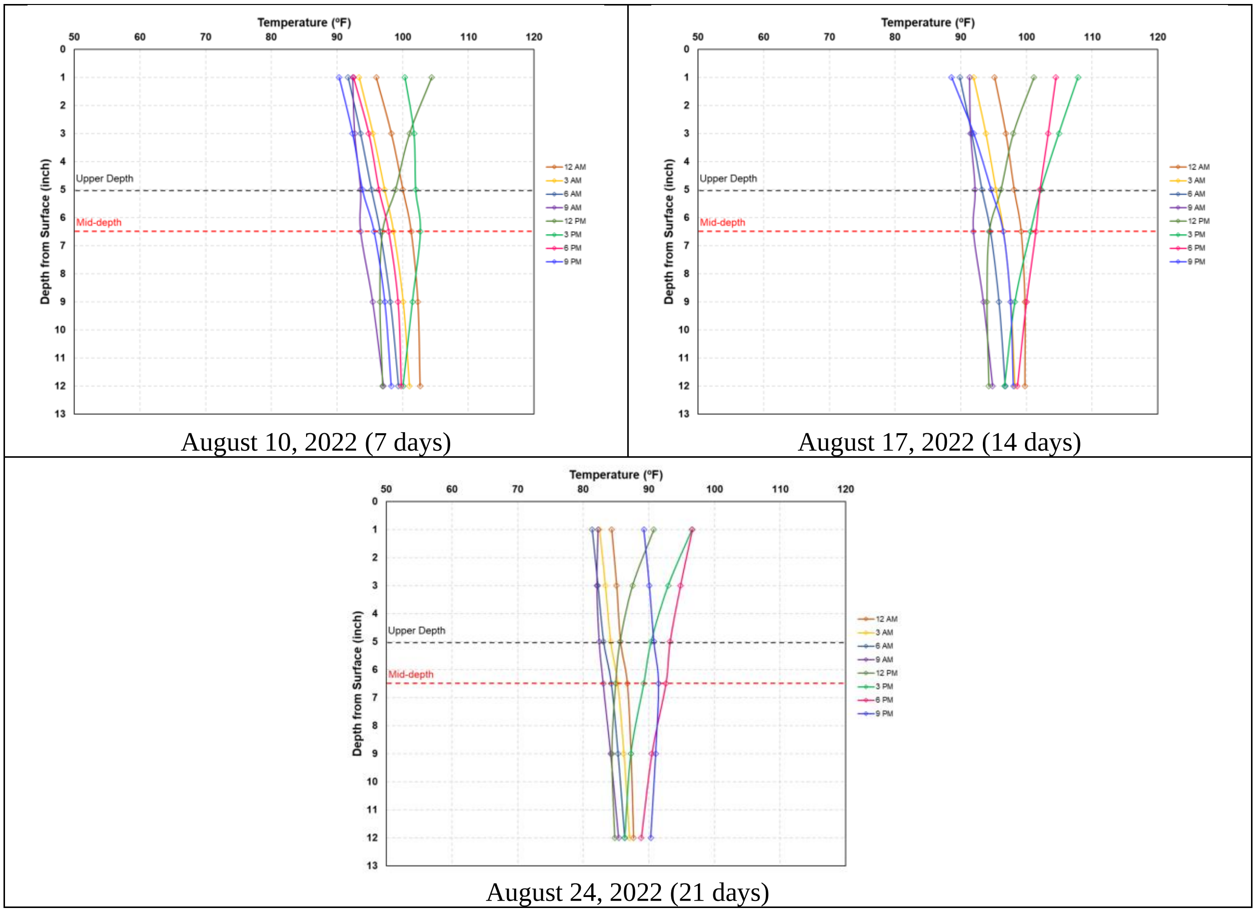

August 10, 2022 (7 days)

August 17, 2022 (14 days)

August 24, 2022 (21 days)

Figure 5.70 IH35E Hillsboro test section temperature gradient at specific days from concrete placement

5.5.d.2 Longitudinal steel strain behaviors

Figures 5.71 and 5.72 show the steel strains of the mid-depth and upper-depth sections, respectively. It can be seen that at the mid-depth section the steel strain went up to about 1600με when the temperature fell below 80°F. On the other hand, the upper-depth section only recorded about 1100με during the same period. Generally, it is observed that the steel strain at the upper-depth section is lower than the mid-depth section by around 400με. This is supported by the hysteresis loops presented in Figure 5.73. It can be observed that at the same temperature, the strain at the mid-depth sections is higher than the upper-depth sections on all three periods. In fact, on the 21st day, it can be seen that the difference in steel strains in mid-depth and upper-depth sections has greatly increased compared to the 7th and 14th day. The added effect of the low temperature also contributed to the increase in the strain. The direction of the hysteresis loop to be counterclockwise is consistent with the directions of the hysteresis loops of the previous instrumented sites.

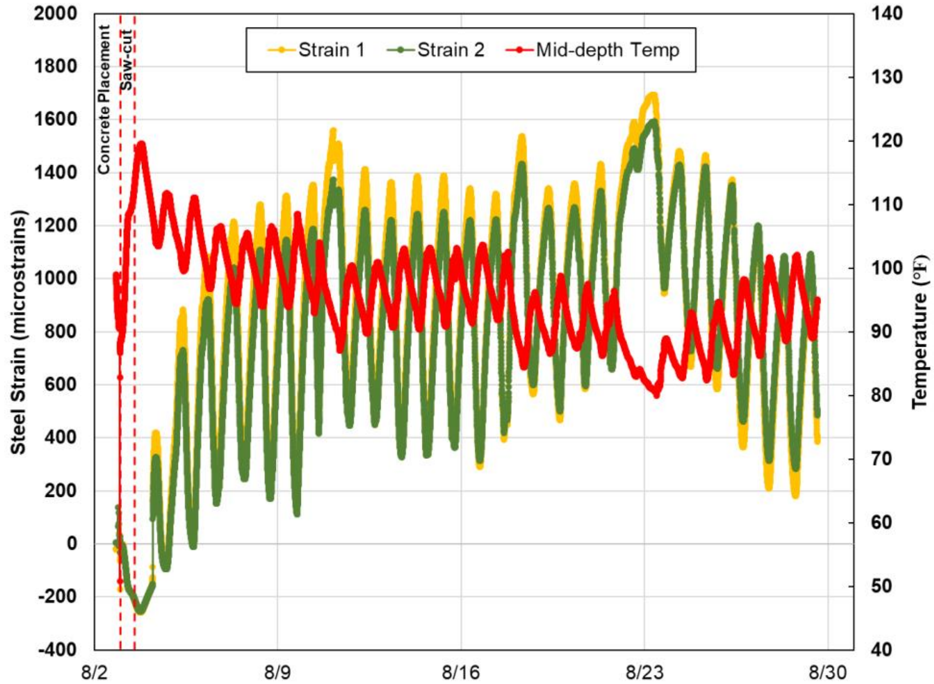

Figure 5.71 Steel strains at the mid-depth section in IH35E Hillsboro

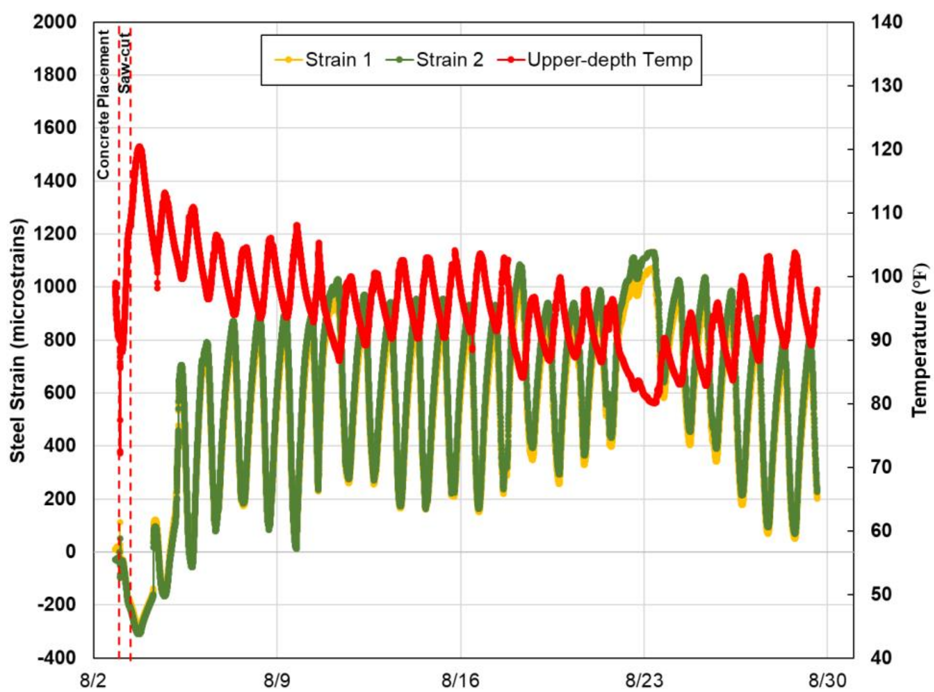

Figure 5.72 Steel strains at the upper-depth section in IH35E Hillsboro

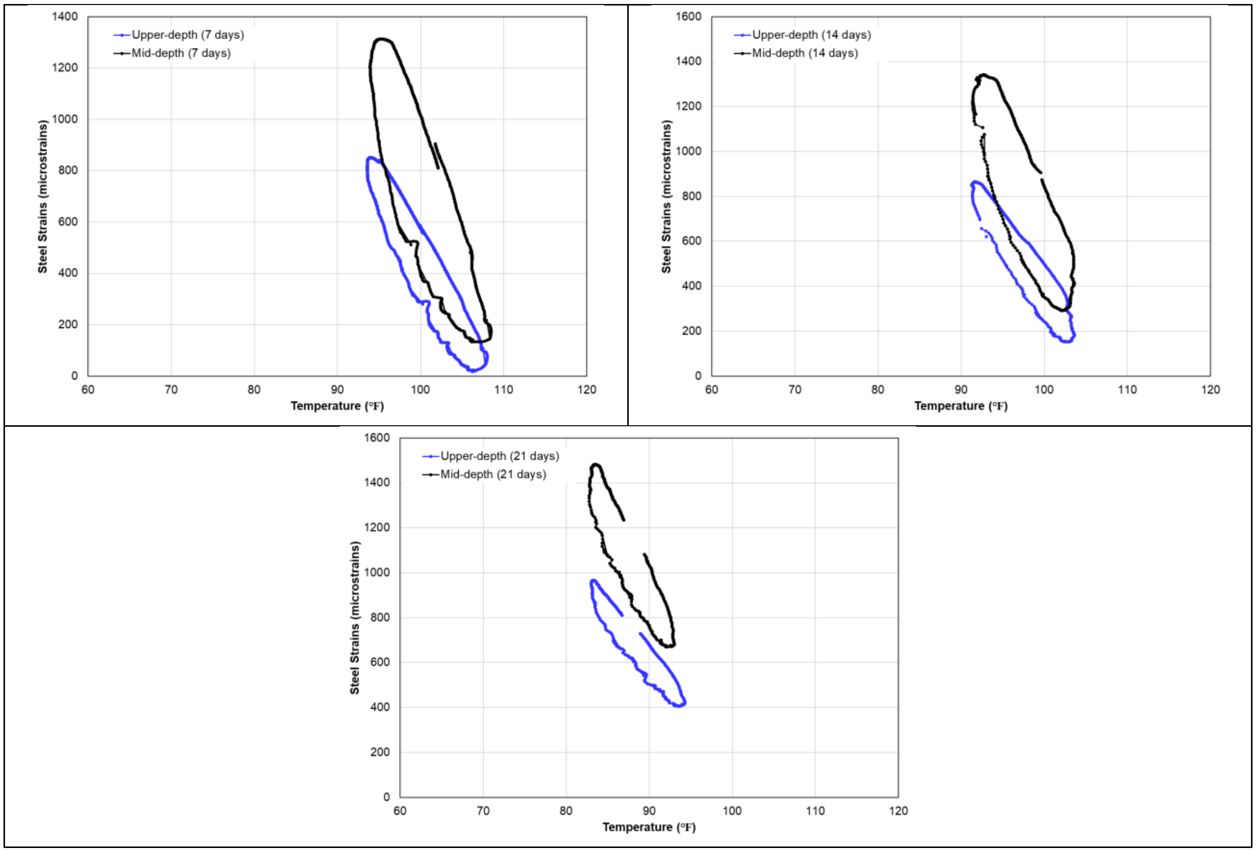

Figure 5.73 Steel strains versus temperature of mid-depth and upper depth sections in IH35E Hillsboro

5.5.d.3 Concrete strain behaviors

In Figures 5.74 and 5.75, four longitudinal concrete strains were recorded from 4 different depths in the slab. The depth indicated in the figures refers to the distance from the surface to the location of the sensor namely: 2-in, 5-in, 6.5-in and 11-in. The 5-in and 6.5-in are the location of the upper-depth and mid-depth reinforcement, respectively. On the first few days after concrete placement, it can be seen that the concrete is generating compressive strains on both mid-depth and upper-depth sections. The active control sawcut was installed 9 hours after concrete placement and the transverse crack across the location of the sensors was observed to have propagated a day after the sawcut. During this period, it can be noticed that at the mid-depth section, there is a jump in concrete strain readings from the compressive side to tension which indicates crack propagation. The concrete strain at the bottom of the slab on the mid-depth section did not significantly jump but a tensile strain was recorded. Meanwhile, in the upper-depth section, the compressive strain was also observed until the transverse crack propagated. However, unlike the mid-depth section the strain at the bottom of the slab remained to be under compression even though the top, mid-depth and upper-depth concrete strains have already recorded tensile strains. This implies that the transverse crack in the upper-depth section did not propagate towards the bottom of the slab until after another day where a sudden surge in tensile strain was recorded at the bottom of the slab. This implies that the restraint that the reinforcement provided when located above the mid-depth limits the crack movement compared to its behavior when the reinforcement is located at the mid-depth.

Looking at the short-term strain behaviors in the mid-depth section, it can be observed that the strains near the surface of the slab recorded that highest strain and corresponding strain variations relative to the strains recorded at the other depths. The maximum strain recorded at 2-in from the surface of the slab was about 1150με. This is primarily due to the higher temperature variation at the surface of the slab and the absence of restraints at the location where concrete volume changes are higher. It can also be observed that the strains and strain variations reduce as the depth increases towards the bottom of the slab. This is an indication that the behavior at this section is the typical curling and warping of the slab. However, the concrete strain at the upper-depth section was behaving differently. Although it can still be observed that the concrete strains at a depth near the surface is the highest (except when the temperature fell below 90°F), the maximum recorded was less than 800 με which is 350με lower than the strains recorded at the mid-depth section. An interesting observation is that, in general, the daily peak concrete strains at 5-in, 6.5-in and 11-in from the surface of the slab are similar. This suggests that, on a daily basis and when the temperature goes down, the concrete slab was moving uniformly from 5-in depth towards the bottom of the slab. This behavior does indicate a significant curling and warping behavior of the slab at this section. This is attributed to the restraint that is provided above the mid-depth which has higher volume changes.

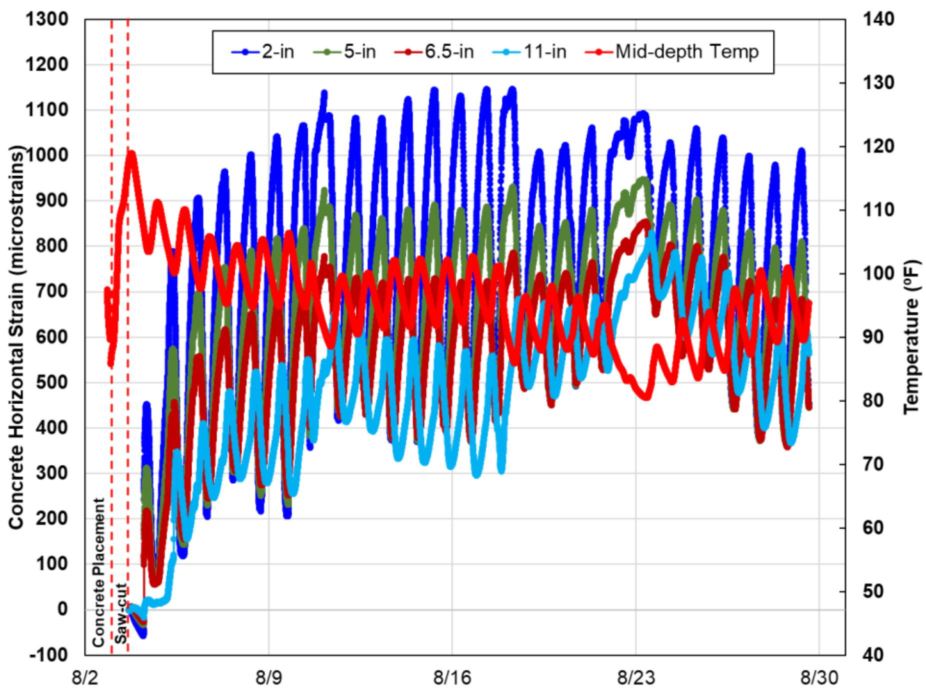

Figure 5.74 Longitudinal concrete strains at the mid-depth section in IH35E Hillsboro

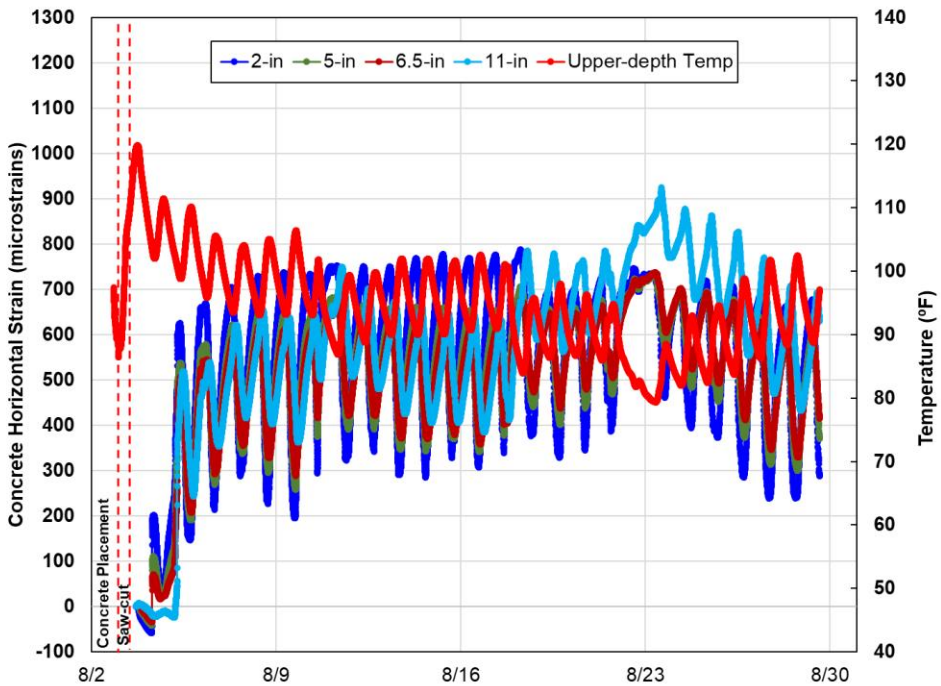

Figure 5.75 Longitudinal concrete strains at the upper-depth section in IH35E Hillsboro

When the longitudinal concrete strain data at the location of the steel is transformed to estimate the crack width at the instrumented section, the generated hysteresis loop presented in Figure 5.76 shows that, initially, the crack width are similar on the 7th day for both the mid-depth and upper depth section. However, as the temperature fell, the strain at the mid-depth section began to increase higher than the upper-depth section as shown in the 14th and 21st day. This indicates the effectiveness of the restraint provided by the reinforcement located at the upper depth section.

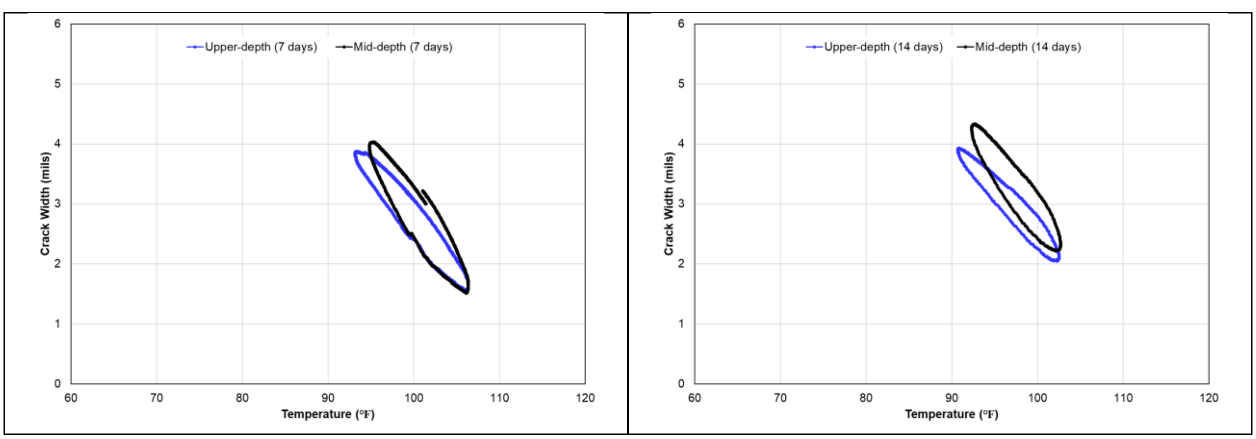

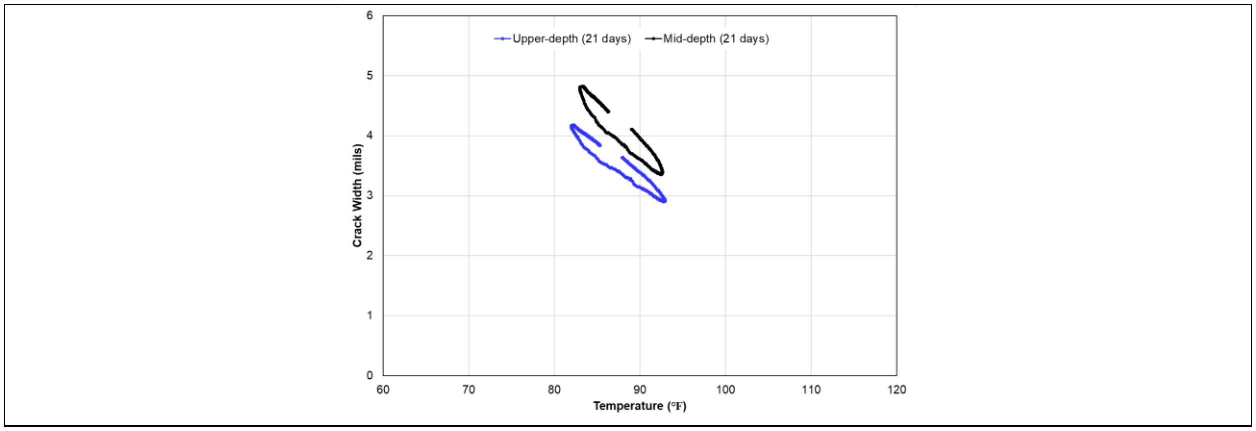

Figure 5.76 Crack width versus temperature of mid-depth and upper depth sections in IH35E Hillsboro

While looking at the vertical concrete strains shown in Figures 5.77 and 5.78, it can be observed that the vertical strains at the mid-depth section are generally higher than the upper-depth section. This finding is consistent with the vertical strain behaviors recorded during the previously instrumented sites. The paving direction is northbound, however, there is no correlation observed with the paving direction and the side of the transverse crack having the higher vertical strains.

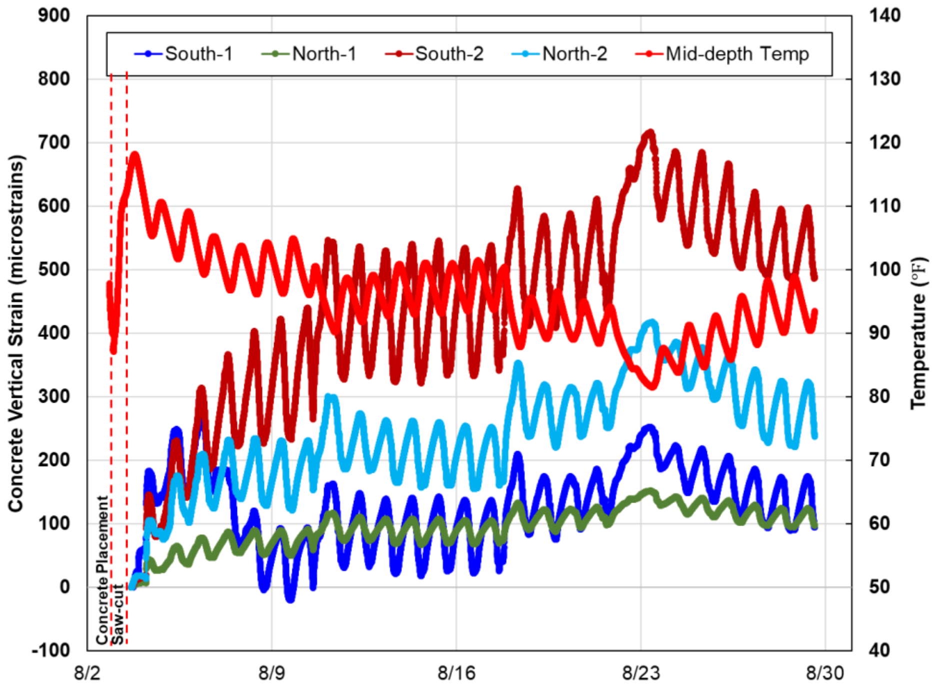

Figure 5.77 Vertical concrete strains at the mid-depth section in IH35E Hillsboro

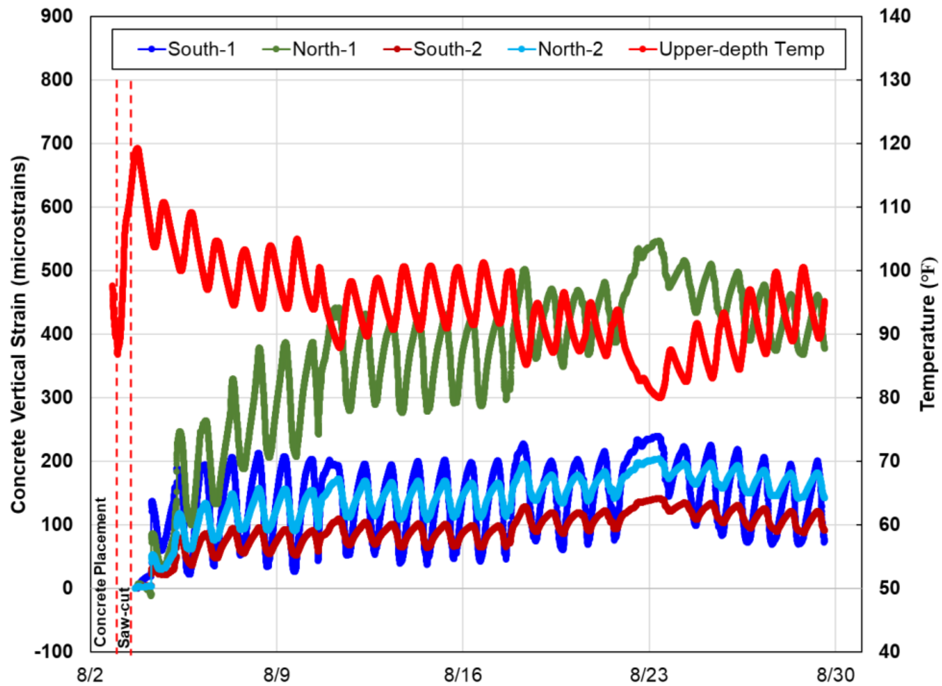

Figure 5.78 Vertical concrete strains at the upper-depth section in IH35E Hillsboro

When the vertical concrete strain versus temperature hysteresis loop is generated as shown in Figure 5.79, it can be observed that the vertical strains at the mid-depth section are higher than the upper-depth section at the same temperature. This comparison is consistent on both the north and south sides of the transverse crack. This pattern is also aligned with the findings in the previous test sections.

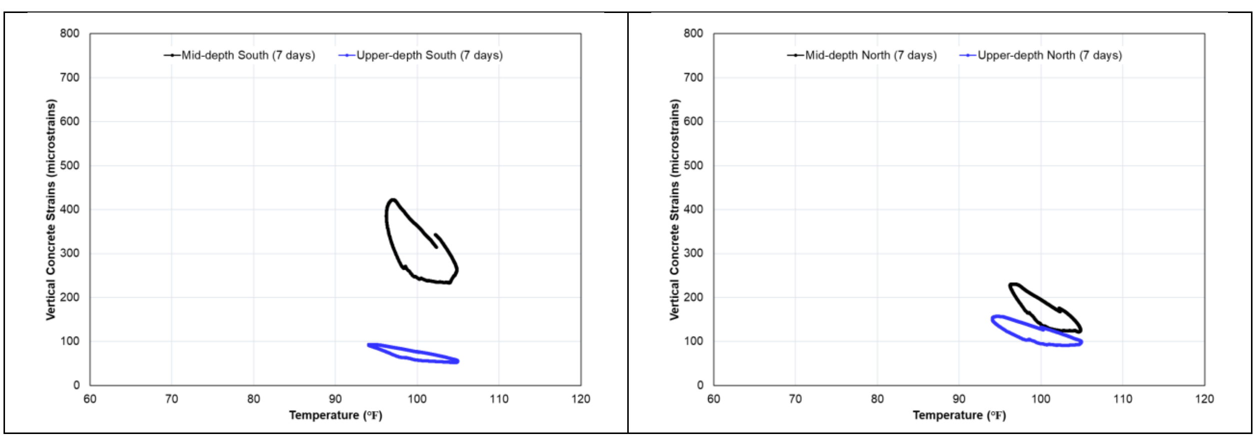

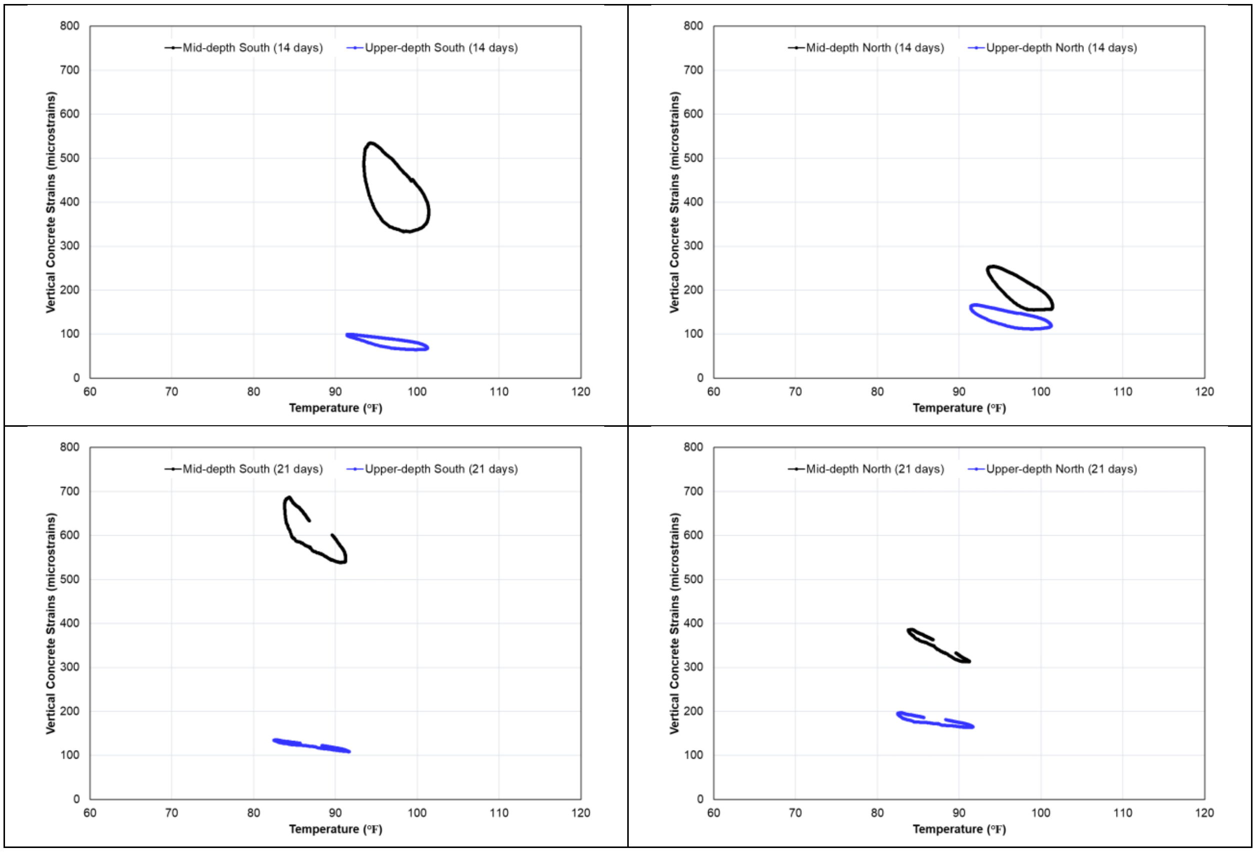

Figure 5.79 Vertical concrete strains versus temperature of mid-depth and upper depth sections in IH35E Hillsboro

5.5.d.4 Determination of In-situ Young's Modulus in Concrete Pavement

The concrete was poured at 11am on 09/06/2022 at STA 212+00. The dataloggers, other than D22020114, have reported data to the server up to six days after the concrete placement. Data obtained from the sensor can be transmitted through LTE network to the cloud using REBEL dataloggers, and the data can be accessed at http://103.177.0.196:997/wavelogix/login. The real-time data will be displayed on the database dashboard. The server data was cleared up due to service upgrading of website backend, so data were not available for the seventh day and later. Datalogger D22020114 (connected to sensor S121) stopped reporting data since the third day probably due to the battery issue. Datalogger D22020113 reported anormal data (excessive large value) which is likely due to the sensor connection failure. Other dataloggers successfully reported meaningful data. All the elastic modulus and temperature profile data were plotted in Figures 5.80 to 5.85. The elastic modulus of concrete on the 6th day is plotted in Figure 5.86. The mean value of elastic modulus of 4 sensors at 6^{th} day is 25.6 GPa, with standard deviation of 2.21 GPa and coefficient of variance (COV) of 8.6%, which is smaller than the acceptance range of field testing specified by ASTM C39 (*ASTM*). The compressive strength of concrete is calculated based on the mean value of modulus 25.6 GPa, and the result is 22.68 MPa, or 3300 psi on day six. As a reference, the cylinder break testing results on the 7th day were 4100 and 4200 psi for two separate cylinders. The sensor results fluctuate following daily temperature change, for example, in Figure 5.85, at 50 hr in both the modulus profile and the temperature profile there exists a peak. Such a phenomenon was not observed in laboratory testing. Possible explanations are 1) the concrete internal thermal stress causes the fluctuation 2) the sensor itself, either the epoxy layer or the piezoelectric layer is influenced by the temperature change.

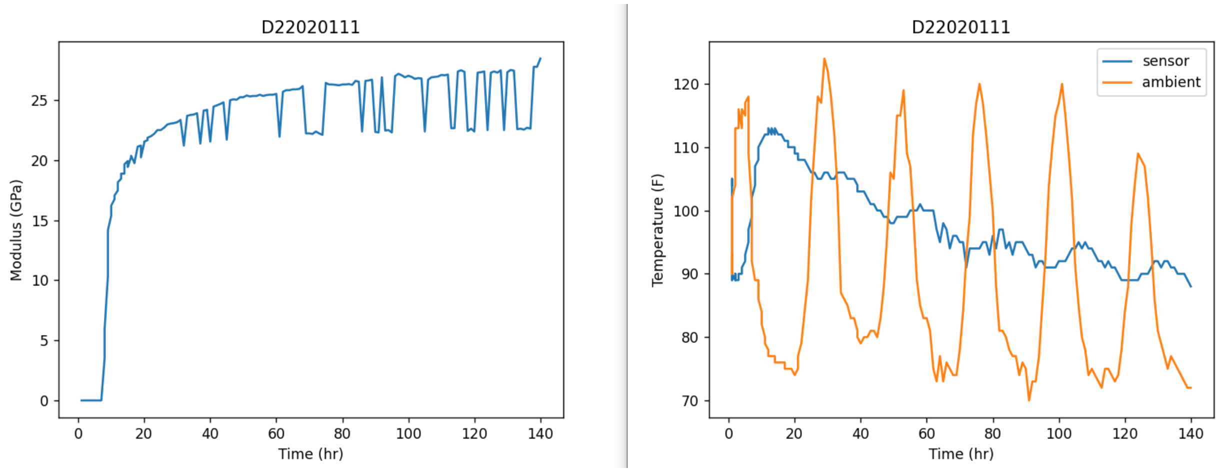

Figure 5.80 Young's modulus and temperature profile of D22020111 (S097, Ground)

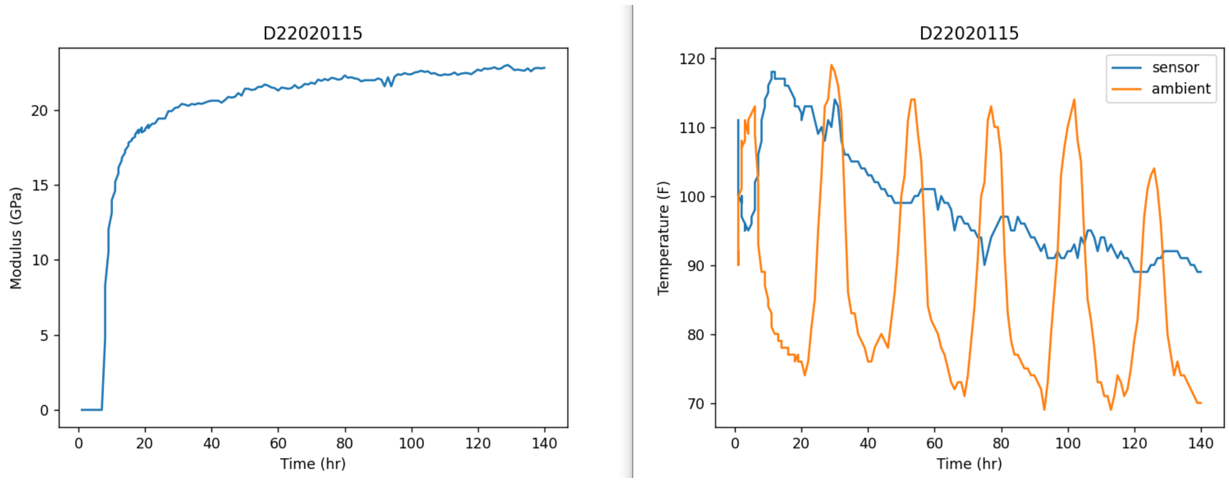

Figure 5.81 Young's modulus and temperature profile of D22020115 (S122, Ground)

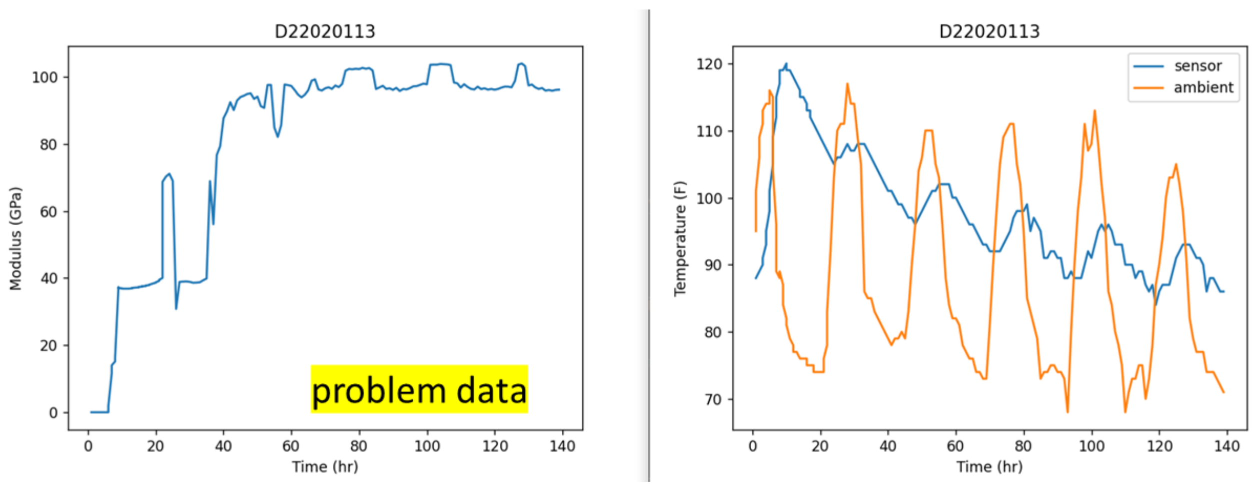

Figure 5.82 Young's modulus and temperature profile of D22020113 (S020, Middle)

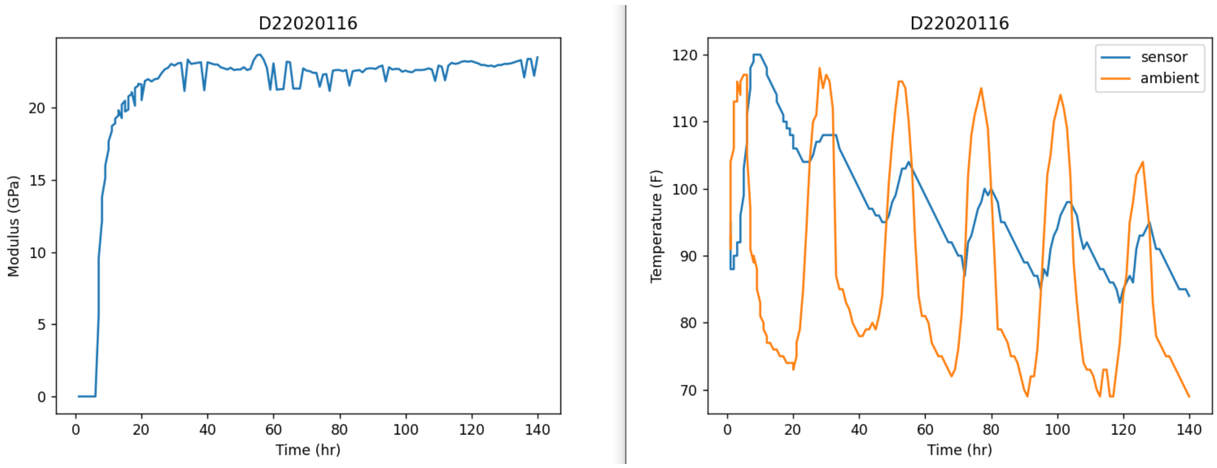

Figure 5.83 Young's modulus and temperature profile of D22020116 (S107, Middle)

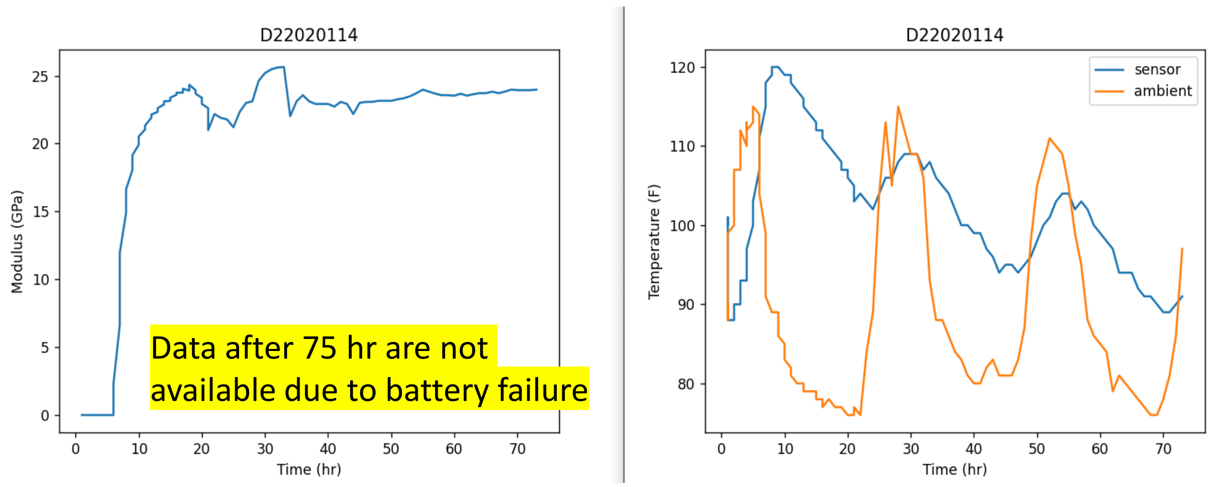

Figure 5.84 Young's modulus and temperature profile of D22020114 (S121, Top)

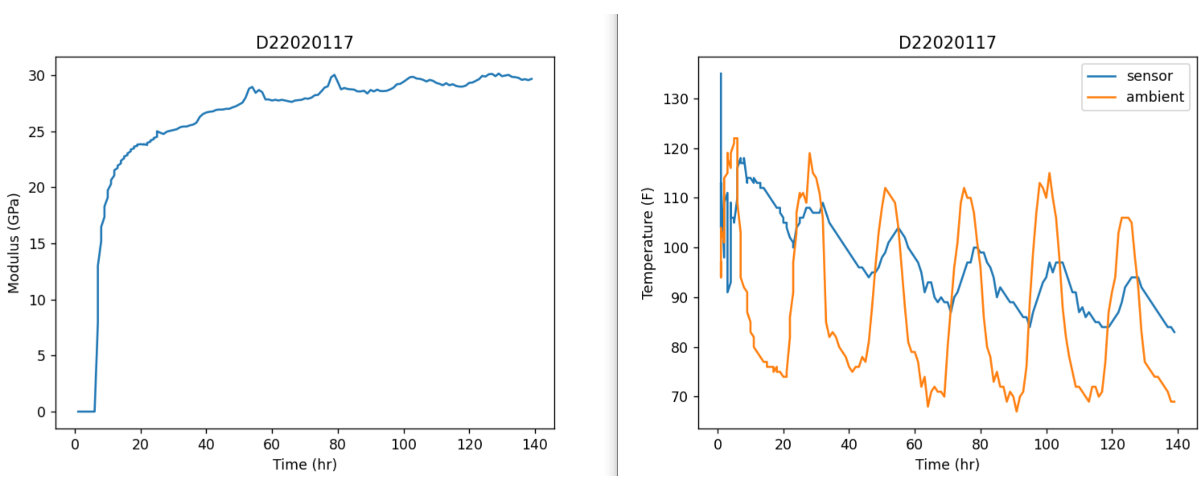

Figure 5.85 Young's modulus and temperature profile of D22020117 (S088, Top)

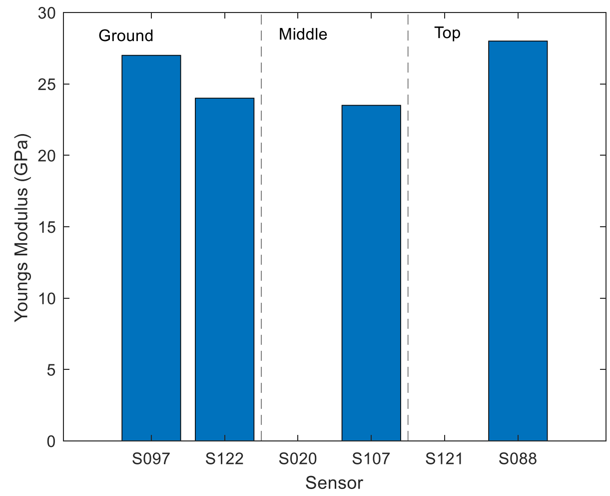

Figure 5.86 Young's modulus of sensors at 6th day

5.6 Transverse Crack Distribution in the Test Sections

The 2008 AASHTO manual recommended that the crack spacing shall be between 3 to 6 feet. However, due to its variability, the crack should be evaluated based on its average as well as the percentage of crack spacing then is beyond the recommended range. It was explained that longer or shorter cracking spacing can be indicative of the likelihood for distress within the pavement life. Although, it was also reported that crack spacing may not be an important CRCP behavior (Won & Medina, 2008).

Meanwhile, studies have shown that placing the reinforcement closer to the surface results in much tighter cracks and fewer punchouts due to shorter cracking interval (Won &Medina, 2008; ARA Inc, 2004). This has also been discussed in Chapter 4 of this report. When the reinforcing steel is placed closer to the surface, it will restrain concrete volume changes more effectively which will induce larger concrete stresses and develop more transverse cracking which results to shorter crack spacing. In order to verify this, the transverse cracks were investigated and compared across mid-depth, upper depth and upper depth low CoTE sections. In El Paso, crack surveys were conducted regularly, and the development of cracks was monitored in detail. In the Waxahachie test section, crack survey was conducted in January 2022 which 257 days from concrete placement. In the San Antonio test section, crack survey was conduct during the first week after concrete placement and another one was performed after 32 days from concrete placement.

Figures 5.87 to 5.90 show the crack maps of the El Paso, Waxahachie and San Antonio test sections, respectively. It can be observed in the El Paso test section that there were only few cracks that developed up to 57 days from concrete placement and a large number of additional cracks were observed after 109 days from concrete placement which is also the time when temperature is going down. However, after 462 days from concrete placement, it can be observed that more additional cracks have propagated at the upper-depth and upper-depth low CoTE sections as shown in Figure 5.88.

It can be observed that there are short-spaced cracks that developed near Sawcut #1. In one of the visual surveys, it was observed that these are reflective cracks that propagated from the manhole near Sawcut #1 as shown in Figure 5.91. The white and orange spray paint marks are cracks observed that went towards the manhole. This might have affected that resulting crack spacing at this segment.

Meanwhile, in the Waxahachie test section, it can be observed that more cracks have developed at Sawcuts #3, #4 and #5 which have upper-depth steel configuration compared to Sawcuts #1 and #2 which have mid-depth steel configurations. In the San Antonio test section, cracks developed during the first section 4 days from concrete placement where the longitudinal steel was placed at mid-depth. For the second section where longitudinal steel of the first half length was at mid-depth and the remaining segment was at the upper depth, cracks developed after 7-8 days from concrete placement while majority of the cracks developed at the third section wherein the longitudinal steel were installed at the upper depth were observed after 32 days from concrete placement.

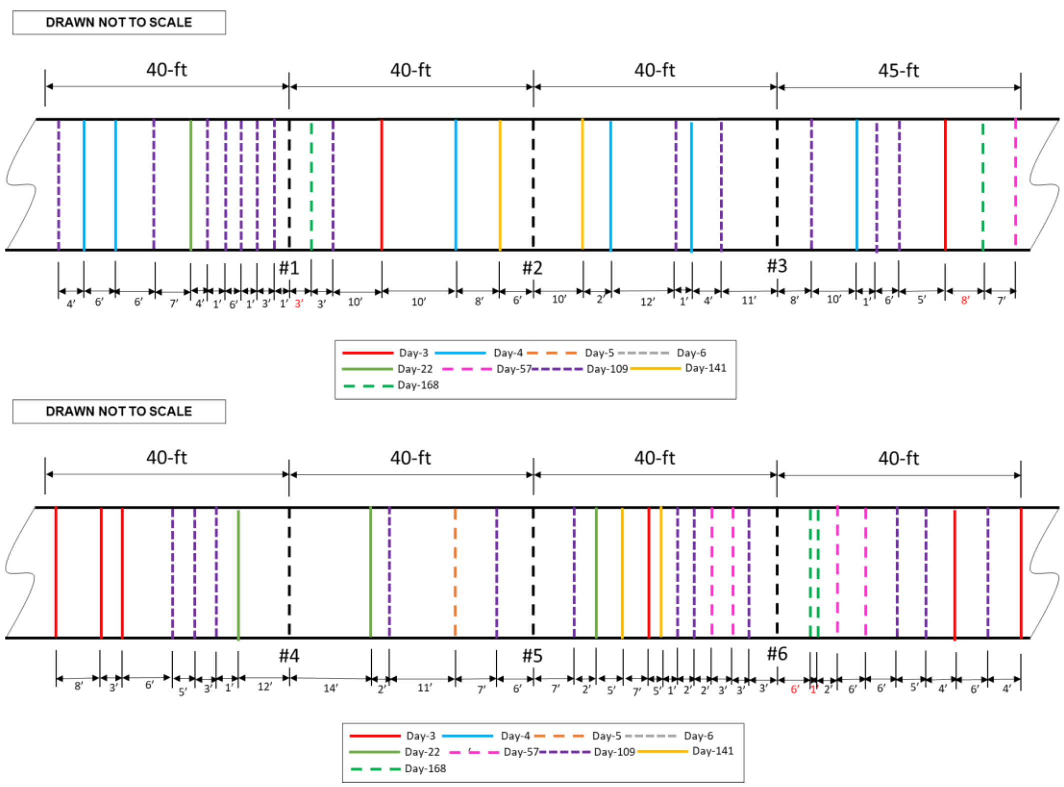

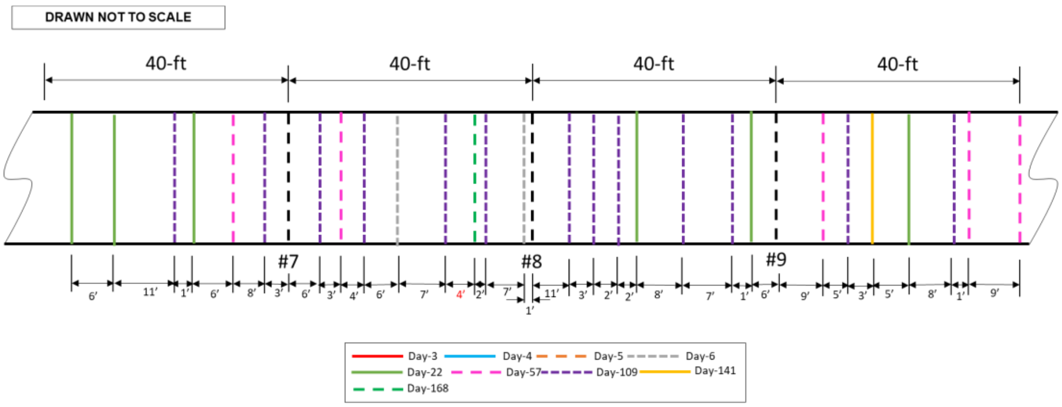

Figure 5.87 US62/180 El Paso test section crack map up to 168 days from concrete placement

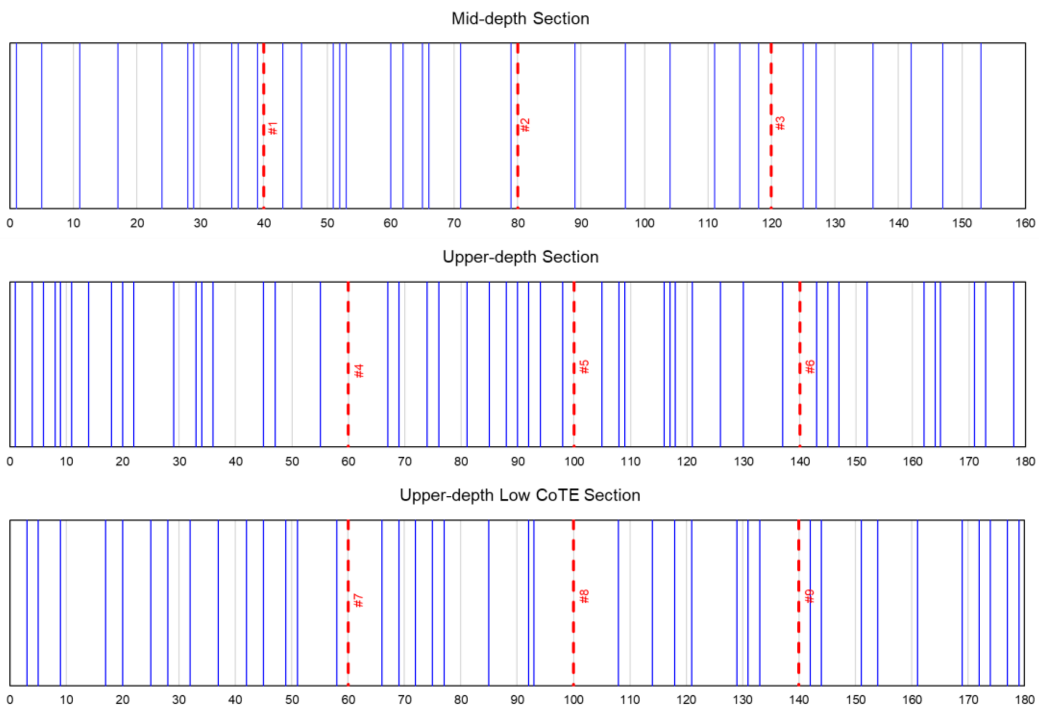

Figure 5.88 US62/180 El Paso test section crack map at 462 days from concrete placement

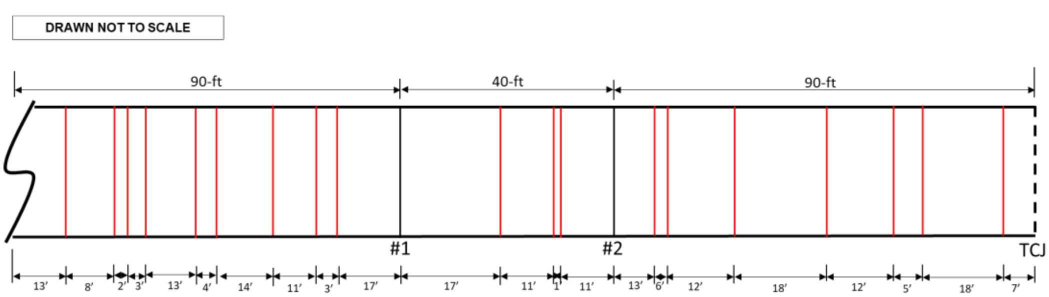

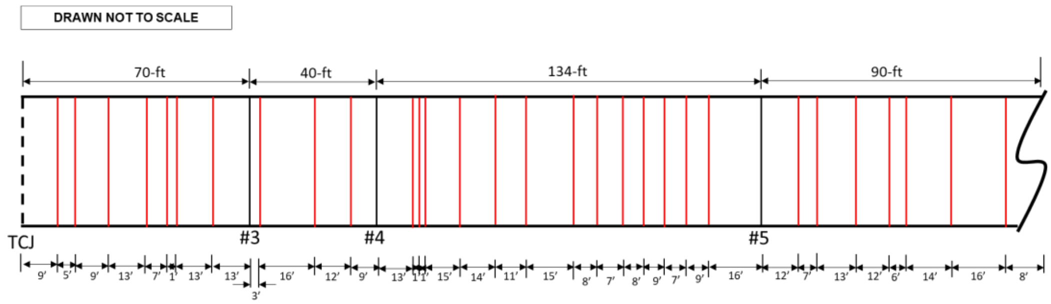

Figure 5.89 IH35 Waxahachie test section crack map at 257 days from concrete placement

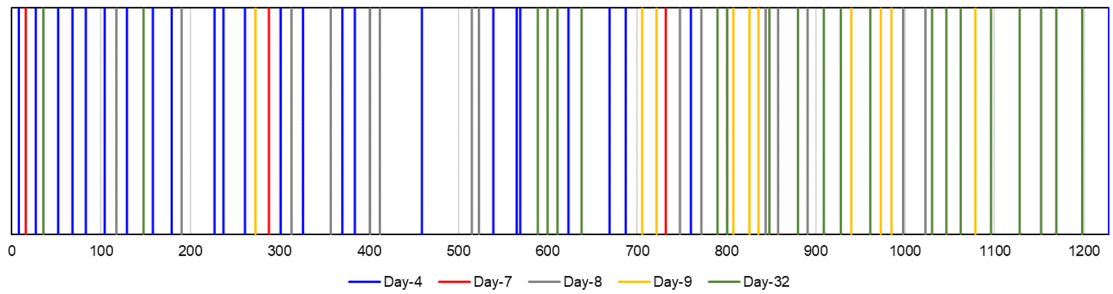

Day 1 Placement Segment

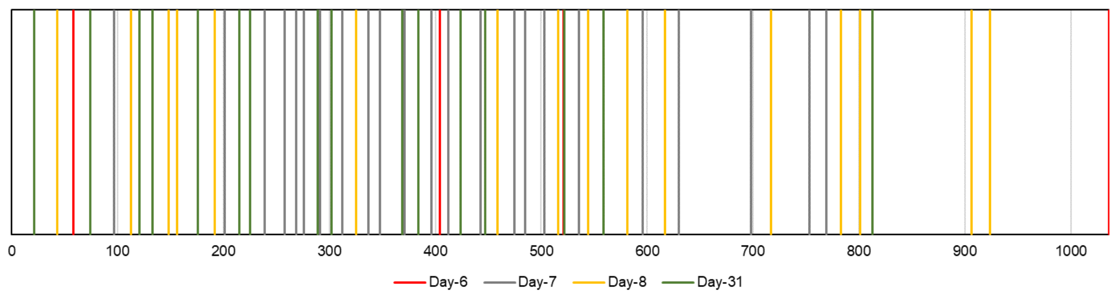

Day 2 Placement Segment

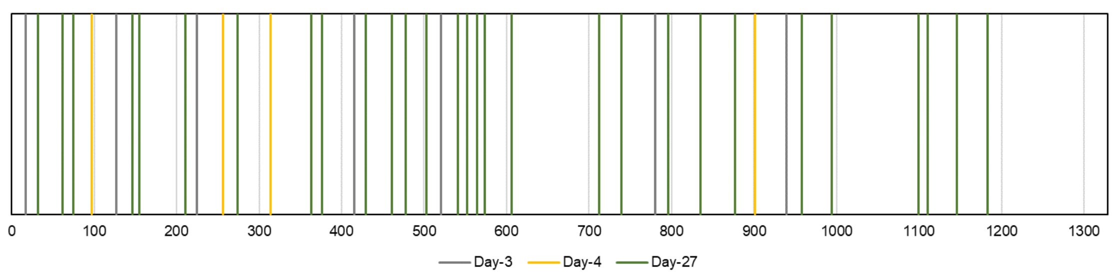

Day 3 Placement Segment

Figure 5.90 IH10 San Antonio test section crack map

Figure 5.91 Development of reflection cracking at SC #1 from the drainage manhole

In order to be able to compare the crack patterns in the mid-depth and upper-depth sections, crack spacing has been calculated. For El Paso mid-depth section, the crack spacing was calculated from Sawcut #1 up to the end of the mid-depth section. This is done to remove the effect of reflection cracks due to the manhole from the comparative analysis.

Figure 5.92 shows the crack spacing development over time in the El Paso test section. At the early age from concrete placement, it can be observed that the mid-depth section has shorter crack spacing compared to the upper-depth sections. However, after 50 days from concrete placement, the crack spacing at the mid-depth is higher compared to the upper-depth sections. At 168 days from concrete placement, the crack spacing across all three sections are relatively similar which may imply that placing the reinforcing steel close to the surface will induce more transverse cracks. But in the latest crack survey after 462 days, it can be seen that the crack spacing at the upper-depth sections are shorter than the mid-depth section. This pattern indicates that the continuous drying shrinkage in the slab coupled with temperature variations induce stresses in concrete and the upper-depth restraints generated additional transverse cracks.

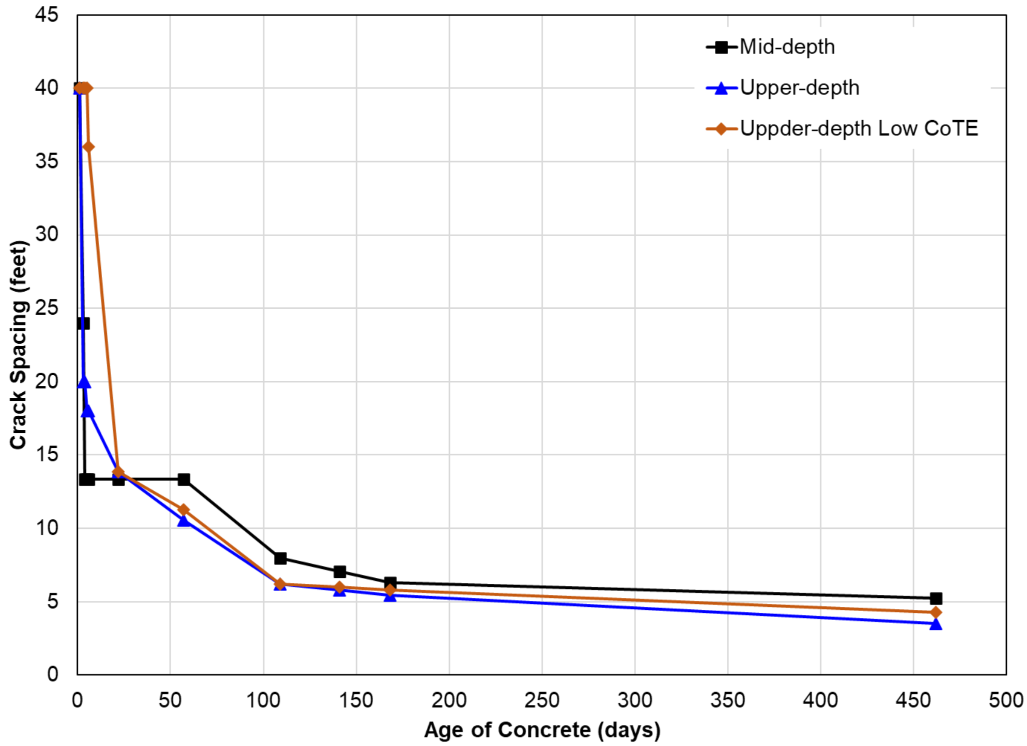

Figure 5.92 Crack spacing at mid-depth, upper-depth and upper-depth low CoTE sections with age of concrete in El Paso test section

In order to verify if the resulting crack spacings in the section indicate difference in behaviors, a t-test for two sample means with known variance has been performed to determine whether the crack spacings at mid-depth versus the upper-depth sections are different. The calculated average crack spacings are 5.14 feet, 3.49 feet and 4.18 feet having a standard deviation of 3.16 feet, 2.23 feet and 2.24 feet for mid-depth, upper-depth and upper-depth low CoTE sections, respectively. Results show that the crack spacing between mid-depth and upper-depth sections are different under a 95% confidence level. Meanwhile, the crack spacing between mid-depth and upper-depth low CoTE section is statistically the same.

Meanwhile, the average crack spacing in Waxahachie test section at 257 days in Table 5.7 shows that the cracking spacing is higher compared to the El Paso crack spacing. This might be attributed to the shorter length of the concrete segment in Waxahachie test section which generates lesser restraint compared to the El Paso test section resulting to longer crack spacing. Despite this condition, it can still be observed that the crack spacing at the upper depth is shorter compared to the mid-depth section.

Table 5.7 IH35 Waxahachie test section summary of average crack spacing at 257 days from concrete placement

Waxahachie Test Section	Length, ft.	No. of Cracks	Average Crack Interval, ft.
Mid-depth	160	14	11.43

Section 1 Mid-depth	120	10	12.00
Transition Zone	80	8	10.00
Section 2 Upper depth	120	13	9.23
Transition Zone	54	6	9.00
Section 3 Upper depth Low CoTE	120	11	10.91
Transition Zone	46	5	9.20
Mid-depth	317	27	11.74

In San Antonio test section as shown in Table 5.8, the average crack spacing at the mid-depth is lower than the average cracking spacing at the upper depth section. The age of concrete during the survey was 32 days and the crack interval may still change as the concrete ages.

Table 5.8 IH10 San Antonio test section summary of average crack spacing at 32 days from concrete placement

San Antonio Test Section	Length, ft.	No. of Cracks	Average Crack Interval, ft.
Day 1 Mid-depth	1230	73	16.85
Day 2 Mid-depth	521	39	13.36
Day 2 Upper depth	515	17	30.29
Day 3 Upper depth	1328	40	33.20

As part of the crack survey in San Antonio, the crack width was also investigated using the calibrated microscope as shown in Figure 5.93. This was conducted to obtain information on the early age crack width behavior between the mid-depth and upper-depth section. Results have shown in Figure 5.94 that the cracks have relatively higher width at the mid-depth test section compared to the upper-depth section even though the crack spacing at the mid-depth section is shorter than the upper-depth section as shown in Table 5.8. This implies that the upper-depth reinforcement may have kept the cracks tighter compared to the mid-depth section.

Figure 5.93 Investigation of crack widths in mid-depth and upper depth section in IH10 San Antonio

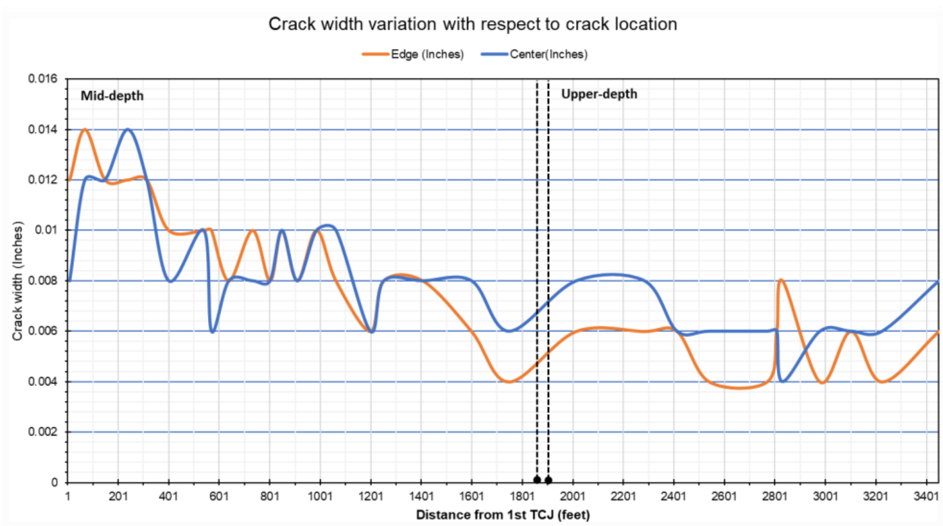

Figure 5.94 Crack width measurement at the mid-depth and upper-depth sections in IH10 San Antonio

5.7 Summary of Findings

Four test sections were included in the investigation namely: IH35 southbound in Waxahachie, US62/180 eastbound in El Paso, IH10 eastbound in San Antonio and IH35E in Hillsboro. Because of the sufficient long-term data in the El Paso test section, the report focused more on analyzing the data collected from El Paso while relevant information from Waxahachie, San

Antonio and Hillsboro were also used for comparison. From the analysis, the following are the findings of this report.

1. The daily temperature range at the surface of the slab is more than twice the range at the bottom of the slab.
2. The temperature at the surface of the slab is higher compared to the bottom of the slab from 12 noon until 6PM and vice versa for the rest of the hours.
3. The thermal gradient of the slab is nonlinear and the change of temperature with depth is significant above the mid-depth of the slab. The change in temperature from the mid-depth towards the bottom of the slab is minimal.
4. The steel strain variation at the mid-depth is lower than the upper depth due to the lower temperature variation. When the temperature went down, higher steel strain was recorded in the upper depth low CoTE section.
5. The transverse crack movement is higher at the mid-depth section when temperature went down on the 78th day (specifically in El Paso test section) which indicates that, when the concrete begins to contract due to cold weather, the transverse cracks begin to widen. However, when the longitudinal steel is located at the upper depth section, the movement is restrained generating lower crack movements compared to the mid-depth section.
6. For vertical strains, it was observed that the mid-depth section produces higher vertical strains than the upper depth sections. The restraint provided by the longitudinal steel located at the upper depth of the slab minimizes the vertical movement of the slab. Hence, the longitudinal steel located at the upper depth provides restraint at the location where volume changes in the slab is significant, thereby reducing the stress that may initiate horizontal cracking.
7. For longitudinal strains at various depths on the slab, it was observed that the mid-depth section is behaving in a typical curling and warping of the slab since the concrete strains at the surface of the slab is highest and moves inversely proportional with temperature. However, the concrete strain magnitude reduces as the depth increases towards the bottom of the slab. Meanwhile in the upper-depth section, the concrete strain magnitude is generally the same regardless of its depth in the slab which implies that the curling and warping behavior in the upper-depth section is restricted.
8. The long-term development of cracks shows that shorter intervals are evident in the mid-depth sections relative to the upper-depth section. This result implies that, when the steel is located above the mid-depth of the slab, the restraints caused by the reinforcement at the upper depth will increase the concrete stresses thereby developing closer spaced transverse cracks.

Chapter 6 Calibration of FEM Models and Development of Optimum Steel Design

6.1 Calibration of FEM Model

In this section, the mechanistic behavior of CRCP experimental sections will be analyzed with 3-dimensional finite element modeling. Most reasonable stiffness values for interface elements between steel and concrete will be determined from input and output (strains steel) obtained in the field experiment. This aims to investigate the degree of effectiveness the finite element modeling can simulate the actual pavement behavior, more specifically stresses and strains in concrete and longitudinal steel. The input values needed and obtained for the analyses – concrete material properties such as modulus, coefficient of thermal expansion, and steel properties as well as concrete temperatures – which are quite accurate, since all of them have been obtained during the field experiments. However, in modeling, the stiffness of interface elements between concrete and steel significantly affect the concrete stresses near longitudinal steel, but these values required assumptions that are difficult to be validated in the field conditions. Certain values have been suggested by previous research for the stiffness of interface elements in the analyses of reinforced concrete members. Those suggested values will be used for the analyses and the predicted CRCP behavior in terms of concrete and steel strains will be compared with actual values obtained in the field experiments. If predicted values from the analyses are close to those measured, the stiffness values used for the interface elements will be utilized for the succeeding simulations. If not, different levels of stiffness values will be used for the interface elements, and a value that yields structural responses most close to those measured in the field experiments will be utilized in the succeeding simulations to determine optimum steel designs. All the numerical modeling were conducted with the ANSYS simulation software through the high-performance computer.

6.1.a Development of CRCP Modelling

6.1.a.1 Effect of the Number of Slabs

To investigate the accuracy of the numerical results, several steel strain data points from the field experiment was selected, which were measured by strain gages. The numerical study was done exactly with the slab dimensions and all the input properties such as, temperature gradient through the slab depth, and the zero-stress temperature accordance with the data from the field experiment. The material which is assumed to be linear elastic have properties as follows: (1) the elastic modulus, coefficient of thermal expansion, and Poisson’s ratio of concrete are 5×10^{6} psi, 5.5×10^{-6} microstrain/°F, and 0.15, respectively; (2) the elastic modulus, coefficient of thermal expansion, and Poisson’s ratio of steel are 29×10^{6} psi, 6.4×10^{-6} microstrain/°F, and 0.3, respectively; and (3) the modulus of subgrade reaction is 300 psi/in.

To reduce the runtime of the analysis, a symmetric nature of CRCP slab was utilized which is similar to the modeling approach used in Chapter 4. Also, since the pavement from the field experiment focuses on environmental loading only, the modeling therefore covers on the environmental loading only. Strain gages are installed at the top of the reinforcement rebars at the location of the transverse crack in the field, therefore, the steel strain amount in the numerical modeling result is tagged at the location, where the mentioned strain gage was installed.

Six different strain values with different steel depth and slab lengths were considered for FEM calibration. The field conditions are collected in Table 6.1 for the FEM simulation.

Table 6.1 Field conditions for the FEM simulation

Steel Location	Case No.	Slab length (ft.) Far West	West	East	Far East	ZST (°F)	Slab thickness (in.)	Steel depth (in.)	Steel spacing (in.)
Mid-depth	Case 1	10	14	12	13	115	12	6	6
	Case 2	13	15	8	10	115	12	6	6
Upper depth	Case 3	15	12	14	13	110	12	4.5	6
	Case 4	13	13	9	12	110	12	4.5	6
Upper depth-Low CoTE	Case 5	6	11	9	10	110	12	4.5	6.5
	Case 6	16	6	9	13	110	12	4.5	6.5

The temperature condition for the modeling considered to be the temperature at 3 PM and 6 AM of September 30, 2021. Since the temperature data from the field was not taken exactly at top and bottom of the slab, the temperature data for top and bottom of the slab was predicted with regression using Excel and are shown in dotted lines in Figure 6.1.

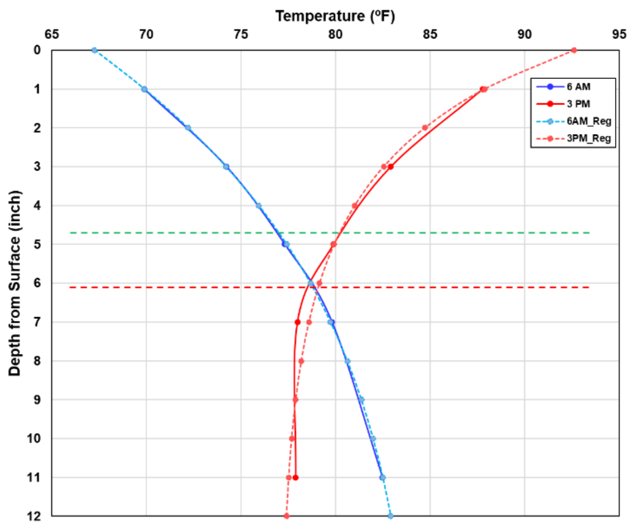

Figure 6.1 Temperature condition for simulation

Figure 6.2 illustrates the finite element mesh model. Twenty-node solid brick elements were used in the mesh representation of concrete and steel. For consistency, equal-sized elements were allocated to the concrete around longitudinal steel. A modulus of subgrade reaction was modeled with a spring element. Elastic supports allow to model the stiffness effects of a distributed support on a surface without specifying actual modeling details of the support.

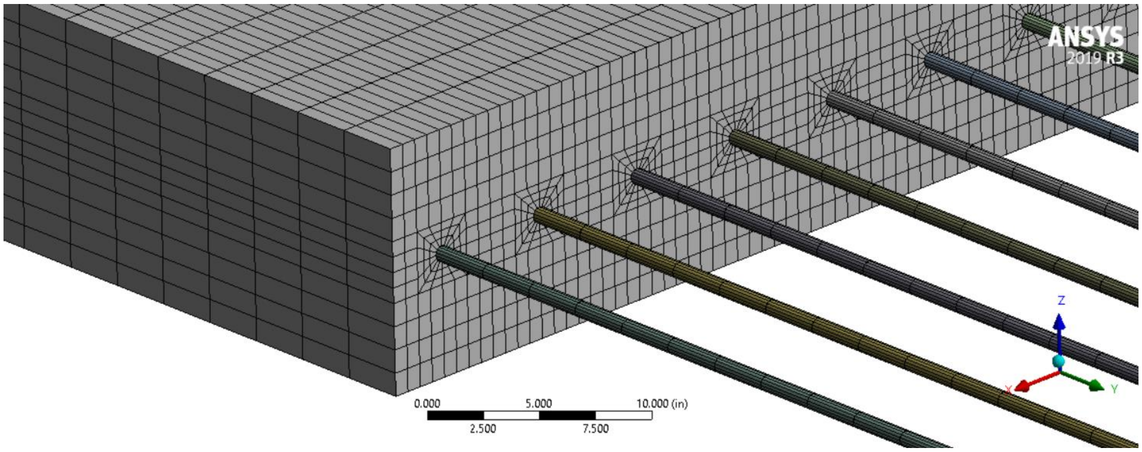

Figure 6.2 Mesh

To validate the finite element modeling to make sure that a higher number of slabs is not needed, three different conditions were created and results of these three models were compared in modeling the case 1, for 3 PM temperature. Figure 6.3 (a; b; c) is showing the three different conditions, which the Figure 6.3 (a) is showing the condition where one whole slab is modeled at east and at west side of the desire transverse crack, which we are going to predict the steel strain. The length of the slabs on the west and east side of the transverse crack are 14 and 12 feet, respectively. The free edges are considered for the boundary conditions, which is conservative for this analysis. Figure 6.3 (b) is showing the second model, which half of the slab on the west and east side of the transverse crack is modeled and the symmetric option is used, therefore, the length of the slabs on the west and east side of the crack are 7 and 6 sinches, respectively. Figure 6.3 (c) is showing the third model, which 2 slabs at west and 2 slabs at east side of the transverse crack are modeled; the far east and far west slabs were used the symmetric option; therefore, half of the slabs were modeled in longitudinal direction, i.e., instead of 10- and 13-feet slabs, 5- and 6.5-feet slabs were modeled with considering the symmetric conditions at the end of the slabs. The condition between rebars and concrete in Figure 6.3 and 6.4 is bonded.

Figure 6.4 (a; b; c) shows the steel strain results considering the unique condition of the field condition. The results show that the first and the second model are giving the exact same results and the result from the third model, considering the extra slabs in far west and far east are getting a slightly smaller steel strain.

The results indicate that considering only one slab on east and one slab on west side of the desired transverse crack is quite satisfactory, since the running time of the model with four slabs are almost 5 times of the other models.

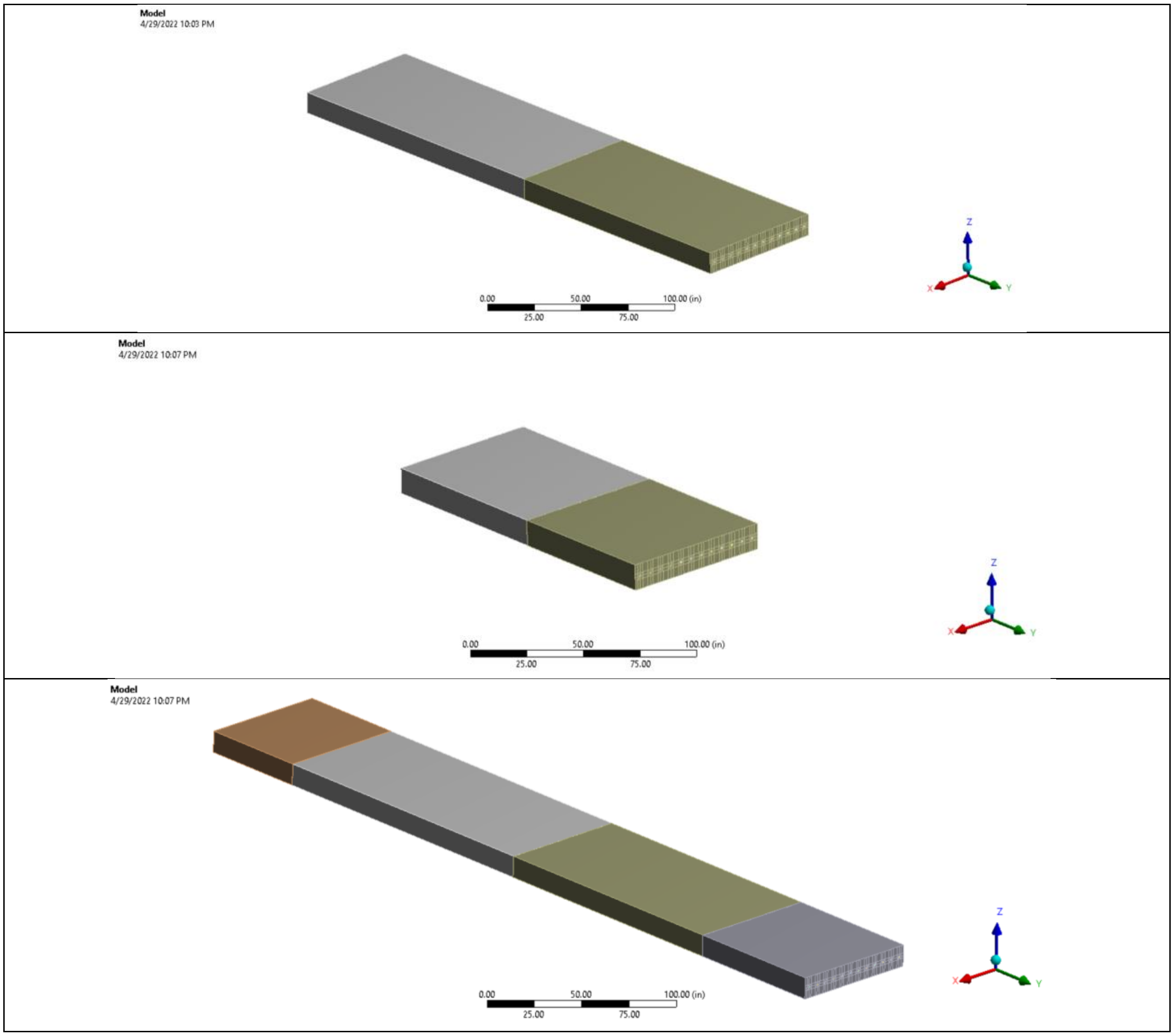

Figure 6.3 Geometry of a) Model with one whole slab on east and west side of the transverse crack; b) Model with one half slab on east and west side of the transverse crack; c) Model with two slabs on east and two slabs on west side of the transverse crack

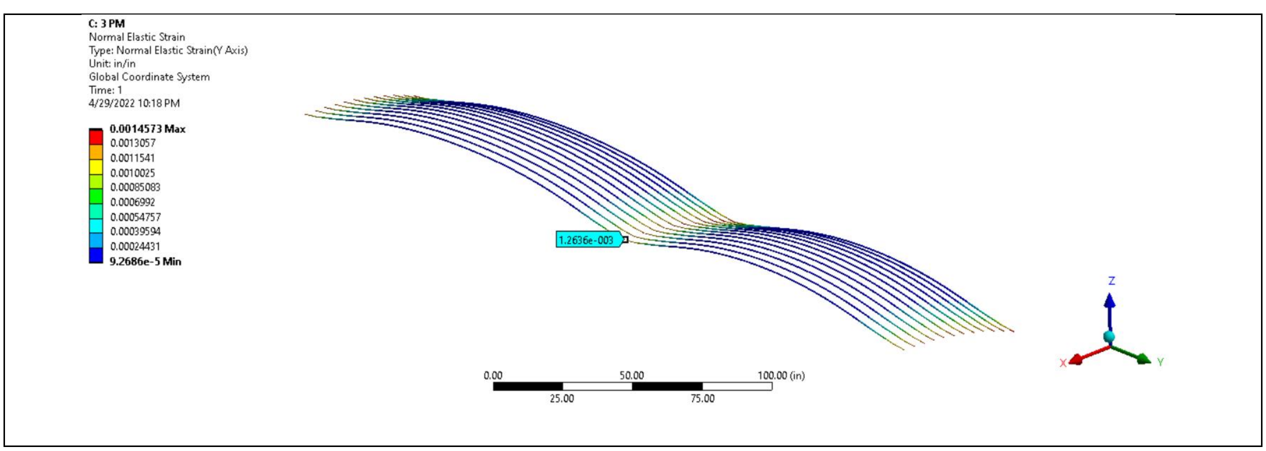

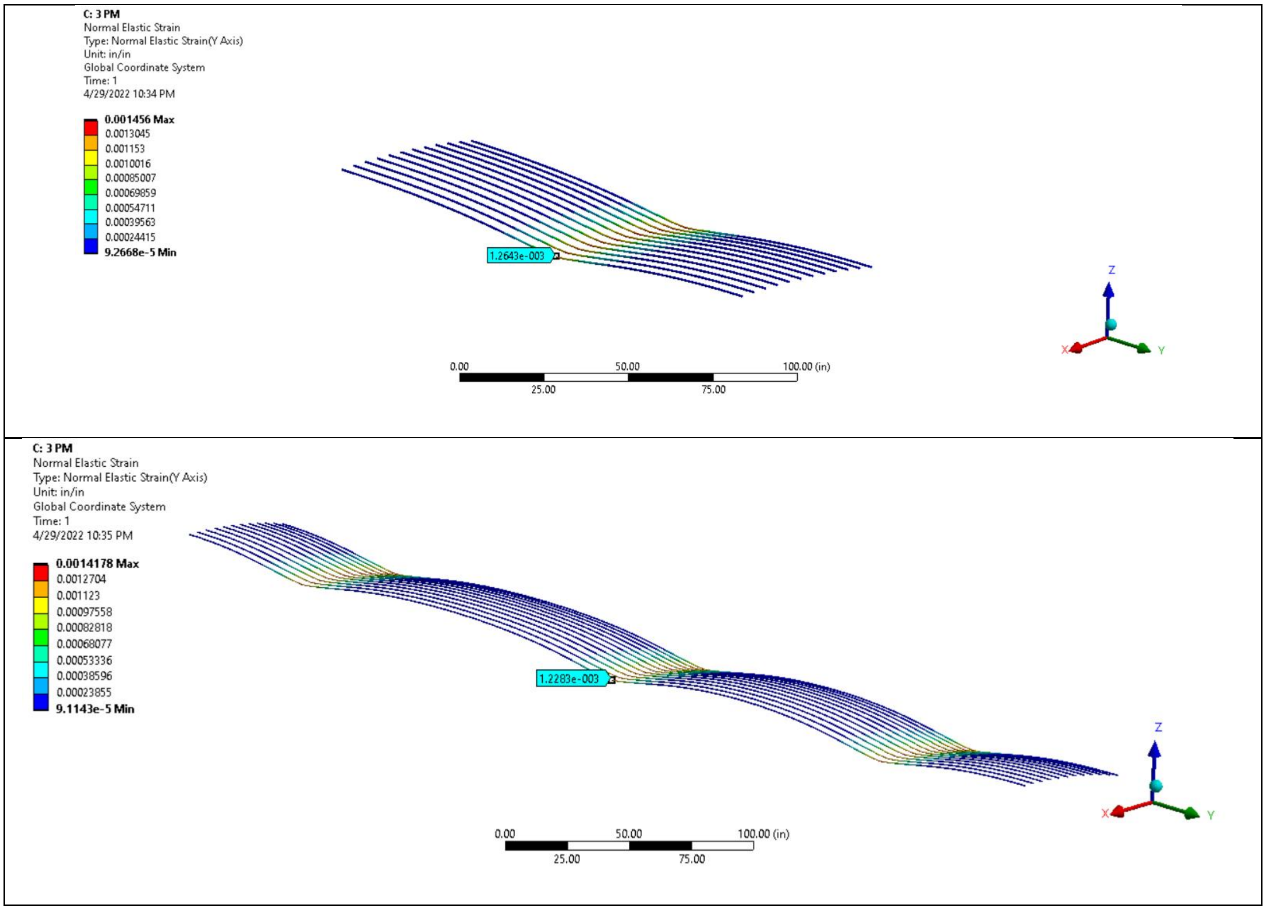

Figure 6.4 Steel strain results from a) Model with one whole slab on east and west side of the transverse crack; b) Model with one half slab on east and west side of the transverse crack; c) Model with two slabs on east and two slabs on west side of the transverse

6.1.a.2 Effect of Bond-Slip Modelling

Interactions between concrete and steel are considered a critical part in CRCP modelling because it is mostly the stress transfer between concrete and steel that causes high levels of concrete stresses and transverse cracks. The relationship between bond slip and bond stress as shown in Figure 6.5 has been used in reinforced concrete modeling. This assumption is also similar to that in Chapter 4 following the same reasoning.

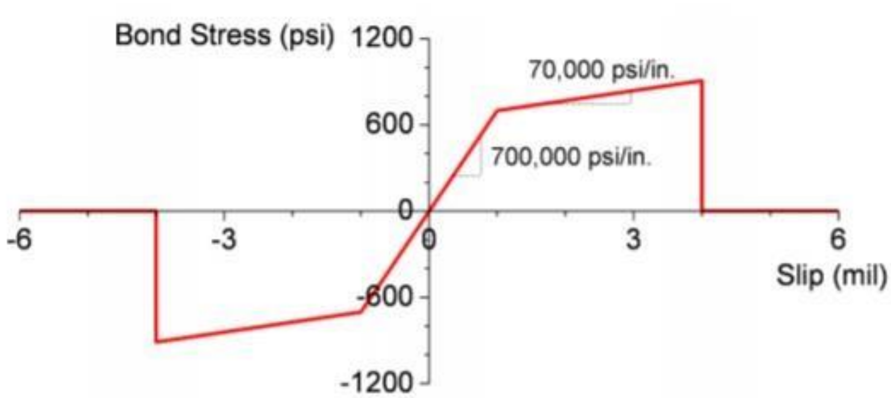

Figure 6.5 Bond-slip #1 behavior between concrete and longitudinal steel

The numerical modeling for all 6 cases was done considering the bond-slip model from Figure 6.5 and also with considering the fully bonded condition. The results are collected in Table 6.2 for both 3 PM and 6 AM temperature conditions.

Table 6.2 Comparison between bond-slip #1 and bonded conditions

		Case 1		Case 2		Case 3		Case 4		Case 5		Case 6	
Time		3:00 PM	6:00 AM	3:00 PM	6:00 AM	3:00 PM	6:00 AM	3:00 PM	6:00 AM	3:00 PM	6:00 AM	3:00 PM	6:00 AM
Field		865	1270	626	1038	690	837	582	1192	687	1410	588	1232
FEM	Bonded	1159	1378	1264	1506	1003	1309	1420	1532	649	891	802	1097
	Bond-slip #1	238	268	225	255	215	266	240	269	182	227	183	234

The results in Table 6.2 indicate that the bond-slip modeling, which is shown in Figure 6.5 is not giving an accurate result and a new bond-slip that gives the results closer to the field results is needed. After several trial and error, the bond-slip modeling shown in Figure 6.6 were chosen.

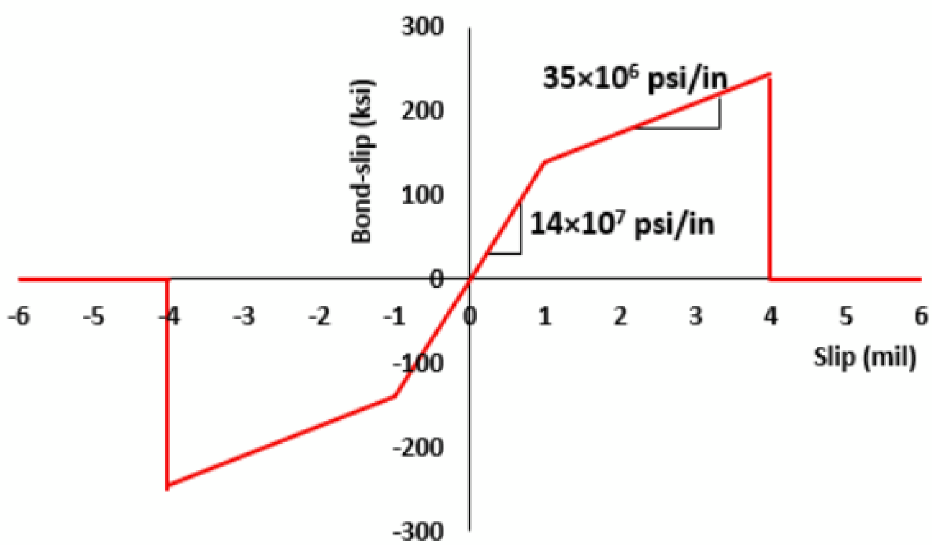

Figure 6.6 Bond-slip #2 behavior between concrete and longitudinal steel

The results from all the case studies with different bond-slip models are collected in Table 6.3.

Table 6.3 Comparison between bond-slip #1, bond-slip #2 and bonded conditions

		Case 1		Case 2		Case 3		Case 4		Case 5		Case 6	
Time		3:00 PM	6:00 AM	3:00 PM	6:00 AM	3:00 PM	6:00 AM	3:00 PM	6:00 AM	3:00 PM	6:00 AM	3:00 PM	6:00 AM
Field		865	1270	626	1038	690	837	582	1192	687	1410	588	1232
FEM	Bonded	1159	1378	1264	1506	1003	1309	1420	1532	649	891	802	1097
	Bond-slip#1	238	268	225	255	215	266	240	269	182	227	183	234
	Bond Slip#2	696	825	762	906	618	803	835	934	385	526	485	662

According to the results shown in Table 6.3, the bonded condition between rebars and concrete gives us the closest results to the field data. Therefore, the bonded behavior between rebars and concrete was selected for future FEM modeling.

6.2 Factorial Experiment

The mechanistic behavior of CRCP experimental sections with various slab thicknesses was analyzed using a 3D finite element model. In this analyses, two slabs with length of 40 ft were used and the symmetric condition was used to model the half of the lengths to reduce the running time, and the analysis was conducted in accordance with the following factorial experiment as shown in Table 6.4. Concrete vertical tensile stresses around the reinforcement at transverse crack area between the two concrete slabs were measured, which is a good indicator of horizontal cracking. To consider the worst temperature loading, the concrete temperature values from El Paso and San Antonio field testing were compared and the temperature gradient with the highest temperature difference between top and bottom of the CRCP was selected for this analysis, which is shown in Figure 6.7. This temperature gradient was modified for the CRCP models with different thicknesses.

Table 6.4 Factorial experiment for Mechanistic Analyses

Input variables	**Values**
Slab thickness [in]	11, 12, 13, 14, 15
Longitudinal steel ratio and bar size	Per TxDOT CRCP Design Standards
CoTE [in/in/°F]	3.5, 4.5, 5.5
Concrete modulus [$\times 10^6$ psi]	3.0, 5.0
Temperature drops from Zero Stress Temperature (ZST) to the middle of slab's temperature (°F)	40, 60
Longitudinal steel depths for 11-in CRCP (in)	2.5, 4.0, 5.5
Longitudinal steel depths for 12-in CRCP (in)	3.0, 4.5, 6.0
Longitudinal steel depths for 13-in CRCP (in)	3.5, 5.0, 6.5
Longitudinal steel depths for 14-in and 15-in two-mat CRCP (in)	Per TxDOT CRCP Design Standards
Slab length (ft)	40

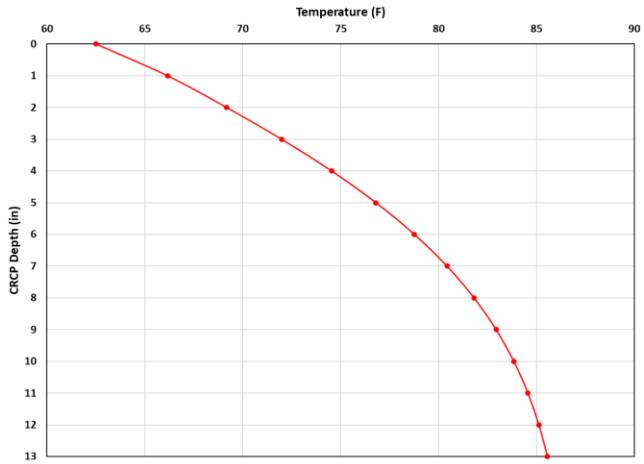

Figure 6.7 Temperature through the CRCP depth

6.3 Analysis of CRCP Behavior

The current reinforcement depth according to the TxDOT CRCP standard design for one-mat design is mid-depth. For this analysis, two other depths were considered with 1.5-in and 3-in reduction for the depth. The aim of this analysis is to determine the effect of steel depth on CRCP with various thicknesses, although some depths used in this analysis are not practical in CRCP construction. The number of total FEM analysis for this section was 132, and the results are shown in Figure 6.8 to Figure 6.12. This vertical tensile stress in these graphs could be a good factor to predict the possibility of horizontal cracking at the reinforcement depth in CRCP. The higher vertical stress has the higher possibility of horizontal cracking. Although these values are not meant to be considered as exact values and their trend is our interest. In these graphs, the lines corresponding to the elastic modulus of 3×10^6 psi and 5×10^6 psi are shown with the solid lines and dotted lines, respectively.

Figure 6.8 shows the effect of longitudinal reinforcement depth on concrete vertical tensile stresses around the reinforcement at transverse crack area for 11-in CRCP with two different temperature drops of 40 °F and 60 °F. The results show that higher elastic modulus values increase the probability of horizontal cracking significantly. Here, the stress values with elastic modulus of 5×10^6 psi are almost twice of the stress values with 3×10^6 psi, however, this probably won't be a problem is CRCP since the transverse cracking happens at early ages of CRCP and the modulus of elasticity of concrete is lower at early ages, and during the time there will be more transverse cracks and smaller crack spacing, which results in lower concrete stresses. Higher CoTE values also increase the concrete stress. Temperature drop is one of the other factors that affect stress values substantially. In this analysis, with a 20°F increase in the temperature drop (40 °F to 60 °F), the vertical tensile stresses almost doubled, and the possibility of horizontal cracking gets higher significantly. According to the results, placing the longitudinal rebars closer to the concrete surface decreases the concrete stresses and the risk of horizontal cracking as well. Figure 6.9 to Figure 6.12 show the exact same findings for 12-in and 13-in one-mat CRCP.

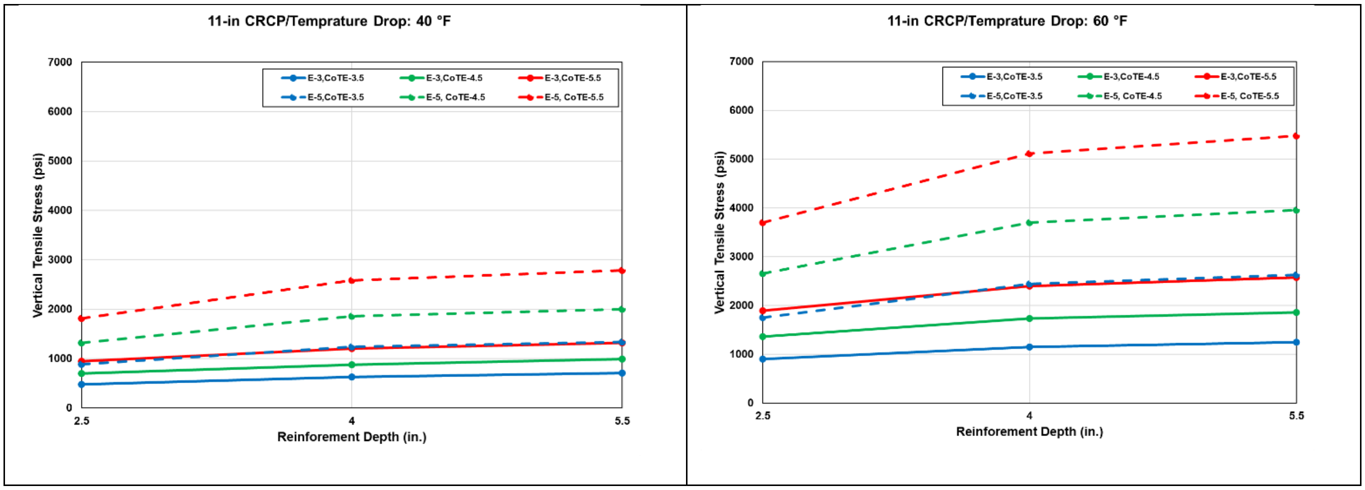

Figure 6.8 Effect of longitudinal reinforcement depth on concrete vertical tensile stress at transverse crack area around the reinforcement for 11-in CRCP for 40 °F and 60 °F temperature drops

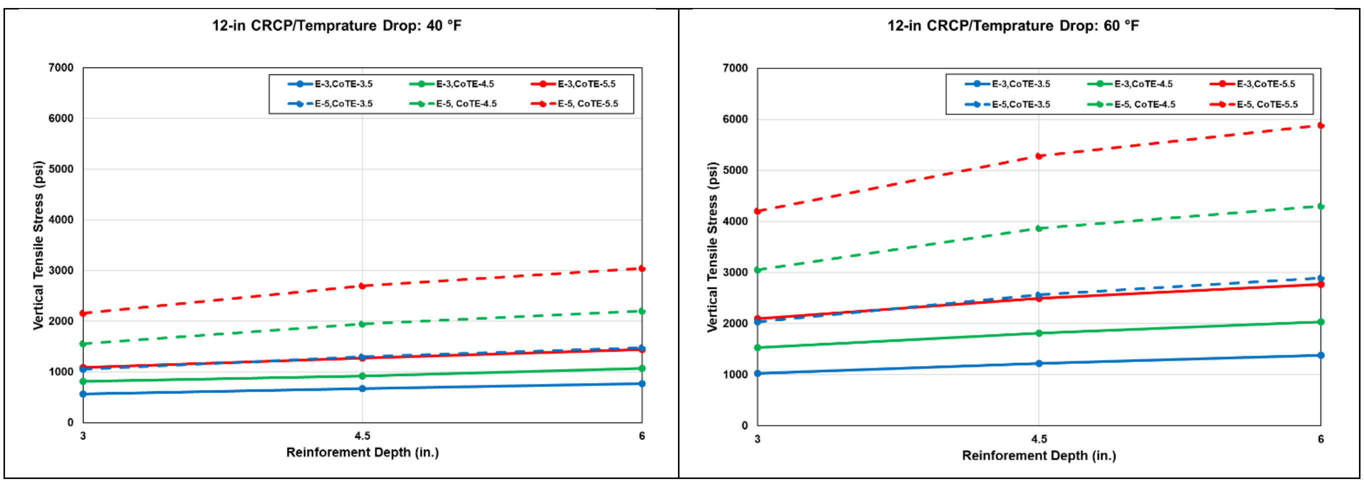

Figure 6.9 Effect of longitudinal reinforcement depth on concrete vertical tensile stress at transverse crack area around the reinforcement for 12-in CRCP for 40 °F and 60 °F temperature drops

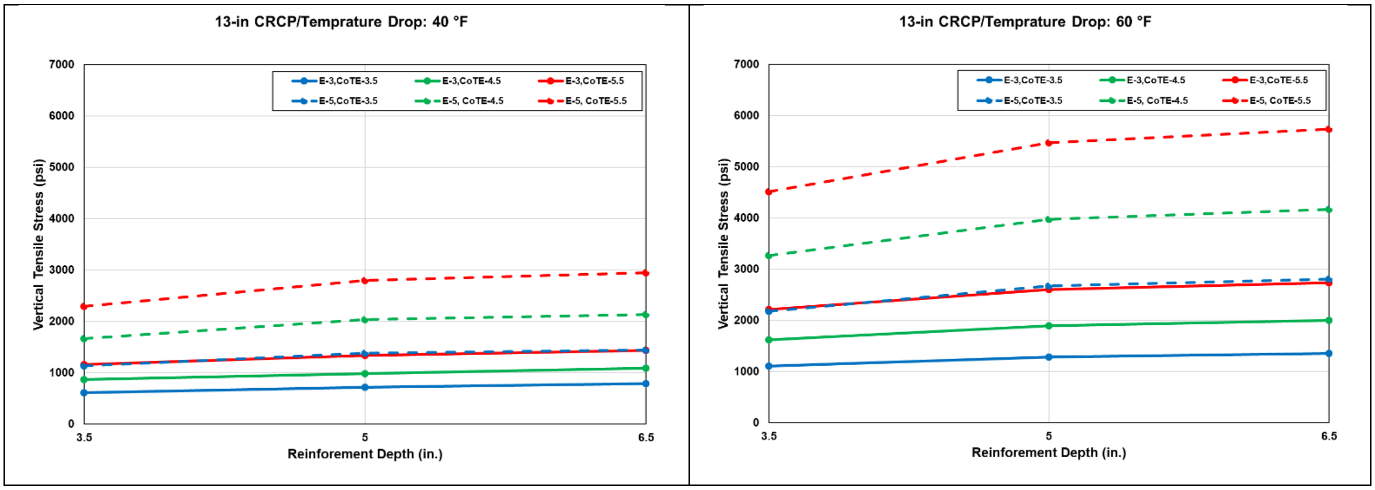

Figure 6.10 Effect of longitudinal reinforcement depth on concrete vertical tensile stress at transverse crack area around the reinforcement for 13-in CRCP for 40 °F and 60 °F temperature drops

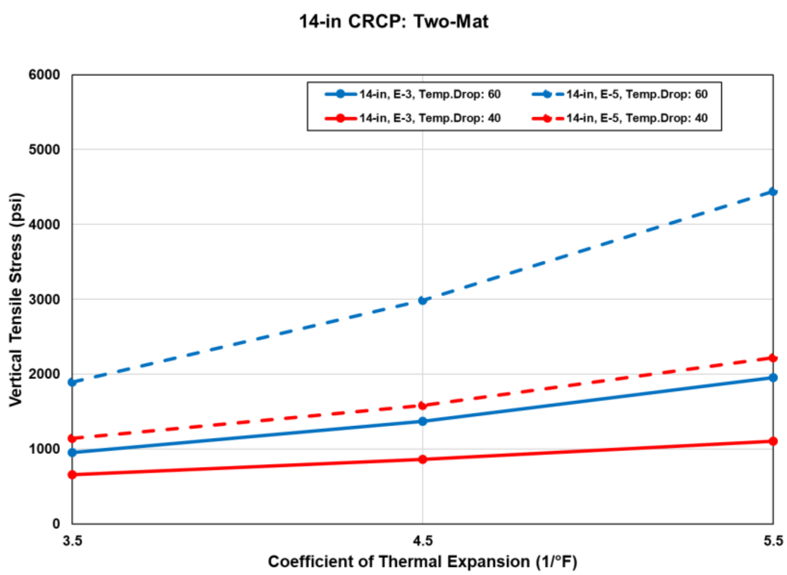

Figure 6.11 Effect of longitudinal reinforcement depth on concrete vertical tensile stress at transverse crack area around the reinforcement for 14-in two-mat CRCP for 40 °F and 60 °F temperature drops

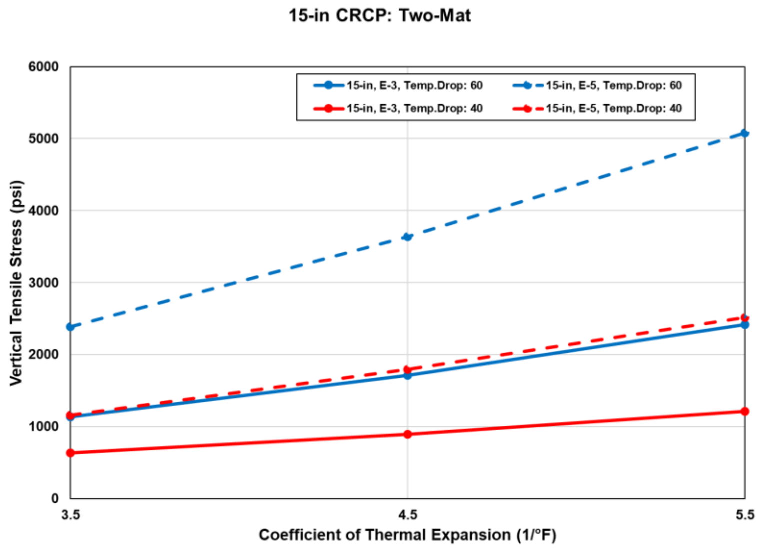

Figure 6.12 Effect of longitudinal reinforcement depth on concrete vertical tensile stress at transverse crack area around the reinforcement for 15-in two-mat CRCP for 40 °F and 60 °F temperature drops

Figure 6.13 shows the comparison of concrete vertical stresses for different CRCP thicknesses with various steel depths for elastic modulus of 3×10^6 psi and 40 °F temperature drop. The X axis values show the steel depth in CRCP. For 11-in, 12-in, and 13-in CRCP since one-mat design is applied, there is only one value for the steel depth. However, for 14-in and 15-in CRCP considering the two-mat design, two values are shown for the steel depth, which are shown in parenthesis. The first number in parentheses is the depth of the top mat, which is closer to the top concrete surface, and the second number in parentheses is the depth of the bottom mat and is closer to the bottom of the concrete slab.

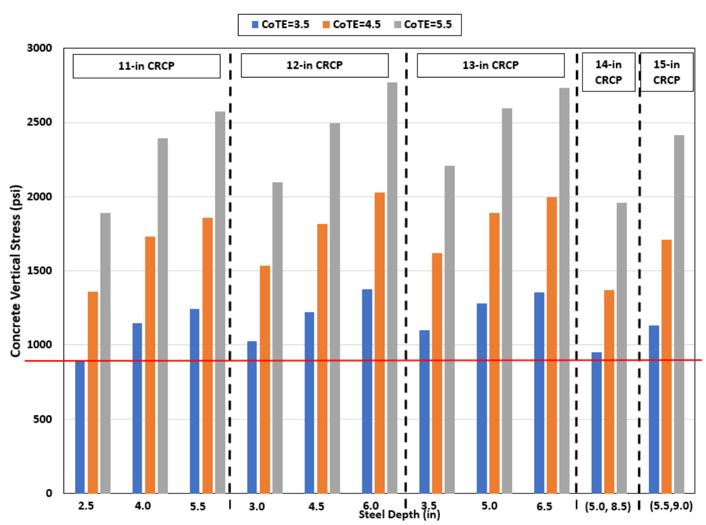

Figure 6.13 Comparison of concrete vertical tensile stresses for different CRCP thicknesses

According to Figure 6.13, higher CoTE value results in higher concrete vertical tensile stresses. Concrete stresses with CoTE values of 5.5×10^{-6} 1/°F and 4.5×10^{-6} 1/°F results in almost 2 times and 1.5 times greater stress values compared to CoTE value of 3.5×10^{-6} 1/°F, respectively. These results indicate that in concrete pavements with higher CoTE value there is a higher possibility of horizontal cracking. The other finding from Figure 6.13 is that placing the reinforcement closer to the concrete surface, even without considering the slab thickness, results in lower concrete stresses and lower chance of horizontal cracking. One of the most interesting findings from Figure 6.13 is that although 14-in and 15-in CRCPs are thicker and the possibility of horizontal cracking should be higher, but since two-mat design is used in 14-in and 15-in CRCP, the concrete stress values are lower than other one-mat designs, and the possibility of horizontal cracking is lower. The reason for lower concrete stresses for two-mat CRCP could be since the bottom mat constraints the lower part of CRCP, the top mat should only resist the curling and warping of the top section of CRCP, and it acts like a CRCP with a smaller thickness.

To evaluate the effect of transverse crack spacing on concrete vertical tensile stresses, 12-in CRCP with five different crack spacings of 10 ft, 20 ft, 40 ft, 60 ft, and 80 ft, with temperature drop of 60 °F, modulus of elasticity of 5×10^{6} psi, and CoTE value of 3.5×10^{-6} 1/°F were modeled, which the result is shown in Figure 6.14.

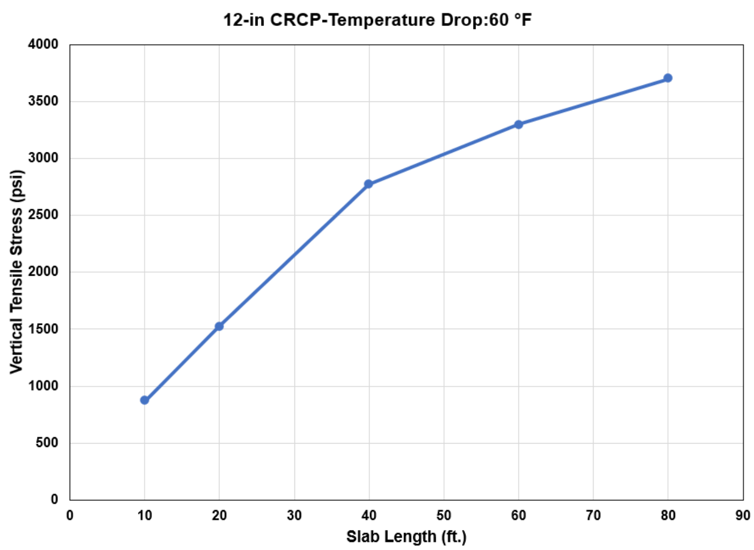

Figure 6.14 Effect of transverse crack spacing on concrete vertical stress

According to Figure 6.14 larger transverse cracks result in larger concrete stresses and higher possibility of horizontal cracking.

6.4 Development of Optimum Steel Design

Although placing the rebars closer to the surface results in a lower possibility of horizontal cracking, however, it is not practical to place them very close to the surface, since it will interfere with the saw-cutting practices. It should also be noted that keeping the reinforcement closer to the surface could increase the corrosion potential due to the reduced concrete cover for the reinforcement and interfere with the consolidation of the concrete. As such, in 2008, AASHTO recommended that the vertical position of reinforcement be at a minimum depth of 3.5 in. to a maximum of one-half of the slab thickness (AASHTO, 2008).

The objective of this chapter was to identify the optimum steel depth in CRCP, as this appears to be a significant issue that has not been properly investigated. In this chapter, structural responses of CRCP with different thicknesses and various reinforcement depths were analyzed. Models were developed for three-dimensional analysis. A factorial experiment was developed which encompasses the worst environmental conditions in Texas, various steel depths, and FEM analyses were conducted. The findings made in this chapter can be summarized as follows:

1) Among variables investigated, transverse crack spacing has the most significant effects on concrete stress near longitudinal reinforcement at crack location: the larger the crack spacing, the greater these vertical concrete stresses.
2) Coefficient of thermal expansion has a significant effect on concrete stresses around reinforcement at transverse crack plane and horizontal cracking. As the coefficient of thermal expansion increases, the concrete stress around reinforcement increases.
3) Reinforcement configurations in CRCP have substantial effects on horizontal cracking. In the two-mat designs considered in this chapter, concrete vertical stresses are smaller than those in the one-mat CRCPs. Therefore, it could be assumed that the two-mat design would develop a lower possibility of horizontal cracking than the one-mat design.
4) The current two-mat design standard is appropriate for 14-in and 15-in CRCPs.
5) Based on the work conducted in this chapter, the optimal reinforcement depths for one-mat CRCPs are suggested as follows.
    a. 11-in CRCP: 4 in.
    b. 12-in CRCP: 4.5 in.
    c. 13-in CRCP: 5 in.

Chapter 7 Conclusions and Recommendations

The primary objective of this study was to identify the mechanisms and associated variables of horizontal cracking in CRCP and to improve current design and/or construction practices in order to prevent or minimized horizontal cracking. This study was composed of two phases – (1) mechanistic modeling and analysis of CRCP, and (2) field experimentation. In the first phase of the study, CRCP responses from temperature and moisture variations (environmental loading) were analyzed with 3-dimensional modeling. In the second phase of the study, elaborate field testing was conducted to investigate the effects of various depths of longitudinal steel on CRCP responses, including concrete stresses that are responsible for horizontal cracking. The findings from both phases of study clearly indicated substantial effects of longitudinal steel depth on horizontal cracking potential. Detailed findings in each phase of the study are as follows:

A. Mechanistic Analysis of CRCP

1. Among the variables that were investigated, transverse crack spacing has the most significant effect on concrete stresses that are responsible for horizontal cracking, i.e. vertical concrete stresses around longitudinal reinforcement at or near a transverse crack, which is called critical concrete vertical stresses in this report. The larger the crack spacing, the greater these vertical concrete stresses.
2. Drying shrinkage and concrete coefficient of thermal expansion (CTE) also have substantial effects on critical concrete vertical stresses. Larger drying shrinkage and CTE will cause higher critical concrete vertical stresses.
3. Reinforcement configurations in CRCP, more specifically steel depth, have substantial effects on cracking, both transverse and horizontal.
4. Comparing the same concrete cover depth for both one-mat and two-mat designs, where the depth of the top layer in the two-mat design is the same as the depth of the one-mat design, critical concrete vertical stresses are smaller in the two-mat design than the one-mat design.

B. Field Experimentation

1. The depth of longitudinal steel has significant effects on how CRCP slabs deform due to environmental loading. When the steel was placed at the mid-depth of the slab, warping and curling was the primary slab behavior. On the other hand, if the steel was placed 1.5-in above the mid-depth, the primary slab behavior from environmental loading was axial.
    a. The reason for this difference in slab behavior was due to the difference in concrete temperature variations through the slab depth. Concrete temperature variations through the slab depth were large and non-linear in the concrete above the mid-depth, they were small and almost linear in the bottom half of the slab.
    b. It follows that warping and curling is the primary behavior of the top half of the concrete slab, while axial behavior is for the bottom half of the slab.
    c. When the steel is placed at the mid-depth of the slab, the steel does not effectively restrain warping and curling of the top half of the concrete. This would result in

large critical concrete vertical stresses, which could cause horizontal cracking at the depth of the longitudinal steel.

   d. On the other hand, if the longitudinal steel is placed above the mid-depth of the slab, referred to as upper-depth in this report, the steel effectively restrains curling and warping behavior, resulting in more axial slab behavior of the overall slab. This more dominant axial slab behavior results in smaller critical concrete vertical stresses and lower potential for horizontal cracking.

2. Larger strains in the steel placed at an upper-depth were observed than those in the steel placed at the mid-depth. This finding is in line with the findings discussed above. The steel placed at upper-depth effectively restrains warping and curling behavior of concrete, resulting in larger steel strains and stresses, which will cause greater concrete stresses and more transverse cracks. In turn, the smaller transverse crack spacing will reduce critical concrete vertical stresses, which will lower the potential for horizontal cracking.
3. When a transverse crack is formed from environmental loading, a sudden increase in concrete vertical strain near the longitudinal steel was observed. After this initial increase, concrete vertical strains followed temperature variations. This finding indicates horizontal cracking occurs at early ages (most of the transverse cracks in CRCP occur at early ages), and temperature drop is a key to the development of horizontal cracks.
4. Hysteresis-type behavior was observed in concrete and steel strains as temperature variations took place. This behavior is due to the temperature and moisture variations through the slab depth. If no variations exist in temperature and moisture through the slab depth, there will be no hysteresis-type strains. This implies that the optimum steel depth should minimize this behavior.

Based on the findings from this research study, the following recommendations are suggested:

1. For CRCP with slab thicknesses of 12-in and greater, the current practice of placing longitudinal steel at the mid-depth needs to be changed, as it increases the potential for horizontal cracking and distresses. It is recommended that, for those slab thicknesses, the longitudinal steel be placed above the mid-depth by about 1.5 inches. This will help ensure more axial behavior of CRCP than warping and curling, which should minimize the potential for horizonal cracking.
2. Currently, TxDOT requires a two-mat steel placement for CRCP with slab thicknesses of 14-in and larger. There is a potential for one-mat placement for these slab thicknesses that might provide good performance, if the steel is placed above the mid-depth. Determining optimum steel depth for 14-in and greater was out of the scope of this research study. It is recommended that TxDOT build a test section for CRCP with 14-in and greater with one-mat placed 2.0-in or 2.5-in above the mid-depth, and compare its behavior (transverse crack developments or crack spacing) and performance with a 2-mat section.
3. In this research project, a total of 4 test sections with upper-depth steel placement were built. It is recommended that the long-term performance of these test sections, along with control sections with the steel placed at the mid-depth, be continuously monitored and documented.

References

AASHTO. Mechanistic-Empirical Pavement Design Guide, Interim Edition: A Manual of Practice. Washington, D.C: American Association of State Highway and Transportation Officials, 2008.

American Concrete Institute (2008). Prediction of Creep, Shrinkage, and Temperature Effects in Concrete Structures. ACI 209R-92 (Re-approved 2008).

ASTM C39/39M -21, Standard Test Method for Compressive Strength of Cylindrical Concrete Specimens.

Desai, (2015), “Drying shrinkage behavior of foam - cement panel: a numerical study”, National Conference on Innovating for Development and Sustainability

Dossey, T. and B.F. McCullough, (1992), “Characterization of Concrete Properties with Age”, Center for Transportation Research, The University of Texas at Austin Austin, Texas 78712-1075, FHWA/TX-92+1244-2

Ha, S.; Yeon, J.; Choi, B.; Jung, Y.; Zollinger, D.G.; Wimsatt, A. and M.C. Won. (2012), “Develop Mechanistic-Empirical Design for CRCP”, Texas Tech University, Multidisciplinary Research in Transportation, Texas Department of Transportation, FHWA/TX-11-0-5832-1.

Hall, K., Dawood, D., Vanikar, S., Tally, R., Jr., Cackler, T., Correa, A., Deem, P., Duit, J., Geary, G., and A. Gisi. (2007). Long-Life Concrete Pavements in Europe and Canada; The National Academies of Sciences, Engineering, and Medicine: Washington, DC, USA.

Kashif, M.; Naseem, A., Iqbal, N., De Winne, P., and H. De Backer. (2021). Evaluating the Early-Age Crack Induction in Advanced Reinforced Concrete Pavement Using Partial Surface Saw-Cuts. Appl. Sci., 11, 1659. https://doi.org/10.3390/app11041659

Kim, S.-M., M. C. Won, and B. F. McCullough, (2000), “Three-Dimensional Nonlinear Finite Element Analysis of Continuously Reinforced Concrete Pavements”, Research Report 1831-1, Center for Transportation Research, University of Texas at Austin

Kong, Z and N. Lu, “Improved Method to Determine Young’s Modulus for Concrete Cylinder Using Electromechanical Spectrum: Principle and Validation”, Journal of Aerospace Engineering, 33(6), 04020079, 2020.

Miller, J. S. & Bellinger, W. Y. (2003), Distress Identification Manual for the Long-Term Pavement Performance Program, Federal Highway Administration, Washington DC.

Teller, L. W. and E.C. Sutherland. (1935). The structural design of concrete pavements: Part 2-observed effects of variations in temperature and moisture on the size, shape, and stress resistance of concrete pavement slabs. Public Roads, 16(9), 169–200.

Westergaard, H.M. (1927), “Analysis of Stresses in Concrete Roads Caused by Variations of Temperature”. Public Roads, 8(3).

Won, MC & Medina, CI (2008), “Analysis of Continuously Reinforced Concrete Pavement Behavior Using Information in the Rigid Pavement Database”, University of Texas at Austin, Center for Transportation Research, Texas Department of Transportation, FHWA/TX-09/0-5445-2.

Appendix A: Maximum Principal Stresses at Concrete Slab Between 2 Adjacent Transverse Cracks for One-Mat CRCP

Table A-1: Max Principal Stress at concrete slab, $E=4\times10^6$ psi, $\alpha_C=3.5\times10^{-6}/^\circ F$, k-value=300 psi/in

Crack Spacing (ft)	Steel Depth (in)	k-value=300							
		400 Micro-strain Ultimate Shrinkage				700 Micro-strain Ultimate Shrinkage			
		3 F˚/in Gradient		-1.5 F˚/in Gradient		3 F˚/in Gradient		-1.5 F˚/in Gradient	
		30 F˚ Drop	50 F˚ Drop	30 F˚ Drop	50 F˚ Drop	30 F˚ Drop	50 F˚ Drop	30 F˚ Drop	50 F˚ Drop
		Max Principal Stress at Slab (psi)	Max Principal Stress at Slab (psi)	Max Principal Stress at Slab (psi)	Max Principal Stress at Slab (psi)	Max Principal Stress at Slab (psi)	Max Principal Stress at Slab (psi)	Max Principal Stress at Slab (psi)	Max Principal Stress at Slab (psi)
4ft	3.5	343	428	414	481	612	679	666	733
	4	333	410	390	452	592	654	635	696
	4.5	330	399	376	431	590	646	623	678
	5	318	379	353	402	570	619	594	643
	5.5	313	366	340	382	566	609	593	625
	6	301	346	329	356	548	585	588	595
	6.5	293	330	329	335	539	569	591	592
8ft	3.5	416	568	569	690	717	838	843	965
	4	404	546	539	652	695	808	804	919
	4.5	398	528	514	618	686	790	778	885
	5	381	499	480	576	659	754	738	834
	5.5	370	474	454	538	646	729	711	797
	6	351	440	422	495	618	690	674	748
	6.5	334	407	394	454	597	657	645	706
12ft	3.5	462	658	669	809	779	935	965	1104
	4	449	633	644	776	755	902	933	1067
	4.5	440	609	621	746	743	879	910	1037
	5	421	574	592	709	713	836	874	993
	5.5	405	542	566	674	694	803	848	957
	6	382	500	536	632	662	757	812	911
	6.5	361	460	509	594	637	717	784	870

Table A-2: Max Principal Stress at concrete slab, $E=4\times10^6$ psi, $\alpha_C=3.5\times10^{-6}/^{\circ}F$, k-value=500 psi/in

Crack Spacing (ft)	Steel Depth (in)	k-value=500							
		400 Micro-strain Ultimate Shrinkage				700 Micro-strain Ultimate Shrinkage			
		3 F˚/in Gradient		-1.5 F˚/in Gradient		3 F˚/in Gradient		-1.5 F˚/in Gradient	
		30 F˚ Drop	50 F˚ Drop	30 F˚ Drop	50 F˚ Drop	30 F˚ Drop	50 F˚ Drop	30 F˚ Drop	50 F˚ Drop
		Max Principal Stress at Slab (psi)	Max Principal Stress at Slab (psi)	Max Principal Stress at Slab (psi)	Max Principal Stress at Slab (psi)	Max Principal Stress at Slab (psi)	Max Principal Stress at Slab (psi)	Max Principal Stress at Slab (psi)	Max Principal Stress at Slab (psi)
4ft	3.5	343	427	416	483	612	679	669	736
	4	332	409	393	454	592	653	639	699
	4.5	329	399	378	433	590	645	644	681
	5	317	379	367	404	569	619	636	645
	5.5	312	366	369	384	566	608	641	643
	6	301	346	366	358	548	584	636	637
	6.5	293	330	366	337	539	569	639	639
8ft	3.5	409	557	577	695	709	827	854	974
	4	397	535	548	659	687	798	817	930
	4.5	391	517	524	626	679	781	793	897
	5	375	489	492	586	653	745	754	849
	5.5	364	465	467	550	640	722	729	813
	6	346	432	436	508	614	684	693	766
	6.5	329	401	409	470	594	653	666	727
12ft	3.5	457	647	679	809	772	924	983	1111
	4	443	920	658	780	747	890	956	1080
	4.5	433	597	640	757	735	867	939	1057
	5	413	563	616	726	705	825	909	1021
	5.5	398	531	596	698	687	794	889	993
	6	375	490	571	665	656	749	859	955
	6.5	355	452	549	634	632	712	837	922

Table A-3: Max Principal Stress at concrete slab, $E=5\times10^6$ psi, $\alpha_C=3.5\times10^{-6}/^\circ F$, k-value=300 psi/in

Crack Spacing (ft)	Steel Depth (in)	k-value=300							
		400 Micro-strain Ultimate Shrinkage				700 Micro-strain Ultimate Shrinkage			
		3 F˚/in Gradient		-1.5 F˚/in Gradient		3 F˚/in Gradient		-1.5 F˚/in Gradient	
		30 F˚ Drop	50 F˚ Drop	30 F˚ Drop	50 F˚ Drop	30 F˚ Drop	50 F˚ Drop	30 F˚ Drop	50 F˚ Drop
		Max Principal Stress at Slab (psi)	Max Principal Stress at Slab (psi)	Max Principal Stress at Slab (psi)	Max Principal Stress at Slab (psi)	Max Principal Stress at Slab (psi)	Max Principal Stress at Slab (psi)	Max Principal Stress at Slab (psi)	Max Principal Stress at Slab (psi)
4ft	3.5	421	520	502	581	755	833	816	895
	4	408	498	474	546	730	801	778	850
	4.5	405	486	458	522	728	793	765	830
	5	390	463	431	489	704	761	730	788
	5.5	386	448	416	465	700	750	718	768
	6	371	424	393	435	679	722	712	733
	6.5	362	405	395	410	669	704	716	717
8ft	3.5	507	683	679	820	876	1017	1016	1159
	4	492	657	642	774	848	980	969	1103
	4.5	484	635	613	734	839	959	940	1063
	5	465	601	573	684	806	915	891	1003
	5.5	452	571	542	640	791	887	860	959
	6	429	532	504	589	759	841	816	902
	6.5	410	494	472	542	735	803	783	854
12ft	3.5	565	797	802	970	955	1140	1165	1334
	4	549	767	769	927	925	1099	1124	1285
	4.5	538	739	740	891	911	1072	1095	1247
	5	514	696	704	843	874	1020	1049	1191
	5.5	496	657	672	799	852	981	1017	1146
	6	468	607	633	746	812	924	972	1088
	6.5	444	569	600	745	783	876	937	1037

Table A-4: Max Principal Stress at concrete slab, E=5×10^6 psi, α_C=3.5×10^{-6}/°F, k-value=500 psi/in

Crack Spacing (ft)	Steel Depth (in)	k-value=500							
		400 Micro-strain Ultimate Shrinkage				700 Micro-strain Ultimate Shrinkage			
		3 F°/in Gradient		-1.5 F°/in Gradient		3 F°/in Gradient		-1.5 F°/in Gradient	
		30 F° Drop	50 F° Drop	30 F° Drop	50 F° Drop	30 F° Drop	50 F° Drop	30 F° Drop	50 F° Drop
		Max Principal Stress at Slab (psi)	Max Principal Stress at Slab (psi)	Max Principal Stress at Slab (psi)	Max Principal Stress at Slab (psi)	Max Principal Stress at Slab (psi)	Max Principal Stress at Slab (psi)	Max Principal Stress at Slab (psi)	Max Principal Stress at Slab (psi)
4ft	3.5	421	519	505	583	754	833	819	898
	4	407	497	477	549	729	801	782	853
	4.5	404	486	460	525	728	730	776	833
	5	390	462	434	491	704	761	766	791
	5.5	385	447	439	467	700	750	773	775
	6	371	424	435	437	679	721	767	768
	6.5	362	405	436	313	669	704	771	771
8ft	3.5	500	673	688	826	869	1007	1029	1169
	4	485	647	653	782	842	971	984	1115
	4.5	478	625	624	743	832	951	955	1077
	5	459	591	586	695	801	908	909	1019
	5.5	446	563	556	653	786	880	879	977
	6	424	524	520	603	755	836	837	921
	6.5	405	488	489	559	732	799	805	876
12ft	3.5	559	786	814	971	947	1129	1187	1344
	4	542	754	786	934	917	1087	1152	1302
	4.5	530	726	763	904	902	1060	1129	1272
	5	507	684	732	864	866	1008	1090	1224
	5.5	489	645	706	827	844	971	1064	1187
	6	462	597	673	784	806	916	1026	1139
	6.5	438	552	646	744	778	871	997	1097

Table A-5: Max Principal Stress at concrete slab, $E=4\times10^6$ psi, $\alpha_C=4.5\times10^{-6}$ /˚F, k-value=300 psi/in

Crack Spacing (ft)	Steel Depth (in)	k-value=300							
		400 Micro-strain Ultimate Shrinkage				700 Micro-strain Ultimate Shrinkage			
		3 F˚/in Gradient		-1.5 F˚/in Gradient		3 F˚/in Gradient		-1.5 F˚/in Gradient	
		30 F˚ Drop	50 F˚ Drop	30 F˚ Drop	50 F˚ Drop	30 F˚ Drop	50 F˚ Drop	30 F˚ Drop	50 F˚ Drop
		Max Principal Stress at Slab (psi)	Max Principal Stress at Slab (psi)	Max Principal Stress at Slab (psi)	Max Principal Stress at Slab (psi)	Max Principal Stress at Slab (psi)	Max Principal Stress at Slab (psi)	Max Principal Stress at Slab (psi)	Max Principal Stress at Slab (psi)
4ft	3.5	363	468	448	534	632	718	700	787
	4	351	448	420	499	611	690	665	744
	4.5	348	435	402	434	608	680	650	721
	5	335	412	377	440	587	650	617	680
	5.5	328	396	359	414	581	636	607	657
	6	315	372	336	383	562	609	602	622
	6.5	305	352	319	357	552	589	605	605
8ft	3.5	447	636	633	789	747	904	906	1063
	4	435	612	598	744	724	871	863	1010
	4.5	428	590	567	702	715	850	832	969
	5	410	556	528	651	868	808	786	910
	5.5	396	525	496	605	670	778	753	864
	6	374	485	458	552	640	732	710	806
	6.5	353	445	424	502	616	692	675	754
12ft	3.5	504	749	750	933	820	1024	1046	1225
	4	490	720	720	891	795	987	1010	1182
	4.5	479	693	694	855	781	958	983	1146
	5	457	650	659	810	748	909	942	1095
	5.5	438	610	629	767	726	868	911	1051
	6	411	558	592	729	689	812	869	996
	6.5	385	508	560	815	658	762	835	946

Table A-6: Max Principal Stress at concrete slab, E=4×10^6 psi, α_C=4.5×10^-6/°F, k-value=500 psi/in

Crack Spacing (ft)	Steel Depth (in)	k-value=500							
		400 Micro-strain Ultimate Shrinkage				700 Micro-strain Ultimate Shrinkage			
		3 F˚/in Gradient		-1.5 F˚/in Gradient		3 F˚/in Gradient		-1.5 F˚/in Gradient	
		30 F˚ Drop	50 F˚ Drop	30 F˚ Drop	50 F˚ Drop	30 F˚ Drop	50 F˚ Drop	30 F˚ Drop	50 F˚ Drop
		Max Principal Stress at Slab (psi)	Max Principal Stress at Slab (psi)	Max Principal Stress at Slab (psi)	Max Principal Stress at Slab (psi)	Max Principal Stress at Slab (psi)	Max Principal Stress at Slab (psi)	Max Principal Stress at Slab (psi)	Max Principal Stress at Slab (psi)
4ft	3.5	362	467	450	537	631	717	703	790
	4	351	447	423	502	611	689	668	747
	4.5	347	434	405	476	608	679	664	723
	5	334	411	379	442	587	650	656	683
	5.5	328	395	362	416	581	636	661	663
	6	315	372	339	385	562	609	656	657
	6.5	304	351	385	359	551	589	568	659
8ft	3.5	438	622	642	793	737	890	919	1072
	4	426	598	608	750	714	858	877	1022
	4.5	419	576	579	710	705	837	848	982
	5	401	544	541	662	678	497	804	926
	5.5	388	514	511	618	663	767	773	882
	6	367	475	474	568	633	724	732	826
	6.5	347	436	442	521	610	685	698	778
12ft	3.5	497	734	759	931	811	1009	1265	1229
	4	481	704	735	893	785	971	1034	1193
	4.5	470	670	714	864	770	942	1013	1165
	5	448	634	686	828	738	894	980	1123
	5.5	429	594	662	794	716	855	955	1088
	6	402	545	632	754	680	800	921	1044
	6.5	381	497	606	772	652	753	894	1004

Table A-7: Max Principal Stress at concrete slab, $E=5\times10^6$ psi, $\alpha_C=4.5\times10^{-6}/°F$, k-value=300 psi/in

Crack Spacing (ft)	Steel Depth (in)	k-value=300							
		400 Micro-strain Ultimate Shrinkage				700 Micro-strain Ultimate Shrinkage			
		3 F˚/in Gradient		-1.5 F˚/in Gradient		3 F˚/in Gradient		-1.5 F˚/in Gradient	
		30 F˚ Drop	50 F˚ Drop	30 F˚ Drop	50 F˚ Drop	30 F˚ Drop	50 F˚ Drop	30 F˚ Drop	50 F˚ Drop
		Max Principal Stress at Slab (psi)	Max Principal Stress at Slab (psi)	Max Principal Stress at Slab (psi)	Max Principal Stress at Slab (psi)	Max Principal Stress at Slab (psi)	Max Principal Stress at Slab (psi)	Max Principal Stress at Slab (psi)	Max Principal Stress at Slab (psi)
4ft	3.5	444	567	542	643	777	878	855	956
	4	430	542	510	602	752	844	814	906
	4.5	426	528	489	572	750	833	796	880
	5	410	501	458	532	724	798	758	831
	5.5	403	482	438	503	718	783	741	805
	6	387	454	412	466	695	750	727	763
	6.5	376	430	391	435	683	727	730	735
8ft	3.5	544	764	753	934	912	1095	1090	1274
	4	529	734	710	880	884	1055	1037	1209
	4.5	520	709	674	830	873	1029	1001	1160
	5	498	668	628	770	839	980	946	1090
	5.5	483	632	590	716	820	945	909	1037
	6	457	584	545	654	785	891	858	968
	6.5	433	538	506	596	757	844	818	909
12ft	3.5	615	905	897	1116	1004	1248	1261	1477
	4	598	846	859	1064	973	1202	1214	1421
	4.5	585	837	825	1018	957	1168	1180	1376
	5	559	781	782	962	917	1107	1128	1311
	5.5	537	740	743	907	891	1059	1089	1256
	6	504	677	697	844	846	991	1037	1187
	6.5	474	617	657	784	810	931	995	1328

Table A-8: Max Principal Stress at concrete slab, $E=5\times10^6$ psi, $\alpha_C=4.5\times10^{-6}$ /°F, k-value=500 psi/in

Crack Spacing (ft)	Steel Depth (in)	k-value=500							
		400 Micro-strain Ultimate Shrinkage				700 Micro-strain Ultimate Shrinkage			
		3 F˚/in Gradient		-1.5 F˚/in Gradient		3 F˚/in Gradient		-1.5 F˚/in Gradient	
		30 F˚ Drop	50 F˚ Drop	30 F˚ Drop	50 F˚ Drop	30 F˚ Drop	50 F˚ Drop	30 F˚ Drop	50 F˚ Drop
		Max Principal Stress at Slab (psi)	Max Principal Stress at Slab (psi)	Max Principal Stress at Slab (psi)	Max Principal Stress at Slab (psi)	Max Principal Stress at Slab (psi)	Max Principal Stress at Slab (psi)	Max Principal Stress at Slab (psi)	Max Principal Stress at Slab (psi)
4ft	3.5	443	566	544	646	777	877	859	960
	4	429	542	513	605	752	843	817	909
	4.5	426	527	492	575	749	832	800	883
	5	410	500	461	535	724	797	787	835
	5.5	403	482	441	505	718	782	794	808
	6	387	454	414	468	695	750	788	790
	6.5	376	430	457	438	683	727	791	792
8ft	3.5	535	750	763	940	903	1082	1104	1284
	4	520	721	721	888	875	1042	1053	1222
	4.5	512	696	687	840	865	1018	1018	1175
	5	491	656	642	783	831	969	965	1107
	5.5	475	621	606	731	813	935	929	1056
	6	450	575	563	671	778	883	880	990
	6.5	427	530	525	615	752	838	842	933
12ft	3.5	607	882	910	1116	995	1232	1530	1484
	4	588	850	878	1069	963	1185	1244	1437
	4.5	575	820	850	1031	947	1151	1216	1399
	5	549	769	813	984	906	1092	1172	1345
	5.5	527	724	782	939	881	1045	1140	1300
	6	494	664	743	886	837	979	1096	1243
	6.5	465	605	710	837	803	921	1061	1269

Table A-9: Max Principal Stress at concrete slab, $E=4\times10^6$ psi, $\alpha_C=5.5\times10^{-6}/^{\circ}F$, k-value=300 psi/in

Crack Spacing (ft)	Steel Depth (in)	k-value=300							
		400 Micro-strain Ultimate Shrinkage				700 Micro-strain Ultimate Shrinkage			
		3 F˚/in Gradient		-1.5 F˚/in Gradient		3 F˚/in Gradient		-1.5 F˚/in Gradient	
		30 F˚ Drop	50 F˚ Drop	30 F˚ Drop	50 F˚ Drop	30 F˚ Drop	50 F˚ Drop	30 F˚ Drop	50 F˚ Drop
		Max Principal Stress at Slab (psi)	Max Principal Stress at Slab (psi)	Max Principal Stress at Slab (psi)	Max Principal Stress at Slab (psi)	Max Principal Stress at Slab (psi)	Max Principal Stress at Slab (psi)	Max Principal Stress at Slab (psi)	Max Principal Stress at Slab (psi)
4ft	3.5	382	505	482	588	650	756	736	842
	4	370	483	452	549	629	725	697	794
	4.5	366	467	430	517	626	713	678	766
	5	352	442	401	478	603	680	642	719
	5.5	344	422	380	447	596	664	624	691
	6	329	395	354	411	576	632	618	651
	6.5	317	370	333	379	563	609	620	620
8ft	3.5	479	702	698	888	777	970	972	1164
	4	467	676	658	836	754	935	924	1104
	4.5	458	650	621	787	744	910	888	1055
	5	439	612	577	728	714	864	837	988
	5.5	423	575	539	673	695	828	798	933
	6	397	528	495	611	662	775	749	866
	6.5	373	480	455	552	634	727	708	806
12ft	3.5	546	835	832	1058	861	1116	1129	1350
	4	532	809	797	1008	835	1074	1089	1299
	4.5	520	776	767	964	820	1040	1058	1257
	5	495	728	728	913	785	985	1012	1199
	5.5	473	678	692	892	759	936	975	1148
	6	441	617	649	803	717	869	928	1058
	6.5	413	569	611	746	682	808	888	1025

Table A-10: Max Principal Stress at concrete slab, E=4×10^6 psi, α_C=5.5×10^{-6}/˚F, k-value=500 psi/in

Crack Spacing (ft)	Steel Depth (in)	k-value=500							
		400 Micro-strain Ultimate Shrinkage				700 Micro-strain Ultimate Shrinkage			
		3 F˚/in Gradient		-1.5 F˚/in Gradient		3 F˚/in Gradient		-1.5 F˚/in Gradient	
		30 F˚ Drop	50 F˚ Drop	30 F˚ Drop	50 F˚ Drop	30 F˚ Drop	50 F˚ Drop	30 F˚ Drop	50 F˚ Drop
		Max Principal Stress at Slab (psi)	Max Principal Stress at Slab (psi)	Max Principal Stress at Slab (psi)	Max Principal Stress at Slab (psi)	Max Principal Stress at Slab (psi)	Max Principal Stress at Slab (psi)	Max Principal Stress at Slab (psi)	Max Principal Stress at Slab (psi)
4ft	3.5	381	504	486	591	650	755	740	845
	4	370	482	455	551	628	725	701	798
	4.5	365	466	433	520	625	712	687	769
	5	351	441	404	481	603	680	678	723
	5.5	344	422	383	450	596	663	682	694
	6	329	394	357	413	575	632	677	654
	6.5	317	370	336	382	562	609	678	623
8ft	3.5	468	685	707	892	766	953	985	1173
	4	456	659	669	843	743	919	939	1116
	4.5	447	634	634	796	733	894	905	1068
	5	428	596	592	740	703	849	856	1005
	5.5	412	561	556	687	686	814	819	952
	6	388	515	514	628	653	764	772	888
	6.5	365	469	476	572	626	718	733	831
12ft	3.5	538	823	841	1055	851	1094	1146	1352
	4	522	791	814	1009	824	1055	1114	1308
	4.5	508	755	789	973	808	1021	1089	1275
	5	483	708	757	932	772	966	1052	1228
	5.5	461	659	728	891	747	918	1023	1187
	6	430	599	694	844	706	854	985	1137
	6.5	460	616	664	798	672	795	953	1089

Table A-11: Max Principal Stress at concrete slab, $E=5\times10^6$ psi, $\alpha_C=5.5\times10^{-6}$/°F, k-value=300 psi/in

Crack Spacing (ft)	Steel Depth (in)	k-value=300							
		400 Micro-strain Ultimate Shrinkage				700 Micro-strain Ultimate Shrinkage			
		3 F˚/in Gradient		-1.5 F˚/in Gradient		3 F˚/in Gradient		-1.5 F˚/in Gradient	
		30 F˚ Drop	50 F˚ Drop	30 F˚ Drop	50 F˚ Drop	30 F˚ Drop	50 F˚ Drop	30 F˚ Drop	50 F˚ Drop
		Max Principal Stress at Slab (psi)	Max Principal Stress at Slab (psi)	Max Principal Stress at Slab (psi)	Max Principal Stress at Slab (psi)	Max Principal Stress at Slab (psi)	Max Principal Stress at Slab (psi)	Max Principal Stress at Slab (psi)	Max Principal Stress at Slab (psi)
4ft	3.5	466	610	583	706	799	922	897	1021
	4	452	583	546	659	773	886	852	965
	4.5	448	565	521	623	770	872	830	932
	5	431	535	487	577	743	833	787	877
	5.5	422	513	463	541	736	814	767	845
	6	404	481	432	498	711	777	744	797
	6.5	390	453	408	462	696	751	747	762
8ft	3.5	581	842	827	1049	948	1173	1166	1390
	4	566	809	778	987	919	1130	1107	1318
	4.5	556	779	736	928	908	1101	1066	1260
	5	533	734	684	858	872	1045	1004	1181
	5.5	514	690	639	794	851	1003	960	1117
	6	484	637	587	721	811	941	902	1037
	6.5	456	616	541	655	778	885	855	967
12ft	3.5	666	1018	993	1265	1053	1359	1358	1627
	4	648	980	950	1204	1022	1309	1307	1562
	4.5	634	940	911	1149	1004	1269	1267	1507
	5	605	882	861	1082	961	1200	1209	1434
	5.5	579	823	816	1018	931	1141	1163	1370
	6	541	749	763	945	881	1061	1105	1291
	6.5	504	674	715	873	839	987	1055	1215

Table A-12: Max Principal Stress at concrete slab, $E=5\times10^6$ psi, $\alpha_C=5.5\times10^{-6}/^\circ F$, k-value=500 psi/in

Crack Spacing (ft)	Steel Depth (in)	k-value=500							
		400 Micro-strain Ultimate Shrinkage				700 Micro-strain Ultimate Shrinkage			
		3 F˚/in Gradient		-1.5 F˚/in Gradient		3 F˚/in Gradient		-1.5 F˚/in Gradient	
		30 F˚ Drop	50 F˚ Drop	30 F˚ Drop	50 F˚ Drop	30 F˚ Drop	50 F˚ Drop	30 F˚ Drop	50 F˚ Drop
		Max Principal Stress at Slab (psi)	Max Principal Stress at Slab (psi)	Max Principal Stress at Slab (psi)	Max Principal Stress at Slab (psi)	Max Principal Stress at Slab (psi)	Max Principal Stress at Slab (psi)	Max Principal Stress at Slab (psi)	Max Principal Stress at Slab (psi)
4ft	3.5	466	609	586	709	798	921	902	1025
	4	452	582	549	662	773	885	855	968
	4.5	447	565	524	626	769	871	834	936
	5	430	535	490	580	743	833	812	881
	5.5	422	512	466	544	735	814	818	848
	6	404	480	435	501	711	777	811	801
	6.5	389	452	411	465	696	750	814	766
8ft	3.5	571	825	838	1055	937	1157	1181	1401
	4	555	793	791	995	908	1114	1124	1331
	4.5	545	763	750	939	897	1086	1084	1276
	5	522	719	700	872	861	1031	1025	1199
	5.5	504	677	657	810	841	990	982	1137
	6	475	629	607	740	802	930	926	1061
	6.5	448	608	563	674	771	877	881	993
12ft	3.5	657	1001	1006	1264	1043	1341	1381	1632
	4	638	961	970	1207	1011	1289	1338	1576
	4.5	622	920	937	1161	992	1248	1305	1531
	5	592	861	896	1105	948	1180	1256	1469
	5.5	565	803	858	1052	918	1122	1219	1416
	6	528	731	814	992	870	1045	1169	1350
	6.5	526	708	775	932	829	974	1128	1288

Appendix B: Concrete Stress Around Longitudinal Steel at Transverse Crack Location for One-Mat CRCP

Table B-1: Max Principal Stress at Transverse Crack, $E=4\times10^6$ psi, $\alpha_C=3.5\times10^{-6}/^\circ F$, k-value=300 psi/in

Crack Spacing (ft)	Steel Depth (in)	k-value=300							
		400 Micro-strain Ultimate Shrinkage				700 Micro-strain Ultimate Shrinkage			
		3 F˚/in Gradient		-1.5 F˚/in Gradient		3 F˚/in Gradient		-1.5 F˚/in Gradient	
		30 F˚ Drop	50 F˚ Drop	30 F˚ Drop	50 F˚ Drop	30 F˚ Drop	50 F˚ Drop	30 F˚ Drop	50 F˚ Drop
		Max Principal Stress at crack (psi)	Max Principal Stress at crack (psi)	Max Principal Stress at crack (psi)	Max Principal Stress at crack (psi)	Max Principal Stress at crack (psi)	Max Principal Stress at crack (psi)	Max Principal Stress at crack (psi)	Max Principal Stress at crack (psi)
4ft	3.5	272	337	304	368	453	506	537	534
	4	298	371	331	390	482	551	528	572
	4.5	301	381	335	398	485	549	535	568
	5	311	396	343	410	495	563	528	579
	5.5	304	393	333	403	477	544	536	556
	6	301	392	324	396	460	533	533	540
	6.5	288	380	306	379	433	506	538	535
8ft	3.5	360	530	440	569	567	681	621	735
	4	399	561	476	597	623	750	675	808
	4.5	412	585	488	620	626	762	675	824
	5	432	615	503	649	648	790	691	853
	5.5	434	623	495	652	634	781	667	840
	6	437	628	487	653	627	777	649	831
	6.5	428	619	466	637	601	751	610	798
12ft	3.5	436	844	542	714	663	885	728	894
	4	483	866	582	755	728	959	799	1002
	4.5	506	878	605	806	742	982	813	1049
	5	533	880	630	864	771	1013	842	1114
	5.5	539	872	631	894	762	1004	826	1129
	6	546	861	629	924	759	995	816	1156
	6.5	544	848	616	969	740	969	785	1175

Table B-2: Max Principal Stress at Transverse Crack, $E=4\times10^6$ psi, $\alpha_C=3.5\times10^{-6}/^\circ F$, k-value=500 psi/in

Crack Spacing (ft)	Steel Depth (in)	k-value=500							
		400 Micro-strain Ultimate Shrinkage				700 Micro-strain Ultimate Shrinkage			
		3 F˚/in Gradient		-1.5 F˚/in Gradient		3 F˚/in Gradient		-1.5 F˚/in Gradient	
		30 F˚ Drop	50 F˚ Drop	30 F˚ Drop	50 F˚ Drop	30 F˚ Drop	50 F˚ Drop	30 F˚ Drop	50 F˚ Drop
		Max Principal Stress at crack (psi)	Max Principal Stress at crack (psi)	Max Principal Stress at crack (psi)	Max Principal Stress at crack (psi)	Max Principal Stress at crack (psi)	Max Principal Stress at crack (psi)	Max Principal Stress at crack (psi)	Max Principal Stress at crack (psi)
4ft	3.5	275	340	336	368	455	507	587	584
	4	300	374	331	390	493	551	578	574
	4.5	303	383	335	398	486	550	583	580
	5	312	397	343	410	496	564	577	579
	5.5	305	394	333	403	475	545	584	580
	6	301	392	332	397	461	533	581	577
	6.5	289	381	334	381	433	506	586	582
8ft	3.5	363	528	440	569	568	682	619	734
	4	402	564	475	598	624	751	674	807
	4.5	414	587	488	620	627	762	675	823
	5	433	616	503	649	648	790	690	853
	5.5	435	623	496	652	634	782	667	840
	6	437	628	488	653	626	776	650	832
	6.5	428	619	468	638	601	751	612	799
12ft	3.5	443	823	542	715	667	882	725	894
	4	488	842	581	756	731	955	795	999
	4.5	509	853	603	805	744	977	808	1044
	5	535	855	628	860	772	1008	837	1105
	5.5	540	852	628	888	763	1000	821	1117
	6	546	854	627	911	759	992	811	1132
	6.5	543	842	615	939	740	968	781	1129

Table B-3: Max Principal Stress at Transverse Crack, $E=5\times10^6$ psi, $\alpha_C=3.5\times10^{-6}/^\circ F$, k-value=300 psi/in

Crack Spacing (ft)	Steel Depth (in)	k-value=300							
		400 Micro-strain Ultimate Shrinkage				700 Micro-strain Ultimate Shrinkage			
		3 F˚/in Gradient		-1.5 F˚/in Gradient		3 F˚/in Gradient		-1.5 F˚/in Gradient	
		30 F˚ Drop	50 F˚ Drop	30 F˚ Drop	50 F˚ Drop	30 F˚ Drop	50 F˚ Drop	30 F˚ Drop	50 F˚ Drop
		Max Principal Stress at crack (psi)	Max Principal Stress at crack (psi)	Max Principal Stress at crack (psi)	Max Principal Stress at crack (psi)	Max Principal Stress at crack (psi)	Max Principal Stress at crack (psi)	Max Principal Stress at crack (psi)	Max Principal Stress at crack (psi)
4ft	3.5	334	412	374	454	560	623	649	650
	4	365	453	407	477	608	678	637	705
	4.5	369	464	410	486	599	675	646	699
	5	381	483	420	500	611	692	638	712
	5.5	373	479	407	491	584	668	648	682
	6	368	477	397	483	567	653	644	662
	6.5	353	463	375	462	535	620	651	646
8ft	3.5	442	646	549	711	701	840	770	913
	4	490	687	587	740	770	924	836	1004
	4.5	506	716	600	765	773	938	834	1020
	5	530	752	618	799	799	972	852	1055
	5.5	532	761	607	801	780	960	820	1037
	6	535	768	596	801	771	954	797	1024
	6.5	525	757	569	780	739	922	747	982
12ft	3.5	536	1042	684	894	820	1100	910	1140
	4	594	1074	724	961	901	1193	998	1276
	4.5	622	1096	750	1023	918	1221	1013	1334
	5	656	1106	781	1096	954	1261	1047	1412
	5.5	664	1104	780	1143	942	1250	1026	1426
	6	673	1087	776	1199	937	1237	1011	1466
	6.5	670	1065	759	1253	914	1204	971	1501

Table B-4: Max Principal Stress at Transverse Crack, $E=5\times10^6$ psi, $\alpha_C=3.5\times10^{-6}$/˚F, k-value=500 psi/in

Crack Spacing (ft)	Steel Depth (in)	k-value=500							
		400 Micro-strain Ultimate Shrinkage				700 Micro-strain Ultimate Shrinkage			
		3 F˚/in Gradient		-1.5 F˚/in Gradient		3 F˚/in Gradient		-1.5 F˚/in Gradient	
		30 F˚ Drop	50 F˚ Drop	30 F˚ Drop	50 F˚ Drop	30 F˚ Drop	50 F˚ Drop	30 F˚ Drop	50 F˚ Drop
		Max Principal Stress at crack (psi)	Max Principal Stress at crack (psi)	Max Principal Stress at crack (psi)	Max Principal Stress at crack (psi)	Max Principal Stress at crack (psi)	Max Principal Stress at crack (psi)	Max Principal Stress at crack (psi)	Max Principal Stress at crack (psi)
4ft	3.5	338	416	398	454	562	624	706	703
	4	368	456	406	477	609	679	694	704
	4.5	372	467	410	486	600	676	702	698
	5	383	485	420	501	612	693	695	712
	5.5	374	480	408	492	585	669	703	698
	6	369	477	398	484	567	654	699	694
	6.5	353	463	397	463	533	620	705	701
8ft	3.5	446	644	459	711	703	841	768	912
	4	495	690	586	739	771	926	834	1002
	4.5	509	718	600	764	774	938	834	1019
	5	532	754	618	799	799	973	852	1055
	5.5	533	762	609	802	781	960	821	1037
	6	536	768	598	801	771	953	798	1024
	6.5	524	757	572	781	739	922	750	982
12ft	3.5	543	1023	683	897	825	1097	906	1140
	4	600	1052	722	963	904	1189	993	1272
	4.5	626	1072	748	1022	920	1216	1007	1327
	5	658	1082	778	1091	955	1256	1041	1400
	5.5	665	1079	777	1123	942	1245	1020	1412
	6	673	1067	774	1172	937	1234	1005	1437
	6.5	669	1053	758	1209	914	1202	966	1450

Table B-5: Max Principal Stress at Transverse Crack, E=4×10^6 psi, α_C=4.5×10^{-6}/°F, k-value=300 psi/in

Crack Spacing (ft)	Steel Depth (in)	k-value=300							
		400 Micro-strain Ultimate Shrinkage				700 Micro-strain Ultimate Shrinkage			
		3 F°/in Gradient		-1.5 F°/in Gradient		3 F°/in Gradient		-1.5 F°/in Gradient	
		30 F° Drop	50 F° Drop	30 F° Drop	50 F° Drop	30 F° Drop	50 F° Drop	30 F° Drop	50 F° Drop
		Max Principal Stress at crack (psi)	Max Principal Stress at crack (psi)	Max Principal Stress at crack (psi)	Max Principal Stress at crack (psi)	Max Principal Stress at crack (psi)	Max Principal Stress at crack (psi)	Max Principal Stress at crack (psi)	Max Principal Stress at crack (psi)
4ft	3.5	312	410	361	444	498	580	550	615
	4	341	448	391	481	538	629	574	664
	4.5	347	462	395	491	535	632	566	662
	5	360	481	403	504	548	650	572	674
	5.5	356	483	393	497	529	635	547	652
	6	355	485	383	490	518	626	544	635
	6.5	345	476	364	473	493	602	580	602
8ft	3.5	419	681	520	688	629	809	705	865
	4	464	702	564	733	690	886	765	951
	4.5	483	730	579	766	700	905	769	975
	5	508	768	596	803	727	941	788	1014
	5.5	515	781	590	812	718	937	766	1009
	6	522	791	582	817	716	935	749	1008
	6.5	518	783	560	804	694	910	709	978
12ft	3.5	548	1255	642	877	760	1251	833	1059
	4	578	1296	693	933	831	1277	915	1191
	4.5	609	1318	721	1004	852	1289	936	1264
	5	642	1317	754	1088	887	1279	973	1355
	5.5	655	1294	760	1151	883	1271	964	1392
	6	665	1242	762	1243	881	1258	962	1514
	6.5	665	1193	751	1337	865	1220	936	1593

Table B-6: Max Principal Stress at Transverse Crack, $E=4\times10^6$ psi, $\alpha_C=4.5\times10^{-6}/^\circ F$, k-value=500 psi/in

Crack Spacing (ft)	Steel Depth (in)	k-value=500							
		400 Micro-strain Ultimate Shrinkage				700 Micro-strain Ultimate Shrinkage			
		3 F˚/in Gradient		-1.5 F˚/in Gradient		3 F˚/in Gradient		-1.5 F˚/in Gradient	
		30 F˚ Drop	50 F˚ Drop	30 F˚ Drop	50 F˚ Drop	30 F˚ Drop	50 F˚ Drop	30 F˚ Drop	50 F˚ Drop
		Max Principal Stress at crack (psi)	Max Principal Stress at crack (psi)	Max Principal Stress at crack (psi)	Max Principal Stress at crack (psi)	Max Principal Stress at crack (psi)	Max Principal Stress at crack (psi)	Max Principal Stress at crack (psi)	Max Principal Stress at crack (psi)
4ft	3.5	317	415	361	444	501	583	605	614
	4	345	452	391	481	541	631	595	663
	4.5	351	466	395	491	537	634	601	661
	5	363	484	404	505	550	652	594	674
	5.5	358	485	393	498	530	636	601	652
	6	356	486	385	491	519	627	598	637
	6.5	345	477	365	474	493	602	603	603
8ft	3.5	425	677	520	689	633	811	704	864
	4	469	701	564	732	693	888	764	950
	4.5	486	733	579	766	702	907	768	974
	5	511	769	596	803	728	941	787	1013
	5.5	517	782	591	812	719	937	766	1008
	6	523	791	583	817	716	934	750	1007
	6.5	518	782	562	804	694	909	711	978
12ft	3.5	536	1212	642	877	764	1207	983	1061
	4	584	1245	692	935	833	1208	910	1190
	4.5	612	1263	720	1004	853	1231	931	1258
	5	644	1260	751	1083	887	1266	966	1344
	5.5	654	1224	756	1130	881	1259	957	1376
	6	663	1198	758	1207	880	1247	952	1431
	6.5	662	1148	748	1288	863	1212	926	1524

Table B-7: Max Principal Stress at Transverse Crack, $E=5\times10^6$ psi, $\alpha_C=4.5\times10^{-6}$/˚F, k-value=300 psi/in

Crack Spacing (ft)	Steel Depth (in)	k-value=300							
		400 Micro-strain Ultimate Shrinkage				700 Micro-strain Ultimate Shrinkage			
		3 F˚/in Gradient		-1.5 F˚/in Gradient		3 F˚/in Gradient		-1.5 F˚/in Gradient	
		30 F˚ Drop	50 F˚ Drop	30 F˚ Drop	50 F˚ Drop	30 F˚ Drop	50 F˚ Drop	30 F˚ Drop	50 F˚ Drop
		Max Principal Stress at crack (psi)	Max Principal Stress at crack (psi)	Max Principal Stress at crack (psi)	Max Principal Stress at crack (psi)	Max Principal Stress at crack (psi)	Max Principal Stress at crack (psi)	Max Principal Stress at crack (psi)	Max Principal Stress at crack (psi)
4ft	3.5	383	501	443	546	614	713	662	757
	4	418	547	480	588	664	773	709	817
	4.5	425	564	484	600	659	775	698	813
	5	441	587	494	616	675	797	705	827
	5.5	436	588	481	607	651	778	673	799
	6	433	590	469	598	637	767	656	778
	6.5	421	579	445	575	605	736	663	736
8ft	3.5	513	826	647	858	777	994	874	1077
	4	569	855	695	906	851	1091	947	1184
	4.5	592	892	712	947	862	1112	950	1211
	5	623	939	732	991	895	1156	971	1258
	5.5	631	955	723	1000	883	1150	942	1249
	6	640	968	712	1004	880	1148	920	1244
	6.5	634	959	684	987	853	1117	869	1205
12ft	3.5	663	1546	808	1117	936	1553	1043	1361
	4	709	1606	862	1195	1025	1597	1144	1531
	4.5	747	1647	897	1298	1052	1622	1169	1621
	5	789	1659	937	1420	1095	1599	1213	1732
	5.5	805	1646	942	1523	1090	1592	1201	1819
	6	818	1596	943	1622	1089	1579	1196	1967
	6.5	820	1550	928	1725	1068	1533	1160	2038

Table B-8: Max Principal Stress at Transverse Crack, E=5×10^6 psi, α_C=4.5×10^{-6}/˚F, k-value=500 psi/in

Crack Spacing (ft)	Steel Depth (in)	k-value=500							
		400 Micro-strain Ultimate Shrinkage				700 Micro-strain Ultimate Shrinkage			
		3 F˚/in Gradient		-1.5 F˚/in Gradient		3 F˚/in Gradient		-1.5 F˚/in Gradient	
		30 F˚ Drop	50 F˚ Drop	30 F˚ Drop	50 F˚ Drop	30 F˚ Drop	50 F˚ Drop	30 F˚ Drop	50 F˚ Drop
		Max Principal Stress at crack (psi)	Max Principal Stress at crack (psi)	Max Principal Stress at crack (psi)	Max Principal Stress at crack (psi)	Max Principal Stress at crack (psi)	Max Principal Stress at crack (psi)	Max Principal Stress at crack (psi)	Max Principal Stress at crack (psi)
4ft	3.5	388	506	443	548	617	716	726	756
	4	423	551	480	588	667	775	713	815
	4.5	429	568	484	600	662	778	721	813
	5	444	589	492	616	677	799	712	827
	5.5	438	590	481	607	652	779	721	799
	6	435	591	470	598	638	768	717	779
	6.5	421	579	447	577	606	736	724	737
8ft	3.5	520	824	648	859	781	997	873	1076
	4	574	858	695	905	854	1093	946	1182
	4.5	596	896	712	947	865	1114	949	1210
	5	626	940	732	991	897	1157	971	1257
	5.5	633	956	724	1001	885	1151	942	1248
	6	640	968	713	1005	880	1148	921	1244
	6.5	634	958	686	988	853	1117	870	1204
12ft	3.5	652	1506	808	1116	942	1513	1234	1364
	4	716	1558	860	1201	1029	1526	1138	1529
	4.5	751	1592	894	1294	1054	1551	1163	1613
	5	792	1603	932	1404	1096	1586	1205	1718
	5.5	805	1592	973	1495	1089	1579	1191	1775
	6	816	1551	938	1583	1087	1568	1184	1904
	6.5	817	1512	925	1674	1067	1524	1149	1968

Table B-9: Max Principal Stress at Transverse Crack, $E=4\times10^6$ psi, $\alpha_C=5.5\times10^{-6}/°F$, k-value=300 psi/in

Crack Spacing (ft)	Steel Depth (in)	k-value=300							
		400 Micro-strain Ultimate Shrinkage				700 Micro-strain Ultimate Shrinkage			
		3 F˚/in Gradient		-1.5 F˚/in Gradient		3 F˚/in Gradient		-1.5 F˚/in Gradient	
		30 F˚ Drop	50 F˚ Drop	30 F˚ Drop	50 F˚ Drop	30 F˚ Drop	50 F˚ Drop	30 F˚ Drop	50 F˚ Drop
		Max Principal Stress at crack (psi)	Max Principal Stress at crack (psi)	Max Principal Stress at crack (psi)	Max Principal Stress at crack (psi)	Max Principal Stress at crack (psi)	Max Principal Stress at crack (psi)	Max Principal Stress at crack (psi)	Max Principal Stress at crack (psi)
4ft	3.5	351	481	416	527	539	651	589	700
	4	382	523	448	569	582	704	631	752
	4.5	391	542	453	582	582	712	623	752
	5	407	565	462	597	597	733	629	765
	5.5	407	570	451	591	582	723	603	743
	6	409	574	441	584	574	717	584	726
	6.5	401	568	421	565	551	695	564	692
8ft	3.5	479	857	600	807	693	944	788	994
	4	530	888	649	867	760	1032	853	1092
	4.5	554	914	668	912	775	1058	861	1127
	5	586	940	688	958	807	1101	883	1177
	5.5	599	956	684	975	804	1101	863	1183
	6	611	968	677	987	805	1103	847	1190
	6.5	609	958	655	982	787	1078	807	1167
12ft	3.5	693	1776	739	1066	863	1777	937	1228
	4	726	1840	801	1115	942	1821	1029	1384
	4.5	752	1877	839	1212	972	1843	1060	1487
	5	770	1879	880	1329	1012	1824	1108	1616
	5.5	781	1846	893	1472	1013	1773	1110	1755
	6	797	1765	901	1611	1016	1672	1116	1952
	6.5	799	1670	899	1762	999	1577	1097	2074

Table B-10: Max Principal Stress at Transverse Crack, E=4×10^6 psi, α_C=5.5×10^{-6}/˚F, k-value=500 psi/in

Crack Spacing (ft)	Steel Depth (in)	k-value=500							
		400 Micro-strain Ultimate Shrinkage				700 Micro-strain Ultimate Shrinkage			
		3 F˚/in Gradient		-1.5 F˚/in Gradient		3 F˚/in Gradient		-1.5 F˚/in Gradient	
		30 F˚ Drop	50 F˚ Drop	30 F˚ Drop	50 F˚ Drop	30 F˚ Drop	50 F˚ Drop	30 F˚ Drop	50 F˚ Drop
		Max Principal Stress at crack (psi)	Max Principal Stress at crack (psi)	Max Principal Stress at crack (psi)	Max Principal Stress at crack (psi)	Max Principal Stress at crack (psi)	Max Principal Stress at crack (psi)	Max Principal Stress at crack (psi)	Max Principal Stress at crack (psi)
4ft	3.5	357	487	415	527	544	655	625	699
	4	387	529	447	568	586	708	630	751
	4.5	396	547	453	582	585	715	622	752
	5	410	569	462	597	600	736	630	765
	5.5	410	572	452	592	584	725	620	744
	6	411	576	442	585	575	719	617	727
	6.5	402	569	422	566	551	696	622	693
8ft	3.5	487	850	599	809	699	947	786	993
	4	536	881	649	867	764	1035	851	1091
	4.5	559	905	667	912	778	1059	860	1126
	5	589	940	689	958	809	1101	882	1176
	5.5	600	956	685	975	805	1101	863	1181
	6	612	966	678	987	806	1102	848	1188
	6.5	609	956	657	981	786	1077	809	1165
12ft	3.5	673	1710	740	1054	868	1707	934	1232
	4	701	1762	800	1118	945	1743	1024	1385
	4.5	724	1790	835	1212	973	1759	1053	1482
	5	763	1787	875	1319	1011	1739	1098	1597
	5.5	779	1756	887	1439	1010	1696	1097	1706
	6	792	1688	895	1562	1012	1614	1101	1875
	6.5	793	1606	889	1694	995	1532	1082	1983

Table B-11: Max Principal Stress at Transverse Crack, $E=5\times10^6$ psi, $\alpha_C=5.5\times10^{-6}/^\circ F$, k-value=300 psi/in

Crack Spacing (ft)	Steel Depth (in)	k-value=300							
		400 Micro-strain Ultimate Shrinkage				700 Micro-strain Ultimate Shrinkage			
		3 F˚/in Gradient		-1.5 F˚/in Gradient		3 F˚/in Gradient		-1.5 F˚/in Gradient	
		30 F˚ Drop	50 F˚ Drop	30 F˚ Drop	50 F˚ Drop	30 F˚ Drop	50 F˚ Drop	30 F˚ Drop	50 F˚ Drop
		Max Principal Stress at crack (psi)	Max Principal Stress at crack (psi)	Max Principal Stress at crack (psi)	Max Principal Stress at crack (psi)	Max Principal Stress at crack (psi)	Max Principal Stress at crack (psi)	Max Principal Stress at crack (psi)	Max Principal Stress at crack (psi)
4ft	3.5	428	586	511	645	663	799	727	862
	4	467	638	549	696	717	864	778	924
	4.5	478	660	555	711	715	872	767	923
	5	497	688	565	729	735	899	775	938
	5.5	497	693	552	720	715	884	742	910
	6	500	698	539	711	704	877	717	889
	6.5	489	691	514	688	675	849	678	846
8ft	3.5	584	1040	743	1005	852	1158	976	1240
	4	647	1083	800	1077	934	1269	1056	1365
	4.5	677	1119	821	1131	952	1299	1064	1404
	5	715	1150	845	1186	991	1353	1089	1467
	5.5	731	1173	838	1206	987	1353	1062	1469
	6	747	1189	828	1222	988	1355	1040	1473
	6.5	745	1180	799	1212	965	1325	989	1440
12ft	3.5	840	2180	931	1409	1061	2196	1175	1591
	4	885	2274	998	1477	1160	2267	1290	1798
	4.5	921	2337	1046	1620	1199	2312	1328	1943
	5	949	2361	1096	1801	1249	2310	1390	2164
	5.5	966	2343	1110	1960	1251	2270	1389	2356
	6	982	2275	1121	2145	1256	2166	1392	2547
	6.5	986	2170	1118	2279	1236	2064	1363	2661

Table B-12: Max Principal Stress at Transverse Crack, $E=5\times10^6$ psi, $\alpha_C=5.5\times10^{-6}/^\circ F$, k-value=500 psi/in

Crack Spacing (ft)	Steel Depth (in)	k-value=500							
		400 Micro-strain Ultimate Shrinkage				700 Micro-strain Ultimate Shrinkage			
		3 F˚/in Gradient		-1.5 F˚/in Gradient		3 F˚/in Gradient		-1.5 F˚/in Gradient	
		30 F˚ Drop	50 F˚ Drop	30 F˚ Drop	50 F˚ Drop	30 F˚ Drop	50 F˚ Drop	30 F˚ Drop	50 F˚ Drop
		Max Principal Stress at crack (psi)	Max Principal Stress at crack (psi)	Max Principal Stress at crack (psi)	Max Principal Stress at crack (psi)	Max Principal Stress at crack (psi)	Max Principal Stress at crack (psi)	Max Principal Stress at crack (psi)	Max Principal Stress at crack (psi)
4ft	3.5	436	594	509	645	669	804	747	860
	4	473	644	549	695	721	869	777	923
	4.5	483	666	555	711	719	876	767	923
	5	501	692	565	729	737	902	775	938
	5.5	500	696	552	721	717	887	742	919
	6	501	700	540	712	706	879	738	890
	6.5	490	692	516	689	676	850	745	847
8ft	3.5	593	1034	744	1006	858	1162	974	1239
	4	654	1077	799	1074	939	1272	1054	1363
	4.5	682	1112	821	1131	956	1301	1062	1403
	5	719	1151	846	1186	994	1353	1088	1466
	5.5	733	1172	839	1206	988	1353	1061	1468
	6	747	1187	829	1221	989	1354	1040	1472
	6.5	745	1178	801	1211	965	1324	991	1439
12ft	3.5	820	2119	931	1404	1068	2132	1170	1596
	4	861	2200	995	1487	1165	2193	1284	1800
	4.5	894	2253	1041	1618	1200	2231	1319	1927
	5	937	2271	1091	1782	1248	2227	1376	2125
	5.5	959	2253	1104	1923	1249	2192	1374	2294
	6	977	2188	1111	2087	1251	2107	1375	2464
	6.5	979	2101	1105	2208	1231	2017	1347	2567

Appendix C: Maximum Principal Stresses at Concrete Slab Between 2 Adjacent Transverse Cracks for Two-Mat CRCP

Table C-1: Max Principal Stress at Concrete Slab, $E=4\times10^6$ psi, $\alpha_C=3.5\times10^{-6}$/˚F, k-value=300 psi/in, Crack Spacing = 4 ft

First Layer Steel Depth (in)	Second Layer Steel Depth (in)	k-value=300							
		400 Microstrain Ultimate Shrinkage				700 Microstrain Ultimate Shrinkage			
		3 F˚/in Gradient		1.5 F˚/in Gradient		3 F˚/in Gradient		1.5 F˚/in Gradient	
		30 F˚ Drop	50 F˚ Drop	30 F˚ Drop	50 F˚ Drop	30 F˚ Drop	50 F˚ Drop	30 F˚ Drop	50 F˚ Drop
		Max Principal Stress at Slab (psi)	Max Principal Stress at Slab (psi)	Max Principal Stress at Slab (psi)	Max Principal Stress at Slab (psi)	Max Principal Stress at Slab (psi)	Max Principal Stress at Slab (psi)	Max Principal Stress at Slab (psi)	Max Principal Stress at Slab (psi)
3.5	6.5	308	367	350	397	559	605	589	636
	7	304	358	344	387	553	596	585	625
	7.5	299	350	338	378	547	588	584	616
	8	293	341	331	369	540	578	584	606
4	6.5	309	363	344	387	562	605	591	629
	7	304	355	337	378	556	597	591	619
	7.5	299	347	331	368	550	588	590	609
	8	294	338	331	359	544	579	590	600
4.5	6.5	306	356	335	375	558	598	591	617
	7	301	348	331	365	552	589	591	606
	7.5	296	340	331	356	546	581	591	597
	8	291	331	330	347	540	571	590	592
5	6.5	301	347	330	361	549	587	588	601
	7	296	339	329	352	544	578	588	590
	7.5	291	331	329	342	538	569	588	589
	8	286	322	329	334	531	560	587	589

Table C-2: Max Principal Stress at Concrete Slab, E=4×10^6 psi, α_C=3.5×10^{-6}/˚F, k-value=500 psi/in, Crack Spacing = 4 ft

First Layer Steel Depth (in)	Second Layer Steel Depth (in)	k-value=500							
		400 Microstrain Ultimate Shrinkage				700 Microstrain Ultimate Shrinkage			
		3 F˚/in Gradient		1.5 F˚/in Gradient		3 F˚/in Gradient		1.5 F˚/in Gradient	
		30 F˚ Drop	50 F˚ Drop	30 F˚ Drop	50 F˚ Drop	30 F˚ Drop	50 F˚ Drop	30 F˚ Drop	50 F˚ Drop
		Max Principal Stress at Slab (psi)	Max Principal Stress at Slab (psi)	Max Principal Stress at Slab (psi)	Max Principal Stress at Slab (psi)	Max Principal Stress at Slab (psi)	Max Principal Stress at Slab (psi)	Max Principal Stress at Slab (psi)	Max Principal Stress at Slab (psi)
3.5	6.5	308	366	368	399	558	605	635	638
	7	303	358	367	389	552	596	634	637
	7.5	298	349	367	380	546	587	634	637
	8	292	340	366	371	540	578	633	636
4	6.5	308	362	369	389	561	605	640	643
	7	303	354	369	380	556	596	639	642
	7.5	298	346	368	371	550	587	639	641
	8	293	337	368	370	543	578	639	641
4.5	6.5	305	356	369	377	557	598	640	642
	7	300	348	368	370	551	589	639	641
	7.5	295	339	368	370	546	580	639	641
	8	290	330	367	369	539	571	638	640
5	6.5	300	347	367	369	549	586	637	639
	7	295	339	366	368	543	578	636	638
	7.5	290	330	366	367	537	569	636	637
	8	285	321	365	367	531	560	636	637

Table C-3: Max Principal Stress at Concrete Slab, E=5×10^6 psi, α_C=3.5×10^{-6}/˚F, k-value=300 psi/in, Crack Spacing = 4 ft

First Layer Steel Depth (in)	Second Layer Steel Depth (in)	k-value=300							
		400 Microstrain Ultimate Shrinkage				700 Microstrain Ultimate Shrinkage			
		3 F˚/in Gradient		1.5 F˚/in Gradient		3 F˚/in Gradient		1.5 F˚/in Gradient	
		30 F˚ Drop	50 F˚ Drop	30 F˚ Drop	50 F˚ Drop	30 F˚ Drop	50 F˚ Drop	30 F˚ Drop	50 F˚ Drop
		Max Principal Stress at Slab (psi)	Max Principal Stress at Slab (psi)	Max Principal Stress at Slab (psi)	Max Principal Stress at Slab (psi)	Max Principal Stress at Slab (psi)	Max Principal Stress at Slab (psi)	Max Principal Stress at Slab (psi)	Max Principal Stress at Slab (psi)
3.5	6.5	380	448	428	482	691	745	725	779
	7	374	438	420	471	683	735	716	767
	7.5	368	428	413	460	677	724	709	756
	8	362	418	405	449	669	713	706	745
4	6.5	380	444	421	471	695	746	722	773
	7	375	435	413	460	688	736	714	761
	7.5	369	425	405	449	681	725	714	749
	8	363	414	398	439	674	715	714	739
4.5	6.5	377	436	410	457	690	738	715	758
	7	372	427	402	446	684	728	715	746
	7.5	366	417	396	435	677	717	715	735
	8	360	406	395	424	669	706	715	724
5	6.5	371	426	398	441	681	724	712	739
	7	366	416	394	430	674	714	712	727
	7.5	360	406	393	419	667	704	711	716
	8	354	396	393	409	659	693	711	712

Table C-4: Max Principal Stress at Concrete Slab, $E=5\times10^6$ psi, $\alpha_C=3.5\times10^{-6}/^\circ F$, k-value=500 psi/in, Crack Spacing = 4 ft

First Layer Steel Depth (in)	Second Layer Steel Depth (in)	k-value=500							
		400 Microstrain Ultimate Shrinkage				700 Microstrain Ultimate Shrinkage			
		3 F˚/in Gradient		1.5 F˚/in Gradient		3 F˚/in Gradient		1.5 F˚/in Gradient	
		30 F˚ Drop	50 F˚ Drop	30 F˚ Drop	50 F˚ Drop	30 F˚ Drop	50 F˚ Drop	30 F˚ Drop	50 F˚ Drop
		Max Principal Stress at Slab (psi)	Max Principal Stress at Slab (psi)	Max Principal Stress at Slab (psi)	Max Principal Stress at Slab (psi)	Max Principal Stress at Slab (psi)	Max Principal Stress at Slab (psi)	Max Principal Stress at Slab (psi)	Max Principal Stress at Slab (psi)
3.5	6.5	379	447	437	484	690	745	764	782
	7	373	437	437	473	683	734	763	770
	7.5	368	428	436	462	676	724	763	766
	8	361	417	435	451	668	713	762	765
4	6.5	380	444	439	473	695	746	771	776
	7	374	434	439	462	688	735	770	773
	7.5	368	424	438	451	681	725	770	772
	8	362	414	438	441	674	714	770	772
4.5	6.5	376	436	439	459	690	737	771	774
	7	371	426	438	448	683	727	771	773
	7.5	365	416	438	440	676	717	770	772
	8	359	406	437	439	669	706	770	771
5	6.5	370	425	437	443	680	724	767	770
	7	365	416	436	438	673	714	767	769
	7.5	359	406	436	437	666	703	767	768
	8	353	395	435	436	659	693	766	768

Table C-5: Max Principal Stress at Concrete Slab, E=4×10^6 psi, α_C=4.5×10^{-6}/˚F, k-value=300 psi/in, Crack Spacing = 4 ft

First Layer Steel Depth (in)	Second Layer Steel Depth (in)	k-value=300							
		400 Microstrain Ultimate Shrinkage				700 Microstrain Ultimate Shrinkage			
		3 F˚/in Gradient		1.5 F˚/in Gradient		3 F˚/in Gradient		1.5 F˚/in Gradient	
		30 F˚ Drop	50 F˚ Drop	30 F˚ Drop	50 F˚ Drop	30 F˚ Drop	50 F˚ Drop	30 F˚ Drop	50 F˚ Drop
		Max Principal Stress at Slab (psi)	Max Principal Stress at Slab (psi)	Max Principal Stress at Slab (psi)	Max Principal Stress at Slab (psi)	Max Principal Stress at Slab (psi)	Max Principal Stress at Slab (psi)	Max Principal Stress at Slab (psi)	Max Principal Stress at Slab (psi)
3.5	6.5	323	396	373	433	573	633	612	672
	7	317	386	365	421	566	622	603	659
	7.5	311	376	358	410	559	612	599	648
	8	304	364	350	398	551	600	598	636
4	6.5	323	392	365	420	576	632	607	663
	7	317	382	357	409	569	622	605	650
	7.5	311	371	349	397	562	611	604	638
	8	305	360	345	386	555	599	604	627
4.5	6.5	320	383	354	405	571	623	605	647
	7	314	373	346	394	565	613	605	635
	7.5	308	363	345	382	558	602	604	623
	8	301	352	344	371	550	591	604	611
5	6.5	314	373	344	389	563	611	602	628
	7	308	363	343	377	556	600	602	616
	7.5	302	353	343	366	549	589	601	604
	8	296	342	342	355	541	578	601	603

Table C-6: Max Principal Stress at Concrete Slab, $E=4\times10^6$ psi, $\alpha_C=4.5\times10^{-6}$/˚F, k-value=500 psi/in, Crack Spacing = 4 ft

First Layer Steel Depth (in)	Second Layer Steel Depth (in)	k-value=500							
		400 Microstrain Ultimate Shrinkage				700 Microstrain Ultimate Shrinkage			
		3 F˚/in Gradient		1.5 F˚/in Gradient		3 F˚/in Gradient		1.5 F˚/in Gradient	
		30 F˚ Drop	50 F˚ Drop	30 F˚ Drop	50 F˚ Drop	30 F˚ Drop	50 F˚ Drop	30 F˚ Drop	50 F˚ Drop
		Max Principal Stress at Slab (psi)	Max Principal Stress at Slab (psi)	Max Principal Stress at Slab (psi)	Max Principal Stress at Slab (psi)	Max Principal Stress at Slab (psi)	Max Principal Stress at Slab (psi)	Max Principal Stress at Slab (psi)	Max Principal Stress at Slab (psi)
3.5	6.5	322	395	388	435	572	632	655	675
	7	316	385	387	423	565	622	654	662
	7.5	310	374	387	412	559	611	654	657
	8	303	363	386	401	550	599	653	656
4	6.5	322	390	389	423	575	631	660	666
	7	316	380	389	411	568	621	659	662
	7.5	310	370	388	400	561	610	659	661
	8	304	359	388	390	554	599	658	661
4.5	6.5	318	382	389	408	571	623	659	663
	7	313	372	388	396	564	612	659	661
	7.5	307	362	387	390	557	601	658	661
	8	300	351	387	389	549	590	658	660
5	6.5	313	372	387	391	562	610	656	659
	7	307	362	386	388	555	600	656	658
	7.5	301	352	385	387	548	589	655	657
	8	295	341	385	386	541	578	655	656

Table C-7: Max Principal Stress at Concrete Slab, E=5×10^6 psi, α_C=4.5×10^{-6}/˚F, k-value=300 psi/in, Crack Spacing = 4 ft

First Layer Steel Depth (in)	Second Layer Steel Depth (in)	k-value=300							
		400 Microstrain Ultimate Shrinkage				700 Microstrain Ultimate Shrinkage			
		3 F˚/in Gradient		1.5 F˚/in Gradient		3 F˚/in Gradient		1.5 F˚/in Gradient	
		30 F˚ Drop	50 F˚ Drop	30 F˚ Drop	50 F˚ Drop	30 F˚ Drop	50 F˚ Drop	30 F˚ Drop	50 F˚ Drop
		Max Principal Stress at Slab (psi)	Max Principal Stress at Slab (psi)	Max Principal Stress at Slab (psi)	Max Principal Stress at Slab (psi)	Max Principal Stress at Slab (psi)	Max Principal Stress at Slab (psi)	Max Principal Stress at Slab (psi)	Max Principal Stress at Slab (psi)
3.5	6.5	397	482	454	524	708	778	751	821
	7	390	471	445	510	699	765	741	807
	7.5	383	458	436	497	691	753	732	793
	8	375	445	427	484	682	739	723	779
4	6.5	397	478	445	510	712	777	746	812
	7	391	466	435	496	704	765	736	797
	7.5	383	454	426	483	695	752	729	783
	8	376	441	418	470	687	739	729	770
4.5	6.5	393	468	432	493	707	768	733	794
	7	387	456	423	479	699	755	730	779
	7.5	380	444	414	465	690	743	730	765
	8	372	431	410	452	681	729	729	752
5	6.5	387	456	418	474	696	753	727	772
	7	380	444	408	460	688	740	726	757
	7.5	373	432	408	446	680	727	726	743
	8	365	419	408	434	671	714	726	730

Table C-8: Max Principal Stress at Concrete Slab, E=5×10^6 psi, α_C=4.5×10^{-6}/˚F, k-value=500 psi/in, Crack Spacing = 4 ft

First Layer Steel Depth (in)	Second Layer Steel Depth (in)	k-value=500							
		400 Microstrain Ultimate Shrinkage				700 Microstrain Ultimate Shrinkage			
		3 F˚/in Gradient		1.5 F˚/in Gradient		3 F˚/in Gradient		1.5 F˚/in Gradient	
		30 F˚ Drop	50 F˚ Drop	30 F˚ Drop	50 F˚ Drop	30 F˚ Drop	50 F˚ Drop	30 F˚ Drop	50 F˚ Drop
		Max Principal Stress at Slab (psi)	Max Principal Stress at Slab (psi)	Max Principal Stress at Slab (psi)	Max Principal Stress at Slab (psi)	Max Principal Stress at Slab (psi)	Max Principal Stress at Slab (psi)	Max Principal Stress at Slab (psi)	Max Principal Stress at Slab (psi)
3.5	6.5	395	481	459	527	707	777	786	825
	7	389	469	458	513	699	764	785	810
	7.5	382	457	458	500	691	752	784	796
	8	374	444	457	486	681	738	783	787
4	6.5	396	476	461	513	711	776	792	815
	7	389	465	460	499	703	764	792	800
	7.5	382	452	460	485	695	751	791	794
	8	375	440	459	472	686	738	791	793
4.5	6.5	392	467	460	495	706	767	792	797
	7	386	455	460	481	698	754	792	795
	7.5	379	443	459	468	690	742	791	794
	8	371	430	458	461	681	729	791	793
5	6.5	386	455	458	476	696	752	789	791
	7	379	443	457	462	688	740	788	790
	7.5	372	431	457	459	679	727	787	789
	8	364	418	456	458	670	714	787	789

Table C-9: Max Principal Stress at Concrete Slab, E=4×10^6 psi, α_C=5.5×10^{-6}/˚F, k-value=300 psi/in, Crack Spacing = 4 ft

First Layer Steel Depth (in)	Second Layer Steel Depth (in)	k-value=300							
		400 Microstrain Ultimate Shrinkage				700 Microstrain Ultimate Shrinkage			
		3 F˚/in Gradient		1.5 F˚/in Gradient		3 F˚/in Gradient		1.5 F˚/in Gradient	
		30 F˚ Drop	50 F˚ Drop	30 F˚ Drop	50 F˚ Drop	30 F˚ Drop	50 F˚ Drop	30 F˚ Drop	50 F˚ Drop
		Max Principal Stress at Slab (psi)	Max Principal Stress at Slab (psi)	Max Principal Stress at Slab (psi)	Max Principal Stress at Slab (psi)	Max Principal Stress at Slab (psi)	Max Principal Stress at Slab (psi)	Max Principal Stress at Slab (psi)	Max Principal Stress at Slab (psi)
3.5	6.5	337	422	397	470	587	660	637	710
	7	331	410	387	456	579	648	627	695
	7.5	323	398	379	442	571	635	618	681
	8	315	385	370	429	562	621	614	668
4	6.5	337	417	387	455	590	658	630	698
	7	331	405	377	441	582	646	621	683
	7.5	323	392	368	427	573	633	620	669
	8	316	379	360	414	565	620	620	656
4.5	6.5	334	407	374	437	585	648	621	680
	7	327	396	365	423	577	636	621	665
	7.5	320	383	360	409	568	623	620	651
	8	312	370	359	396	560	610	620	638
5	6.5	327	395	360	418	575	634	618	658
	7	321	384	358	404	568	622	618	644
	7.5	314	371	357	390	559	609	617	630
	8	306	358	357	377	550	596	617	618

Table C-10: Max Principal Stress at Concrete Slab, E=4×10^6 psi, α_C=5.5×10^{-6}/°F, k-value=500 psi/in, Crack Spacing = 4 ft

First Layer Steel Depth (in)	Second Layer Steel Depth (in)	k-value=500							
		400 Microstrain Ultimate Shrinkage				700 Microstrain Ultimate Shrinkage			
		3 F°/in Gradient		1.5 F°/in Gradient		3 F°/in Gradient		1.5 F°/in Gradient	
		30 F° Drop	50 F° Drop	30 F° Drop	50 F° Drop	30 F° Drop	50 F° Drop	30 F° Drop	50 F° Drop
		Max Principal Stress at Slab (psi)	Max Principal Stress at Slab (psi)	Max Principal Stress at Slab (psi)	Max Principal Stress at Slab (psi)	Max Principal Stress at Slab (psi)	Max Principal Stress at Slab (psi)	Max Principal Stress at Slab (psi)	Max Principal Stress at Slab (psi)
3.5	6.5	336	421	411	473	586	659	677	713
	7	329	409	410	459	578	647	676	699
	7.5	322	397	409	445	570	634	675	685
	8	314	383	408	432	561	620	674	678
4	6.5	336	415	410	458	588	657	681	701
	7	329	403	409	443	581	645	681	687
	7.5	322	391	409	430	572	632	680	683
	8	314	378	408	417	564	618	679	682
4.5	6.5	332	406	409	440	584	647	681	685
	7	326	394	408	426	576	635	680	684
	7.5	318	382	408	412	567	622	680	682
	8	311	369	407	409	559	609	679	681
5	6.5	326	394	407	421	574	633	678	681
	7	319	382	406	409	567	621	677	680
	7.5	312	370	405	408	558	608	676	679
	8	305	357	405	407	549	595	676	678

Table C-11: Max Principal Stress at Concrete Slab, E=5×10^6 psi, α_C=5.5×10^{-6}/˚F, k-value=300 psi/in, Crack Spacing = 4 ft

First Layer Steel Depth (in)	Second Layer Steel Depth (in)	k-value=300							
		400 Microstrain Ultimate Shrinkage				700 Microstrain Ultimate Shrinkage			
		3 F˚/in Gradient		1.5 F˚/in Gradient		3 F˚/in Gradient		1.5 F˚/in Gradient	
		30 F˚ Drop	50 F˚ Drop	30 F˚ Drop	50 F˚ Drop	30 F˚ Drop	50 F˚ Drop	30 F˚ Drop	50 F˚ Drop
		Max Principal Stress at Slab (psi)	Max Principal Stress at Slab (psi)	Max Principal Stress at Slab (psi)	Max Principal Stress at Slab (psi)	Max Principal Stress at Slab (psi)	Max Principal Stress at Slab (psi)	Max Principal Stress at Slab (psi)	Max Principal Stress at Slab (psi)
3.5	6.5	414	513	482	567	724	809	780	866
	7	406	499	471	551	715	795	769	849
	7.5	398	485	461	535	705	780	758	833
	8	388	469	450	519	694	764	747	816
4	6.5	414	507	471	550	728	808	773	853
	7	406	493	460	534	718	793	762	836
	7.5	398	479	449	518	709	778	751	819
	8	389	463	439	502	698	763	746	804
4.5	6.5	410	496	456	530	722	797	758	832
	7	402	482	445	513	713	782	747	815
	7.5	394	468	434	497	703	767	747	798
	8	384	452	426	482	693	751	746	783
5	6.5	403	482	439	507	711	780	744	807
	7	395	469	428	491	702	765	743	790
	7.5	386	454	424	475	692	750	743	773
	8	377	439	423	460	682	735	742	758

Table C-12: Max Principal Stress at Concrete Slab, E=5×10^6 psi, α_C=5.5×10^{-6}/˚F, k-value=500 psi/in, Crack Spacing = 4 ft

First Layer Steel Depth (in)	Second Layer Steel Depth (in)	k-value=500							
		400 Microstrain Ultimate Shrinkage				700 Microstrain Ultimate Shrinkage			
		3 F˚/in Gradient		1.5 F˚/in Gradient		3 F˚/in Gradient		1.5 F˚/in Gradient	
		30 F˚ Drop	50 F˚ Drop	30 F˚ Drop	50 F˚ Drop	30 F˚ Drop	50 F˚ Drop	30 F˚ Drop	50 F˚ Drop
		Max Principal Stress at Slab (psi)	Max Principal Stress at Slab (psi)	Max Principal Stress at Slab (psi)	Max Principal Stress at Slab (psi)	Max Principal Stress at Slab (psi)	Max Principal Stress at Slab (psi)	Max Principal Stress at Slab (psi)	Max Principal Stress at Slab (psi)
3.5	6.5	412	512	485	570	723	808	809	870
	7	404	498	484	554	713	794	808	852
	7.5	396	483	483	538	704	779	808	836
	8	387	468	482	522	693	763	807	820
4	6.5	413	505	484	553	726	806	816	857
	7	405	492	483	537	717	792	815	840
	7.5	396	477	482	521	708	777	815	823
	8	387	462	481	505	697	762	814	817
4.5	6.5	408	495	483	532	721	795	816	836
	7	401	481	482	516	712	781	815	819
	7.5	392	466	481	500	702	766	815	818
	8	383	451	480	484	692	750	814	816
5	6.5	401	481	480	510	710	779	812	816
	7	394	467	479	494	701	764	811	814
	7.5	385	453	479	481	691	749	811	813
	8	376	437	478	480	681	734	810	812

Table C-13: Max Principal Stress at Concrete Slab, $E=4\times10^6$ psi, $\alpha_C=3.5\times10^{-6}$/˚F, k-value=300 psi/in, Crack Spacing = 8 ft

First Layer Steel Depth (in)	Second Layer Steel Depth (in)	k-value=300							
		400 Microstrain Ultimate Shrinkage				700 Microstrain Ultimate Shrinkage			
		3 F˚/in Gradient		1.5 F˚/in Gradient		3 F˚/in Gradient		1.5 F˚/in Gradient	
		30 F˚ Drop	50 F˚ Drop	30 F˚ Drop	50 F˚ Drop	30 F˚ Drop	50 F˚ Drop	30 F˚ Drop	50 F˚ Drop
		Max Principal Stress at Slab (psi)	Max Principal Stress at Slab (psi)	Max Principal Stress at Slab (psi)	Max Principal Stress at Slab (psi)	Max Principal Stress at Slab (psi)	Max Principal Stress at Slab (psi)	Max Principal Stress at Slab (psi)	Max Principal Stress at Slab (psi)
3.5	6.5	365	477	477	567	644	734	733	825
	7	357	463	466	551	634	718	721	808
	7.5	348	448	455	535	623	702	710	792
	8	338	431	444	520	611	686	699	775
4	6.5	364	470	464	550	643	728	722	809
	7	355	455	453	533	632	712	710	792
	7.5	346	439	442	517	621	696	698	775
	8	336	423	431	502	610	679	687	759
4.5	6.5	358	458	449	530	635	715	705	787
	7	350	443	437	513	624	699	693	769
	7.5	340	427	426	497	613	683	681	752
	8	331	411	415	481	601	666	670	736
5	6.5	351	444	432	508	623	698	686	762
	7	342	429	420	491	612	682	673	744
	7.5	333	413	409	474	601	665	661	726
	8	323	396	398	458	589	648	649	710

Table C-14: Max Principal Stress at Concrete Slab, E=4×10^6 psi, α_C=3.5×10^{-6}/˚F, k-value=500 psi/in, Crack Spacing = 8 ft

First Layer Steel Depth (in)	Second Layer Steel Depth (in)	k-value=500							
		400 Microstrain Ultimate Shrinkage				700 Microstrain Ultimate Shrinkage			
		3 F˚/in Gradient		1.5 F˚/in Gradient		3 F˚/in Gradient		1.5 F˚/in Gradient	
		30 F˚ Drop	50 F˚ Drop	30 F˚ Drop	50 F˚ Drop	30 F˚ Drop	50 F˚ Drop	30 F˚ Drop	50 F˚ Drop
		Max Principal Stress at Slab (psi)	Max Principal Stress at Slab (psi)	Max Principal Stress at Slab (psi)	Max Principal Stress at Slab (psi)	Max Principal Stress at Slab (psi)	Max Principal Stress at Slab (psi)	Max Principal Stress at Slab (psi)	Max Principal Stress at Slab (psi)
3.5	6.5	358	467	489	578	638	726	750	840
	7	350	452	478	562	628	711	738	823
	7.5	341	438	468	547	617	696	727	808
	8	332	422	458	532	606	680	717	792
4	6.5	356	459	477	561	637	720	739	825
	7	348	445	466	545	627	705	727	808
	7.5	339	430	455	530	616	690	716	792
	8	330	414	445	515	605	674	706	777
4.5	6.5	351	448	462	542	629	708	723	804
	7	343	433	451	526	619	693	711	787
	7.5	334	418	440	510	608	677	700	771
	8	325	402	430	495	597	661	689	755
5	6.5	344	434	446	521	617	691	704	780
	7	335	419	435	505	607	676	692	763
	7.5	326	404	424	489	596	660	680	746
	8	317	388	414	473	585	644	669	730

Table C-15: Max Principal Stress at Concrete Slab, E=5×10^6 psi, α_C=3.5×10^{-6}/˚F, k-value=300 psi/in, Crack Spacing = 8 ft

First Layer Steel Depth (in)	Second Layer Steel Depth (in)	k-value=300							
		400 Microstrain Ultimate Shrinkage				700 Microstrain Ultimate Shrinkage			
		3 F˚/in Gradient		1.5 F˚/in Gradient		3 F˚/in Gradient		1.5 F˚/in Gradient	
		30 F˚ Drop	50 F˚ Drop	30 F˚ Drop	50 F˚ Drop	30 F˚ Drop	50 F˚ Drop	30 F˚ Drop	50 F˚ Drop
		Max Principal Stress at Slab (psi)	Max Principal Stress at Slab (psi)	Max Principal Stress at Slab (psi)	Max Principal Stress at Slab (psi)	Max Principal Stress at Slab (psi)	Max Principal Stress at Slab (psi)	Max Principal Stress at Slab (psi)	Max Principal Stress at Slab (psi)
3.5	6.5	446	576	569	673	788	892	885	992
	7	436	558	556	654	776	874	871	971
	7.5	426	540	543	636	763	855	858	952
	8	414	521	531	618	750	835	845	933
4	6.5	445	567	554	653	788	886	873	973
	7	435	549	541	634	775	867	858	953
	7.5	424	531	528	615	762	848	845	933
	8	413	512	516	597	749	829	832	915
4.5	6.5	438	553	537	630	779	871	854	948
	7	428	536	523	610	766	852	839	927
	7.5	417	517	510	591	753	833	825	907
	8	406	498	497	572	739	813	812	888
5	6.5	429	536	517	604	764	850	830	918
	7	419	519	503	584	752	831	815	897
	7.5	408	500	490	564	738	812	801	877
	8	396	480	477	546	724	792	788	857

Table C-16: Max Principal Stress at Concrete Slab, E=5×10^6 psi, α_C=3.5×10^{-6}/˚F, k-value=500 psi/in, Crack Spacing = 8 ft

First Layer Steel Depth (in)	Second Layer Steel Depth (in)	k-value=500							
		400 Microstrain Ultimate Shrinkage				700 Microstrain Ultimate Shrinkage			
		3 F˚/in Gradient		1.5 F˚/in Gradient		3 F˚/in Gradient		1.5 F˚/in Gradient	
		30 F˚ Drop	50 F˚ Drop	30 F˚ Drop	50 F˚ Drop	30 F˚ Drop	50 F˚ Drop	30 F˚ Drop	50 F˚ Drop
		Max Principal Stress at Slab (psi)	Max Principal Stress at Slab (psi)	Max Principal Stress at Slab (psi)	Max Principal Stress at Slab (psi)	Max Principal Stress at Slab (psi)	Max Principal Stress at Slab (psi)	Max Principal Stress at Slab (psi)	Max Principal Stress at Slab (psi)
3.5	6.5	439	565	582	685	782	884	903	1008
	7	430	548	569	666	770	866	889	988
	7.5	420	531	557	649	758	848	876	970
	8	409	512	545	631	745	829	864	952
4	6.5	437	557	568	665	782	878	891	990
	7	428	539	555	647	770	860	877	971
	7.5	418	522	542	629	757	842	864	952
	8	407	503	531	611	744	823	852	934
4.5	6.5	431	543	551	643	773	863	872	966
	7	422	526	538	624	760	845	858	946
	7.5	411	508	525	605	748	827	845	927
	8	400	489	513	587	735	808	832	908
5	6.5	422	526	532	618	759	844	850	937
	7	413	509	519	599	746	826	835	917
	7.5	402	491	506	580	734	807	822	897
	8	391	472	493	562	720	788	809	879

Table C-17: Max Principal Stress at Concrete Slab, E=4×10^6 psi, α_C=4.5×10^{-6}/˚F, k-value=300 psi/in, Crack Spacing = 8 ft

First Layer Steel Depth (in)	Second Layer Steel Depth (in)	k-value=300							
		400 Microstrain Ultimate Shrinkage				700 Microstrain Ultimate Shrinkage			
		3 F˚/in Gradient		1.5 F˚/in Gradient		3 F˚/in Gradient		1.5 F˚/in Gradient	
		30 F˚ Drop	50 F˚ Drop	30 F˚ Drop	50 F˚ Drop	30 F˚ Drop	50 F˚ Drop	30 F˚ Drop	50 F˚ Drop
		Max Principal Stress at Slab (psi)	Max Principal Stress at Slab (psi)	Max Principal Stress at Slab (psi)	Max Principal Stress at Slab (psi)	Max Principal Stress at Slab (psi)	Max Principal Stress at Slab (psi)	Max Principal Stress at Slab (psi)	Max Principal Stress at Slab (psi)
3.5	6.5	388	527	524	640	666	781	780	898
	7	378	509	510	620	653	762	766	877
	7.5	367	489	497	601	640	743	752	857
	8	355	469	484	582	626	722	739	838
4	6.5	386	518	508	618	664	774	766	878
	7	376	499	494	598	652	755	752	857
	7.5	364	480	481	578	638	735	738	836
	8	353	459	468	559	625	714	725	817
4.5	6.5	380	504	490	594	656	759	747	852
	7	370	485	476	573	643	739	732	830
	7.5	358	466	462	553	630	719	717	810
	8	346	445	449	534	616	698	704	789
5	6.5	372	487	470	568	643	739	724	823
	7	361	469	456	547	630	720	709	800
	7.5	350	449	442	526	616	699	694	779
	8	337	428	429	506	602	678	680	759

Table C-18: Max Principal Stress at Concrete Slab, E=4×10^6 psi, α_C=4.5×10^{-6}/˚F, k-value=500 psi/in, Crack Spacing = 8 ft

First Layer Steel Depth (in)	Second Layer Steel Depth (in)	k-value=500							
		400 Microstrain Ultimate Shrinkage				700 Microstrain Ultimate Shrinkage			
		3 F˚/in Gradient		1.5 F˚/in Gradient		3 F˚/in Gradient		1.5 F˚/in Gradient	
		30 F˚ Drop	50 F˚ Drop	30 F˚ Drop	50 F˚ Drop	30 F˚ Drop	50 F˚ Drop	30 F˚ Drop	50 F˚ Drop
		Max Principal Stress at Slab (psi)	Max Principal Stress at Slab (psi)	Max Principal Stress at Slab (psi)	Max Principal Stress at Slab (psi)	Max Principal Stress at Slab (psi)	Max Principal Stress at Slab (psi)	Max Principal Stress at Slab (psi)	Max Principal Stress at Slab (psi)
3.5	6.5	379	512	537	651	656	769	798	914
	7	369	495	524	632	644	750	784	894
	7.5	358	477	512	614	632	732	771	875
	8	347	457	500	596	618	712	759	856
4	6.5	377	503	522	631	655	761	785	895
	7	367	486	509	612	643	743	771	875
	7.5	356	467	496	593	630	724	758	855
	8	345	447	484	574	616	704	745	837
4.5	6.5	371	490	505	608	646	747	766	870
	7	361	472	491	588	634	728	752	850
	7.5	350	453	479	569	621	709	738	830
	8	339	433	466	550	608	689	725	810
5	6.5	363	474	486	583	634	728	745	842
	7	353	456	473	563	621	709	730	821
	7.5	342	436	459	543	608	689	716	801
	8	330	417	447	524	595	669	703	781

Table C-19: Max Principal Stress at Concrete Slab, $E=5\times10^6$ psi, $\alpha_C=4.5\times10^{-6}/^{\circ}F$, k-value=300 psi/in, Crack Spacing = 8 ft

First Layer Steel Depth (in)	Second Layer Steel Depth (in)	k-value=300							
		400 Microstrain Ultimate Shrinkage				700 Microstrain Ultimate Shrinkage			
		3 F˚/in Gradient		1.5 F˚/in Gradient		3 F˚/in Gradient		1.5 F˚/in Gradient	
		30 F˚ Drop	50 F˚ Drop	30 F˚ Drop	50 F˚ Drop	30 F˚ Drop	50 F˚ Drop	30 F˚ Drop	50 F˚ Drop
		Max Principal Stress at Slab (psi)	Max Principal Stress at Slab (psi)	Max Principal Stress at Slab (psi)	Max Principal Stress at Slab (psi)	Max Principal Stress at Slab (psi)	Max Principal Stress at Slab (psi)	Max Principal Stress at Slab (psi)	Max Principal Stress at Slab (psi)
3.5	6.5	473	634	622	757	814	947	939	1076
	7	461	612	606	733	800	925	922	1051
	7.5	449	590	591	711	785	902	906	1028
	8	434	566	576	689	768	878	891	1005
4	6.5	471	623	604	732	813	940	923	1053
	7	459	602	588	708	799	917	906	1028
	7.5	446	579	572	685	783	894	890	1004
	8	432	555	558	663	767	870	875	981
4.5	6.5	465	608	583	703	804	922	901	1022
	7	452	586	567	679	789	899	883	997
	7.5	439	562	551	655	773	876	866	973
	8	425	538	536	633	757	851	851	949
5	6.5	454	588	560	672	788	899	874	988
	7	442	566	543	648	773	876	856	962
	7.5	429	542	527	624	757	852	839	937
	8	415	518	512	601	741	827	823	913

Table C-20: Max Principal Stress at Concrete Slab, E=5×10^6 psi, α_C=4.5×10^{-6}/˚F, k-value=500 psi/in, Crack Spacing = 8 ft

First Layer Steel Depth (in)	Second Layer Steel Depth (in)	k-value=500							
		400 Microstrain Ultimate Shrinkage				700 Microstrain Ultimate Shrinkage			
		3 F˚/in Gradient		1.5 F˚/in Gradient		3 F˚/in Gradient		1.5 F˚/in Gradient	
		30 F˚ Drop	50 F˚ Drop	30 F˚ Drop	50 F˚ Drop	30 F˚ Drop	50 F˚ Drop	30 F˚ Drop	50 F˚ Drop
		Max Principal Stress at Slab (psi)	Max Principal Stress at Slab (psi)	Max Principal Stress at Slab (psi)	Max Principal Stress at Slab (psi)	Max Principal Stress at Slab (psi)	Max Principal Stress at Slab (psi)	Max Principal Stress at Slab (psi)	Max Principal Stress at Slab (psi)
3.5	6.5	464	620	637	769	805	936	958	1093
	7	453	599	621	747	791	914	942	1069
	7.5	441	577	607	725	776	892	927	1047
	8	427	554	592	704	760	868	912	1025
4	6.5	462	610	620	745	804	928	943	1071
	7	451	588	604	723	790	906	927	1047
	7.5	438	566	589	700	775	883	911	1024
	8	425	543	575	679	759	860	896	1002
4.5	6.5	456	594	599	718	794	911	921	1042
	7	444	572	583	695	780	888	904	1017
	7.5	431	550	568	672	765	865	888	994
	8	418	527	554	650	749	842	873	971
5	6.5	445	574	577	688	779	888	896	1008
	7	434	553	561	665	765	865	878	984
	7.5	421	530	545	642	749	842	862	959
	8	408	507	531	619	733	818	847	936

Table C-21: Max Principal Stress at Concrete Slab, E=4×10^6 psi, α_C=5.5×10^{-6}/˚F, k-value=300 psi/in, Crack Spacing = 8 ft

First Layer Steel Depth (in)	Second Layer Steel Depth (in)	k-value=300							
		400 Microstrain Ultimate Shrinkage				700 Microstrain Ultimate Shrinkage			
		3 F˚/in Gradient		1.5 F˚/in Gradient		3 F˚/in Gradient		1.5 F˚/in Gradient	
		30 F˚ Drop	50 F˚ Drop	30 F˚ Drop	50 F˚ Drop	30 F˚ Drop	50 F˚ Drop	30 F˚ Drop	50 F˚ Drop
		Max Principal Stress at Slab (psi)	Max Principal Stress at Slab (psi)	Max Principal Stress at Slab (psi)	Max Principal Stress at Slab (psi)	Max Principal Stress at Slab (psi)	Max Principal Stress at Slab (psi)	Max Principal Stress at Slab (psi)	Max Principal Stress at Slab (psi)
3.5	6.5	411	574	571	714	687	829	830	974
	7	399	552	555	690	673	806	813	949
	7.5	386	530	540	667	658	783	797	926
	8	372	505	526	645	641	758	782	903
4	6.5	409	564	553	688	685	820	813	950
	7	397	542	537	664	671	797	796	925
	7.5	384	518	521	641	655	773	780	901
	8	369	493	507	618	639	748	764	877
4.5	6.5	403	548	532	660	676	803	790	919
	7	390	526	516	635	662	780	773	894
	7.5	377	502	500	611	646	756	756	869
	8	363	477	485	588	629	730	741	845
5	6.5	393	529	509	629	662	781	764	885
	7	381	506	493	604	648	757	747	859
	7.5	367	482	476	580	632	733	730	834
	8	353	457	461	556	615	707	714	810

Table C-22: Max Principal Stress at Concrete Slab, $E=4\times10^6$ psi, $\alpha_C=5.5\times10^{-6}/^\circ F$, k-value=500 psi/in, Crack Spacing = 8 ft

First Layer Steel Depth (in)	Second Layer Steel Depth (in)	k-value=500							
		400 Microstrain Ultimate Shrinkage				700 Microstrain Ultimate Shrinkage			
		3 F˚/in Gradient		1.5 F˚/in Gradient		3 F˚/in Gradient		1.5 F˚/in Gradient	
		30 F˚ Drop	50 F˚ Drop	30 F˚ Drop	50 F˚ Drop	30 F˚ Drop	50 F˚ Drop	30 F˚ Drop	50 F˚ Drop
		Max Principal Stress at Slab (psi)	Max Principal Stress at Slab (psi)	Max Principal Stress at Slab (psi)	Max Principal Stress at Slab (psi)	Max Principal Stress at Slab (psi)	Max Principal Stress at Slab (psi)	Max Principal Stress at Slab (psi)	Max Principal Stress at Slab (psi)
3.5	6.5	400	556	586	726	675	812	849	991
	7	389	536	571	704	661	791	833	967
	7.5	376	514	557	682	647	768	818	945
	8	363	490	543	661	631	744	803	923
4	6.5	398	546	569	702	673	803	833	968
	7	386	525	553	679	660	781	817	944
	7.5	374	502	539	657	645	758	801	921
	8	361	479	524	635	629	735	787	899
4.5	6.5	391	531	549	675	664	787	812	939
	7	380	509	533	651	650	765	795	915
	7.5	367	487	518	629	636	741	779	891
	8	354	463	503	606	620	717	764	868
5	6.5	382	512	527	646	651	765	787	907
	7	371	490	511	622	637	743	770	882
	7.5	358	467	496	599	622	719	754	858
	8	344	444	481	576	606	695	739	834

Table C-23: Max Principal Stress at Concrete Slab, E=5×10^6 psi, α_C=5.5×10^{-6}/˚F, k-value=300 psi/in, Crack Spacing = 8 ft

First Layer Steel Depth (in)	Second Layer Steel Depth (in)	k-value=300							
		400 Microstrain Ultimate Shrinkage				700 Microstrain Ultimate Shrinkage			
		3 F˚/in Gradient		1.5 F˚/in Gradient		3 F˚/in Gradient		1.5 F˚/in Gradient	
		30 F˚ Drop	50 F˚ Drop	30 F˚ Drop	50 F˚ Drop	30 F˚ Drop	50 F˚ Drop	30 F˚ Drop	50 F˚ Drop
		Max Principal Stress at Slab (psi)	Max Principal Stress at Slab (psi)	Max Principal Stress at Slab (psi)	Max Principal Stress at Slab (psi)	Max Principal Stress at Slab (psi)	Max Principal Stress at Slab (psi)	Max Principal Stress at Slab (psi)	Max Principal Stress at Slab (psi)
3.5	6.5	501	690	677	842	840	1004	996	1163
	7	487	664	658	814	823	977	976	1134
	7.5	472	637	640	788	806	950	957	1107
	8	455	609	623	761	786	921	940	1080
4	6.5	499	677	656	812	839	994	977	1135
	7	485	652	637	784	822	967	957	1106
	7.5	469	624	619	757	804	939	938	1078
	8	453	595	601	730	785	910	920	1050
4.5	6.5	492	659	631	779	828	974	950	1100
	7	477	633	612	750	811	947	930	1070
	7.5	462	605	593	722	793	919	911	1041
	8	445	576	576	695	774	889	892	1013
5	6.5	480	637	605	743	812	948	920	1060
	7	466	610	585	714	795	921	899	1029
	7.5	450	582	566	685	776	892	879	1000
	8	433	553	548	657	757	862	861	971

Table C-24: Max Principal Stress at Concrete Slab, E=5×10^{6} psi, α_C=5.5×10^{-6}/˚F, k-value=500 psi/in, Crack Spacing = 8 ft

First Layer Steel Depth (in)	Second Layer Steel Depth (in)	k-value=500							
		400 Microstrain Ultimate Shrinkage				700 Microstrain Ultimate Shrinkage			
		3 F˚/in Gradient		1.5 F˚/in Gradient		3 F˚/in Gradient		1.5 F˚/in Gradient	
		30 F˚ Drop	50 F˚ Drop	30 F˚ Drop	50 F˚ Drop	30 F˚ Drop	50 F˚ Drop	30 F˚ Drop	50 F˚ Drop
		Max Principal Stress at Slab (psi)	Max Principal Stress at Slab (psi)	Max Principal Stress at Slab (psi)	Max Principal Stress at Slab (psi)	Max Principal Stress at Slab (psi)	Max Principal Stress at Slab (psi)	Max Principal Stress at Slab (psi)	Max Principal Stress at Slab (psi)
3.5	6.5	490	673	693	856	828	988	1017	1181
	7	477	648	675	829	812	962	997	1154
	7.5	462	622	658	804	795	935	980	1127
	8	446	594	641	778	777	907	962	1101
4	6.5	488	660	673	827	827	978	998	1155
	7	474	635	654	800	811	952	979	1127
	7.5	460	609	637	774	793	925	961	1099
	8	444	581	620	748	775	897	944	1073
4.5	6.5	480	642	649	795	817	959	973	1121
	7	467	617	630	767	800	932	953	1092
	7.5	452	590	613	741	783	905	935	1064
	8	436	562	596	714	764	876	917	1037
5	6.5	469	620	624	760	800	933	944	1082
	7	456	595	605	732	784	906	924	1053
	7.5	441	568	587	705	766	878	905	1025
	8	425	539	569	678	747	850	887	997

Table C-25: Max Principal Stress at Concrete Slab, E=4×10^6 psi, α_C=3.5×10^{-6}/˚F, k-value=300 psi/in, Crack Spacing = 12 ft

First Layer Steel Depth (in)	Second Layer Steel Depth (in)	k-value=300							
		400 Microstrain Ultimate Shrinkage				700 Microstrain Ultimate Shrinkage			
		3 F˚/in Gradient		1.5 F˚/in Gradient		3 F˚/in Gradient		1.5 F˚/in Gradient	
		30 F˚ Drop	50 F˚ Drop	30 F˚ Drop	50 F˚ Drop	30 F˚ Drop	50 F˚ Drop	30 F˚ Drop	50 F˚ Drop
		Max Principal Stress at Slab (psi)	Max Principal Stress at Slab (psi)	Max Principal Stress at Slab (psi)	Max Principal Stress at Slab (psi)	Max Principal Stress at Slab (psi)	Max Principal Stress at Slab (psi)	Max Principal Stress at Slab (psi)	Max Principal Stress at Slab (psi)
3.5	6.5	401	545	584	694	693	808	865	977
	7	391	526	573	679	680	789	854	961
	7.5	380	507	563	664	667	769	843	946
	8	368	486	553	650	653	749	832	930
4	6.5	398	534	572	678	690	799	854	962
	7	387	515	561	663	677	780	842	946
	7.5	376	495	550	647	663	759	831	930
	8	364	475	540	632	649	739	820	914
4.5	6.5	391	519	558	660	679	783	839	942
	7	380	500	547	644	666	763	826	925
	7.5	369	480	536	628	652	743	815	908
	8	356	459	525	612	638	722	803	892
5	6.5	381	502	542	640	665	762	820	919
	7	370	482	531	623	652	742	807	901
	7.5	359	461	519	606	638	722	795	884
	8	346	440	508	590	623	701	784	867

Table C-26: Max Principal Stress at Concrete Slab, E=4×10^6 psi, α_C=3.5×10^{-6}/˚F, k-value=500 psi/in, Crack Spacing = 12 ft

First Layer Steel Depth (in)	Second Layer Steel Depth (in)	k-value=500							
		400 Microstrain Ultimate Shrinkage				700 Microstrain Ultimate Shrinkage			
		3 F˚/in Gradient		1.5 F˚/in Gradient		3 F˚/in Gradient		1.5 F˚/in Gradient	
		30 F˚ Drop	50 F˚ Drop	30 F˚ Drop	50 F˚ Drop	30 F˚ Drop	50 F˚ Drop	30 F˚ Drop	50 F˚ Drop
		Max Principal Stress at Slab (psi)	Max Principal Stress at Slab (psi)	Max Principal Stress at Slab (psi)	Max Principal Stress at Slab (psi)	Max Principal Stress at Slab (psi)	Max Principal Stress at Slab (psi)	Max Principal Stress at Slab (psi)	Max Principal Stress at Slab (psi)
3.5	6.5	394	533	609	713	686	798	901	1006
	7	384	516	600	701	673	780	891	993
	7.5	374	497	591	689	661	761	882	981
	8	363	478	583	676	647	741	873	968
4	6.5	391	523	599	700	682	789	892	995
	7	381	505	590	688	670	770	882	981
	7.5	370	486	581	675	657	751	873	968
	8	359	466	573	663	643	732	864	955
4.5	6.5	384	508	588	685	672	773	880	979
	7	373	489	579	672	659	754	870	965
	7.5	363	470	570	659	646	735	860	951
	8	351	450	561	647	633	715	850	938
5	6.5	374	490	575	669	658	753	865	960
	7	364	472	566	656	645	734	854	945
	7.5	353	452	556	642	632	715	844	931
	8	341	432	547	629	618	695	834	917

Table C-27: Max Principal Stress at Concrete Slab, E=5×10^{6} psi, α_C=3.5×10^{-6}/˚F, k-value=300 psi/in, Crack Spacing = 12 ft

First Layer Steel Depth (in)	Second Layer Steel Depth (in)	k-value=300							
		400 Microstrain Ultimate Shrinkage				700 Microstrain Ultimate Shrinkage			
		3 F˚/in Gradient		1.5 F˚/in Gradient		3 F˚/in Gradient		1.5 F˚/in Gradient	
		30 F˚ Drop	50 F˚ Drop	30 F˚ Drop	50 F˚ Drop	30 F˚ Drop	50 F˚ Drop	30 F˚ Drop	50 F˚ Drop
		Max Principal Stress at Slab (psi)	Max Principal Stress at Slab (psi)	Max Principal Stress at Slab (psi)	Max Principal Stress at Slab (psi)	Max Principal Stress at Slab (psi)	Max Principal Stress at Slab (psi)	Max Principal Stress at Slab (psi)	Max Principal Stress at Slab (psi)
3.5	6.5	492	661	693	824	850	986	1038	1171
	7	479	638	680	805	834	962	1024	1151
	7.5	466	615	667	787	818	938	1010	1132
	8	452	590	655	768	801	913	997	1113
4	6.5	488	648	679	804	847	975	1025	1152
	7	475	625	665	785	831	952	1010	1132
	7.5	462	602	652	766	814	927	996	1112
	8	447	577	639	747	797	902	982	1093
4.5	6.5	480	631	661	781	834	956	1005	1127
	7	467	607	647	761	818	932	990	1106
	7.5	453	583	633	741	802	907	975	1085
	8	438	558	620	722	784	882	961	1066
5	6.5	468	609	642	756	817	931	982	1098
	7	455	586	627	735	801	906	966	1076
	7.5	441	561	613	715	784	881	951	1055
	8	426	535	600	695	766	856	937	1034

Table C-28: Max Principal Stress at Concrete Slab, E=5×10^6 psi, α_C=3.5×10^{-6}/˚F, k-value=500 psi/in, Crack Spacing = 12 ft

First Layer Steel Depth (in)	Second Layer Steel Depth (in)	k-value=500							
		400 Microstrain Ultimate Shrinkage				700 Microstrain Ultimate Shrinkage			
		3 F˚/in Gradient		1.5 F˚/in Gradient		3 F˚/in Gradient		1.5 F˚/in Gradient	
		30 F˚ Drop	50 F˚ Drop	30 F˚ Drop	50 F˚ Drop	30 F˚ Drop	50 F˚ Drop	30 F˚ Drop	50 F˚ Drop
		Max Principal Stress at Slab (psi)	Max Principal Stress at Slab (psi)	Max Principal Stress at Slab (psi)	Max Principal Stress at Slab (psi)	Max Principal Stress at Slab (psi)	Max Principal Stress at Slab (psi)	Max Principal Stress at Slab (psi)	Max Principal Stress at Slab (psi)
3.5	6.5	485	649	723	847	843	975	1079	1206
	7	472	627	711	831	828	953	1067	1189
	7.5	460	605	700	815	812	930	1056	1173
	8	446	581	690	800	795	906	1044	1156
4	6.5	480	636	710	830	839	965	1069	1191
	7	468	614	699	814	824	942	1056	1173
	7.5	455	591	688	798	808	919	1044	1156
	8	442	568	677	782	792	895	1032	1140
4.5	6.5	472	619	696	811	827	946	1053	1170
	7	460	596	684	794	811	923	1040	1152
	7.5	446	573	672	778	795	899	1027	1134
	8	433	549	661	761	779	875	1015	1117
5	6.5	460	597	680	790	810	921	1033	1145
	7	448	575	667	773	794	898	1020	1127
	7.5	435	551	655	755	778	874	1007	1109
	8	421	527	644	739	761	850	995	1091

Table C-29: Max Principal Stress at Concrete Slab, $E=4\times10^6$ psi, $\alpha_C=4.5\times10^{-6}/^{\circ}F$, k-value=300 psi/in, Crack Spacing = 12 ft

First Layer Steel Depth (in)	Second Layer Steel Depth (in)	k-value=300							
		400 Microstrain Ultimate Shrinkage				700 Microstrain Ultimate Shrinkage			
		3 F°/in Gradient		1.5 F°/in Gradient		3 F°/in Gradient		1.5 F°/in Gradient	
		30 F° Drop	50 F° Drop	30 F° Drop	50 F° Drop	30 F° Drop	50 F° Drop	30 F° Drop	50 F° Drop
		Max Principal Stress at Slab (psi)	Max Principal Stress at Slab (psi)	Max Principal Stress at Slab (psi)	Max Principal Stress at Slab (psi)	Max Principal Stress at Slab (psi)	Max Principal Stress at Slab (psi)	Max Principal Stress at Slab (psi)	Max Principal Stress at Slab (psi)
3.5	6.5	431	610	649	791	721	871	931	1075
	7	418	587	636	773	705	846	917	1056
	7.5	405	562	624	755	689	821	904	1037
	8	390	537	612	737	672	795	891	1019
4	6.5	427	597	635	772	717	859	917	1056
	7	414	573	622	753	701	834	903	1037
	7.5	400	548	609	734	684	809	890	1017
	8	386	522	596	716	667	783	877	998
4.5	6.5	419	580	618	750	705	840	899	1033
	7	406	555	604	730	689	815	884	1012
	7.5	392	530	591	711	673	789	870	992
	8	377	504	578	691	655	763	857	972
5	6.5	408	558	600	726	690	816	878	1005
	7	395	534	586	705	673	790	863	984
	7.5	381	508	572	685	656	764	848	963
	8	366	482	559	665	639	738	834	943

Table C-30: Max Principal Stress at Concrete Slab, $E=4\times10^6$ psi, $\alpha_C=4.5\times10^{-6}/^{\circ}F$, k-value=500 psi/in, Crack Spacing = 12 ft

First Layer Steel Depth (in)	Second Layer Steel Depth (in)	k-value=500							
		400 Microstrain Ultimate Shrinkage				700 Microstrain Ultimate Shrinkage			
		3 F˚/in Gradient		1.5 F˚/in Gradient		3 F˚/in Gradient		1.5 F˚/in Gradient	
		30 F˚ Drop	50 F˚ Drop	30 F˚ Drop	50 F˚ Drop	30 F˚ Drop	50 F˚ Drop	30 F˚ Drop	50 F˚ Drop
		Max Principal Stress at Slab (psi)	Max Principal Stress at Slab (psi)	Max Principal Stress at Slab (psi)	Max Principal Stress at Slab (psi)	Max Principal Stress at Slab (psi)	Max Principal Stress at Slab (psi)	Max Principal Stress at Slab (psi)	Max Principal Stress at Slab (psi)
3.5	6.5	423	596	677	811	711	857	969	1105
	7	410	573	666	796	696	833	958	1089
	7.5	397	550	656	782	681	810	947	1074
	8	383	525	646	767	664	785	936	1059
4	6.5	418	582	665	796	707	845	958	1091
	7	406	559	655	780	692	821	947	1074
	7.5	392	536	644	765	676	797	936	1058
	8	379	511	634	750	660	772	925	1043
4.5	6.5	410	564	652	778	696	826	944	1071
	7	397	541	641	762	680	802	932	1055
	7.5	384	517	630	746	664	777	920	1038
	8	370	492	619	730	648	752	909	1022
5	6.5	399	543	637	758	680	802	927	1049
	7	386	520	626	742	665	778	914	1032
	7.5	373	496	614	725	648	753	902	1015
	8	379	506	603	709	632	728	891	998

Table C-31: Max Principal Stress at Concrete Slab, E=5×10^6 psi, α_C=4.5×10^{-6}/˚F, k-value=300 psi/in, Crack Spacing = 12 ft

First Layer Steel Depth (in)	Second Layer Steel Depth (in)	k-value=300							
		400 Microstrain Ultimate Shrinkage				700 Microstrain Ultimate Shrinkage			
		3 F˚/in Gradient		1.5 F˚/in Gradient		3 F˚/in Gradient		1.5 F˚/in Gradient	
		30 F˚ Drop	50 F˚ Drop	30 F˚ Drop	50 F˚ Drop	30 F˚ Drop	50 F˚ Drop	30 F˚ Drop	50 F˚ Drop
		Max Principal Stress at Slab (psi)	Max Principal Stress at Slab (psi)	Max Principal Stress at Slab (psi)	Max Principal Stress at Slab (psi)	Max Principal Stress at Slab (psi)	Max Principal Stress at Slab (psi)	Max Principal Stress at Slab (psi)	Max Principal Stress at Slab (psi)
3.5	6.5	528	740	769	938	884	1061	1114	1286
	7	513	712	753	915	866	1032	1097	1262
	7.5	496	683	737	892	846	1002	1081	1238
	8	479	652	722	870	826	970	1065	1215
4	6.5	524	725	751	913	880	1048	1097	1262
	7	508	696	734	890	861	1018	1080	1238
	7.5	491	666	718	866	841	988	1063	1213
	8	474	635	703	843	821	956	1047	1190
4.5	6.5	514	704	730	885	867	1025	1074	1232
	7	498	675	713	861	847	995	1056	1207
	7.5	482	644	697	837	827	963	1039	1182
	8	464	613	681	813	806	931	1022	1158
5	6.5	501	678	707	855	847	996	1048	1198
	7	485	649	690	830	828	965	1029	1172
	7.5	468	618	673	805	808	933	1011	1146
	8	450	586	656	780	786	901	994	1121

Table C-32: Max Principal Stress at Concrete Slab, E=5×10^6 psi, α_C=4.5×10^{-6}/˚F, k-value=500 psi/in, Crack Spacing = 12 ft

First Layer Steel Depth (in)	Second Layer Steel Depth (in)	k-value=500							
		400 Microstrain Ultimate Shrinkage				700 Microstrain Ultimate Shrinkage			
		3 F˚/in Gradient		1.5 F˚/in Gradient		3 F˚/in Gradient		1.5 F˚/in Gradient	
		30 F˚ Drop	50 F˚ Drop	30 F˚ Drop	50 F˚ Drop	30 F˚ Drop	50 F˚ Drop	30 F˚ Drop	50 F˚ Drop
		Max Principal Stress at Slab (psi)	Max Principal Stress at Slab (psi)	Max Principal Stress at Slab (psi)	Max Principal Stress at Slab (psi)	Max Principal Stress at Slab (psi)	Max Principal Stress at Slab (psi)	Max Principal Stress at Slab (psi)	Max Principal Stress at Slab (psi)
3.5	6.5	519	725	801	962	875	1047	1159	1322
	7	504	698	788	943	857	1019	1144	1301
	7.5	489	670	775	924	838	990	1130	1282
	8	472	640	762	905	818	959	1117	1262
4	6.5	514	709	787	942	870	1033	1145	1303
	7	499	682	773	922	852	1005	1130	1282
	7.5	483	653	759	902	833	975	1116	1261
	8	466	623	746	883	813	945	1102	1242
4.5	6.5	504	688	769	919	856	1011	1126	1278
	7	489	660	755	898	838	982	1111	1256
	7.5	473	631	741	878	819	952	1096	1235
	8	456	601	728	858	799	921	1082	1214
5	6.5	491	663	750	893	837	982	1104	1249
	7	476	634	735	872	819	952	1088	1227
	7.5	459	605	721	851	799	922	1073	1205
	8	442	583	707	830	779	891	1058	1184

Table C-33: Max Principal Stress at Concrete Slab, E=4×10^6 psi, α_C=5.5×10^{-6}/˚F, k-value=300 psi/in, Crack Spacing = 12 ft

First Layer Steel Depth (in)	Second Layer Steel Depth (in)	k-value=300							
		400 Microstrain Ultimate Shrinkage				700 Microstrain Ultimate Shrinkage			
		3 F˚/in Gradient		1.5 F˚/in Gradient		3 F˚/in Gradient		1.5 F˚/in Gradient	
		30 F˚ Drop	50 F˚ Drop	30 F˚ Drop	50 F˚ Drop	30 F˚ Drop	50 F˚ Drop	30 F˚ Drop	50 F˚ Drop
		Max Principal Stress at Slab (psi)	Max Principal Stress at Slab (psi)	Max Principal Stress at Slab (psi)	Max Principal Stress at Slab (psi)	Max Principal Stress at Slab (psi)	Max Principal Stress at Slab (psi)	Max Principal Stress at Slab (psi)	Max Principal Stress at Slab (psi)
3.5	6.5	462	675	715	890	750	935	999	1175
	7	447	647	700	868	732	906	983	1153
	7.5	431	617	686	847	713	875	968	1131
	8	413	586	672	826	693	844	953	1109
4	6.5	458	660	699	867	746	921	983	1153
	7	443	631	683	845	727	891	966	1130
	7.5	426	601	668	823	708	861	951	1107
	8	408	569	654	801	687	829	936	1085
4.5	6.5	449	640	679	841	733	899	962	1126
	7	434	610	663	818	715	869	945	1102
	7.5	416	579	648	795	695	837	929	1078
	8	401	547	633	772	674	805	913	1055
5	6.5	437	615	658	813	716	871	938	1095
	7	421	585	642	789	697	841	920	1070
	7.5	404	554	626	765	677	809	903	1045
	8	414	566	610	742	656	776	887	1022

Table C-34: Max Principal Stress at Concrete Slab, E=4×10^6 psi, α_C=5.5×10^{-6}/°F, k-value=500 psi/in, Crack Spacing = 12 ft

First Layer Steel Depth (in)	Second Layer Steel Depth (in)	k-value=500							
		400 Microstrain Ultimate Shrinkage				700 Microstrain Ultimate Shrinkage			
		3 F°/in Gradient		1.5 F°/in Gradient		3 F°/in Gradient		1.5 F°/in Gradient	
		30 F° Drop	50 F° Drop	30 F° Drop	50 F° Drop	30 F° Drop	50 F° Drop	30 F° Drop	50 F° Drop
		Max Principal Stress at Slab (psi)	Max Principal Stress at Slab (psi)	Max Principal Stress at Slab (psi)	Max Principal Stress at Slab (psi)	Max Principal Stress at Slab (psi)	Max Principal Stress at Slab (psi)	Max Principal Stress at Slab (psi)	Max Principal Stress at Slab (psi)
3.5	6.5	452	657	746	911	739	917	1040	1207
	7	437	630	734	893	721	889	1027	1188
	7.5	422	602	722	876	703	861	1014	1170
	8	428	572	710	859	684	831	1002	1152
4	6.5	447	641	732	893	733	903	1027	1189
	7	432	614	720	875	716	875	1014	1170
	7.5	421	585	707	857	697	846	1001	1152
	8	437	574	695	839	678	816	988	1133
4.5	6.5	438	621	717	872	721	881	1010	1167
	7	423	593	704	853	703	853	996	1148
	7.5	432	567	691	834	685	823	983	1128
	8	448	592	679	816	665	792	970	1109
5	6.5	425	596	700	849	704	854	991	1142
	7	427	568	686	830	686	825	977	1122
	7.5	443	586	673	810	667	795	963	1102
	8	459	610	661	791	647	764	949	1082

Table C-35: Max Principal Stress at Concrete Slab, $E=5\times10^6$ psi, $\alpha_C=5.5\times10^{-6}$/˚F, k-value=300 psi/in, Crack Spacing = 12 ft

First Layer Steel Depth (in)	Second Layer Steel Depth (in)	k-value=300							
		400 Microstrain Ultimate Shrinkage				700 Microstrain Ultimate Shrinkage			
		3 F˚/in Gradient		1.5 F˚/in Gradient		3 F˚/in Gradient		1.5 F˚/in Gradient	
		30 F˚ Drop	50 F˚ Drop	30 F˚ Drop	50 F˚ Drop	30 F˚ Drop	50 F˚ Drop	30 F˚ Drop	50 F˚ Drop
		Max Principal Stress at Slab (psi)	Max Principal Stress at Slab (psi)	Max Principal Stress at Slab (psi)	Max Principal Stress at Slab (psi)	Max Principal Stress at Slab (psi)	Max Principal Stress at Slab (psi)	Max Principal Stress at Slab (psi)	Max Principal Stress at Slab (psi)
3.5	6.5	566	818	845	1053	920	1139	1193	1404
	7	547	784	827	1026	898	1104	1173	1376
	7.5	528	748	809	1000	876	1067	1154	1348
	8	506	711	791	973	851	1029	1136	1321
4	6.5	561	801	824	1025	915	1123	1173	1376
	7	542	766	805	997	893	1087	1152	1347
	7.5	522	729	787	969	870	1050	1133	1319
	8	501	691	769	942	845	1011	1114	1291
4.5	6.5	551	776	800	992	901	1096	1146	1342
	7	532	741	780	963	879	1060	1125	1312
	7.5	511	704	761	935	855	1022	1105	1282
	8	489	665	743	907	830	983	1086	1254
5	6.5	536	747	774	957	880	1064	1116	1303
	7	517	711	754	927	858	1027	1095	1272
	7.5	496	673	734	897	833	988	1074	1241
	8	474	651	715	869	808	949	1054	1211

Table C-36: Max Principal Stress at Concrete Slab, E=5×10^6 psi, α_C=5.5×10^{-6}/˚F, k-value=500 psi/in, Crack Spacing = 12 ft

First Layer Steel Depth (in)	Second Layer Steel Depth (in)	k-value=500							
		400 Microstrain Ultimate Shrinkage				700 Microstrain Ultimate Shrinkage			
		3 F˚/in Gradient		1.5 F˚/in Gradient		3 F˚/in Gradient		1.5 F˚/in Gradient	
		30 F˚ Drop	50 F˚ Drop	30 F˚ Drop	50 F˚ Drop	30 F˚ Drop	50 F˚ Drop	30 F˚ Drop	50 F˚ Drop
		Max Principal Stress at Slab (psi)	Max Principal Stress at Slab (psi)	Max Principal Stress at Slab (psi)	Max Principal Stress at Slab (psi)	Max Principal Stress at Slab (psi)	Max Principal Stress at Slab (psi)	Max Principal Stress at Slab (psi)	Max Principal Stress at Slab (psi)
3.5	6.5	555	800	881	1079	908	1121	1240	1441
	7	537	767	866	1056	887	1087	1224	1417
	7.5	519	733	850	1034	865	1052	1208	1394
	8	498	697	835	1012	842	1015	1192	1371
4	6.5	549	781	864	1055	903	1104	1224	1419
	7	531	748	848	1032	881	1070	1207	1394
	7.5	512	713	832	1009	859	1035	1191	1370
	8	498	677	817	986	836	998	1175	1347
4.5	6.5	538	757	844	1028	888	1078	1203	1390
	7	520	723	827	1004	866	1043	1185	1364
	7.5	501	687	811	980	844	1007	1168	1340
	8	511	678	795	956	820	970	1151	1316
5	6.5	523	727	822	999	867	1046	1178	1357
	7	505	693	805	974	846	1010	1159	1331
	7.5	505	670	788	949	823	974	1142	1305
	8	525	701	772	924	799	936	1125	1280

Appendix D: Concrete Stress Around Longitudinal Steel at Transverse Crack Location for Two-Mat CRCP

Table D-1: Max Principal Stress at Transverse Crack, $E=4\times10^6$ psi, $\alpha_C=3.5\times10^{-6}/^{\circ}F$, k-value=300 psi/in, Crack Spacing = 4 ft

First Layer Steel Depth (in)	Second Layer Steel Depth (in)	k-value=300							
		400 Microstrain Ultimate Shrinkage				700 Microstrain Ultimate Shrinkage			
		3 F˚/in Gradient		1.5 F˚/in Gradient		3 F˚/in Gradient		1.5 F˚/in Gradient	
		30 F˚ Drop	50 F˚ Drop	30 F˚ Drop	50 F˚ Drop	30 F˚ Drop	50 F˚ Drop	30 F˚ Drop	50 F˚ Drop
		Max Principal Stress at Slab (psi)	Max Principal Stress at Slab (psi)	Max Principal Stress at Slab (psi)	Max Principal Stress at Slab (psi)	Max Principal Stress at Slab (psi)	Max Principal Stress at Slab (psi)	Max Principal Stress at Slab (psi)	Max Principal Stress at Slab (psi)
3.5	6.5	252	331	293	362	436	477	462	503
	7	251	320	286	354	435	474	456	494
	7.5	251	313	284	350	435	474	455	492
	8	250	305	279	344	433	469	449	484
4	6.5	260	341	303	373	440	487	471	517
	7	259	328	295	362	440	484	465	508
	7.5	258	317	288	353	439	480	459	499
	8	258	310	286	349	439	479	458	497
4.5	6.5	266	364	324	397	440	497	482	539
	7	262	340	304	373	438	487	466	515
	7.5	262	326	297	361	437	483	461	505
	8	260	315	290	351	435	478	455	496
5	6.5	292	405	354	437	440	512	505	576
	7	266	363	322	393	437	495	476	533
	7.5	264	340	306	371	435	486	463	513
	8	262	323	295	356	433	479	454	499

Table D-2: Max Principal Stress at Transverse Crack, $E=4\times10^6$ psi, $\alpha_C=3.5\times10^{-6}$/˚F, k-value=500 psi/in, Crack Spacing = 4 ft

First Layer Steel Depth (in)	Second Layer Steel Depth (in)	k-value=500							
		400 Microstrain Ultimate Shrinkage				700 Microstrain Ultimate Shrinkage			
		3 F˚/in Gradient		1.5 F˚/in Gradient		3 F˚/in Gradient		1.5 F˚/in Gradient	
		30 F˚ Drop	50 F˚ Drop	30 F˚ Drop	50 F˚ Drop	30 F˚ Drop	50 F˚ Drop	30 F˚ Drop	50 F˚ Drop
		Max Principal Stress at Slab (psi)	Max Principal Stress at Slab (psi)	Max Principal Stress at Slab (psi)	Max Principal Stress at Slab (psi)	Max Principal Stress at Slab (psi)	Max Principal Stress at Slab (psi)	Max Principal Stress at Slab (psi)	Max Principal Stress at Slab (psi)
3.5	6.5	255	331	293	362	437	478	460	502
	7	254	320	287	354	436	475	454	493
	7.5	255	313	284	350	437	475	453	491
	8	253	305	280	344	434	471	448	483
4	6.5	263	342	303	373	441	488	470	517
	7	262	329	295	362	441	485	463	507
	7.5	261	317	288	353	440	481	458	498
	8	261	313	286	349	440	481	457	496
4.5	6.5	267	365	324	398	441	497	482	539
	7	265	340	305	373	439	488	466	514
	7.5	264	326	297	362	438	484	460	504
	8	262	317	290	352	437	480	454	496
5	6.5	292	405	355	437	441	512	506	577
	7	268	364	323	395	438	495	476	533
	7.5	266	340	306	372	436	487	462	513
	8	264	324	296	357	433	480	454	499

Table D-3: Max Principal Stress at Transverse Crack, $E=5\times10^6$ psi, $\alpha_C=3.5\times10^{-6}/^\circ F$, k-value=300 psi/in, Crack Spacing = 4 ft

First Layer Steel Depth (in)	Second Layer Steel Depth (in)	k-value=300							
		400 Microstrain Ultimate Shrinkage				700 Microstrain Ultimate Shrinkage			
		3 F˚/in Gradient		1.5 F˚/in Gradient		3 F˚/in Gradient		1.5 F˚/in Gradient	
		30 F˚ Drop	50 F˚ Drop	30 F˚ Drop	50 F˚ Drop	30 F˚ Drop	50 F˚ Drop	30 F˚ Drop	50 F˚ Drop
		Max Principal Stress at Slab (psi)	Max Principal Stress at Slab (psi)	Max Principal Stress at Slab (psi)	Max Principal Stress at Slab (psi)	Max Principal Stress at Slab (psi)	Max Principal Stress at Slab (psi)	Max Principal Stress at Slab (psi)	Max Principal Stress at Slab (psi)
3.5	6.5	311	406	360	447	540	589	570	619
	7	309	394	352	436	538	585	563	609
	7.5	309	386	349	432	539	584	563	607
	8	307	376	344	424	536	579	556	597
4	6.5	321	419	371	458	545	601	580	635
	7	320	404	362	445	544	597	573	624
	7.5	318	391	353	434	543	592	567	614
	8	318	383	351	429	543	591	566	612
4.5	6.5	327	447	395	487	544	613	593	660
	7	324	418	372	457	542	600	574	631
	7.5	322	402	363	443	541	595	568	621
	8	320	388	355	432	539	590	562	610
5	6.5	357	494	432	533	545	632	618	705
	7	329	446	393	481	540	610	585	653
	7.5	326	418	374	455	538	599	569	629
	8	322	398	361	437	535	590	560	613

Table D-4: Max Principal Stress at Transverse Crack, $E=5\times10^6$ psi, $\alpha_C=3.5\times10^{-6}/^\circ F$, k-value=500 psi/in, Crack Spacing = 4 ft

First Layer Steel Depth (in)	Second Layer Steel Depth (in)	k-value=500							
		400 Microstrain Ultimate Shrinkage				700 Microstrain Ultimate Shrinkage			
		3 F˚/in Gradient		1.5 F˚/in Gradient		3 F˚/in Gradient		1.5 F˚/in Gradient	
		30 F˚ Drop	50 F˚ Drop	30 F˚ Drop	50 F˚ Drop	30 F˚ Drop	50 F˚ Drop	30 F˚ Drop	50 F˚ Drop
		Max Principal Stress at Slab (psi)	Max Principal Stress at Slab (psi)	Max Principal Stress at Slab (psi)	Max Principal Stress at Slab (psi)	Max Principal Stress at Slab (psi)	Max Principal Stress at Slab (psi)	Max Principal Stress at Slab (psi)	Max Principal Stress at Slab (psi)
3.5	6.5	314	407	360	446	541	590	568	618
	7	313	394	353	436	540	586	561	607
	7.5	313	386	350	432	540	586	561	605
	8	311	376	344	424	538	581	554	595
4	6.5	324	420	371	458	546	602	579	634
	7	323	404	361	445	546	598	572	623
	7.5	321	391	353	434	544	594	566	613
	8	321	383	351	429	544	593	564	611
4.5	6.5	330	448	395	488	546	614	592	660
	7	326	418	372	458	543	601	574	631
	7.5	325	402	363	444	542	596	567	620
	8	323	388	355	432	540	591	561	610
5	6.5	357	494	432	533	546	633	620	704
	7	331	447	393	483	541	611	584	652
	7.5	328	418	374	456	539	600	569	628
	8	324	398	362	437	536	591	559	613

Table D-5: Max Principal Stress at Transverse Crack, $E=4\times10^6$ psi, $\alpha_C=4.5\times10^{-6}/^\circ F$, k-value=300 psi/in, Crack Spacing = 4 ft

First Layer Steel Depth (in)	Second Layer Steel Depth (in)	k-value=300							
		400 Microstrain Ultimate Shrinkage				700 Microstrain Ultimate Shrinkage			
		3 F˚/in Gradient		1.5 F˚/in Gradient		3 F˚/in Gradient		1.5 F˚/in Gradient	
		30 F˚ Drop	50 F˚ Drop	30 F˚ Drop	50 F˚ Drop	30 F˚ Drop	50 F˚ Drop	30 F˚ Drop	50 F˚ Drop
		Max Principal Stress at Slab (psi)	Max Principal Stress at Slab (psi)	Max Principal Stress at Slab (psi)	Max Principal Stress at Slab (psi)	Max Principal Stress at Slab (psi)	Max Principal Stress at Slab (psi)	Max Principal Stress at Slab (psi)	Max Principal Stress at Slab (psi)
3.5	6.5	291	401	339	432	469	535	509	574
	7	282	389	331	421	469	531	502	563
	7.5	282	381	328	416	469	531	501	561
	8	280	371	322	408	467	526	494	552
4	6.5	297	415	353	447	474	546	520	592
	7	291	400	344	433	474	543	513	580
	7.5	290	387	335	421	473	539	506	570
	8	290	379	333	416	473	538	504	567
4.5	6.5	318	445	378	478	475	560	534	620
	7	296	416	354	447	473	548	515	590
	7.5	295	399	344	433	473	544	508	578
	8	293	384	336	420	471	539	501	567
5	6.5	353	501	414	530	476	591	563	667
	7	313	446	375	474	474	560	527	614
	7.5	299	418	355	446	472	550	511	588
	8	296	396	342	428	469	542	500	571

Table D-6: Max Principal Stress at Transverse Crack, $E=4\times10^6$ psi, $\alpha_C=4.5\times10^{-6}$/˚F, k-value=500 psi/in, Crack Spacing = 4 ft

First Layer Steel Depth (in)	Second Layer Steel Depth (in)	k-value=500							
		400 Microstrain Ultimate Shrinkage				700 Microstrain Ultimate Shrinkage			
		3 F˚/in Gradient		1.5 F˚/in Gradient		3 F˚/in Gradient		1.5 F˚/in Gradient	
		30 F˚ Drop	50 F˚ Drop	30 F˚ Drop	50 F˚ Drop	30 F˚ Drop	50 F˚ Drop	30 F˚ Drop	50 F˚ Drop
		Max Principal Stress at Slab (psi)	Max Principal Stress at Slab (psi)	Max Principal Stress at Slab (psi)	Max Principal Stress at Slab (psi)	Max Principal Stress at Slab (psi)	Max Principal Stress at Slab (psi)	Max Principal Stress at Slab (psi)	Max Principal Stress at Slab (psi)
3.5	6.5	291	402	340	432	472	538	507	573
	7	287	389	332	421	472	534	500	562
	7.5	287	381	329	416	472	534	499	559
	8	285	371	323	408	470	529	493	550
4	6.5	298	416	354	447	477	549	519	592
	7	296	401	344	433	477	546	511	579
	7.5	295	387	335	421	476	541	505	569
	8	295	379	333	416	476	540	503	566
4.5	6.5	318	447	378	480	477	562	534	620
	7	299	417	354	448	475	551	515	589
	7.5	299	399	345	434	475	546	507	577
	8	297	384	336	421	473	541	500	566
5	6.5	353	502	414	530	478	591	564	667
	7	313	448	376	476	475	562	527	614
	7.5	302	418	356	448	474	552	510	588
	8	299	396	343	429	471	544	500	571

Table D-7: Max Principal Stress at Transverse Crack, $E=5\times10^6$ psi, $\alpha_C=4.5\times10^{-6}$/˚F, k-value=300 psi/in, Crack Spacing = 4 ft

First Layer Steel Depth (in)	Second Layer Steel Depth (in)	k-value=300							
		400 Microstrain Ultimate Shrinkage				700 Microstrain Ultimate Shrinkage			
		3 F˚/in Gradient		1.5 F˚/in Gradient		3 F˚/in Gradient		1.5 F˚/in Gradient	
		30 F˚ Drop	50 F˚ Drop	30 F˚ Drop	50 F˚ Drop	30 F˚ Drop	50 F˚ Drop	30 F˚ Drop	50 F˚ Drop
		Max Principal Stress at Slab (psi)	Max Principal Stress at Slab (psi)	Max Principal Stress at Slab (psi)	Max Principal Stress at Slab (psi)	Max Principal Stress at Slab (psi)	Max Principal Stress at Slab (psi)	Max Principal Stress at Slab (psi)	Max Principal Stress at Slab (psi)
3.5	6.5	355	492	417	532	580	659	628	706
	7	346	478	407	519	579	654	620	693
	7.5	346	469	404	513	580	654	619	690
	8	344	458	397	503	577	648	611	680
4	6.5	362	509	432	549	586	673	640	727
	7	359	492	421	532	586	669	632	713
	7.5	357	476	411	518	584	663	624	701
	8	356	467	408	512	584	662	623	697
4.5	6.5	387	546	461	586	588	690	656	759
	7	365	510	432	549	585	675	634	723
	7.5	363	491	421	531	584	670	625	709
	8	360	473	411	516	582	663	618	697
5	6.5	429	611	504	647	590	724	688	815
	7	381	547	457	580	586	691	647	751
	7.5	368	513	433	546	583	677	628	721
	8	364	487	418	524	580	667	616	701

Table D-8: Max Principal Stress at Transverse Crack, $E=5\times10^6$ psi, $\alpha_C=4.5\times10^{-6}/^{\circ}F$, k-value=500 psi/in, Crack Spacing = 4 ft

First Layer Steel Depth (in)	Second Layer Steel Depth (in)	k-value=500							
		400 Microstrain Ultimate Shrinkage				700 Microstrain Ultimate Shrinkage			
		3 F˚/in Gradient		1.5 F˚/in Gradient		3 F˚/in Gradient		1.5 F˚/in Gradient	
		30 F˚ Drop	50 F˚ Drop	30 F˚ Drop	50 F˚ Drop	30 F˚ Drop	50 F˚ Drop	30 F˚ Drop	50 F˚ Drop
		Max Principal Stress at Slab (psi)	Max Principal Stress at Slab (psi)	Max Principal Stress at Slab (psi)	Max Principal Stress at Slab (psi)	Max Principal Stress at Slab (psi)	Max Principal Stress at Slab (psi)	Max Principal Stress at Slab (psi)	Max Principal Stress at Slab (psi)
3.5	6.5	356	493	417	532	584	663	626	704
	7	352	478	408	519	583	658	618	692
	7.5	352	469	404	513	584	657	617	689
	8	350	458	397	503	581	652	609	678
4	6.5	364	510	432	549	589	676	639	726
	7	364	492	421	532	589	672	630	712
	7.5	362	476	410	518	588	666	623	699
	8	362	466	408	511	588	665	621	696
4.5	6.5	387	547	461	588	590	693	655	759
	7	369	511	433	550	587	678	633	722
	7.5	367	491	421	532	587	672	624	708
	8	365	473	411	517	584	666	617	695
5	6.5	429	611	504	646	592	724	689	814
	7	381	549	457	582	588	692	646	750
	7.5	372	513	434	548	585	679	627	720
	8	368	487	418	525	582	669	615	700

Table D-9: Max Principal Stress at Transverse Crack, E=4×10^6 psi, α_C=5.5×10^{-6}/˚F, k-value=300 psi/in, Crack Spacing = 4 ft

First Layer Steel Depth (in)	Second Layer Steel Depth (in)	k-value=300							
		400 Microstrain Ultimate Shrinkage				700 Microstrain Ultimate Shrinkage			
		3 F˚/in Gradient		1.5 F˚/in Gradient		3 F˚/in Gradient		1.5 F˚/in Gradient	
		30 F˚ Drop	50 F˚ Drop	30 F˚ Drop	50 F˚ Drop	30 F˚ Drop	50 F˚ Drop	30 F˚ Drop	50 F˚ Drop
		Max Principal Stress at Slab (psi)	Max Principal Stress at Slab (psi)	Max Principal Stress at Slab (psi)	Max Principal Stress at Slab (psi)	Max Principal Stress at Slab (psi)	Max Principal Stress at Slab (psi)	Max Principal Stress at Slab (psi)	Max Principal Stress at Slab (psi)
3.5	6.5	335	471	384	502	500	589	555	644
	7	319	457	375	488	499	585	547	631
	7.5	310	450	371	483	500	585	545	628
	8	309	438	364	472	498	580	538	617
4	6.5	344	488	401	521	506	604	567	664
	7	327	472	390	504	506	600	558	650
	7.5	320	457	380	490	505	595	550	637
	8	319	447	377	483	505	594	548	634
4.5	6.5	370	526	430	559	508	622	584	699
	7	340	491	402	522	507	608	561	662
	7.5	326	472	390	505	506	603	552	647
	8	324	455	380	490	504	597	544	634
5	6.5	414	615	472	624	535	686	618	755
	7	368	529	427	555	508	624	576	692
	7.5	338	495	403	522	507	612	556	661
	8	329	470	388	499	504	602	544	641

Table D-10: Max Principal Stress at Transverse Crack, $E=4\times10^6$ psi, $\alpha_C=5.5\times10^{-6}/^\circ F$, k-value=500 psi/in, Crack Spacing = 4 ft

First Layer Steel Depth (in)	Second Layer Steel Depth (in)	k-value=500							
		400 Microstrain Ultimate Shrinkage				700 Microstrain Ultimate Shrinkage			
		3 F°/in Gradient		1.5 F°/in Gradient		3 F°/in Gradient		1.5 F°/in Gradient	
		30 F° Drop	50 F° Drop	30 F° Drop	50 F° Drop	30 F° Drop	50 F° Drop	30 F° Drop	50 F° Drop
		Max Principal Stress at Slab (psi)	Max Principal Stress at Slab (psi)	Max Principal Stress at Slab (psi)	Max Principal Stress at Slab (psi)	Max Principal Stress at Slab (psi)	Max Principal Stress at Slab (psi)	Max Principal Stress at Slab (psi)	Max Principal Stress at Slab (psi)
3.5	6.5	337	472	385	502	505	594	553	643
	7	320	458	376	488	504	590	545	630
	7.5	317	450	372	482	505	590	543	626
	8	316	438	365	472	503	585	536	615
4	6.5	346	490	401	521	510	608	565	664
	7	328	473	390	505	510	604	556	649
	7.5	326	457	379	490	510	599	548	636
	8	325	447	376	483	510	598	546	632
4.5	6.5	371	528	430	561	511	625	583	698
	7	341	493	402	523	510	611	561	662
	7.5	331	473	391	506	510	606	551	647
	8	329	455	380	491	508	600	543	633
5	6.5	414	619	472	630	535	686	619	755
	7	368	532	427	558	511	627	575	692
	7.5	339	496	404	524	509	614	556	660
	8	332	470	388	501	507	605	543	640

Table D-11: Max Principal Stress at Transverse Crack, E=5×10^6 psi, α_C=5.5×10^{-6}/˚F, k-value=300 psi/in, Crack Spacing = 4 ft

First Layer Steel Depth (in)	Second Layer Steel Depth (in)	k-value=300							
		400 Microstrain Ultimate Shrinkage				700 Microstrain Ultimate Shrinkage			
		3 F˚/in Gradient		1.5 F˚/in Gradient		3 F˚/in Gradient		1.5 F˚/in Gradient	
		30 F˚ Drop	50 F˚ Drop	30 F˚ Drop	50 F˚ Drop	30 F˚ Drop	50 F˚ Drop	30 F˚ Drop	50 F˚ Drop
		Max Principal Stress at Slab (psi)	Max Principal Stress at Slab (psi)	Max Principal Stress at Slab (psi)	Max Principal Stress at Slab (psi)	Max Principal Stress at Slab (psi)	Max Principal Stress at Slab (psi)	Max Principal Stress at Slab (psi)	Max Principal Stress at Slab (psi)
3.5	6.5	409	577	472	618	617	726	684	791
	7	389	561	461	602	616	720	674	776
	7.5	380	553	457	595	617	719	673	772
	8	378	539	448	582	614	713	664	760
4	6.5	419	598	490	640	625	744	697	815
	7	398	579	476	620	625	738	687	798
	7.5	392	561	465	602	623	732	678	783
	8	392	551	461	594	623	730	675	779
4.5	6.5	450	643	524	685	628	766	716	855
	7	413	602	490	640	625	748	689	811
	7.5	401	580	477	619	625	741	679	794
	8	397	560	465	601	622	733	670	779
5	6.5	502	747	575	759	654	839	755	922
	7	447	647	520	679	628	769	705	846
	7.5	413	607	492	639	625	752	683	809
	8	404	578	474	611	622	740	668	785

Table D-12: Max Principal Stress at Transverse Crack, $E=5\times10^6$ psi, $\alpha_C=5.5\times10^{-6}/^{\circ}F$, k-value=500 psi/in, Crack Spacing = 4 ft

First Layer Steel Depth (in)	Second Layer Steel Depth (in)	k-value=500							
		400 Microstrain Ultimate Shrinkage				700 Microstrain Ultimate Shrinkage			
		3 F˚/in Gradient		1.5 F˚/in Gradient		3 F˚/in Gradient		1.5 F˚/in Gradient	
		30 F˚ Drop	50 F˚ Drop	30 F˚ Drop	50 F˚ Drop	30 F˚ Drop	50 F˚ Drop	30 F˚ Drop	50 F˚ Drop
		Max Principal Stress at Slab (psi)	Max Principal Stress at Slab (psi)	Max Principal Stress at Slab (psi)	Max Principal Stress at Slab (psi)	Max Principal Stress at Slab (psi)	Max Principal Stress at Slab (psi)	Max Principal Stress at Slab (psi)	Max Principal Stress at Slab (psi)
3.5	6.5	410	578	473	618	623	731	682	789
	7	391	562	462	601	622	725	672	774
	7.5	388	553	458	594	623	725	670	771
	8	386	539	449	582	620	719	662	758
4	6.5	420	600	490	640	630	748	695	814
	7	401	580	476	620	630	743	685	796
	7.5	399	561	464	602	628	737	676	782
	8	399	550	461	594	628	735	674	777
4.5	6.5	450	645	524	687	632	770	715	854
	7	414	603	491	642	629	752	689	810
	7.5	406	580	477	620	629	745	678	792
	8	403	559	465	602	626	737	669	777
5	6.5	503	751	575	765	654	839	756	922
	7	447	649	520	682	631	772	705	845
	7.5	414	608	492	641	629	755	682	808
	8	408	578	474	613	625	743	668	783

Table D-13: Max Principal Stress at Transverse Crack, E=4×10^6 psi, α_C=3.5×10^{-6}/°F, k-value=300 psi/in, Crack Spacing = 8 ft

First Layer Steel Depth (in)	Second Layer Steel Depth (in)	k-value=300							
		400 Microstrain Ultimate Shrinkage				700 Microstrain Ultimate Shrinkage			
		3 F°/in Gradient		1.5 F°/in Gradient		3 F°/in Gradient		1.5 F°/in Gradient	
		30 F° Drop	50 F° Drop	30 F° Drop	50 F° Drop	30 F° Drop	50 F° Drop	30 F° Drop	50 F° Drop
		Max Principal Stress at Slab (psi)	Max Principal Stress at Slab (psi)	Max Principal Stress at Slab (psi)	Max Principal Stress at Slab (psi)	Max Principal Stress at Slab (psi)	Max Principal Stress at Slab (psi)	Max Principal Stress at Slab (psi)	Max Principal Stress at Slab (psi)
3.5	6.5	371	570	456	604	524	629	603	712
	7	360	564	447	603	522	604	592	706
	7.5	353	560	444	608	523	604	590	713
	8	345	558	439	613	520	598	581	720
4	6.5	382	575	468	608	537	648	624	725
	7	369	564	455	610	535	628	611	710
	7.5	357	560	445	612	533	621	600	716
	8	350	556	442	617	533	619	598	721
4.5	6.5	410	628	499	649	552	692	662	779
	7	381	579	469	618	542	646	624	731
	7.5	366	564	456	620	539	637	611	720
	8	353	551	445	621	535	627	599	718
5	6.5	464	751	566	778	596	772	721	866
	7	408	633	500	644	556	683	658	782
	7.5	381	584	469	628	547	656	626	740
	8	362	562	451	626	540	640	606	721

Table D-14: Max Principal Stress at Transverse Crack, E=4×10^6 psi, α_C=3.5×10^{-6}/˚F, k-value=500 psi/in, Crack Spacing = 8 ft

First Layer Steel Depth (in)	Second Layer Steel Depth (in)	k-value=500							
		400 Microstrain Ultimate Shrinkage				700 Microstrain Ultimate Shrinkage			
		3 F˚/in Gradient		1.5 F˚/in Gradient		3 F˚/in Gradient		1.5 F˚/in Gradient	
		30 F˚ Drop	50 F˚ Drop	30 F˚ Drop	50 F˚ Drop	30 F˚ Drop	50 F˚ Drop	30 F˚ Drop	50 F˚ Drop
		Max Principal Stress at Slab (psi)	Max Principal Stress at Slab (psi)	Max Principal Stress at Slab (psi)	Max Principal Stress at Slab (psi)	Max Principal Stress at Slab (psi)	Max Principal Stress at Slab (psi)	Max Principal Stress at Slab (psi)	Max Principal Stress at Slab (psi)
3.5	6.5	370	565	454	600	526	629	601	707
	7	359	560	445	600	523	606	590	703
	7.5	352	557	443	606	524	606	588	709
	8	344	554	437	611	521	600	579	715
4	6.5	381	575	466	607	539	648	623	724
	7	368	561	454	608	537	630	609	707
	7.5	355	556	444	610	534	622	598	711
	8	348	552	441	614	534	621	596	715
4.5	6.5	409	629	499	647	553	692	660	778
	7	380	578	469	616	544	647	623	730
	7.5	365	562	455	617	541	638	610	714
	8	352	549	444	618	536	629	598	712
5	6.5	462	752	566	776	595	771	719	864
	7	407	634	500	647	557	683	657	781
	7.5	380	583	469	624	548	657	625	739
	8	360	560	451	623	541	641	605	716

Table D-15: Max Principal Stress at Transverse Crack, $E=5\times10^6$ psi, $\alpha_C=3.5\times10^{-6}/°F$, k-value=300 psi/in, Crack Spacing = 8 ft

First Layer Steel Depth (in)	Second Layer Steel Depth (in)	k-value=300							
		400 Microstrain Ultimate Shrinkage				700 Microstrain Ultimate Shrinkage			
		3 F°/in Gradient		1.5 F°/in Gradient		3 F°/in Gradient		1.5 F°/in Gradient	
		30 F° Drop	50 F° Drop	30 F° Drop	50 F° Drop	30 F° Drop	50 F° Drop	30 F° Drop	50 F° Drop
		Max Principal Stress at Slab (psi)	Max Principal Stress at Slab (psi)	Max Principal Stress at Slab (psi)	Max Principal Stress at Slab (psi)	Max Principal Stress at Slab (psi)	Max Principal Stress at Slab (psi)	Max Principal Stress at Slab (psi)	Max Principal Stress at Slab (psi)
3.5	6.5	457	701	565	754	650	779	744	884
	7	444	693	554	749	646	748	731	874
	7.5	437	689	551	756	647	747	729	882
	8	428	688	544	760	643	738	718	888
4	6.5	470	711	579	756	666	802	768	891
	7	455	694	563	756	663	776	752	879
	7.5	441	690	551	758	659	766	739	889
	8	433	688	547	763	659	764	737	895
4.5	6.5	502	766	616	801	685	856	812	955
	7	470	717	578	764	671	797	766	897
	7.5	453	699	562	765	667	785	750	895
	8	437	683	549	765	662	773	737	892
5	6.5	567	920	691	956	734	951	882	1061
	7	502	774	611	794	689	846	805	956
	7.5	471	724	577	772	676	809	766	906
	8	448	698	555	769	667	788	743	891

Table D-16: Max Principal Stress at Transverse Crack, $E=5\times10^6$ psi, $\alpha_C=3.5\times10^{-6}/^\circ F$, k-value=500 psi/in, Crack Spacing = 8 ft

First Layer Steel Depth (in)	Second Layer Steel Depth (in)	k-value=500							
		400 Microstrain Ultimate Shrinkage				700 Microstrain Ultimate Shrinkage			
		3 F˚/in Gradient		1.5 F˚/in Gradient		3 F˚/in Gradient		1.5 F˚/in Gradient	
		30 F˚ Drop	50 F˚ Drop	30 F˚ Drop	50 F˚ Drop	30 F˚ Drop	50 F˚ Drop	30 F˚ Drop	50 F˚ Drop
		Max Principal Stress at Slab (psi)	Max Principal Stress at Slab (psi)	Max Principal Stress at Slab (psi)	Max Principal Stress at Slab (psi)	Max Principal Stress at Slab (psi)	Max Principal Stress at Slab (psi)	Max Principal Stress at Slab (psi)	Max Principal Stress at Slab (psi)
3.5	6.5	456	695	564	749	651	779	742	880
	7	443	689	553	747	648	749	728	870
	7.5	436	686	550	753	649	748	726	877
	8	426	685	542	758	645	740	715	884
4	6.5	470	711	578	755	668	802	766	889
	7	454	693	562	754	665	778	751	874
	7.5	440	687	550	755	661	768	737	882
	8	432	684	546	760	661	766	735	888
4.5	6.5	502	768	616	800	686	856	810	954
	7	469	716	579	762	673	799	765	896
	7.5	452	697	562	763	668	787	749	889
	8	436	682	548	762	663	775	735	886
5	6.5	566	922	691	951	733	950	881	1059
	7	502	775	612	795	690	846	804	955
	7.5	470	722	578	769	677	810	766	905
	8	447	696	556	766	668	789	742	886

Table D-17: Max Principal Stress at Transverse Crack, E=4×10^6 psi, α_C=4.5×10^{-6}/°F, k-value=300 psi/in, Crack Spacing = 8 ft

First Layer Steel Depth (in)	Second Layer Steel Depth (in)	k-value=300							
		400 Microstrain Ultimate Shrinkage				700 Microstrain Ultimate Shrinkage			
		3 F°/in Gradient		1.5 F°/in Gradient		3 F°/in Gradient		1.5 F°/in Gradient	
		30 F° Drop	50 F° Drop	30 F° Drop	50 F° Drop	30 F° Drop	50 F° Drop	30 F° Drop	50 F° Drop
		Max Principal Stress at Slab (psi)	Max Principal Stress at Slab (psi)	Max Principal Stress at Slab (psi)	Max Principal Stress at Slab (psi)	Max Principal Stress at Slab (psi)	Max Principal Stress at Slab (psi)	Max Principal Stress at Slab (psi)	Max Principal Stress at Slab (psi)
3.5	6.5	450	733	534	727	580	743	676	843
	7	440	734	522	734	565	721	662	845
	7.5	435	729	519	742	567	712	660	856
	8	433	730	511	749	564	708	650	865
4	6.5	464	739	550	740	593	768	701	851
	7	451	734	534	745	581	736	686	855
	7.5	439	729	521	750	579	712	673	861
	8	434	726	516	757	579	707	670	869
4.5	6.5	501	805	588	817	636	828	747	907
	7	467	736	550	759	591	765	702	862
	7.5	451	727	533	763	588	731	686	871
	8	439	718	519	765	584	715	673	869
5	6.5	589	960	678	979	705	962	818	1027
	7	506	811	588	812	624	823	743	912
	7.5	471	751	550	774	599	765	705	882
	8	449	717	528	773	592	733	682	878

Table D-18: Max Principal Stress at Transverse Crack, E=4×10^6 psi, α_C=4.5×10^{-6}/˚F, k-value=500 psi/in, Crack Spacing = 8 ft

First Layer Steel Depth (in)	Second Layer Steel Depth (in)	k-value=500							
		400 Microstrain Ultimate Shrinkage				700 Microstrain Ultimate Shrinkage			
		3 F˚/in Gradient		1.5 F˚/in Gradient		3 F˚/in Gradient		1.5 F˚/in Gradient	
		30 F˚ Drop	50 F˚ Drop	30 F˚ Drop	50 F˚ Drop	30 F˚ Drop	50 F˚ Drop	30 F˚ Drop	50 F˚ Drop
		Max Principal Stress at Slab (psi)	Max Principal Stress at Slab (psi)	Max Principal Stress at Slab (psi)	Max Principal Stress at Slab (psi)	Max Principal Stress at Slab (psi)	Max Principal Stress at Slab (psi)	Max Principal Stress at Slab (psi)	Max Principal Stress at Slab (psi)
3.5	6.5	449	735	532	732	579	744	673	851
	7	438	729	521	731	569	717	660	841
	7.5	433	724	518	739	571	708	658	850
	8	431	723	510	745	568	703	647	859
4	6.5	464	733	548	737	592	769	700	848
	7	450	729	532	741	585	737	684	850
	7.5	437	724	520	746	582	708	671	859
	8	432	720	516	753	582	706	668	868
4.5	6.5	501	806	588	813	634	828	745	905
	7	466	731	550	755	594	765	701	856
	7.5	450	722	534	759	591	731	685	865
	8	436	713	519	760	587	718	671	862
5	6.5	590	961	682	976	704	962	816	1031
	7	508	812	589	816	623	823	742	911
	7.5	471	753	551	771	601	765	704	873
	8	447	719	529	768	594	735	681	870

Table D-19: Max Principal Stress at Transverse Crack, E=5×10^6 psi, α_C=4.5×10^{-6}/˚F, k-value=300 psi/in, Crack Spacing = 8 ft

First Layer Steel Depth (in)	Second Layer Steel Depth (in)	k-value=300							
		400 Microstrain Ultimate Shrinkage				700 Microstrain Ultimate Shrinkage			
		3 F˚/in Gradient		1.5 F˚/in Gradient		3 F˚/in Gradient		1.5 F˚/in Gradient	
		30 F˚ Drop	50 F˚ Drop	30 F˚ Drop	50 F˚ Drop	30 F˚ Drop	50 F˚ Drop	30 F˚ Drop	50 F˚ Drop
		Max Principal Stress at Slab (psi)	Max Principal Stress at Slab (psi)	Max Principal Stress at Slab (psi)	Max Principal Stress at Slab (psi)	Max Principal Stress at Slab (psi)	Max Principal Stress at Slab (psi)	Max Principal Stress at Slab (psi)	Max Principal Stress at Slab (psi)
3.5	6.5	553	896	662	909	712	917	833	1054
	7	542	899	648	916	700	890	817	1061
	7.5	537	896	644	925	701	880	815	1076
	8	531	904	635	933	697	878	802	1090
4	6.5	571	905	681	922	728	949	862	1058
	7	556	901	661	927	719	911	844	1067
	7.5	542	897	645	932	716	882	828	1074
	8	537	901	640	940	716	880	826	1088
4.5	6.5	612	979	725	1003	780	1019	916	1110
	7	575	904	679	941	732	946	862	1074
	7.5	557	895	659	944	727	905	843	1089
	8	542	887	642	945	722	881	827	1082
5	6.5	715	1174	827	1205	866	1180	1001	1273
	7	616	989	719	991	766	1016	909	1115
	7.5	580	911	678	955	741	946	863	1096
	8	555	885	651	951	731	903	835	1088

Table D-20: Max Principal Stress at Transverse Crack, E=5×10^6 psi, α_C=4.5×10^{-6}/˚F, k-value=500 psi/in, Crack Spacing = 8 ft

First Layer Steel Depth (in)	Second Layer Steel Depth (in)	k-value=500							
		400 Microstrain Ultimate Shrinkage				700 Microstrain Ultimate Shrinkage			
		3 F˚/in Gradient		1.5 F˚/in Gradient		3 F˚/in Gradient		1.5 F˚/in Gradient	
		30 F˚ Drop	50 F˚ Drop	30 F˚ Drop	50 F˚ Drop	30 F˚ Drop	50 F˚ Drop	30 F˚ Drop	50 F˚ Drop
		Max Principal Stress at Slab (psi)	Max Principal Stress at Slab (psi)	Max Principal Stress at Slab (psi)	Max Principal Stress at Slab (psi)	Max Principal Stress at Slab (psi)	Max Principal Stress at Slab (psi)	Max Principal Stress at Slab (psi)	Max Principal Stress at Slab (psi)
3.5	6.5	553	891	660	907	711	919	831	1050
	7	541	895	647	914	704	887	814	1051
	7.5	535	891	643	922	705	876	812	1066
	8	529	898	634	928	701	873	799	1079
4	6.5	571	899	679	919	727	950	861	1053
	7	555	896	659	924	723	911	842	1060
	7.5	540	892	644	928	719	877	826	1068
	8	535	894	639	936	719	874	823	1080
4.5	6.5	612	981	726	998	779	1020	914	1109
	7	574	899	680	937	735	946	861	1067
	7.5	556	890	659	940	730	905	841	1080
	8	540	883	642	941	725	884	825	1074
5	6.5	717	1176	832	1199	864	1180	999	1270
	7	616	991	721	996	765	1017	908	1114
	7.5	579	913	679	951	743	946	862	1087
	8	553	881	651	947	733	905	835	1081

Table D-21: Max Principal Stress at Transverse Crack, $E=4\times10^6$ psi, $\alpha_C=5.5\times10^{-6}$/˚F, k-value=300 psi/in, Crack Spacing = 8 ft

First Layer Steel Depth (in)	Second Layer Steel Depth (in)	k-value=300							
		400 Microstrain Ultimate Shrinkage				700 Microstrain Ultimate Shrinkage			
		3 F˚/in Gradient		1.5 F˚/in Gradient		3 F˚/in Gradient		1.5 F˚/in Gradient	
		30 F˚ Drop	50 F˚ Drop	30 F˚ Drop	50 F˚ Drop	30 F˚ Drop	50 F˚ Drop	30 F˚ Drop	50 F˚ Drop
		Max Principal Stress at Slab (psi)	Max Principal Stress at Slab (psi)	Max Principal Stress at Slab (psi)	Max Principal Stress at Slab (psi)	Max Principal Stress at Slab (psi)	Max Principal Stress at Slab (psi)	Max Principal Stress at Slab (psi)	Max Principal Stress at Slab (psi)
3.5	6.5	527	941	610	871	656	909	746	1013
	7	520	945	596	886	626	902	731	1025
	7.5	524	950	591	897	609	900	729	1048
	8	527	953	596	912	606	897	718	1069
4	6.5	546	952	630	904	673	920	776	1029
	7	533	948	610	895	641	907	758	1044
	7.5	524	953	595	910	623	902	743	1063
	8	526	944	597	924	623	890	741	1084
4.5	6.5	608	995	676	1000	726	994	829	1053
	7	555	941	629	918	663	908	778	1059
	7.5	540	940	609	932	636	895	760	1089
	8	530	939	599	938	631	884	745	1090
5	6.5	720	1177	801	1183	813	1175	913	1267
	7	620	1009	675	991	719	999	826	1080
	7.5	575	941	629	948	659	917	782	1092
	8	551	921	602	950	642	877	755	1103

Table D-22: Max Principal Stress at Transverse Crack, $E=4\times10^6$ psi, $\alpha_C=5.5\times10^{-6}$/˚F, k-value=500 psi/in, Crack Spacing = 8 ft

First Layer Steel Depth (in)	Second Layer Steel Depth (in)	k-value=500							
		400 Microstrain Ultimate Shrinkage				700 Microstrain Ultimate Shrinkage			
		3 F˚/in Gradient		1.5 F˚/in Gradient		3 F˚/in Gradient		1.5 F˚/in Gradient	
		30 F˚ Drop	50 F˚ Drop	30 F˚ Drop	50 F˚ Drop	30 F˚ Drop	50 F˚ Drop	30 F˚ Drop	50 F˚ Drop
		Max Principal Stress at Slab (psi)	Max Principal Stress at Slab (psi)	Max Principal Stress at Slab (psi)	Max Principal Stress at Slab (psi)	Max Principal Stress at Slab (psi)	Max Principal Stress at Slab (psi)	Max Principal Stress at Slab (psi)	Max Principal Stress at Slab (psi)
3.5	6.5	527	929	608	868	654	902	744	1007
	7	517	947	594	881	626	901	728	1019
	7.5	519	940	590	894	614	892	726	1040
	8	521	943	592	904	612	904	715	1060
4	6.5	548	940	628	905	672	911	774	1022
	7	536	938	608	890	641	900	756	1034
	7.5	520	942	594	905	628	891	741	1054
	8	522	935	593	918	629	897	738	1073
4.5	6.5	611	997	678	996	725	996	827	1053
	7	558	932	629	911	663	901	776	1045
	7.5	543	929	609	925	640	888	758	1078
	8	533	931	594	929	636	878	743	1074
5	6.5	722	1179	805	1178	811	1176	910	1267
	7	622	1011	680	994	718	1001	825	1074
	7.5	578	943	631	942	659	919	781	1083
	8	555	915	604	943	645	879	754	1091

Table D-23: Max Principal Stress at Transverse Crack, $E=5\times10^6$ psi, $\alpha_C=5.5\times10^{-6}$/˚F, k-value=300 psi/in, Crack Spacing = 8 ft

First Layer Steel Depth (in)	Second Layer Steel Depth (in)	k-value=300							
		400 Microstrain Ultimate Shrinkage				700 Microstrain Ultimate Shrinkage			
		3 F˚/in Gradient		1.5 F˚/in Gradient		3 F˚/in Gradient		1.5 F˚/in Gradient	
		30 F˚ Drop	50 F˚ Drop	30 F˚ Drop	50 F˚ Drop	30 F˚ Drop	50 F˚ Drop	30 F˚ Drop	50 F˚ Drop
		Max Principal Stress at Slab (psi)	Max Principal Stress at Slab (psi)	Max Principal Stress at Slab (psi)	Max Principal Stress at Slab (psi)	Max Principal Stress at Slab (psi)	Max Principal Stress at Slab (psi)	Max Principal Stress at Slab (psi)	Max Principal Stress at Slab (psi)
3.5	6.5	649	1155	757	1102	803	1115	919	1289
	7	639	1164	740	1113	773	1109	901	1300
	7.5	637	1177	735	1130	753	1119	899	1325
	8	640	1186	733	1147	748	1116	886	1349
4	6.5	671	1151	780	1124	824	1118	953	1303
	7	657	1167	756	1137	791	1117	932	1313
	7.5	644	1184	737	1146	770	1131	914	1341
	8	642	1176	732	1163	769	1110	912	1363
4.5	6.5	734	1204	832	1221	889	1211	1016	1325
	7	680	1164	777	1158	817	1120	953	1328
	7.5	662	1163	752	1173	785	1124	932	1365
	8	648	1170	732	1175	779	1106	915	1361
5	6.5	873	1439	980	1454	996	1440	1117	1585
	7	750	1222	825	1212	881	1220	1010	1353
	7.5	696	1157	775	1187	814	1119	956	1360
	8	665	1150	743	1186	792	1095	925	1370

Table D-24: Max Principal Stress at Transverse Crack, E=5×10^6 psi, α_C=5.5×10^{-6}/˚F, k-value=500 psi/in, Crack Spacing = 8 ft

First Layer Steel Depth (in)	Second Layer Steel Depth (in)	k-value=500							
		400 Microstrain Ultimate Shrinkage				700 Microstrain Ultimate Shrinkage			
		3 F˚/in Gradient		1.5 F˚/in Gradient		3 F˚/in Gradient		1.5 F˚/in Gradient	
		30 F˚ Drop	50 F˚ Drop	30 F˚ Drop	50 F˚ Drop	30 F˚ Drop	50 F˚ Drop	30 F˚ Drop	50 F˚ Drop
		Max Principal Stress at Slab (psi)	Max Principal Stress at Slab (psi)	Max Principal Stress at Slab (psi)	Max Principal Stress at Slab (psi)	Max Principal Stress at Slab (psi)	Max Principal Stress at Slab (psi)	Max Principal Stress at Slab (psi)	Max Principal Stress at Slab (psi)
3.5	6.5	649	1144	756	1099	802	1108	917	1283
	7	638	1154	739	1110	773	1103	898	1294
	7.5	635	1167	733	1126	758	1111	896	1318
	8	636	1176	730	1143	754	1109	882	1340
4	6.5	672	1142	778	1120	823	1122	952	1296
	7	656	1157	754	1130	791	1110	930	1307
	7.5	642	1173	736	1141	775	1121	912	1331
	8	639	1167	729	1157	775	1103	909	1353
4.5	6.5	738	1206	832	1216	888	1213	1014	1318
	7	680	1154	777	1151	817	1113	952	1321
	7.5	660	1159	753	1167	790	1115	931	1354
	8	645	1160	732	1169	784	1099	912	1351
5	6.5	876	1441	983	1451	994	1441	1114	1584
	7	754	1225	827	1210	880	1222	1009	1340
	7.5	700	1149	777	1180	814	1122	956	1351
	8	669	1143	745	1179	795	1090	924	1359

Table D-25: Max Principal Stress at Transverse Crack, E=4×10^6 psi, α_C=3.5×10^{-6}/˚F, k-value=300 psi/in, Crack Spacing = 12 ft

First Layer Steel Depth (in)	Second Layer Steel Depth (in)	k-value=300							
		400 Microstrain Ultimate Shrinkage				700 Microstrain Ultimate Shrinkage			
		3 F˚/in Gradient		1.5 F˚/in Gradient		3 F˚/in Gradient		1.5 F˚/in Gradient	
		30 F˚ Drop	50 F˚ Drop	30 F˚ Drop	50 F˚ Drop	30 F˚ Drop	50 F˚ Drop	30 F˚ Drop	50 F˚ Drop
		Max Principal Stress at Slab (psi)	Max Principal Stress at Slab (psi)	Max Principal Stress at Slab (psi)	Max Principal Stress at Slab (psi)	Max Principal Stress at Slab (psi)	Max Principal Stress at Slab (psi)	Max Principal Stress at Slab (psi)	Max Principal Stress at Slab (psi)
3.5	6.5	486	902	578	849	620	861	708	1044
	7	476	903	585	867	593	850	715	1061
	7.5	472	892	594	888	591	833	724	1096
	8	470	887	602	912	587	825	733	1121
4	6.5	501	884	597	876	636	856	740	1057
	7	487	883	594	898	611	839	725	1091
	7.5	475	876	599	912	607	822	722	1117
	8	469	868	607	939	607	805	731	1159
4.5	6.5	538	897	639	934	682	903	797	1096
	7	502	876	603	928	626	835	748	1118
	7.5	486	857	607	944	621	808	733	1141
	8	472	843	611	964	615	784	731	1170
5	6.5	637	1069	759	1139	760	1072	886	1297
	7	541	897	638	971	668	901	800	1149
	7.5	503	849	615	975	638	823	758	1170
	8	482	828	617	988	626	785	738	1196

Table D-26: Max Principal Stress at Transverse Crack, $E=4\times10^6$ psi, $\alpha_C=3.5\times10^{-6}/^{\circ}F$, k-value=500 psi/in, Crack Spacing = 12 ft

First Layer Steel Depth (in)	Second Layer Steel Depth (in)	k-value=500							
		400 Microstrain Ultimate Shrinkage				700 Microstrain Ultimate Shrinkage			
		3 F˚/in Gradient		1.5 F˚/in Gradient		3 F˚/in Gradient		1.5 F˚/in Gradient	
		30 F˚ Drop	50 F˚ Drop	30 F˚ Drop	50 F˚ Drop	30 F˚ Drop	50 F˚ Drop	30 F˚ Drop	50 F˚ Drop
		Max Principal Stress at Slab (psi)	Max Principal Stress at Slab (psi)	Max Principal Stress at Slab (psi)	Max Principal Stress at Slab (psi)	Max Principal Stress at Slab (psi)	Max Principal Stress at Slab (psi)	Max Principal Stress at Slab (psi)	Max Principal Stress at Slab (psi)
3.5	6.5	481.51	867	574	834	617	841	701	1020
	7	470.3	868	572	850	594	829	694	1036
	7.5	465.69	861	579	870	595	813	703	1064
	8	462.93	855	586	890	591	802	710	1089
4	6.5	497.08	859	593	864	633	840	733	1033
	7	481.43	855	579	879	615	824	718	1056
	7.5	469.32	848	584	891	610	806	705	1083
	8	463.54	840	590	911	610	789	707	1112
4.5	6.5	535.07	887	635	921	678	900	789	1064
	7	497.16	850	594	905	630	822	741	1078
	7.5	480.25	835	590	918	624	798	725	1097
	8	466.9	823	593	935	617	776	713	1124
5	6.5	634.33	1064	752	1122	756	1068	876	1266
	7	539.39	893	635	953	665	899	792	1106
	7.5	498.29	830	598	944	640	821	751	1124
	8	476.54	811	598	954	628	788	727	1143

Table D-27: Max Principal Stress at Transverse Crack, $E=5\times10^6$ psi, $\alpha_C=3.5\times10^{-6}$/°F, k-value=300 psi/in, Crack Spacing = 12 ft

First Layer Steel Depth (in)	Second Layer Steel Depth (in)	k-value=300							
		400 Microstrain Ultimate Shrinkage				700 Microstrain Ultimate Shrinkage			
		3 F˚/in Gradient		1.5 F˚/in Gradient		3 F˚/in Gradient		1.5 F˚/in Gradient	
		30 F˚ Drop	50 F˚ Drop	30 F˚ Drop	50 F˚ Drop	30 F˚ Drop	50 F˚ Drop	30 F˚ Drop	50 F˚ Drop
		Max Principal Stress at Slab (psi)	Max Principal Stress at Slab (psi)	Max Principal Stress at Slab (psi)	Max Principal Stress at Slab (psi)	Max Principal Stress at Slab (psi)	Max Principal Stress at Slab (psi)	Max Principal Stress at Slab (psi)	Max Principal Stress at Slab (psi)
3.5	6.5	603.31	1138	728	1107	771	1085	886	1365
	7	591.86	1140	735	1126	738	1082	895	1396
	7.5	587.97	1134	745	1148	733	1069	906	1407
	8	583.51	1131	754	1181	728	1063	916	1474
4	6.5	621.9	1112	745	1131	791	1072	916	1364
	7	605.2	1115	744	1161	758	1064	898	1407
	7.5	592.14	1115	749	1177	752	1056	901	1450
	8	586.44	1116	758	1218	753	1041	914	1491
4.5	6.5	664.9	1132	795	1203	842	1113	983	1407
	7	623.96	1110	752	1192	778	1061	924	1432
	7.5	605.29	1091	756	1208	770	1032	912	1460
	8	590.29	1078	760	1229	762	1009	915	1500
5	6.5	783.18	1347	939	1461	941	1331	1092	1660
	7	666.51	1117	787	1233	830	1115	984	1466
	7.5	627.15	1084	763	1244	791	1038	934	1490
	8	601.9	1063	765	1257	775	999	922	1520

Table D-28: Max Principal Stress at Transverse Crack, E=5×10^6 psi, α_C=3.5×10^{-6}/˚F, k-value=500 psi/in, Crack Spacing = 12 ft

First Layer Steel Depth (in)	Second Layer Steel Depth (in)	k-value=500							
		400 Microstrain Ultimate Shrinkage				700 Microstrain Ultimate Shrinkage			
		3 F˚/in Gradient		1.5 F˚/in Gradient		3 F˚/in Gradient		1.5 F˚/in Gradient	
		30 F˚ Drop	50 F˚ Drop	30 F˚ Drop	50 F˚ Drop	30 F˚ Drop	50 F˚ Drop	30 F˚ Drop	50 F˚ Drop
		Max Principal Stress at Slab (psi)	Max Principal Stress at Slab (psi)	Max Principal Stress at Slab (psi)	Max Principal Stress at Slab (psi)	Max Principal Stress at Slab (psi)	Max Principal Stress at Slab (psi)	Max Principal Stress at Slab (psi)	Max Principal Stress at Slab (psi)
3.5	6.5	598.87	1100	719	1087	768	1056	871	1329
	7	586.14	1105	720	1105	737	1056	872	1341
	7.5	581.7	1100	729	1127	738	1043	882	1379
	8	575.88	1098	736	1152	732	1038	891	1404
4	6.5	617.84	1084	741	1118	788	1054	908	1335
	7	599.76	1087	727	1139	763	1043	890	1368
	7.5	586.14	1084	732	1152	756	1033	875	1402
	8	580.19	1081	739	1178	756	1022	884	1433
4.5	6.5	661.3	1106	790	1185	839	1110	975	1374
	7	619.24	1084	740	1167	782	1045	916	1391
	7.5	599.62	1067	738	1182	773	1019	898	1411
	8	584.4	1056	741	1201	764	998	885	1442
5	6.5	780.78	1332	929	1437	937	1327	1081	1619
	7	662.46	1099	785	1215	827	1113	976	1419
	7.5	621.87	1064	745	1210	794	1035	926	1441
	8	596.39	1044	745	1220	778	991	899	1463

Table D-29: Max Principal Stress at Transverse Crack, E=4×10^6 psi, α_C=4.5×10^{-6}/˚F, k-value=300 psi/in, Crack Spacing = 12 ft

First Layer Steel Depth (in)	Second Layer Steel Depth (in)	k-value=300							
		400 Microstrain Ultimate Shrinkage				700 Microstrain Ultimate Shrinkage			
		3 F˚/in Gradient		1.5 F˚/in Gradient		3 F˚/in Gradient		1.5 F˚/in Gradient	
		30 F˚ Drop	50 F˚ Drop	30 F˚ Drop	50 F˚ Drop	30 F˚ Drop	50 F˚ Drop	30 F˚ Drop	50 F˚ Drop
		Max Principal Stress at Slab (psi)	Max Principal Stress at Slab (psi)	Max Principal Stress at Slab (psi)	Max Principal Stress at Slab (psi)	Max Principal Stress at Slab (psi)	Max Principal Stress at Slab (psi)	Max Principal Stress at Slab (psi)	Max Principal Stress at Slab (psi)
3.5	6.5	624.24	1322	695	1090	717	1272	832	1332
	7	626.48	1318	705	1118	692	1238	844	1374
	7.5	626.32	1326	716	1150	681	1244	857	1396
	8	623.51	1287	728	1192	671	1198	869	1473
4	6.5	625.15	1296	711	1132	739	1233	841	1354
	7	625.03	1300	718	1175	709	1226	850	1409
	7.5	622.75	1293	726	1197	681	1209	858	1465
	8	618.92	1260	737	1255	665	1172	871	1519
4.5	6.5	687.4	1306	778	1244	803	1237	903	1431
	7	625.04	1280	732	1227	736	1202	862	1463
	7.5	620.04	1248	737	1254	702	1165	870	1500
	8	613.38	1227	744	1290	676	1139	879	1555
5	6.5	815.62	1484	929	1511	912	1450	1010	1699
	7	694.21	1266	776	1296	795	1198	908	1516
	7.5	639.55	1222	751	1311	734	1144	888	1558
	8	615.57	1195	754	1336	691	1109	892	1600

Table D-30: Max Principal Stress at Transverse Crack, E=4×10^6 psi, α_C=4.5×10^{-6}/˚F, k-value=500 psi/in, Crack Spacing = 12 ft

First Layer Steel Depth (in)	Second Layer Steel Depth (in)	k-value=500							
		400 Microstrain Ultimate Shrinkage				700 Microstrain Ultimate Shrinkage			
		3 F˚/in Gradient		1.5 F˚/in Gradient		3 F˚/in Gradient		1.5 F˚/in Gradient	
		30 F˚ Drop	50 F˚ Drop	30 F˚ Drop	50 F˚ Drop	30 F˚ Drop	50 F˚ Drop	30 F˚ Drop	50 F˚ Drop
		Max Principal Stress at Slab (psi)	Max Principal Stress at Slab (psi)	Max Principal Stress at Slab (psi)	Max Principal Stress at Slab (psi)	Max Principal Stress at Slab (psi)	Max Principal Stress at Slab (psi)	Max Principal Stress at Slab (psi)	Max Principal Stress at Slab (psi)
3.5	6.5	604.29	1274	680	1070	717	1208	810	1295
	7	605.85	1281	688	1099	691	1215	820	1321
	7.5	605.85	1266	698	1130	673	1194	832	1362
	8	602.87	1254	708	1162	654	1181	842	1403
4	6.5	612.47	1247	694	1120	739	1187	830	1326
	7	605.36	1244	700	1148	709	1180	825	1365
	7.5	602.92	1236	706	1170	679	1164	831	1412
	8	599.21	1221	715	1206	670	1147	841	1458
4.5	6.5	684.38	1253	765	1221	799	1200	896	1390
	7	618.59	1227	712	1195	735	1162	840	1409
	7.5	601.52	1202	716	1220	700	1134	837	1441
	8	594.11	1187	722	1250	681	1113	843	1484
5	6.5	811.41	1454	918	1480	908	1423	1001	1649
	7	691.27	1222	773	1263	791	1175	900	1458
	7.5	636.41	1184	729	1265	731	1119	853	1496
	8	612.49	1159	730	1285	696	1087	853	1528

Table D-31: Max Principal Stress at Transverse Crack, $E=5\times10^6$ psi, $\alpha_C=4.5\times10^{-6}$/°F, k-value=300 psi/in, Crack Spacing = 12 ft

First Layer Steel Depth (in)	Second Layer Steel Depth (in)	k-value=300							
		400 Microstrain Ultimate Shrinkage				700 Microstrain Ultimate Shrinkage			
		3 F°/in Gradient		1.5 F°/in Gradient		3 F°/in Gradient		1.5 F°/in Gradient	
		30 F° Drop	50 F° Drop	30 F° Drop	50 F° Drop	30 F° Drop	50 F° Drop	30 F° Drop	50 F° Drop
		Max Principal Stress at Slab (psi)	Max Principal Stress at Slab (psi)	Max Principal Stress at Slab (psi)	Max Principal Stress at Slab (psi)	Max Principal Stress at Slab (psi)	Max Principal Stress at Slab (psi)	Max Principal Stress at Slab (psi)	Max Principal Stress at Slab (psi)
3.5	6.5	766.01	1658	878	1441	890	1577	1048	1749
	7	771.14	1662	889	1478	860	1573	1060	1796
	7.5	773.79	1688	902	1520	847	1597	1075	1852
	8	773.14	1641	915	1572	838	1537	1097	1914
4	6.5	768.05	1638	895	1497	917	1567	1055	1793
	7	770.29	1645	902	1531	881	1567	1065	1827
	7.5	770.11	1652	910	1575	848	1558	1075	1900
	8	768.5	1609	923	1630	830	1504	1093	1965
4.5	6.5	838.83	1650	961	1608	989	1574	1114	1854
	7	771.27	1625	915	1586	914	1537	1087	1892
	7.5	767.7	1595	921	1611	874	1496	1096	1927
	8	762.39	1573	926	1664	838	1471	1104	1996
5	6.5	1000.3	1874	1151	1943	1123	1843	1242	2163
	7	850.06	1610	953	1650	981	1530	1118	1952
	7.5	782.6	1563	934	1684	913	1474	1113	1994
	8	758.26	1534	937	1711	860	1436	1117	2042

Table D-32: Max Principal Stress at Transverse Crack, E=5×10^6 psi, α_C=4.5×10^{-6}/˚F, k-value=500 psi/in, Crack Spacing = 12 ft

First Layer Steel Depth (in)	Second Layer Steel Depth (in)	k-value=500							
		400 Microstrain Ultimate Shrinkage				700 Microstrain Ultimate Shrinkage			
		3 F˚/in Gradient		1.5 F˚/in Gradient		3 F˚/in Gradient		1.5 F˚/in Gradient	
		30 F˚ Drop	50 F˚ Drop	30 F˚ Drop	50 F˚ Drop	30 F˚ Drop	50 F˚ Drop	30 F˚ Drop	50 F˚ Drop
		Max Principal Stress at Slab (psi)	Max Principal Stress at Slab (psi)	Max Principal Stress at Slab (psi)	Max Principal Stress at Slab (psi)	Max Principal Stress at Slab (psi)	Max Principal Stress at Slab (psi)	Max Principal Stress at Slab (psi)	Max Principal Stress at Slab (psi)
3.5	6.5	746.08	1625	861	1409	890	1553	1022	1700
	7	750.15	1601	870	1437	859	1566	1033	1720
	7.5	752.51	1624	882	1474	838	1544	1047	1773
	8	751.5	1621	892	1511	821	1538	1059	1851
4	6.5	748.67	1573	876	1462	918	1512	1028	1722
	7	750.04	1586	882	1500	881	1515	1036	1777
	7.5	749.48	1592	888	1526	847	1508	1043	1838
	8	747.78	1586	898	1579	829	1498	1055	1893
4.5	6.5	836.7	1596	948	1585	986	1534	1106	1800
	7	756.04	1569	894	1552	914	1496	1053	1828
	7.5	748.18	1542	899	1580	872	1462	1059	1861
	8	742.4	1528	904	1614	842	1440	1066	1915
5	6.5	997.02	1845	1136	1909	1120	1819	1231	2128
	7	847.73	1564	950	1627	980	1507	1108	1881
	7.5	780.41	1522	911	1633	911	1447	1074	1928
	8	748.6	1496	912	1656	861	1412	1075	1964

Table D-33: Max Principal Stress at Transverse Crack, E=4×10^6 psi, α_C=5.5×10^{-6}/˚F, k-value=300 psi/in, Crack Spacing = 12 ft

First Layer Steel Depth (in)	Second Layer Steel Depth (in)	k-value=300							
		400 Microstrain Ultimate Shrinkage				700 Microstrain Ultimate Shrinkage			
		3 F˚/in Gradient		1.5 F˚/in Gradient		3 F˚/in Gradient		1.5 F˚/in Gradient	
		30 F˚ Drop	50 F˚ Drop	30 F˚ Drop	50 F˚ Drop	30 F˚ Drop	50 F˚ Drop	30 F˚ Drop	50 F˚ Drop
		Max Principal Stress at Slab (psi)	Max Principal Stress at Slab (psi)	Max Principal Stress at Slab (psi)	Max Principal Stress at Slab (psi)	Max Principal Stress at Slab (psi)	Max Principal Stress at Slab (psi)	Max Principal Stress at Slab (psi)	Max Principal Stress at Slab (psi)
3.5	6.5	801.15	1871	820	1381	876	1776	974	1647
	7	805.7	1865	833	1422	873	1759	999	1705
	7.5	806.55	1885	851	1468	865	1718	1026	1771
	8	812.45	1808	871	1529	862	1685	1052	1845
4	6.5	799.8	1836	841	1443	874	1742	988	1717
	7	802.63	1840	852	1487	868	1737	1020	1765
	7.5	801.52	1793	862	1544	859	1716	1035	1850
	8	802.71	1761	882	1612	847	1643	1066	1928
4.5	6.5	840.86	1838	925	1581	933	1743	1022	1803
	7	802	1801	871	1568	866	1699	1041	1857
	7.5	796.98	1748	879	1622	850	1636	1063	1922
	8	790.71	1702	892	1669	834	1583	1086	1990
5	6.5	1000.8	1979	1101	1916	1097	1931	1188	2122
	7	850.61	1763	921	1658	937	1662	1068	1943
	7.5	800.04	1701	902	1699	861	1590	1085	2003
	8	784.4	1654	913	1743	826	1532	1102	2065

Table D-34: Max Principal Stress at Transverse Crack, E=4×10^6 psi, α_C=5.5×10^{-6}/°F, k-value=500 psi/in, Crack Spacing = 12 ft

First Layer Steel Depth (in)	Second Layer Steel Depth (in)	k-value=500							
		400 Microstrain Ultimate Shrinkage				700 Microstrain Ultimate Shrinkage			
		3 F°/in Gradient		1.5 F°/in Gradient		3 F°/in Gradient		1.5 F°/in Gradient	
		30 F° Drop	50 F° Drop	30 F° Drop	50 F° Drop	30 F° Drop	50 F° Drop	30 F° Drop	50 F° Drop
		Max Principal Stress at Slab (psi)	Max Principal Stress at Slab (psi)	Max Principal Stress at Slab (psi)	Max Principal Stress at Slab (psi)	Max Principal Stress at Slab (psi)	Max Principal Stress at Slab (psi)	Max Principal Stress at Slab (psi)	Max Principal Stress at Slab (psi)
3.5	6.5	771.74	1794	801	1351	848	1689	941	1601
	7	775.83	1764	813	1389	845	1671	961	1639
	7.5	776.74	1787	826	1423	838	1695	984	1691
	8	776.34	1715	842	1474	829	1610	1005	1754
4	6.5	772.49	1739	829	1410	848	1662	955	1654
	7	774.09	1747	829	1452	842	1658	975	1710
	7.5	772.41	1737	837	1491	833	1637	989	1785
	8	769.41	1676	849	1543	821	1577	1012	1846
4.5	6.5	835.85	1749	912	1551	928	1668	997	1748
	7	774.18	1713	847	1525	841	1622	993	1782
	7.5	769.01	1671	853	1572	827	1577	1010	1833
	8	762.67	1635	861	1611	812	1539	1030	1892
5	6.5	992.68	1927	1087	1873	1090	1885	1166	2079
	7	845.25	1686	915	1612	933	1600	1017	1862
	7.5	794.09	1634	871	1637	857	1538	1028	1923
	8	763.13	1588	874	1672	816	1490	1042	1970

Table D-35: Max Principal Stress at Transverse Crack, E=5×10^6 psi, α_C=5.5×10^{-6}/˚F, k-value=300 psi/in, Crack Spacing = 12 ft

First Layer Steel Depth (in)	Second Layer Steel Depth (in)	k-value=300							
		400 Microstrain Ultimate Shrinkage				700 Microstrain Ultimate Shrinkage			
		3 F˚/in Gradient		1.5 F˚/in Gradient		3 F˚/in Gradient		1.5 F˚/in Gradient	
		30 F˚ Drop	50 F˚ Drop	30 F˚ Drop	50 F˚ Drop	30 F˚ Drop	50 F˚ Drop	30 F˚ Drop	50 F˚ Drop
		Max Principal Stress at Slab (psi)	Max Principal Stress at Slab (psi)	Max Principal Stress at Slab (psi)	Max Principal Stress at Slab (psi)	Max Principal Stress at Slab (psi)	Max Principal Stress at Slab (psi)	Max Principal Stress at Slab (psi)	Max Principal Stress at Slab (psi)
3.5	6.5	983.93	2345	1046	1818	1084	2236	1258	2180
	7	993.25	2353	1064	1871	1083	2228	1284	2245
	7.5	998.68	2331	1084	1932	1075	2194	1314	2321
	8	1014.2	2307	1110	2010	1085	2162	1349	2410
4	6.5	982.44	2307	1063	1899	1082	2201	1265	2253
	7	988.94	2326	1080	1948	1077	2209	1305	2297
	7.5	991.24	2281	1094	2022	1068	2144	1323	2410
	8	1005.4	2252	1121	2106	1071	2110	1375	2504
4.5	6.5	1024.5	2297	1138	2042	1141	2187	1299	2351
	7	989.35	2281	1099	2036	1075	2169	1324	2409
	7.5	986.83	2231	1115	2106	1059	2096	1349	2483
	8	988.64	2186	1130	2159	1048	2044	1372	2561
5	6.5	1225.5	2502	1365	2457	1350	2455	1500	2738
	7	1040	2239	1131	2135	1150	2129	1350	2504
	7.5	985.38	2180	1141	2192	1057	2055	1369	2570
	8	979.19	2135	1153	2241	1035	1988	1387	2642

Table D-36: Max Principal Stress at Transverse Crack, E=5×10^6 psi, α_C=5.5×10^{-6}/˚F, k-value=500 psi/in, Crack Spacing = 12 ft

First Layer Steel Depth (in)	Second Layer Steel Depth (in)	k-value=500							
		400 Microstrain Ultimate Shrinkage				700 Microstrain Ultimate Shrinkage			
		3 F˚/in Gradient		1.5 F˚/in Gradient		3 F˚/in Gradient		1.5 F˚/in Gradient	
		30 F˚ Drop	50 F˚ Drop	30 F˚ Drop	50 F˚ Drop	30 F˚ Drop	50 F˚ Drop	30 F˚ Drop	50 F˚ Drop
		Max Principal Stress at Slab (psi)	Max Principal Stress at Slab (psi)	Max Principal Stress at Slab (psi)	Max Principal Stress at Slab (psi)	Max Principal Stress at Slab (psi)	Max Principal Stress at Slab (psi)	Max Principal Stress at Slab (psi)	Max Principal Stress at Slab (psi)
3.5	6.5	953.44	2247	1020	1787	1054	2150	1214	2124
	7	960.92	2250	1036	1834	1053	2142	1240	2181
	7.5	965.35	2295	1054	1863	1047	2111	1268	2253
	8	975.75	2212	1075	1951	1049	2085	1293	2327
4	6.5	954.23	2213	1039	1852	1054	2121	1227	2195
	7	959.56	2229	1051	1907	1049	2126	1256	2235
	7.5	960.95	2188	1061	1967	1042	2127	1270	2331
	8	965.47	2163	1080	2034	1034	2042	1299	2410
4.5	6.5	1020.7	2226	1123	2023	1137	2140	1257	2279
	7	960.96	2195	1066	1991	1050	2094	1272	2318
	7.5	957.5	2145	1078	2054	1035	2037	1292	2378
	8	955.26	2113	1091	2091	1020	1992	1315	2468
5	6.5	1218.7	2450	1347	2431	1344	2411	1467	2699
	7	1035.6	2164	1126	2089	1146	2070	1296	2420
	7.5	968.76	2109	1099	2126	1054	2000	1309	2487
	8	948.88	2063	1107	2165	1013	1939	1323	2540